Nonlinear acoustic behaviours of perforated plates under grazing flow

Emanuele Sarpero

N°d'ordre NNT: 2025ECDL0017

THÈSE de DOCTORAT DE L'ÉCOLE CENTRALE DE LYON

École Doctorale N° 162
Mécanique Énergétique Génie Civil Acoustique

Spécialité de doctorat : Acoustique

Soutenue le 18/06/2025, par

Sarpero Emanuele

Nonlinear acoustic behaviours of perforated plates under grazing flow

---

Devant le jury composé de :

PIOT, Estelle ONERA Toulouse	Directrice de Recherche	**Rapportrice**
GABARD, Gwénaël Le Mans Université	Professeur	**Rapporteur**
LECLAIRE, Philippe ISAT Nevers	Professeur	**Examinateur**
ATALLA, Noureddine Université de Sherbrooke	Professeur	**Examinateur**
GALLAND, Marie-Annick École Centrale de Lyon	Professeure	**Directrice de thèse**
DRAGNA, Didier École Centrale de Lyon	Maître de conférences	**Co-Directeur de thèse**
GOURDON, Emmanuel École Nationale des Travaux Publics de l'État	Professeur	**Co-Directeur de thèse**

Abstract

This thesis studies the nonlinear acoustic behaviour of perforated plates under grazing flow from an experimental, analytical and numerical point of view. Perforated liners are widely used in aeronautics for noise reduction in aircraft engines, but their response to high sound pressure levels under flow is still difficult to predict.

From an experimental point of view, Kundt tube and duct measurements in the CAIMAN wind tunnel are carried out. A major contribution is the development of a procedure for precisely controlling the incident pressure level to study the behaviour of perforated plates at high levels. On the numerical front, simulations of acoustic propagation in ducts are carried out by solving linearized Euler equations in the time domain using finite-difference methods. A time-domain admittance boundary condition is implemented to take into account an admittance that varies with both frequency and velocity in the perforations.

A study was carried out on a first perforated plate. At normal incidence, the results show that the absorption coefficient of the perforated plate depends strongly on the amplitude of the sound. Comparisons are made with nonlinear impedance models in the literature, showing good overall agreement for different excitation levels. At grazing incidence, the results confirm that transmission loss varies strongly with level. The presence of a flow, even at low Mach numbers, tends to drastically reduce transmission loss and reduce the effect of sound level on the results. Comparisons with numerical simulations show that they faithfully reproduce the evolution of transmission loss with excitation level and with the presence of a flow.

Subsequently, a second perforated liner was designed with the aim of increasing transmission loss at high excitation levels and in the presence of flow. Wind tunnel measurements confirmed the significant increase in transmission loss under such conditions for this plate. Comparisons with numerical simulations again show good agreement and validate the methodology to design a more efficient liner in nonlinear regime and under flow.

The thesis also introduces a new nonlinear dynamic approach to the study of perforated plates, employing a multiple scale method. This research provides a better understanding of the nonlinear acoustic behaviour of perforated structures. The experimental techniques and numerical models developed provide essential tools for future research, facilitating the design of high-performance acoustic liner for noise control in academic and industrial applications.

Keywords: [perforated liners, nonlinear aeroacoustics, flow duct acoustics, transmission loss, nonlinear impedance models, multiple scale method, time domain acoustic simulations, two-source method]

Résumé

Cette thèse étudie le comportement acoustique non linéaire des plaques perforées sous un écoulement rasant d'un point de vue expérimental, analytique et numérique. Les revêtements perforés sont largement utilisés en aéronautique pour la réduction du bruit des moteurs d'avion, mais leur réponse à des niveaux de pression acoustique élevés sous écoulement reste encore difficile à prédire.

D'un point de vue expérimental, des mesures en tube de Kundt et en conduit dans la soufflerie CAIMAN sont réalisées. Une procédure permettant de contrôler précisement le niveau de pression incident pour étudier le comportement des plaques perforées à fort niveau à été developpé. Sur le plan numérique, des simulations de la propagation acoustique en conduit sont réalisées en résolvant les équations d'Euler linéarisées dans le domaine temporel par méthodes différences finies. Une condition limite d'admittance dans le domaine temporel est implémentée permettant de prendre en compte une admittance qui varie à la fois avec la fréquence et avec la vitesse dans les perforations.

Une étude est menée pour une première plaque perforée. En incidence normale, les résultats mettent en évidence que le coefficient d'absorption de la plaque perforée dépend fortement de l'amplitude du son. Des comparaisons avec des modèles d'impédance nonlinéaires de la littérature sont réalisées et montrent un bon accord global pour les différents niveaux d'excitation. En incidence rasante, les résultats confirment que la perte par transmission varie fortement avec le niveau sonore. La présence d'un écoulement, même pour des nombres de Mach faibles, tend à diminuer drastiquement la perte par transmission et à réduire l'effet du niveau sonore sur les résultats. Des comparaisons avec les simulations numériques montrent que celles-ci arrivent à reproduire fidèlement l'évolution de la perte par transmission avec le niveau d'excitation et avec la présence d'un écoulement.

Par la suite, une seconde plaque perforée est concue avec l'objectif d'augmenter la perte par transmission pour un niveau d'excitation acoustique élevé et en présence d'un écoulement. Les mesures en soufflerie permettent de confirmer l'augmentation significative de la perte de transmission dans de telles conditions pour cette plaque. Les comparaisons avec les simulations numériques montrent là encore un bon accord et valident la méthodologie pour concevoir un revêtement plus efficace en régime non linéaire et sous écoulement.

La thèse introduit également une nouvelle approche dynamique non linéaire pour étudier les plaques perforées, par l'utilisation d'une méthode à échelles multiples. Cette recherche permet de mieux comprendre le comportement acoustique non linéaire des structures perforées. Les techniques expérimentales et les modèles numériques développés fournissent des outils essentiels pour les recherches futures, facilitant la conception de revêtements acoustiques performants pour le contrôle du bruit dans les applications académiques et industrielles.

Mots clés: [Revêtements perforés, aéroacoustique non linéaire, acoustique des conduits sous écoulement, perte de transmission, modèles d'impédance non linéaire, méthode des échelles multiples, simulations acoustiques dans le domaine temporel, méthode à deux sources]

Résumé détaillé

Introduction

Cette thèse étudie le comportement acoustique non linéaire des plaques perforées sous un écoulement rasant et sous un fort niveau d'excitation acoustique. Les plaques perforées sont couramment utilisées dans l'industrie aéronautique pour la réduction du bruit des moteurs d'avion et sont aussi employées dans l'automobile, les infrastructures et l'architecture pour leurs propriétés acoustiques et leur capacité à absorber le son. Cependant, leur performance en présence d'un écoulement rasant et sous excitation acoustique élevée reste encore mal comprise. Les objectifs principaux de cette recherche sont d'améliorer la compréhension de la réponse acoustique des plaques perforées et de développer des modèles prédictifs plus précis pour l'industrie. L'étude s'appuie sur une approche à la fois expérimentale, analytique et numérique.

Contexte et motivation

L'optimisation des revêtements acoustiques perforés repose sur une compréhension fine des interactions entre l'onde acoustique incidente, l'écoulement rasant et la dynamique des perforations. Il est donc essentiel de développer une approche intégrant ces effets dans un cadre théorique et expérimental rigoureux. La variabilité des effets d'écoulement en fonction de la vitesse et de la fréquence des ondes acoustiques, la nécessité d'introduire des modèles non linéaires pour tenir compte des régimes acoustiques à forte amplitude et la difficulté d'obtenir des données expérimentales précises pour calibrer ces modèles constituent des défis majeurs.

Objectifs de la recherche

Le premier objectif est de modéliser efficacement l'impédance du revêtement d'un point de vue analytique, à travers la comparaison de modèles d'impédance existants adaptés au contexte de recherche. La propagation restera linéaire tout au long de l'étude. Sur le plan expérimental, l'étude utilise la soufflerie CAIMAN du LMFA, à l'École Centrale de Lyon, une installation spécifiquement conçue pour la caractérisation des traitements acoustiques en présence d'écoulement. L'objectif est de caractériser le banc d'essai, ainsi que de mettre en œuvre et d'adapter les techniques de mesure pour qualifier le comportement du revêtement sous fort niveau d'excitation acoustique et sous écoulement. Un premier aspect portera sur le développement et la réalisation de revêtements à tester en soufflerie acoustique, en se concentrant sur les matériaux et les techniques de fabrication. Un point central sera ensuite l'élaboration d'un protocole expérimental robuste permettant de contrôler le niveau d'excitation acoustique dans les bancs d'essai.

Du point de vue numérique, les deux objectifs de l'étude sont d'étendre les approches précédemment développées au LMFA pour y intégrer des conditions aux limites d'impédance non linéaire et prendre en compte les effets de l'écoulement et de les valider avec les experiences. De plus, la recherche vise à exploiter les outils analytiques développés au sein du laboratoire LTDS pour l'analyse transitoire de résonateurs non linéaires appliqués aux plaques perforées, en les intégrant aux simulations numériques. Des comparaisons seront effectuées avec les modèles existants. L'objectif est de développer un cadre prédictif robuste pour évaluer la perte par transmission obtenue à des niveaux de pression acoustique élevés et en régime d'écoulement.

Méthodologie

Le Chapitre 1 passe en revue les principaux modèles analytiques utilisés pour la modélisation des plaques perforées. Après une analyse des phénomènes physiques dans les régimes linéaire, non linéaire et en presence d'écoulement, le chapitre détaille chaque modèle. Tout d'abord, le modèle de Guess introduit une condition aux limites d'impédance. Ensuite, le modèle de fluide équivalent présente une condition aux limites d'impédance en traitant la plaque comme un milieu poreux. Enfin, l'approche Rice-Cummings définit une condition aux limites à l'aide d'un système d'équations différentielles décrivant les phénomènes physiques sous-jacents. Une première comparaison qualitative de ces modèles est également présentée. Le Chapitre 2 décrit l'étude expérimentale menée dans le cadre de cette thèse. Il commence par discuter des différentes techniques de fabrication et des matériaux disponibles pour la production de liners. Après avoir sélectionné les meilleures options, le chapitre détaille le processus de fabrication et d'assemblage. Il décrit ensuite les techniques de caractérisation et la methodologie employée dans le cas des forts niveaux acoustiques. Les mesures en incidence normale se feront à l'aide d'un tube d'impédance et en incidence rasante avec la veine d'essai Caiman du LMFA. Avant l'étude expérimentale, les bancs sont caractérisés d'un point de vue thermodynamique et acoustique. Une caractérisation de l'écoulement est également effectuée sur le banc caïman. Lors de la phase de mesure, une attention particulière est portée au contrôle des niveaux acoustiques déterminés à l'aide d'une procédure itérative. Le Chapitre 3 présente une revue des méthodes numériques actuelles pour la propagation dans les conduits. Après avoir presenté l'approche multimodale, il se concentre sur la résolution des équations d'Euler linéarisées par méthode de différences finies dans le domaine temporel (FDTD). Le chapitre introduit ensuite une condition aux limites d'admittance nonlinéraire appropriée pour modéliser le liner dans les simulations numériques. Enfin, il discute de plusieurs cas d'application pour ces simulations. Le Chapitre 4 présente les résultats des études numériques, analytiques et expérimentales d'un liner de référence. Il commence par montrer l'évolution des propriétés acoustiques en incidence normale, comparant différents modèles dans les gammes linéaire et non linéaire. Ensuite, il examine le comportement acoustique du liner de référence en incidence rasante, en mettant l'accent sur les effets des forts niveaux d'excitation acoustique et de l'écoulement. L'efficacité du liner et l'influence des divers phénomènes sont évaluées, suivies d'une comparaison des différentes approches numériques. Le Chapitre 5 porte sur l'extension de la méthode Rice-Cummings au régime non linéaire, en utilisant la méthode des échelles multiples pour définir l'impédance. Après avoir détaillé la procédure et effectué les calculs analytiques nécessaires, la méthode est appliquée à différentes plaques perforées pour validation. Les résultats obtenus sont comparés à d'autres modèles. Le dernier Chapitre 6 aborde le développement d'une procedure de conception de liner avec une performance améliorée pour les régimes non linéaires et sous écoulement. Après avoir étudié les valeurs optimales d'impédance, le processus de création d'un tel liner est détaillé. Le liner est testé en suivant les procédures décrites dans le Chapitre 4, d'abord en incidence normale, puis en incidence rasante avec écoulement. Des comparaisons sont effectuées entre les différents modèles et avec le liner de référence.

Résultats et conclusions

Les résultats expérimentaux et numériques ont mis en évidence plusieurs phénomènes importants. Il a été observé une forte dépendance de l'impédance acoustique de la plaque perforée à la vitesse de l'écoulement et au niveau d'excitation acoustique, indiquant la nécessité d'utiliser des modèles adaptés pour capter ces effets. Les comparaisons entre les modèles de fluide équivalent et les résultats expérimentaux ont montré une bonne corrélation pour des niveaux d'excitation modérés, validant ainsi l'utilisation de cette approche pour certaines applications. La méthode des échelles multiples s'est révélée efficace pour prédire les effets non linéaires. Enfin, les validations expérimentales des hypothèses numériques ont renforcé la pertinence des approches analytiques proposées, ouvrant la voie à des applications industrielles plus précises et efficaces.

Des investigations expérimentales ont été menées à l'aide d'un tube d'impédance et d'une soufflerie pour mesurer la réponse acoustique des plaques perforées dans des conditions contrôlées. Ces mesures ont permis de mieux comprendre les variations d'impédance en fonction des niveaux d'excitation et des régimes d'écoulement, comme présenté aux Chapitres 4 et 6. Le développement d'une procédure expérimentale rigoureuse a permis de contrôler précisément les niveaux de pression incidente, garantissant une

acquisition de données fiable, comme détaillé au Chapitre 2. Les résultats expérimentaux ont révélé une forte dépendance de l'impédance et des indicateurs acoustiques tels que le coefficient d'absorption et la perte par transmission à l'amplitude sonore et à l'écoulement, confirmant la nécessité d'intégrer les effets non linéaires et d'écoulement dans les modèles prédictifs. De plus, les résultats expérimentaux présentés dans cette étude constituent une base de données solide et précise pour des études ultérieures, aussi bien expérimentales que numériques.

Sur le plan numérique, des simulations en différences finies dans le domaine temporel ont été utilisées pour modéliser la propagation acoustique dans les conduits. Une avancée majeure a été l'implémentation d'une condition aux limites d'admittance en domaine temporel, présentée au Chapitre 3, qui a permis une simulation plus précise de l'impédance des plaques perforées en fonction de la fréquence et de la vitesse acoustique dans les perforations. Ces modèles numériques ont été validés à partir des données expérimentales, démontrant leur capacité à capturer les interactions complexes entre les ondes sonores, les perforations et l'écoulement. La forte concordance entre les résultats numériques et expérimentaux a confirmé l'efficacité de l'approche développée pour prédire les variations d'impédance dans des situations pratiques, comme illustré aux Chapitres 4 et 6.

Les modèles classiques d'impédance, tels que le modèle de Guess et l'approche fluide équivalent, ont été analysés et étendus afin de prendre en compte les nonlinéarités et les effets d'écoulement. La formulation de Rice-Cummings, initialement développée pour les résonateurs de Helmholtz, a été adaptée aux plaques perforées au moyen d'une approche multi-échelle, aboutissant à une expression affinée de l'impédance pour l'analyse transitoire dynamique des résonateurs non linéaires. Les modifications introduites dans cette thèse permettent une compréhension plus complète des facteurs influençant la résistance et la réactance acoustiques dans les structures perforées, en particulier pour les plaques perforées, comme présenté au Chapitre 5. Ces améliorations permettent une prédiction numérique facilitée par le traitement associé à des conditions aux limites du comportement de l'impédance à des niveaux élevés de pression acoustique et en présence d'un écoulement, répondant ainsi à un défi majeur dans le domaine.

Les principaux effets observés dans un régime non linéaire sont le décalage de la fréquence de résonance vers des valeurs plus élevées et un élargissement spectral de l'évolution des indicateurs acoustiques. Ce phénomène a été observé pour le coefficient d'absorption et l'impédance en incidence normale, ainsi que pour la perte par transmission (TL) en incidence rasante. Lors de l'introduction d'un écoulement, des effets similaires ont été observés, avec un décalage global de la fréquence et un élargissement du pic, entraînant une performance de plus en plus faible du revêtement. Il a été noté qu'au-delà d'un certain régime, les effets d'écoulement deviennent prédominants sur les effets non linéaires, ce qui a pour conséquence une performance affaiblie et une homogénéisation de l'impédance et de la vitesse acoustique le long du revêtement. Sans écoulement ou pour un écoulement de faible vitesse, l'impédance et la vitesse acoustique ne sont pas uniformes le long du revêtement, ce qui peut être modélisé avec la condition aux limites d'impédance proposée.

Au-delà des prédictions théoriques et numériques, cette thèse apporte une contribution aux applications pratiques dans l'amélioration des revêtements acoustiques. La meilleure compréhension du comportement des plaques perforées a permis la conception de revêtements plus efficaces en régime non linéaire et en présence d'écoulement, comme présenté au Chapitre 6, avec de meilleures performances dans ces conditions réalistes.

Les principaux résultats de cette recherche soulignent le rôle critique des effets non linéaires dans les plaques perforées. Les niveaux d'excitation élevés induisent une augmentation de la résistance de la plaque. L'introduction d'un écoulement modifie davantage la réponse en impédance et la perte par transmission et change le comportement de propagation du son. Ces résultats mettent en évidence les limites des modèles purement linéaires et la nécessité d'introduire des corrections dépendantes de la nonlinéarité et de l'écoulement pour des prédictions précises de l'impédance.

En conclusion, en intégrant des approches expérimentales, numériques et analytiques, cete these établit une base solide pour les recherches futures dans la technologie des liners acoustiques. Les résultats contribuent au développement de solutions de contrôle du bruit plus efficaces, avec des implications importantes pour la recherche académique et les applications industrielles. Ce travail ouvre la voie à une innovation continue dans le domaine de l'acoustique, favorisant les avancées dans la conception et l'optimisation des systèmes de réduction du bruit haute performance.

Acknowledgments

Je tiens tout d'abord à remercier mes directeurs de thèse, Marie Annick Galland, Emmanuel Gourdon et Didier Dragna pour leur soutien humain et professionnel inestimable, leurs encouragements constants et leurs conseils durant ces précieuses années passées ensemble. Merci au Jury de these, Estelle Piot, Gwenael Gabard, Philippe Leclaire et Noureddine Atalla pour avoir evaluè mes traveaux et avoir pu recevoir des utils conseils lors de la soutenance. Je remercie les directeurs des deux laboratoires, Christophe Bailly pour le LMFA et Jean-Luc Loubet pour le LTDS pour avoir créé des environnements de travail stimulants, sains et interactifs. Merci au personnel technique pour avoir soutenu ma partie expérimentale, Joachim Blanc Gonnet à l'ENTPE, Pascal Souchotte, Jean Charles Vingiano, Edouard Salze, Antonio Pereira, Oracio Correira et Emmanuel Jondeau au LMFA. Merci au personnel administratif pour les bonnes relations, Marie Noel Paillhes, Marie Gabrielle Perriaux, Syvliane Gouyot, Fatima El Bourkissi, Emelyne Rabany au LMFA, Pascale Avouac et Cécile Demornex à l'ENTPE. Je tiens à remercier les chercheurs et professeurs avec lesquels j'ai toujours eu l'occasion de comparer et de progresser, en particulier pour les relations étroites créées avec Marc Jacob, président de mon CST, Michel Roger, Gilles Robert, Vincent Clair, Philippe Blanc Benon, Daniel Jouve pour le centre acoustique, Alireza Ture Savadkoohi, Claude Henri Lamarque, Catherine Marquis Favre et Mathieu Lavandier pour l'ENTPE.

Bien sûr, je ne peux pas épargner mes amis et collègues, sans qui le voyage aurait été incroyablement plus long. Merci à tous les doctorants, postdocs et stagiaires que j'ai rencontrés sur mon chemin. Emilian, Pierre Louis, Hugo, Allan, Milo pour être le coeur du laboratoire, Simon avec qui nous avons aussi partagé des joies musicales, le sage Igor pour avoir toujours veillé à l'ordre public du bureau. Parmi les personnes déjà présentes à ce laboratoire, un grand merci à Jean pour m'avoir formé en tant que rappresentnat et Léo pour sa bonne humeur et Hemant pour avoir partagè les premiers mois ensemble. Merci à l'equipe italienne, Marilina, Stefano, Livia, Andrea, Jean et les autres. Merci à Alexis, avec qui nous avons partagé joies et peines pendant ces années de travail expérimental et de journées froides au J12. Outre les innombrables bêtises et leçons de langues, un merci tout particulier à Jules et Loïc, grâce à qui les journées étaient souvent plus douces. A l'ENTPE, merci à Aurélie, Melisandre, Maxime et Benjamin pour ces années de bonne humeur, de belles conférences et de longues pauses. Merci à tous les autres qui sont trop nombreux pour être tous cités.

Manju, Yuling, Laura et Giovanni, bien plus que des collègues, des amis et des compagnons de vie au fil des années, merci pour votre soutien constant et tous les bons moments passés ensemble, et à tous ceux à venir. Merci à Emile, le premier qui m'a accueilli en terre étrangère, que je considère plus comme le côté bourguignon de la famille, qui avec Arina représente maintenant un centre fort de ma vie.

Et maintenant, mes tantes, qui ont veillé toujours de manière omniprésente, à distance et pas que, Gina et Franca, peut-être avons-nous également conclu ce chapitre plus ou moins sans effets collateraux. Enfin, toute ma gratitude à ma famille, Vania, Guido et Mady, qui n'ont pas besoin de mots supplémentaires.

Table of contents

List of Acronyms and Symbols

Acronyms

err	Error	
MPP	Macro-perforated plate	
mPP	Micro-perforated plate	
nl	Nonlinear	
POA	Percentage Open Area	
PP	Perforated plate	
rms	Root mean square	
SPL	Sound Pressure Level	dB
TL	Transmission loss	dB

Greek letters

α	Absorption coefficient	
α_∞	Tortuosity	m
β	Nonlinear coefficient	m
δ_T	Thermal penetration depth	m
δ_V	Viscous penetration depth	m
ϵ	Perforation end length correction	m
κ	Thermal conductivity	$\mathrm{kg\,m\,s^{-3}\,K^{-1}}$
λ	Wavelength	m
μ	Dynamic viscosity	$\mathrm{kg\,m^{-1}\,s^{-1}}$
ν	Kinematic viscosity	$\mathrm{m^2\,s^{-1}}$
ω	Angular frequency	rad
ϕ	Perforation ratio	m
σ	Resistivity	m
ϱ	Density	$\mathrm{kg\,m^{-3}}$
ε	Multiple scale parameter	

Latin letters

C_D	Discharge coefficient	
c_0	Sound speed in air	$\mathrm{m\,s^{-1}}$
c_p	Specific heat	$\mathrm{J\,kg^{-1}\,K^{-1}}$
d_p	Diameter of the perforation	m
f	Frequency	Hz
H	Cavity length	m
h	Perforation length	m
k	Acoustic wave number	$\mathrm{m^{-1}}$
L_x, l_x	Duct horizontal dimension	m
L_y, l_y	Duct vertical dimension	m
L_z, l_z	Duct axial dimension	m
ℓ	Perforation end length correction	m
M	Mach number of mean flow	
M_0	Acoustic Mach number	
p	Pressure	Pa
Re	Reynolds number	
r_h	Relative humidity	
R	Resistance	$\mathrm{Pa\,s\,m^{-1}}$
S_0	Surface of the perforation	$\mathrm{m^2}$
S_c	Surface of the cavity	$\mathrm{m^3}$
Sh	Shear number	
t	Time	s
T	Temperature	°C or K
u	Mean flow velocity	$\mathrm{m\,s^{-1}}$
v	Local acoustic velocity	$\mathrm{m\,s^{-1}}$
V_c	Volume of the cavity	$\mathrm{m^3}$
X	Reactance	$\mathrm{Pa\,s\,m^{-1}}$
Y	Admittance	$\mathrm{m\,Pa^{-1}\,s^{-1}}$
Z	Impedance	$\mathrm{Pa\,s\,m^{-1}}$
Z_{N}	Dimensionless normalized impedance	

Symbols

$\Im$	Imaginary part
j	Imaginary unit so that $j^2 = -1$
π	Pi number
$\Re$	Real part

General introduction

Context

Controlling noise emissions in ducted flow environments is a critical challenge in various industrial sectors. This issue arises in applications such as jet engine nacelles, exhaust systems, and ventilation ducts, where high sound pressure levels can be generated. In aeronautical and automotive industries, for example, noise reduction is a key requirement for improving passenger comfort, ensuring regulatory compliance, and enhancing overall system efficiency. In extreme cases, such as aircraft engine nacelles, the high acoustic levels reached necessitate effective noise mitigation strategies. To address this issue, different noise control techniques have been developed. One of the most common solution to reduce noise is the use of perforated layers, with applications for example in HVAC duct silencers (Figure 1(a)) or engine nacelles liners (Figure 1(b)).

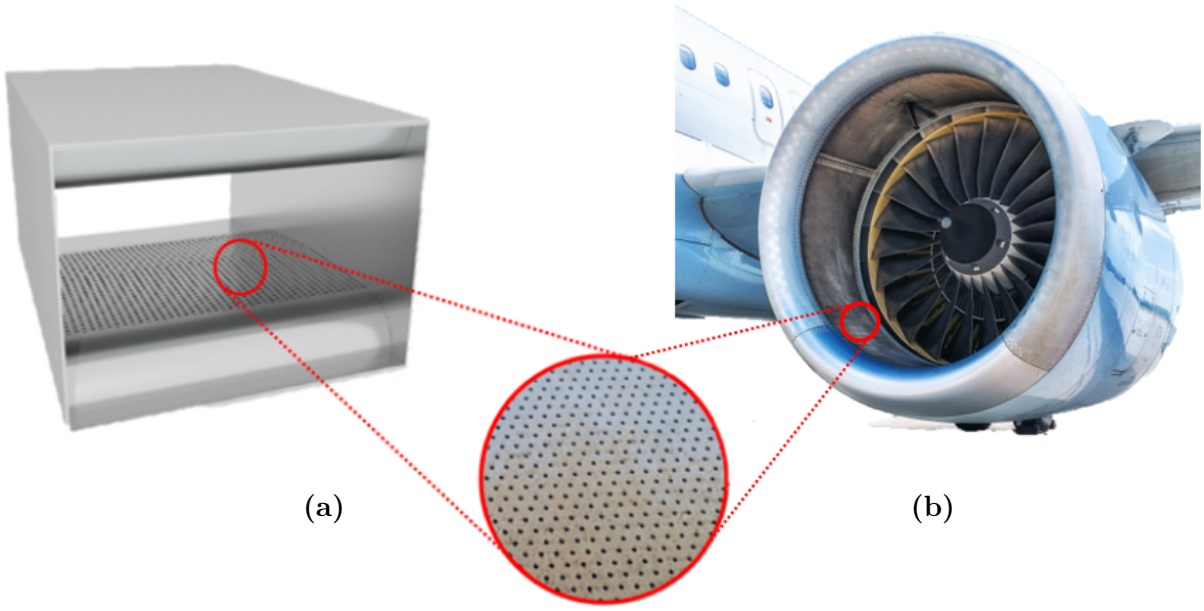

Figure 1: Application of perforated plates for (a) HVAC duct silencers [credits:Kinetics Noise Control] and (b) for engine nacelles liners [credits: Safran Aircraft Engines]

Traditional passive solutions include acoustic liners, such as perforated plates backed by honeycomb structures, which are designed to absorb and dissipate sound energy. These reduction devices must be resistant due to hostile environment conditions, being subjected to strong airflow and low temperatures in altitude. The use of certain materials, such as ceramic porous ones, cannot be used because of their tendency to absorb water, leading to freeze in flight. For this reason the most commons used devices in turbo reactors are metallic liners. Acoustic liners have been researched since the mid 20^{th} century for reducing noise, especially in aircraft. Typically, these passive devices are installed in the walls of aircraft

nacelle inlets and bypass ducts to absorb both tonal noise and broadband noise generated by the fan. These liners are usually designed as a single-degree-of-freedom (SDOF) system, as illustrated in Figure 2(a), or double-degree-of-freedom (DDOF) system, in Figure 2(b) , where the DDOF configuration is essentially an SDOF system with a porous septum embedded, often consisting of a porous wire mesh or perforated sheet.

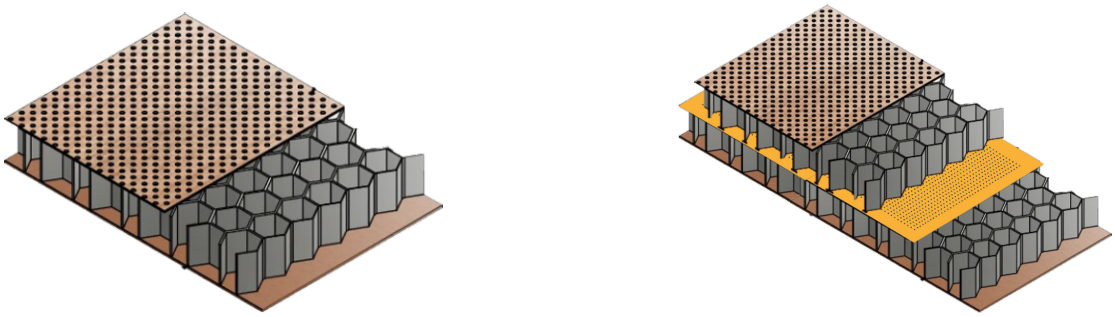

(a) SDOF (b) DDOF

Figure 2: Examples of Single Degree of Freedom and Double Degree of Freedom liners [credits: Bonomo et al.[27]]

The perforated plate can be assimilated to an Helmholtz resonator, particularly effective at certain discrete frequencies. The use of a DDOF widen the spectre of frequency, resulting versatile in broadband conditions, such as in the different phases of a flight (takeoff, landing etc.). The wire mesh utterly implement the broadband effect. Depending on the dimension of the perforations, the plates can be divided in micro-perforated (mPP), with a perforation diameter below 1 mm, and macro-perforated plates (MPP), with a perforation diameter above 1 mm. Combinations of the two are also studied, as well as heterogeneous honeycomb structures configurations. Recent research has explored advanced concepts, such as periodic media and acoustic metamaterials [71, 117]. The combination of passive and active noise control strategies is also being investigated to enhance overall efficiency. Other innovative strategies, such as electroacoustic liners [46] and plasma-based liners [132] provides promising results and advanced technologies.

The simplicity and repetitiveness of the liners geometries makes them easy to manufacture, and their acoustic behaviour is relatively easy to model at low sound pressure levels, where the properties of the liner does not depend on the excitation acoustic level. This regime is called linear regime. At higher acoustic levels, such as those experienced during aircraft flights or in strong ventilation systems (up to 170 dB), the acoustic performance of the liners changes due to nonlinear effects at the perforations (found on the upper plate of the liner), complicating the modeling of these materials and the predictions on their behaviour. At high sound pressure levels, the acoustic properties of the liners exhibit a nonlinear dependency on the acoustic velocity in the perforations. This regime is called nonlinear regime. When adding a grazing flow to the system, the behaviour of the liners is further modified, and the influence on the properties of the perforates is significant. Accurate modeling of acoustic propagation in flow ducts is essential for designing effective noise reduction solutions. However, most existing studies and design process assume linear acoustic behaviour, both in terms of wave propagation and liner response. When considering nonlinearities and the presence of flow, complex and non-classical acoustic responses result necessary to implement. In literature, precise details, in particular of experimental studies and setups, are not always presented, making it difficult to reproduce and compare results. Few studies have presented precise methodologies for liners design and construction, with a direct study of their acoustic behaviour in nonlinear regime and under flow.

In the past years, the acoustic behaviour of perforated plates, in particular under normal incidence, has been widely studied, both in linear and nonlinear regime. Many impedance models have been developed, following different approaches. Guess [62] presented a well established surface impedance model, taking into account both nonlinear and flow effects. Atalla [13] introduced an impedance model based on an equivalent fluid approach, further recently modified by Laly et al. [92] to account for nonlinear effects. Recently, detailed studies on microperforated plates have been introduced by Tayong et al. [144], presenting a deep insight in perforations interactions. The effect of nonlinear regime on, microperforated

have been assessed by Gallerand et al. [57]. Gallerand and Leclaire [58] provide an important study on the vibrational implications of an added damping effect induced by viscous and thermal exchanges in the boundary layers near perforations.

Recent works have presented an in-depth investigation into the study of liners, such as those presented by Jones et al. [81] at NASA and the experimental and numerical studies carried out in collaboration with ONERA in Toulouse [79], presenting results for well-tested experimental benches. An extensive theoretical and numerical study has recently been presented by Moufid [111], in which the nonlinear effects observed at high acustic regimes and in the presence of flow are mainly [112, 113] in continuity to the studies of Monteghetti et al. [109]. Spillere at al. [139, 138] from University of Santa Catarina presented an experimental study on properties of acoustic liners with flow, assessing interesting results on the influence of flow on liners transmission losses in both downstream and upstream configurations and on impedance. Shah et al. [133] experimentally studied at KTH Stockholm the properties of perforates in nonlinear regime and in presence of flow using a three-port measurement method. Billard [21] presented a study on the nonlinear behaviour of liners in the presence of flow, comparing to an experimental validation for several perforated plates based on previous studies conducted at LAUM laboratories in Le Mans [22]. In recent researches, the LMFA of Ecole Centrale de Lyon has developed numerical tools to predict acoustic propagation in a lined flow duct in the linear regime as well as acoustic propagation in outdoor environment in the nonlinear regime. Alomar et al. [10] have recently developed a numerical simulation, following Troian et al. in linear regime and mean flow [150], based on an equivalent fluid model. From a numerical point of view, the Euler equations have been solved in the time domain by finite difference methods. A preliminary work of Diab et al. [51] extended this approach using a time domain admittance boundary condition to study the nonlinear behaviour of perforated plates and acoustic liners. Even if performing an experimental validation of the study in normal incidence without flow, they limited the study of a liner under flow just to a numerical prediction. It is in this frame that this thesis aims to investigate, presenting a comprehensive and detailed study of liners behaviours in linear, nonlinear and flow regimes by experimental measures and analytical and numerical validations.

Objectives

This thesis investigates the nonlinear effects within lined ducts under flow conditions. The propagation will remain linear in all the course of the study. The first objective is to efficiently model the liner impedance from an analytical point of view through comparison of existing impedance models suitable for the research context.

Experimentally, the study employs the CAIMAN wind tunnel at the LMFA, Ecole Centrale de Lyon, a facility specifically designed for characterising acoustic treatments in flow conditions. The study aims to characterise the bench and to implement and adapt measurement techniques to account for nonlinear acoustic effects of the liner. A first aspect will be the development and realisation of liners to be tested in acoustic wind tunnel, concentrating on materials and realisation techniques. A core point will be the creation of a robust experimental protocol for correctly studying nonlinear acoustic behaviours and in presence of flow.

On the numerical side, the research aims to extend previous approaches from LMFA to incorporate nonlinear impedance boundary conditions and account for flow effects. Additionally, the research aims to employ analytical tools developed within the LTDS laboratory for transient analysis of nonlinear resonators for perforated plates applications, integrating them with numerical simulations. Comparisons will be made with existing models. The goal is to develop a robust prediction framework for assessing the transmission loss obtained at high SPL and flow regimes.

Through a combination of experimental validation and numerical modeling, this thesis aims to provide new insights into the nonlinear acoustic behaviour of liners. The findings will contribute to the development of more efficient noise reduction technologies for aerospace, automotive, and industrial applications.

Structure of the thesis

In this section the structure of the thesis and a short abstract of each chapter is presented.

Chapter 1: Impedance models of perforated plates

The first chapter focuses on a state-of-the-art of the main analytical models used for modelling perforated plates. After an analysis of the physical phenomena of perforated plates in linear, nonlinear and flow regimes, the models will be detailed, with attention paid to each of these fields. An initial qualitative comparison will be made between the three models.

Chapter 2: Description and characterisation of the experimental study

In this chapter, the outline of the experimental study conducted in the thesis is presented. It begins by discussing various manufacturing techniques and materials for liner production. After selecting the best options, the chapter details the fabrication and assembly process. It then describes the acoustic characterisation techniques, including normal incidence measurements using an impedance tube and grazing incidence measurements using the Caiman acoustic flow duct. Both downstream and upstream configurations are analysed. Thermodynamic, acoustic, and flow characterisations are performed, with special focus on the iterative process for determining and controlling acoustic levels.

Chapter 3: Numerical methods for duct acoustic propagation

The chapter presents a review of current numerical methods for duct propagation. After presenting the multimodal approach, it focuses on the finite difference time domain (FDTD) method. The chapter introduces the appropriate impedance boundary condition for modeling the liner in numerical simulations.

Chapter 4: Study of the acoustic behaviours of a reference liner

This chapter presents the results from numerical, analytical, and experimental studies of a reference liner. It begins by showing the evolution of acoustic properties under normal incidence, comparing different models, impedance approaches, and acoustic signals in both linear and nonlinear ranges. Next, it examines the acoustic behaviour of the reference liner under grazing incidence, emphasizing nonlinear effects and flow presence, both downstream and upstream. The efficiency of the liner and the influence of various phenomena are evaluated, followed by a comparison of different numerical approaches.

Chapter 5: Nonlinear dynamic approach to the study of perforated plates

Chapter 5 focuses on the analytical development of a differential equations approach to the nonlinear regime, using the multiple scales method. After detailing the procedure and performing the analytical calculations, the method is applied to various perforated plates for validation. The results are compared with other models, including direct numerical simulations.

Chapter 6: Study of the acoustic behaviours of an improved perforated plate liner

The final chapter discusses the development of a high-performance liner for nonlinear and under-flow regimes. After determining optimal impedance values in the Caiman flow duct case, the process for creating such a liner is detailed. The liner is tested using the procedures described in Chapter 4, first under normal incidence and then under grazing incidence with flow. Comparisons are made between different models and with the reference liner.

1 Impedance models of perforated plates

Contents

Abstract

This chapter provides a detailed examination of impedance models for perforated plates, integrating both theoretical and practical perspectives. Section 1.3.3 considers the Guess model, outlining its formulations for both linear and nonlinear regimes and its modifications for flow effects. Section 1.4 introduces the equivalent fluid approach, emphasizing its suitability for different perforation scales and its extensions to nonlinear and flow conditions. Finally, Section 1.5 presents an exact analytical solution for impedance from differential equations, drawing from the foundational work of Cummings and Rice. Together, these models form a comprehensive framework for understanding and predicting the acoustic behaviour of perforated plates, contributing to the advancement of noise control technologies.

1.1 Introduction

Perforated plates are broadly used in noise control applications, particularly in the aerospace, automotive and industrial sectors. Their ability to attenuate sound depends on their impedance properties, which regulate the way sound waves interact with perforations. These plates are often incorporated into acoustic liners, the design of which has a direct impact on overall noise reduction performance. Understanding and accurately predicting their impedance is essential for developing effective acoustic treatments. Impedance modelling allows the underlying physical mechanisms to be analysed, including the effects of viscous and thermal boundary layers, vortex generation and the influence of air flow. The study of impedance can be carried out under linear acoustics, nonlinear acoustics and flow conditions.

The development of impedance models has been supported by both theoretical and experimental research. In the linear acoustic regime, impedance is primarily determined by viscous, thermal and inertial effects. The Guess model [62] is one of the most widely adopted analytical models, as it accounts for viscosity, radiation, and backing effects. Derived from Crandall's theoretical framework on acoustic propagation in short tubes [40], it has been extensively validated for macro-perforated plates. Ingard et al. [70] refined the understanding of resistance corrections, while Melling [107] provided experimental validation, further strengthening the model's reliability. An alternative approach is the equivalent fluid model, originally developed by Johnson and Allard [74, 7] and later refined by Atalla and Sgard [13]. This method treats the perforated plate as a homogeneous medium with specific flow resistivity and tortuosity, offering a practical way to model acoustic behaviour. Laly et al. [93] improved this model by including orifice interaction effects, utilizing Fok function approximations [54, 107, 127, 128].

Below a given acoustic level, the acoustic properties does not depend on the SPL. This regime is called linear. When exceeding this level, the assumption of linearity no longer holds, and the acoustic properties depend also on the SPL. This regime is called nonlinear, requiring nonlinear modeling approaches. Nonlinear effects arise primarily due to increased acoustic velocities in the perforations, leading to vortex shedding and enhanced acoustic resistance. Ingard et al. [70] introduced a nonlinear resistance correction, which was later incorporated into the Guess model [62]. More recent studies by Roncen et al. [122, 123] investigated how impedance varies spatially in high SPL conditions, particularly in aeroacoustic liners. Within the equivalent fluid framework, Laly et al. [93] proposed a nonlinear extension, modifying resistivity and tortuosity parameters based on Maa's work [98]. The correction for flow resistivity in the nonlinear regime follows a Forchheimer-type law, with coefficients introduced by Cummings [44], Rice [119], and Groeneweg [61], providing a more refined description of perforated plate behaviour under intense acoustic excitation.

In many practical applications, perforated plates are subjected to a grazing mean flow, which further alters their impedance characteristics. The presence of grazing flow affects both the resistive and reactive components of impedance, generally increasing resistance and decreasing reactance. Ingard and Ising [70] developed an empirical correction for this effect, based on observations of the interaction between the turbulent boundary layer and the perforations. Guess [62] incorporated these findings into his model, introducing an empirical coefficient derived from experimental data. Subsequent work by Kooi et al. [88] improved impedance predictions by considering the impact of boundary layer profiles. Dai and Aurégan [45] developed a more advanced impedance model that accounts for multiple nonlinear regimes under flow conditions. In [14], Auregan and Pachebat compare acoustic measurements and an equivalent fluid model showing that the main effect of high sound level on sound propagation through rigid porous materials is the variation of the flow resistivity. Additionally, Wen et al. [152] proposed an impedance extraction method for perforated plates under grazing flow, validating their model through experimental comparisons. More recently, Meng et al. [108] introduced a semi-empirical approach using the Particle Velocity Match (PVM) technique, which incorporates boundary layer displacement thickness. Their results closely aligned with predictions from the Guess model, reinforcing the accuracy and applicability of these models. Recently, different approaches and developments have been accomplished into the study of perforates under flow,

such as the studies presented by Inagaki et al, [68], Zhang et al. [156], Mallick et al.[99] and Crouse et al.[42].

1.2 Acoustic phenomena in perforations

The study of the behaviour of perforated materials for noise reduction in aeronautics is a topic of relevant and current interest. The correct prediction of the acoustic behaviour of such materials is of primary importance for the effective modelling of more complex structures to be placed in environments with high noise levels and in the presence of flows. The most widely used acoustic treatment in aeronautics is the perforated liner. This technology consists of a rigid perforated plate backed by a resonant cavity, typically defined as honeycomb, with a rigid termination. The degrees of freedom of the system are defined by the number of layers of the liner. Considering a cylindrical orifice, the shape of the perforations play a key role in the velocity field near the inlet and outlet of the perforations. In the course of this discussion, we will focus on SDOF MPPs for issues of experimental realisation accuracy. In addition, the convention $e^{+j\omega t}$ is employed, where $\omega = 2\pi f$ is the angular frequency and f the frequency.

1.2.1 Linear acoustic regime

An acoustic liner can be considered as an array of adjacent Helmholtz resonators with individuals or common backup cavities. Each resonator is called a cell. The simple Helmholtz resonator consists of a perforated plate ( ) backed by a rigid end cavity ( ), as presented in Figure 1.1).

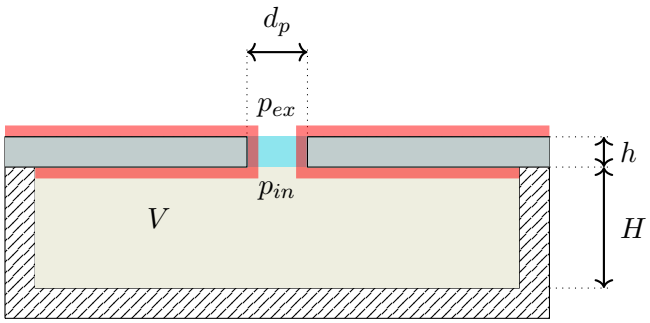

Figure 1.1: Scheme of an Helmholtz resonator

Let us detail the dimensions of the resonator: H is the cavity length, h is the perforation length, d_p is the diameter of the perforation, with the radius $r_p = d_p/2$, V_p is the volume of the perforation (in Fig. 1.1), and V is the cavity volume (in Fig. 1.1). In addition, we denote by p_{out} the pressure on the external side of the perforation and p_{in} is the pressure on the internal side of the perforation (cavity side). We define also S_0 the perforation surface (equal to $S_0 = \pi r_p^2$ for cylindrical perforations) and S_c the surface of the cavity (equal to $S_c = \pi r_c^2$ for cylindrical cavities of radius r_c).

The resonant frequency of this device, called also the Helmholtz resonance frequency f_h, is given by:

$$f_h = \frac{c_0}{2\pi}\sqrt{\frac{S_0}{Vh}} \tag{1.1}$$

with c_0 the sound speed (depending on temperature, e.g. $c_0 = 343$ m/s at $T = 20°C$).

When impacted by an acoustic wave, the surfaces of the resonator are exposed to visco-thermal losses, that occur in viscous and thermal boundary layers of characteristic size δ_V and δ_T, respectively:

$$\delta_V = \sqrt{\frac{2\mu}{\varrho_0 \omega}} \qquad \delta_T = \sqrt{\frac{2\kappa}{\varrho_0 c_p \omega}} \tag{1.2}$$

where μ is the fluid dynamic viscosity, ϱ_0 the fluid density, κ is the thermal conductivity, and c_p the specific heat. For the thermodynamic properties it has been made reference to the experimental values of pressure and temperature, and for dynamic viscosity μ it has been adopted a classical Sutherland law defined as:

$$\mu = \mu_0 \frac{T_0 + S}{T + S} \left(\frac{T}{T_0} \right)^{3/2} \tag{1.3}$$

where μ_0 is the reference viscosity, T the measured temperature in [K], $T_0 = 273.11$K the reference temperature and the constant $S = 110.56$K [83, 153]. We define the cinematic viscosity $\nu = \mu/\varrho_0$. The thickness of the viscous and thermal boundary layer is represented by the line ( ) in Fig. 1.1.

Considering the perforation, it is possible to define the ratio of the total surface of the perforations to the plate surface thanks to the perforation ratio $\phi = S_0/S_c$ or its percentage value the Percentage Open Area POA.

The acoustic impedance of the perforation can be expressed as [86]:

$$Z_{perf}(\omega) = \frac{p_{in} - p_{ex}}{v} = R_{perf}(\omega) + \mathrm{j} X_{perf}(\omega) \tag{1.4}$$

where v is the acoustic velocity in the perforation. R_{perf} and X_{perf} are the perforation acoustic resistance and reactance, respectively. In the linear acoustic regime, the impedance does not depend on the acoustic level and on the amplitude of the acoustic velocity v. The evaluation of the surface normal impedance of a single perforation is crucial in the study of a resonator. The resistive component of the impedance arises from thermoviscous effects within the perforation due to losses in the boundary layer and at the edges of the perforations, where the acoustic flow is distorted. The reactive component reflects the motion of the air in the cavity, increasing its effective mass, which is effectively thicker than the perforation depth due to the mass loading caused by sound radiation from the perforation and the distortion of acoustic flow at the plate surface. The addition of correction lengths to the perforation depth accounts for this inertial effect.

Among different approaches, a surface impedance model provided by Guess [62] will be detailed in Sec. 1.3.3. This approach is based on the Crandall theory on acoustic propagation in short tubes [40]. An equivalent fluid approach, developed by Atalla and Sgard [13], will be presented in Sec. 1.4. In this method, the tortuosity is a function of the correction length induced by the radiation from a micro-perforated plate.

1.2.2 Nonlinear acoustic regime

In the nonlinear acoustic regime, the root mean square (rms) value of the acoustic particle velocity in the perforations (v_{rms}) reaches high values (order of magnitude of a few tens of ms^{-1}). At both the perforation's inflow and outflow (in Fig. 1.2), acoustic energy is converted into vorticity and eventually dissipated by viscous forces [43, 44, 136]. This process primarily raises the acoustic resistance of the material, potentially enhancing or reducing the performance of the resonator. In such case, the impedance depends also on the orifice axial velocity. The Mach number is a dimensionless number indicating the ratio of a given velocity (of a sound or of a flow) to the sound speed c_0. At this regard, a perforation Mach number $M_0 = v_{\mathrm{rms}}/c_0$ can be defined.

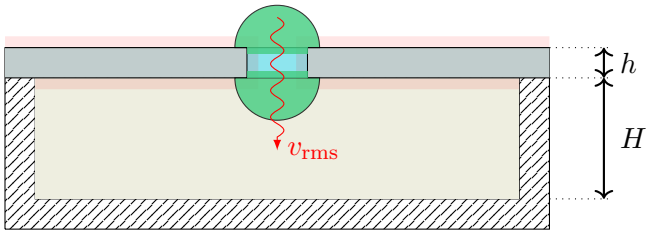

Figure 1.2: Scheme of an Helmholtz resonator in a nonlinear acoustic regime

Following several studies [62, 70, 98, 107] the impedance modifies adding a nonlinear specific term as:

$$Z_{perf} = Z_{perf}(\omega, v_{\text{rms}}) = R_{perf}(\omega) + \mathrm{j}X_{perf}(\omega) + \Theta_{perf}(\omega, v_{\text{rms}}) \tag{1.5}$$

The term Θ_{perf} represents the nonlinear component of the impedance. The primary requirement is the evaluation of the nonlinear term of the resistance $R_{perf}(\omega, v_{\text{rms}})$, as the reactance typically remains relatively constant with increasing sound pressure levels [62, 107, 105]. During the recent years, the evaluation of the nonlinear effects has been the focus of different studies corroborated both by numerical and experimental results [137, 143].

In this study, the nonlinear approach proposed by Guess will be detailed in Section 1.3.2, and the one developed in the equivalent fluid model in Section 1.4.

1.2.3 Nonlinear acoustic regime under a grazing flow

For aeronautical applications, it is necessary to account for a grazing flow on the liner. The characteristics of the flow play a considerable effect on the perforation, altering its nonlinear behaviour and acting as an inducement or obstruction to acoustic propagation within the perforation due to the flow boundary layer (Fig.1.3).

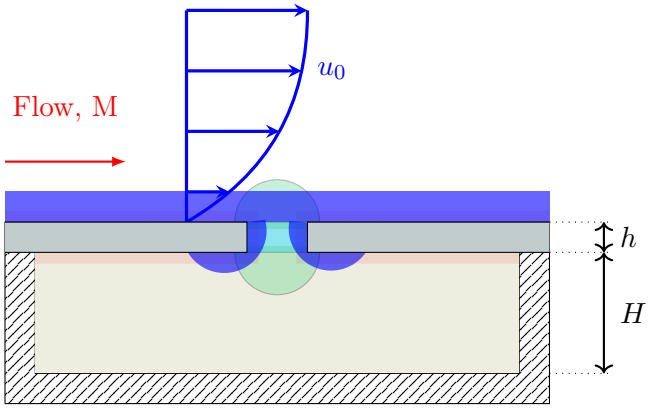

Figure 1.3: Sketch of an Helmholtz resonator in a nonlinear acoustic regime in presence of a grazing flow.

Most experimental research and accompanying empirical models suggest that a grazing flow across the surface of a perforation increases acoustic resistance while decreasing acoustic reactance [124]. This

phenomenon is due to the interaction between the grazing flow and the sound pressure field that causes some of the flow to be drawn into the cavity during the inflow phase and expelled during the outflow phase (■ in Fig.1.3). Away from the perforation, the grazing flow remains steady. The actual area through which the sound particle flow enters and exits the cavity appears as smaller than the real orifice area [63, 97].

1.3 Guess Impedance model

1.3.1 Guess impedance model in linear regime

A well-spread and validated surface impedance model for perforated plate liner is the one proposed by Guess [62]. It includes the classical impedance terms related to viscosity, radiation, and backing effects, along with terms accounting for high sound amplitude and steady grazing flow.

Following Kinsler and Frey [86], the specific acoustic impedance Z_{perf} for a short tube considering viscous and mass effects is given by:

$$Z_{perf} = -\mathrm{j}\varrho_0\omega t\left[\frac{2}{Kr_p}\frac{J_1(Kr_p)}{J_0(Kr_p)} - 1\right] \tag{1.6}$$

where J_0 and J_1 are the zeroth and first order Bessel function of the first kind and K is defined such that $K^2 = -\mathrm{j}\omega/\nu$. A non-dimensional acoustic impedance Z for a perforated plate can be derived as

$$Z = \frac{Z_{perf}}{\phi\varrho_0 c_0} \tag{1.7}$$

that is approximated to take into account viscous edges effects. When the boundary layer thickness is thinner then the perforation radius, such as in macro-perforated liners (with a diameter superior to 1 mm), it is possible to approximate the specific acoustic impedance as

$$Z \simeq \frac{\sqrt{2\nu\omega}\ell}{\phi c_0 r_p} + \mathrm{j}\left(\frac{\sqrt{2\nu\omega}\ell}{\phi c_0 r_p} + \frac{\omega h}{\phi c_0}\right) \tag{1.8}$$

The correction length $\ell = h + 2r_p$ accounts for the viscous effects occurring at both entrances of the perforation [69]. The normalized impedance provided by Guess is obtained by adding the remaining effects, namely interaction, radiation, and back-plate reflection, as :

$$Z = \frac{\sqrt{2\nu\omega}\ell}{\phi c_0 r_p} + \frac{2\pi^2}{\phi}\left(r_p\omega\right)^2 + \mathrm{j}\left(\frac{\sqrt{2\nu\omega}\ell}{\phi c_0 r_p} + \frac{\omega(h+\epsilon_1)}{\phi c_0} - \cot\left(kH\right)\right) \tag{1.9}$$

The term ϵ_1 is a correction to the mass inertance being equal to $\epsilon_0(1-0.7\sqrt{\phi})$. As explained by Crandall [40], the term $\epsilon_0 = 16r_p/(3\pi)$ is regarded as an end correction. The term $(1-0.7\sqrt{\phi})$ represents the influence of orifice interactions, combining both internal and external effects [21]. The term $\cot(kH)$ takes into account the back-plate effects, being k the angular wavenumber.

1.3.2 Guess impedance model in nonlinear regime

Nonlinearities are known to induce frequency coupling, complicating the definition of impedance for nonlinear effects at specific frequencies. Guess addressed this issue by predicting the influence of nonlinearities

on impedance at a designated frequency based on the study carried by Ingard et al. [70]. Ingard established a correction for nonlinear resistance through empirical investigation employing a tube with an orifice plate and an acoustic driver, which facilitated measurements of acoustic pressure and velocity. The results revealed a linear relationship between pressure and velocity at low amplitudes and a quadratic relationship at elevated amplitudes. They demonstrated that, at high sound pressure levels, the impedance of a Helmholtz resonator is particularly proportional to the perforation acoustic velocity.

Taking into account the nonlinear resistance correction proposed by Ingard [70], the normalized Guess impedance modifies such that

$$Z = \frac{\sqrt{2\nu\omega}\ell}{\phi c_0 r_p} + \frac{2\pi^2}{\phi}\left(r_p\omega\right)^2 + \frac{1-\phi^2}{\phi}\frac{v_{\mathrm{rms}}}{c_0} + \mathrm{j}\left(\frac{\sqrt{2\nu\omega}\ell}{\phi c_0 r_p} + \frac{\omega(h+\epsilon_2)}{\phi c_0} - \cot\left(kH\right)\right) \tag{1.10}$$

with M_0 the orifice Mach number. Note that M_0 was based on the velocity amplitude in the perforation in the original Guess model. In this study, we use instead the rms acoustic particle velocity in the perforation, yielding $M_0 = v_{\mathrm{rms}}/c_0$. In addition, the end correction ϵ_1 is also modified such that

$$\epsilon_2 = \frac{16 r_p}{3\pi}(1 - 0.7\sqrt{\phi})\frac{1 + 5\cdot 10^3 M_0^2}{1 + 10^4 M_0^2} \tag{1.11}$$

where the factor $[(1 + 5\cdot 10^3 M_0^2)/\ (1 + 10^4 M_0^2)]$ aims at accounting for nonlinear effects on the end correction [61].

1.3.3 Guess nonlinear impedance model in the presence of flow

The impedance expression under grazing flow involves the module of the flow velocity $|u'|$, which estimates the magnitude of turbulent velocity fluctuations within the perforations due to a turbulent boundary layer at the relevant frequency, expressed as:

$$Z = \frac{\sqrt{2\nu\omega}\ell}{\phi c_0 r_p} + \frac{2\pi^2}{\phi}\left(r_p\omega\right)^2 + \frac{1-\phi^2}{\phi}\left(\frac{v_{\mathrm{rms}}}{c_0} + \frac{|u'|}{c_0}\right) + \mathrm{j}\left(\frac{\sqrt{2\nu\omega}\ell}{\phi c_0 r_p} + \frac{\omega(h+\epsilon_3)}{\phi c_0} - \cot\left(kH\right)\right) \tag{1.12}$$

The term $|u'|/c_0$ is derived experimentally by Ingard et al. [70] who considered a steady flow superimposed through the perforation. Ingard and Ising asses that the turbulent boundary layer at the surface of the perforated plate causes fluctuating flow through the perforation, which is superimposed on the acoustic fluctuations. They assumed that these turbulent velocity fluctuations occur at a much lower frequency than the acoustic fluctuations and, as a result, act like a quasi-steady flow through the perforations. Consequently, the grazing flow's impact on impedance is considered similar to that of acoustic velocity.

Guess used an approximation for $|u'|/c_0$ based on the experimental data from Dean [47] such that:

$$\frac{|u'|}{c_0} \sim k_{\mathrm{G}} M \tag{1.13}$$

with $k_{\mathrm{G}} = 0.3$ being an empirical coefficient and $M = u_{\mathrm{av}}/c_0$ is the Mach number associated to the average flow velocity u_{av}. Allam et al. [6] employed a value of $k_{\mathrm{G}} = 0.15$ for perforated liners with a perforation of diameter 1 mm, thickness 1 mm and a Mach number up to 0.15. This model implicitly accounts for the boundary layer thickness's effect on resistance through the empirical parameter k_{G}, which is derived from resistance measurements.

The end correction ϵ_3 is modified to account for the grazing flow effects becoming

$$\epsilon_3 = \frac{16 r_p}{3\pi}(1 - 0.7\sqrt{\phi})\frac{1 + 5 \cdot 10^3 M_0^2}{1 + 10^4 M_0^2}\frac{1}{1 + 305 M^3} \tag{1.14}$$

The correction factor $1/\left(1 + 305M^3\right)$ has been determined empirically and can be found in Groeneweg [61] and Rice [119]. As a consequence, the reactance is supposed to decrease with increasing Mach numbers. More recently, Meng et al. [108] introduced a semi-empirical model for the impedance of circular perforations exposed to grazing flow using the Particle Velocity Match (PVM) technique. Their model incorporates the impact of the boundary layer via a convection speed that depends on the Mach number and the dimensionless boundary layer displacement thickness. This model is based on the assumptions that the Mach number is relatively small and the aperture is acoustically compact. As shown in recent studies, the Meng approximation is suitable with the Guess prediction [21].

1.4 Equivalent fluid approach

The equivalent fluid method (EFM) for analyzing porous media was initially developed by Johnson and Allard [7, 74]. In this framework, effective tortuosity is treated as a function of the correction length caused by the dynamic tortuosity of the medium interacting with the perforated plate. A key aspect involves determining the surface impedance of the perforated plate when coupled with an air cavity. The resistance accounts for viscous effects within the perforations (concentrated in the viscous boundary layers) and near the perforation openings (where acoustic flow distortion occurs). The reactance corresponds to the movement of the air mass within the perforations. When this displacement exceeds the plate's thickness, acoustic radiation correction lengths must be considered. Allard explains that, in this scenario, both the viscous and the thermal parameters are equivalent to the hydraulic radius of the perforations.

1.4.1 Linear regime

The JCAL approach [8, 90, 31], which involves several non-acoustical physical parameters (flow resistivity σ, tortuosity, porosity, viscous characteristic length and thermal characteristic length), was adopted by Atalla [13] to predict the impedance of a micro-perforated plate in the linear regime.

The normalized surface impedance of the perforated plate with a layer of air is written as:

$$Z = \frac{\mathrm{j}\omega h}{c_0 \phi}\alpha_\infty \left(1 + \frac{\sigma\phi}{j\omega\varrho_0\alpha_\infty}\sqrt{1 + \frac{4\mathrm{j}\omega\varrho_0\eta\alpha_\infty^2}{\phi^2\sigma^2\Lambda^2}}\right) - \coth(\mathrm{j}kH) \tag{1.15}$$

with σ the air flow resistivity, ϕ the porosity, and Λ the viscous characteristic length equal to the hydraulic radius of the perforation ($\Lambda = r_p$). The term $\coth(\mathrm{j}kH)$ represents the backup cavity reactance.

The resistivity of the perforated plate material is obtained from the Poiseuille's law:

$$\sigma = \frac{8\mu}{\phi r_p^2} \tag{1.16}$$

The tortuosity α_∞ accounts for sound radiation effects at the extremities of the perforation and is expressed as:

$$\alpha_\infty = 1 + \frac{2\epsilon}{h} \tag{1.17}$$

where the correction length ϵ is related to the POA and the perforation radius. Following Laly et al. [93],

the correction length ϵ can be expressed as:

$$\epsilon = \Psi 0.48\sqrt{\pi} r_p \left[\sum_{n=0}^{8} a_n (\sqrt{\phi})^n\right] \tag{1.18}$$

where $0.48\sqrt{\pi r_p^2}$ is the correction length for a single circular orifice, the sum of the coefficients a_n is an approximation of the Fok function that accounts for orifice interaction effects [54, 107, 127, 128], and Ψ is a constant set to $\Psi = 4/3$. The coefficients a_n are given by a_0= 1, a_1= -1.4092, a_2= 0, a_3= 0.33818, a_4= 0, a_5= 0.06793, a_6= -0.02287, a_7= 0.003015 and a_8= -0.01614. We note that the correction length in the EFM is different to that used in the Guess model.

1.4.2 Influence of the nonlinear acoustic regime

Starting from the works of Maa [98], Laly et al. [92] proposed an extension of the Atalla model in nonlinear regime. The impedance is now expressed as:

$$Z = \frac{\mathrm{j}\omega h}{c_0 \phi} \alpha_{\infty \mathrm{NL}} \left(1 + \frac{\sigma_{\mathrm{NL}} \phi}{\mathrm{j}\omega \varrho_0 \alpha_{\infty \mathrm{NL}}} \sqrt{1 + \frac{4\mathrm{j}\omega \varrho_0 \eta \alpha_{\infty \mathrm{NL}}^2}{\phi^2 \sigma_{\mathrm{NL}}^2 \Lambda^2}}\right) - \coth(\mathrm{j}kH) \tag{1.19}$$

The dependency on the rms velocity in the orifice v_{rms} is crucial. The variation of the flow resistivity with the rms velocity is accounted for using a classic Forchheimer-type law as:

$$\sigma_{\mathrm{NL}} = \sigma + \frac{\beta\sqrt{2} c_0 \varrho_0}{\pi h C_D^2} \frac{(1-\phi^2)}{\phi} M_0 \tag{1.20}$$

where C_D is a parameter called the discharge coefficient that depends on the perforation geometry and the edge sharpness, varying between 0.6 and 0.8 and β is a coefficient varying between 1 and 2 [92].

The tortuosity $\alpha_{\infty \mathrm{NL}}$ in the nonlinear regime is defined as:

$$\alpha_{\infty \mathrm{NL}} = 1 + \frac{2\epsilon_{\mathrm{NL}}}{h} \tag{1.21}$$

with the end correction ϵ_{NL} which in nonlinear regime is modified as:

$$\epsilon_{\mathrm{NL}} = \epsilon \left(1 + \frac{\sqrt{2}}{\phi} M_0\right)^{-1} \tag{1.22}$$

The model proposed by Laly is suitable for micro-perforated liners (radius $\leq$ 0.5 mm) and for a POA range from 1% to 5%.

1.4.3 Extension to the flow effect

In order to complete the model, we propose an extension of the equivalent fluid model to incorporate the effect of an average flow on the surface impedance. A similar approach to that presented for the Guess model is considered, in order to better compare the two approaches. Thus, the flow resistivity is modified as:

$$\sigma_{\mathrm{NL}} = \sigma + \frac{\beta\sqrt{2} c_0 \varrho_0}{\pi h C_D^2} \frac{(1-\phi^2)}{\phi} (M_0 + k_G M) \tag{1.23}$$

The end correction is also modified to take into account the effect of the flow following Eq. (1.14):

$$\epsilon_{\mathrm{NL}} = \epsilon\left(1 + \frac{\sqrt{2}v_{\mathrm{rms}}}{\phi c_0}\right)^{-1}\left(\frac{1}{1+305M^3}\right) \tag{1.24}$$

1.5 Rice-Cummings differential equations approach

The Guess model and the EFM provide a nonlinear impedance as a boundary condition to represent the behaviour of a perforated plate under acoustic excitation at high level. In this section, we introduce an alternative approach, referred to as the Rice-Cummings approach, in which the boundary condition is defined by a system of differential equations. This makes this approach attractive for a direct numerical implementation in a time-domain solver. The Rice-Cummings approach builds on the model firstly presented by Rice [119] to consider the response of a perforated plate liner with multiple frequency excitation and refined by Cummings [44] to account for nonlinear effects.

1.5.1 Theoretical formulation

The derivation begins with the assumption that the cross-sectional area of the cavity (S_c) is significantly larger than that of the perforation neck (S_0). Consequently, the acoustic velocities within the cavity v are much smaller than those in the perforation neck, allowing to treat the pressure (p_{in}) and density (ϱ_{in}) perturbations inside the cavity as spatially uniform. We recall a schematic of the acoustic properties in a resonator perforation in Figure 1.4.

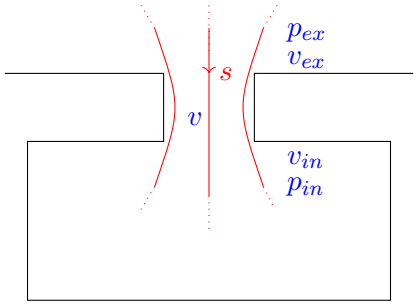

Figure 1.4: Schematic of acoustic properties inside an Helmholtz resonator

The integral mass conservation law for the cavity volume ($V = S_c H$) ensures the rate of mass change equals the neck flow. Let's assume an adiabatic compression in the cavity so that $p_{\mathrm{in}} = c_0^2 \varrho_{\mathrm{in}}$. For density perturbations (ϱ_{in}) we obtain:

$$V\frac{\mathrm{d}\varrho_{\mathrm{in}}}{\mathrm{d}t} \approx -\varrho_0 v S_0 \tag{1.25}$$

Applying the momentum equation along a streamline from a point just inside the neck to one just outside it gives:

$$\varrho_0\left(\frac{\partial \boldsymbol{v}}{\partial t} + \boldsymbol{v}\cdot\nabla\boldsymbol{v}\right) + \nabla p = \mu\nabla^2\boldsymbol{v} \tag{1.26}$$

Integrating this equation along the streamline at a curvilinear abscissa s and considering the velocity

and pressure as averaged across the perforation cross-section [107], the equation becomes:

$$\varrho_0 \int_{\text{in}}^{\text{ex}} \frac{\partial \langle \boldsymbol{v} \rangle}{\partial t} \cdot \mathbf{d}\boldsymbol{s} + \frac{1}{2}\varrho_0 \left(\bar{v}_{\text{ex}}^2 - \bar{v}_{\text{in}}^2 \right) + (p_{\text{ex}} - p_{\text{in}}) = \int_{\text{in}}^{\text{ex}} \mu \langle \nabla^2 \boldsymbol{v} \rangle \cdot \mathbf{d}\boldsymbol{s} \tag{1.27}$$

For a fixed streamline, the time derivative of the velocity integral simplifies to:

$$\int_{\text{in}}^{\text{ex}} \frac{\partial \langle \boldsymbol{v} \rangle}{\partial t} \cdot \mathbf{d}\boldsymbol{s} = \frac{\mathrm{d}}{\mathrm{d}t} \int_{\text{in}}^{\text{ex}} \langle \boldsymbol{v} \rangle \cdot \mathbf{d}\boldsymbol{s} = \frac{\mathrm{d}}{\mathrm{d}t} \ell v \tag{1.28}$$

where ℓ is the corrected length. This correction takes into account the effects of the ends of the perforation and of the viscosity in the effective dimension of the perforation. In literature many corrections have been analysed [67, 73, 121], mostly based on a comparison with experimental values. For coherence in the study, we will assume the Guess formulation [62] which is $\ell = h + 2r_p$. The velocity component v represents the normal velocity in the perforation, which is negligible in linear regime. For the stress term line integral we observe that, apart from v itself, it depends on flow profile, Reynolds number, wall heat exchange, turbulence, separation from sharp edges. Following Melling [107], we will take these effects together in a resistance factor R. We thus have:

$$\int_{\text{in}}^{\text{ex}} \mu \langle \nabla^2 \boldsymbol{v} \rangle \cdot \mathbf{ds} = -Rv \tag{1.29}$$

Therefore, we have altogether:

$$\varrho_0 \ell \frac{\mathrm{d}}{\mathrm{d}t} v + \frac{1}{2}\varrho_0 v \left| v \right| + Rv = p_{\text{in}} \ - p_{\text{ex}} \tag{1.30}$$

where the term $\frac{1}{2}\varrho_0 v \left| v \right|$ represents the nonlinear response of the system.

To sum up, a perforated plate liner with a POA ϕ and with cavity of volume V_c can be represented by the system of differential equations:

$$\begin{cases} \varrho_0 \ell \frac{\mathrm{d}}{\mathrm{d}t} v + \frac{1}{2}\varrho_0 v \left| v \right| + Rv = p_{\text{in}} - p_{\text{ex}} \\ \frac{\mathrm{d}}{\mathrm{d}t} p_{\text{in}} = -\varrho_0 c_0^2 v \frac{S_0}{V_c} = -\varrho_0 c_0^2 v \frac{\phi}{H} \end{cases} \tag{1.31}$$

This system of equations can be easily implemented as boundary conditions in a time-domain solver of the acoustic equations. It will be employed to simulate the response of a perforated plate at grazing incidence in Chapter 4 and at normal incidence in Chapter 5.

1.5.2 Impedance calculation in linear regime

For comparison with previous models, it is interesting to derive an equivalent impedance from the system of equations (1.31). In this section, we will limit ourselves to the linear case. In Chapter 5, we will derive using an analytical method, referred to as the multiple scale method, an equivalent impedance in the nonlinear regime.

Considering a harmonic excitation, in complex notation we note $p_i(t) = P_i \mathrm{e}^{\mathrm{j}\omega t}$, with P_i the generic amplitude of the pressure (external or internal). We obtain:

$$\begin{cases} \varrho_0 \ell (\mathrm{j}\omega) v + Rv = P_{\text{in}} - P_{\text{ex}} & \text{(1.32a)} \\ (\mathrm{j}\omega) P_{\text{in}} = -\varrho_0 c_0^2 v \frac{\phi}{H} & \text{(1.32b)} \end{cases}$$

and further:

$$\varrho_0 \ell (\mathrm{j}\omega)^2 v + R(\mathrm{j}\omega) v = (\mathrm{j}\omega) P_{\text{in}} - (\mathrm{j}\omega) P_{\text{ex}} = -\varrho_0 c_0^2 v \frac{\phi}{H} - (\mathrm{j}\omega) P_{\text{ex}} \tag{1.33}$$

which can be manipulated as:

$$\left[-\varrho_0 \ell \omega^2 + R(\mathrm{j}\omega) + \varrho_0 c_0^2 \frac{\phi}{H} \right] v = -(\mathrm{j}\omega) P_{\text{ex}} \tag{1.34}$$

From Eq. (1.34), the normalized surface impedance can be written as:

$$Z = -\frac{1}{\varrho_0 c_0} \frac{P_{\text{ex}}}{V_{\text{ex}}} = -\frac{1}{\varrho_0 c_0 \phi} \frac{P_{\text{ex}}}{v} = \frac{\ell}{c_0 \phi} \mathrm{j}\omega + \frac{R}{\varrho_0 c_0 \phi} + \frac{c_0}{H} \frac{1}{\mathrm{j}\omega} \tag{1.35}$$

We note that the imaginary part of the surface impedance is null at a frequency, corresponding to the Helmholtz frequency, $f = 2\pi c_0 \sqrt{\phi/(H\ell)}$ and that the normalized resistance is constant and equal to R/ϕ.

1.6 Conclusion

This chapter investigates the impedance of perforated plates using three approaches: the Guess model, the equivalent fluid model, and the Rice-Cummings approach. Each method addresses distinct physical phenomena, focusing on the linear, nonlinear, and flow-modified behaviour of the plates. The Guess model and the EFM take to the expression of an impedance in function of the geometrical parameters of the plate. They consider the behaviours under nonlinear regime and with flow by introducing parameters adjusted empirically. The baseline phenomena of the two approaches are the same (influence of the acoustic and flow velocities). The Rice-Cummings approach consist in a modeling by differential equations, particularly suitable for a study in nonlinear regime employing a multiple scale method (Chapter 5).

In the linear regime, impedance is influenced by viscous, thermal and inertial effects. The Guess model offers an analytical framework that incorporates viscosity, radiation, and backing cavity effects, making it particularly suitable for macro-perforated plates. The equivalent fluid model, which treats the perforated plate as a homogenized porous medium, captures the effects of tortuosity and resistivity.

Nonlinear effects occur when high sound pressure levels induce vortex shedding and increase resistance in the perforations. The Guess model accounts for these effects through empirical corrections, reflecting how acoustic velocity impacts impedance. The equivalent fluid model extends its resistivity and tortuosity formulations to the nonlinear regime by incorporating Forchheimer-type corrections, improving the model's accuracy in high-intensity acoustic environments. In the Rice-Cummings approach, the presence of nonlinear regime is induced by the consideration of the acoustic velocity in the definition of the resistance.

When a grazing flow is present, impedance is further altered by increased resistance and reduced reactance due to boundary layer interactions. The Guess model incorporates empirical flow corrections, considering Mach number and boundary layer thickness. Similarly, the equivalent fluid model is extended to account for flow effects, offering an alternative approach for modeling perforated plates under flow. While both models capture flow-induced variations, their accuracy depends on empirical parameters that require experimental validation.

The models outlined in this chapter lay the groundwork for subsequent investigations in this thesis. The following chapters will apply these formulations to specific case studies, integrating numerical simulations and experimental validations (Chapters 4,5,6). By comparing theoretical predictions with experimental data, this research seeks to refine impedance models and improve their applicability in noise reduction techniques.

2 Description and characterisation of the experimental study

Contents

Abstract

This chapter explores the methodology implemented for the experimental protocol. Section 2.2 discusses material selection and fabrication techniques, emphasizing precision in manufacturing the perforated plate. Having found in a galvanised steel plate obtained by laser jet the best material and technology for the production, the assembly of the liner is detailed. Section 2.3 presents the impedance tube method for acoustic characterization, analyzing impedance, reflection, and absorption under controlled conditions. Nonlinear behaviour is considered through controlling sound pressure level by presenting a novel iterative procedure. Section 2.4 details liner assembly in the Caiman wind tunnel, presenting the duct and implementing a scrupulous aerodynamic and acoustic characterization, profiling the flow, verifying the anechoicity of the terminations and the acoustical parameters of the measurements. The chapter concludes with the presentation of the two-source transmission loss method to evaluate liner performance under flow conditions, providing insights for future optimization.

2.1 Introduction

The study of acoustic liners is essential for applications in aeroacoustics, where noise reduction and material performance under varying flow conditions are critical. This chapter outlines the methodology and experimental framework established to characterize and analyze the acoustic properties of a perforated plate liner. The objective is to assess material suitability, fabrication techniques, and acoustic performance under both linear and nonlinear regimes in the presence of flow.

The chapter begins by detailing the selection process for materials and manufacturing techniques for the liner components in Section 2.2. A key focus is placed on ensuring precision and repeatability, particularly for the perforated plate, whose geometry and structural properties significantly influence acoustic performance. Two primary fabrication approaches were considered: a single-component solution and a modular design. The latter is selected for its flexibility and adaptability in experimental scenarios, enabling separate optimization of the plate and cavity materials. The focus will first be on the mechanical properties of a perforated liner (Section 2.2.1) and then on the actual development of an acoustic liner to be placed in wind tunnels (Section 2.2.2).

The chapter continues with the acoustic characterisation of the perforated plate using an impedance tube under normal incidence (Section 2.3). This experimental setup provides critical insights into the liner's impedance, reflection coefficient, and absorption coefficient, allowing for a detailed understanding of its behaviour in controlled conditions. The study incorporates both harmonic and broadband excitation techniques. In particular, a procedure to precisely control the acoustic pressure level will be presented in Section 2.3.3.2.

Attention then shifts to the assembly and integration of the liner into a dynamic testing environment (Section 2.4). A polycarbonate honeycomb cavity, coupled with a silicone sealing system, forms the resonant structure that backs the steel perforated plate. This assembly is tested in the Caiman subsonic wind tunnel under grazing incidence and varied flow velocities. The characterisation of the duct's aerodynamic properties in Section 2.4.3 and acoustic properties in Section 2.4.4 is a central component of this study, addressing challenges such as minimizing transverse leaks and accurately measuring sound transmission and reflection.

The chapter concludes by presenting methods for evaluating liner performance, including a two-source transmission loss measurement technique that allows us to get rid of the reflections by the duct terminations. These results provide a comprehensive understanding of the liner's functionality and its potential applications in mitigating aeroacoustic noise. By combining material science, experimental acoustics, and aerodynamic analysis, this chapter establishes a rigorous framework for studying acoustic liners, setting the stage for advanced exploration in subsequent sections.

2.2 Liner characterisation and realisation

The first step in the design of a liner is the choice of the material and the manufacturing technique for its production. The liner consists of two main parts: the perforated plate and the resonant cavity. The assembly methodology of the liner profoundly influences the choice of materials. As a matter of mechanical solidity and compactness of the liner, one solution could be to produce a single component that includes the perforated plate and the cavity. This solution guarantees that there is no leakage between the plate and the cavity and solidity of the structure. The problem with this solution lies in manufacturing. Using a metallic material to manufacture a single component with a complex internal volume is mechanically challenging and the processing cost is certainly high. Using an additive manufacturing technique, such as 3D printing, involves a certain complexity of impression. In addition, the material has to be carefully chosen in order to guarantee mechanical rigidity and realisation precision at the time.

The second option is to create the perforated plate and the cavity separately and to mechanically assemble them in a second time. This solution allows for versatility in application, as it is possible for one plate configuration to use different types of cavities and vice versa. However, having two separate pieces implies a mechanical assembly of the components. The material discontinuity could result in leakages between the different liner cells and mechanical vibration due to imperfect contact. For this reason, additional attention must be paid to the assembly phase and the type of joint or mechanical contact to be used as bond.

2.2.1 Characterisation of the materials

In the course of this study, the option of realizing the plate and cavity as two separate pieces is chosen. This allows the most suitable material to be selected for the two components, which does not necessarily have to coincide, and allows greater versatility in terms of studying different configurations. Being able to reuse the same cavity for different plate designs or vice versa provides benefits in terms of time and cost.

Concerning the perforated plate, it is first necessary to measure its acoustic behaviour in normal incidence, with the aid of an impedance tube, which will be detailed in Section 2.3. The study carried out by Diab et al. [51], in which several circular metal perforated plates, both macro- and micro-perforated, were tested in an impedance tube, is taken as a starting point. The initial aim is to reproduce the behaviour of such plates starting from the realisation. The material in question must have certain mechanical characteristics, allowing for optimum rigidity of the plate, in order not to transmit parasitic and residual vibrations when acoustically excited, and a fair degree of ductility so that it can be subjected to mechanical processing without being damaged. The materials considered are of metallic and plastic types.

Concerning the mechanical techniques for executing the perforations, these must be highly precise in order to guarantee the best possible definition of the edges of the perforation (absence of shavings, impurities and burrs on the edge of the perforation, good conicity of the hole) and not deform the perforation geometry guaranteeing its circularity. The quality of the perforation is crucial for a correct analysis of acoustic propagation in the edges of the perforation. Any changes in the shape and definition of the perforation directly affect the acoustic propagation within them, significantly changing the analysed configuration. Several studies have been done on the shape of the perforation (circular, oval or triangular) , and the sharpness of the perforation edges [77, 125, 145, 146]. As can be deduced from these studies, changing one of these parameters leads to different plate behaviours. For the types of materials considered, the perforation techniques can be grouped into two types: removal of material with regard to metals, and discontinuous deposition of material with regard to additive processing of plastic resins.

	Young modulus	Plastic deformation coefficient	Cost
(a) Galvanized Steel	200 GPa	0.15	0.7 €/ kg
(b) VisiJet M3 Crystal	1.43 GPa	0.068	270 €/ kg
(c) FORMLABs Clear2	2.8 GPa	0.062	162 €/ℓ
(d) FORMLABs Rigid4000	4.1 GPa	0.056	228 €/ℓ

Table 2.1: Properties and cost of the considered plate materials

Four different materials are considered, whose type and mechanical properties are listed in Tab 2.1. At first, a macroperforated plate is examined with a thickness of 1 mm and perforation diameter of 2 mm.

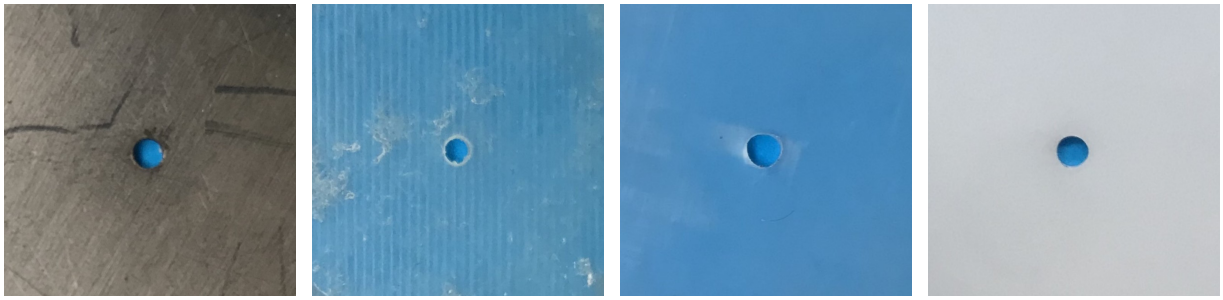

(a) (b) (c) (d)

Figure 2.1: Representation of a single macroperforation in the considered materials:(a) galvanised steel, (b) VisijetM3Crystal, (c) Clear2 resin, (d) Rigid4000 resin

Figure 2.1 shows the different types of plates. The plate (a) is made of galvanised steel, which allows high rigidity and resistance to manufacturing while ensuring good ductility when drilling. The perforations are obtained by laser jet cutting. Plate (b) is made from the plastic material VisijetM3Crystal from 3D Systems©. The technique used to make the component is the 3D Multi Jet Printing (MJP) technique, which achieves high resolution by means of a support material (a wax, removed in post processing) and the deposition of liquid photopolymers onto a build surface using inkjet technology. At the end of the process, the result is a printed stack made of the UV curable plastic material 'VisiJet M3 Crystal' wrapped in a wax backing. In order to melt the wax support both externally and, in particular, internally from the perforation channels, it is necessary to proceed with a post-heating process in a static oven at 60 °C in order to obtain a pure resin component. This phase is particularly delicate because at a temperature below 60 °C the wax in the inner interstices cannot be completely melted, while at a higher temperature the piece would undergo a thermoplastic deformation that would compromise its structure and therefore the definition of the perforations, as explained by Sarpero et al. [129, 130]. Plate (c) is made of Clear2 resin by Formlabs©, a polycarbonate resin. Plate (d) is Rigid4000 resin from Formlabs©. This is a glass-reinforced resin that can be used to produce highly rigid parts with an excellent precision. For both of these materials, the fabrication technique is the FDM, fuse deposition modelling [71]. Once the macroperforated material has been produced, an optical analysis of the perforations is carried out. A Olympus BX51 Fluorescence Microscope is used for that.

The core points for assessing the suitability of materials are as follows:

1. correct shape of the perforation, being sure that the circularity is respected and that there are no dissymmetries in realisation;
2. correct size of the perforation, by which is meant ensuring that the design diameter is respected during realisation;
3. good surface definition, being the absence of defects or manufacturing residues, both on the edge and inside the cavity.

All these factors, if not respected, may introduce sources of error and significantly alter the acoustic behaviour of the plate. In addition, the theoretical analysis would also be compromised, as substantial differences to the modelled geometric parameters would be introduced.

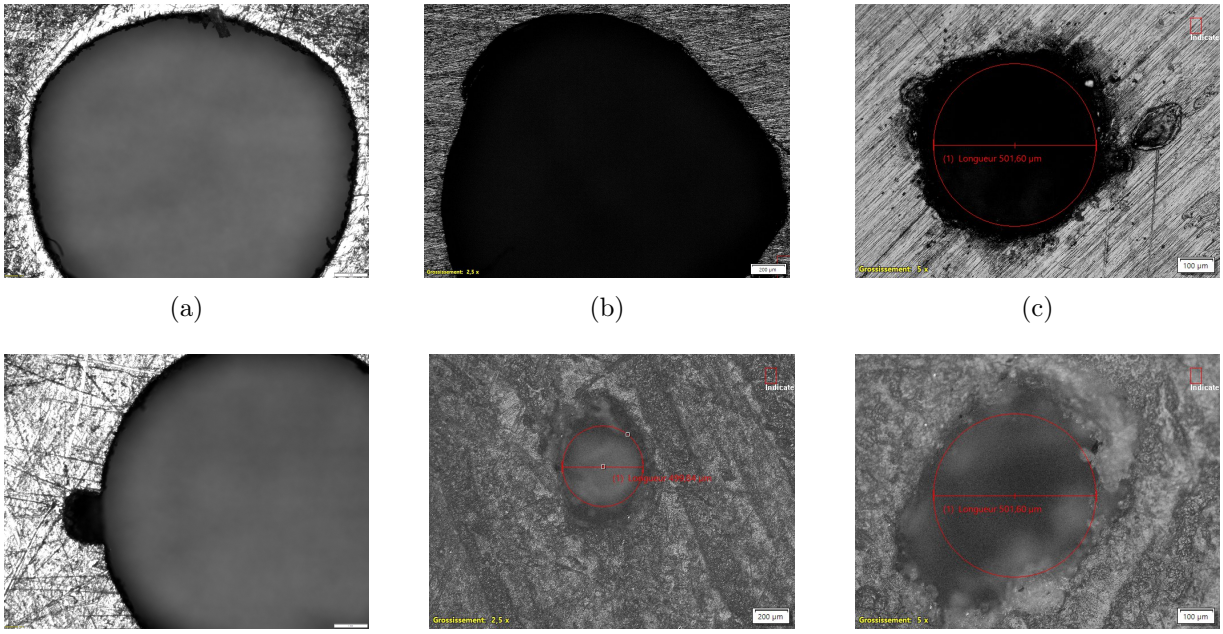

(a) (b) (c)

(d) (e) (f)

Figure 2.2: Examples of realisation defects which may occur during material fabrication: (a),(b),(c) present irregular edge shapes in metallic plates, (d) local damage in metallic plate, (e) and (f) impurities in the perforation neck in 3D-printed plates

Examples of such realisation defects are illustrated in Figure 2.2. Image 2.2a and 2.2b represents a perforation with an irregular shape, which is triangular rather than circular. Image 2.2c represents a difference in the size of the perforation from the design (red circle). This may be due to incorrect mechanical processing (plate not perfectly clamped, multiple perforation steps) or the use of a tool with a worn perforation head. Figure 2.2d shows a local damage in the perforation, due to a misuse of the tool or to a collision on the plate. Lastly, in Figure 2.2e and 2.2f, we can observe the presence of impurities in the perforation, which may be related to an excess of material that has not been removed correctly, or to processing residues related to milling (swarfs) or to a material deposition technique (3D printing).

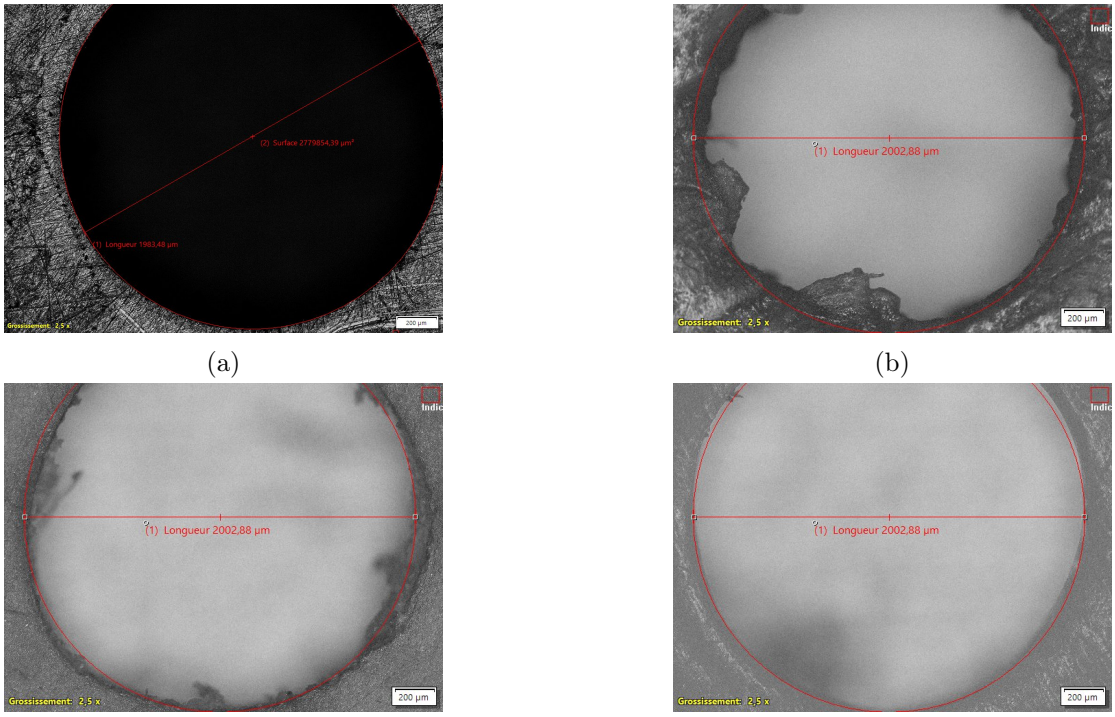

(a) (b) (c) (d)

Figure 2.3: Enlargement of the definition of a macroperforation in the considered materials: (a) Galvanized Steel, (b) VisiJet M3 Crystal, (c) FORMLABs Clear2 resin, (d) FORMLABs Rigid4000 resin

Returning to the materials analysed, examples of macroscopic analysis for the four types of material are presented in Figure 2.3. Image 2.3a represents galvanised steel. It can be observed that the perforation is sharp and clean, being well executed in shape and size, and with no impurities. The plate appears to have excellent rigidity and was not flexed during drilling. Image 2.3b represents Visijet M3 Crystal resin. The problem with this technique is the removal of the wax backing, particularly within the perforation. Although from a macroscopic viewpoint the perforation appears to be clean, microscopic analysis reveals a considerable deposit of residual material, which changes both the shape and size of the perforation. The plate is also slightly curved on its thickness due to the thermal expansion undergone during post-treatment. Image 2.3c represents Clear2 resin. It can be seen that the shape of the perforation is not perfectly circular, and there are also impurities remaining in the perforation. The plate is not deformed in bending, although the material appears to be very easily deformable by applying light manual pressure. Image 2.3d represents the Rigid4000 resin, presenting a good appearance of shape and size of the perforation, despite some slight imperfections. The plate exhibits good rigidity and the deflection due to digital pressure is considerably less than in the case of Clear2 resin.

For a more accurate analysis, four plates similar to the previous ones but with a perforation of 0.5 mm in diameter are opted for, as can be seen in Figure 2.4.

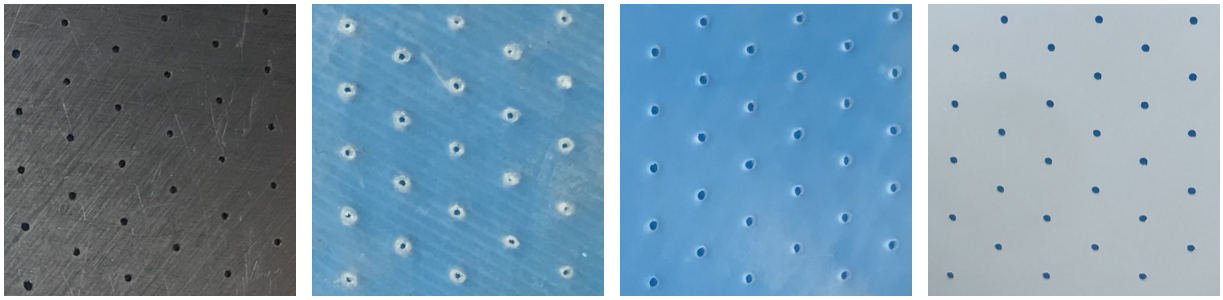

(a) (b) (c) (d)

Figure 2.4: Representation of microperforations in the considered materials: (a) Galvanized Steel, (b) VisiJet M3 Crystal, (c) FORMLABs Clear2 resin, (d) FORMLABs Rigid4000 resin

The microscopic analysis of the microperforations is illustrated in Figure 2.5. For the the galvanised steel plate in Fig. 2.5a, the shape, definition and size of the perforation are close to the design specifications. Perforation of the Visijet plate in Fig. 2.5b, on the other hand, is highly deformed, presenting a large amount of residual material that significantly reduces the size of the perforation. Finally, for Clear2 and Rigid4000 resins in Figs. 2.5c and 2.5d, the shape and size of the perforation is compromised.

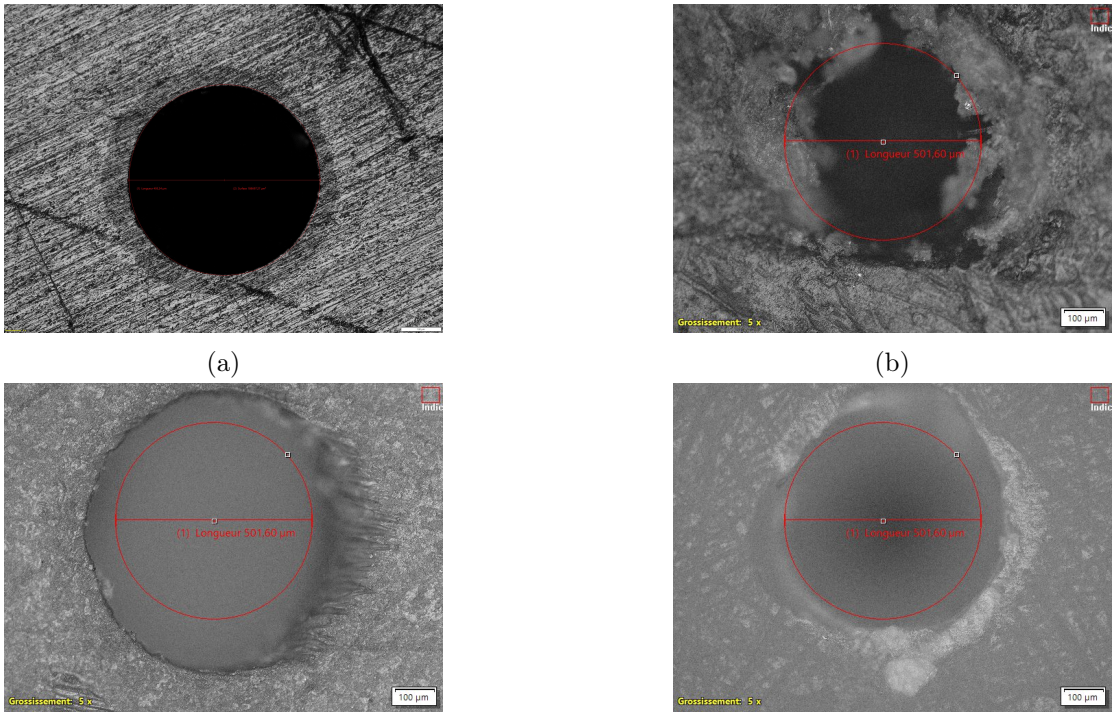

(a) (b)

(c) (d)

Figure 2.5: Enlargement of the definition of a microperforation in the considered materials: (a) Galvanized Steel, (b) VisiJet M3 Crystal, (c) FORMLABs Clear2 resin, (d) FORMLABs Rigid4000 resin

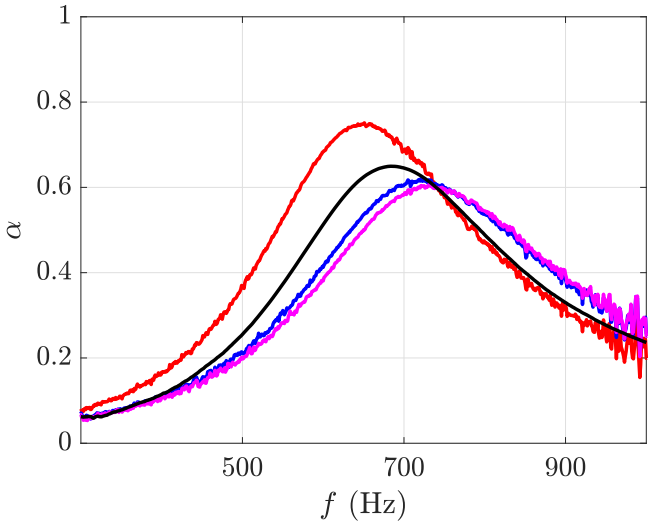

Figure 2.6: Absorption coefficient α of a three perforation plate for different tested materials: Galvanised steel (—), Visijet M3 Crystal(—), resin Clear2 (—) and resin Rigid4000 (—)

In order to assess the influence of the materials and the realisation techniques on the acoustic properties, we have measured the absorption coefficient α of the perforated plates (see section 2.3 for more details). In Figure 2.6, we present the absorption coefficient of a macroperforated plate with three perforations of diameter 2 mm made of different materials, using broadband excitation at 92 dB. The absorption coefficient for the plate made of galvanised steel is the reference one. In particular, note that it presents a smooth evolution with the frequency. For the plate made with Visijet M3, the peak is observed at a smaller frequency, probably due to a smaller perforation diameter, and the peak amplitude is increased. The two resins give similar results: the peak is centered at higher frequencies and the peak amplitude is reduced. As a conclusion, the material and the technique, with relative deformations and errors, directly affect the acoustic property of a sample, modifying its behaviour. From here rise the importance of the choice of a robust material and a precise realisation technique. Recent studies from Jamois et al. [71, 72] demonstrated the influence of the realisation technique on a given sample, in particular when considering 3D printing technologies.

Conclusion

Four different types of material were considered for the realisation of the liner perforated plate. Following a microscopic analysis of two different types of perforations carried out on the materials considered, galvanised steel turns out to be the most suitable choice for the realisation of the plate, both in terms of structural rigidity and, in particular, for the precision of realisation of the perforations by laser jet cutting. In fact, for both a macro and a micro perforation, the design characteristics are respected with precision, making it possible to guarantee a certain reliability with regard to the geometric characteristics of the perforations.

2.2.2 From the perforated plate to the liner

Concerning the perforated plate, it is first necessary to study its acoustic behaviour in normal incidence, with the aid of an impedance tube, which will be detailed in Section 2.3. The study carried out by Diab et al [51], in which several circular metal perforated plates, both macro- and micro-perforated, were tested in an impedance tube, is taken as a starting point.

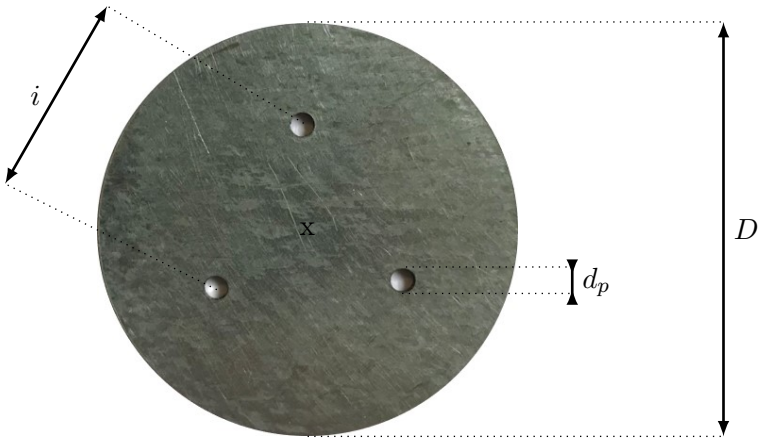

Figure 2.7: Schematic representation of the perforated plate tested in impedance tube

The perforated plate shown in Figure 2.7, made of galvanised steel by means of a laser jet cutting technique, is considered. Adapting to the dimensions of the impedance tube, the plate turns out to have a nominal diameter $D = 29$ mm, presenting three perforations of diameter $d_p = 2$ mm each spaced by a center-to-center distance of $i = 11,5$ mm. The perforation ratio of the plate is $\phi = 1.42\%$. The plate is 1 mm thick. The configuration is completed by adding an empty volume of 30 mm depth behind the plate ended by a rigid termination, in order to create a resonant structure. The choice of such plate is justified by the simplicity of realisation, being macroperforated, and in particular when foreseeing the implementation of an extended liner with similar characteristics. Moreover, this particular sample geometry has already been tested by Diab et al. [51], providing a good baseline for comparing results. The objective is to measure the acoustic characteristics of such a plate, mainly the real and imaginary components of the surface impedance Z and the absorption coefficient α. After carrying out the optical controls described in Section 2.2.1, the plate is found to be suitable for testing.

Once the characteristics in the impedance tube have been assessed, it is necessary to implement a liner to be tested in duct. The liner consists of the assembly shown in Figure 2.8. The dimensions of the liner have been designed to ensure a minimum of clearance with the duct structure, allowing the liner to be inserted into its holder, without having to apply any kind of pressure that would induce deformation of the assembly.

Figure 2.8: Assembly of the fabricated liner: (I) Honeycomb cavity, (II) sealing joint and (III) perforated plate

A metallic perforated plate (I) is assembled to a resonant cavity (II) via a silicone joint (III). Once unified, the liner is backed by a rigid end and fixed to the duct structure by means of a removable sample holder. The surfacing of the liner inside the duct is ensured by a system of adjustable screws fixed to the metal plate, which can move the liner until it is perfectly aligned with the inner wall of the duct. The dimensions and characteristics of the duct in question are detailed in Section 2.4.1.

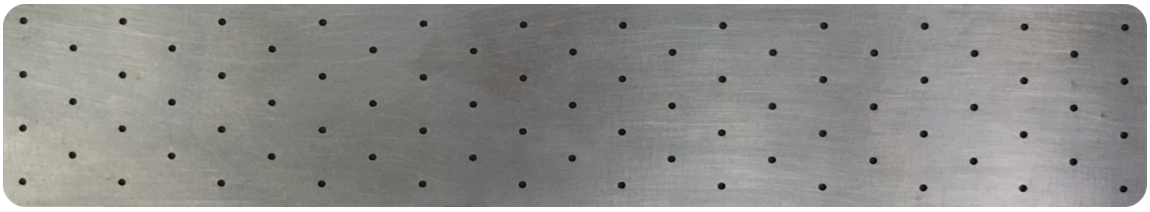

Figure 2.9: Front view of the liner metallic perforated plate

Figure 2.9 shows the perforated plate of the liner, realized in galvanised steel by laser cutting jet. The plate was designed following the geometrical parameters of the circular plate depicted in Figure 2.7, with a perforation diameter of 2 mm and a thickness of 1 mm. The plate measures 0.3 m $\times$ 0.07 m, with four rounded angles of diameter 20 mm. In total, for the plate considered, there are 81 perforations uniformly distributed over the entire surface of the plate. Considering the total free surface, the perforation ratio of the plate ϕ is 1.41%. An optical control was carried out on the perforations to check their suitability. Finally, support screws are attached to the plate to enable it to be anchored to the holder and the duct itself. In particular, in the presence of flow, the liner is subject to aerodynamic stresses and must remain firm. Once finished, the side facing the cavity is sandpapered in order to apply the backup cavity and joint. On the other hand, the side facing the inside of the duct is smoothed to remove all possible impurities and make the surface roughness as smooth as possible.

The backup cavity is 3D printed using the FDM (fused deposition modelling) technique using a polycarbonate material. This realisation allows the cavity to be designed according to the perforated plate configuration. In this case, through a honeycomb structure, each perforation is backed up by a hexagonal cavity, trying to maintain as much as possible the perforation rate of the metal plate shown in Figure 2.9. The cavity wall thickness is 1 mm, and the cavity depth is 30 mm. Once backed with the

rigid end, the liner cells presents as depicted in Figure 2.10.

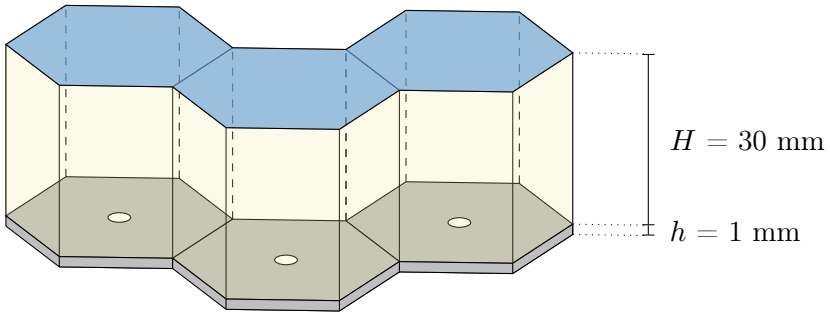

Figure 2.10: Sketch of liner cells

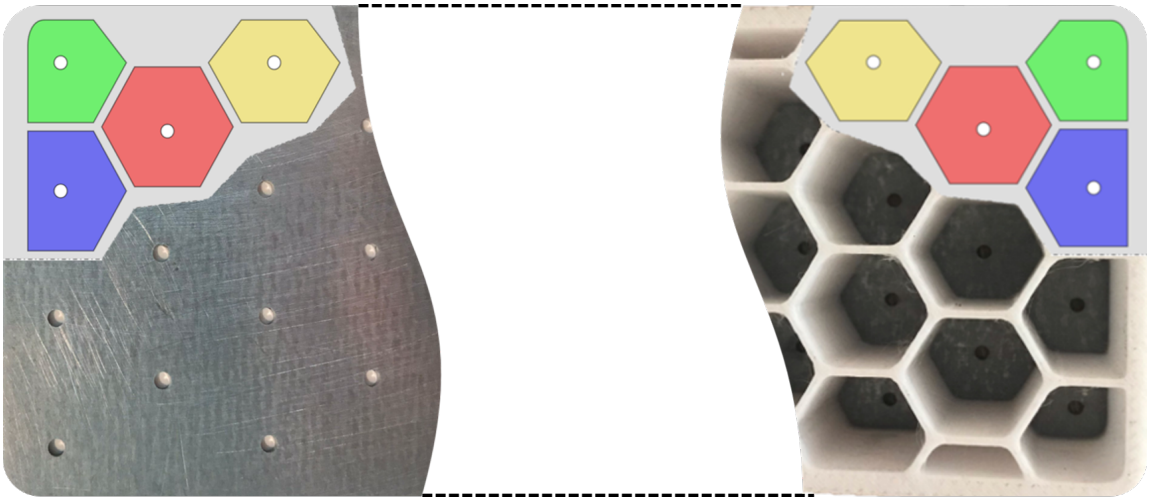

Figure 2.11: Enlargement of the liner with and without honeycomb structure and overlay with graphical representation of the different cells surfaces

An internal view of the overlay of the honeycomb to the metal plate is depicted in Figure 2.11. The different types of cavities in the honeycomb design have been coloured. A compromise needs to be made taking into account the size of the liner and the duct, while trying to keep the size of the cavities as constant as possible. Over the eighty-one perforations results: fifty-three complete cavities (), presenting a local perforation rate of $\phi = 1.84\%$; twenty partial cavities on the major edges (), presenting a local perforation rate of $\phi = 2.19\%$; four partial cavities on the minor edges (), presenting a local perforation rate of $\phi = 2.29\%$; four partial cavities on the corners (), presenting a local perforation rate of $\phi = 2.78\%$. Considering the free surface on the cavity side, the overall perforation rate is $\phi = 1.99\%$.

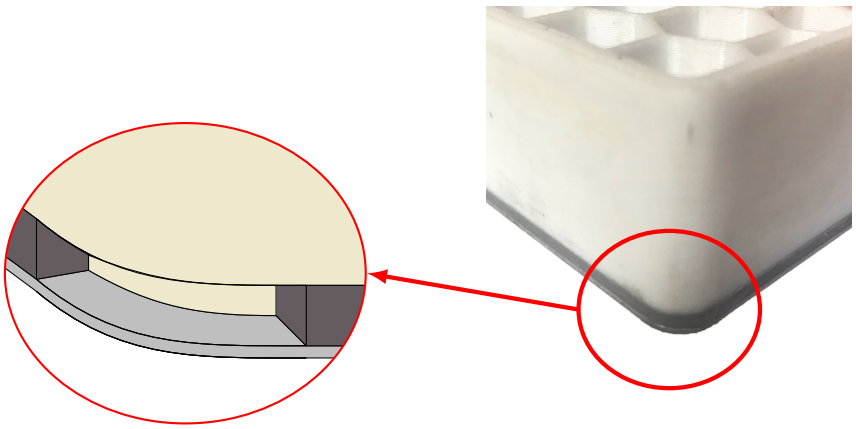

Figure 2.12: Enlargement of the silicone joint and its perimetral cavity in the honeycomb structure

In order to ensure maximum sealing of the perforated plate to the backup cavity, a perimeter cavity is created on the outer edge of the poly-carbonate cavity, as can be seen in Figure 2.12. This cavity is then filled with a layer of acetic silicone Silicomet JS 545 from Loctite©. Silicomet JS 545 is a single-component silicone elastomer adhesive that cross-links with moisture in the ambient air to form a flexible seal. It is specially designed to withstand oils, heat transfer fluids, temperature and vibration, which turns to be particularly suitable for wind tunnel applications. This system provides a tight seal against transverse leaks that may occur at any intersections between the two components. A tight sealing, without the presence of the cavity in the upper part of honeycomb structure, is ensured on the rigid end side of the liner.

2.3 Experimental study in impedance tube

Once the perforated plate described in Section 2.2.2 (Figure 2.7) has been realised, it is necessary to characterise its acoustic behaviour under normal incidence. The surface impedance of a sample in the linear regime relates the pressure p and the normal velocity v at the surface of the material. The so-called direct methods of assessing the impedance of a material are based on the measurement of pressure by one or more microphones and the related calculation of velocity.

The method used in this discussion is the Chung and Blaser method [35, 36, 37, 48], a well established method employing the two-microphone principle. This method makes it possible to determine the reflection and absorption coefficient at any point in the tube by measuring the transfer function between two microphones mounted in the wall of the tube and separated by a certain distance. Both harmonic and broadband excitation can be used.

2.3.1 Description of the impedance tube

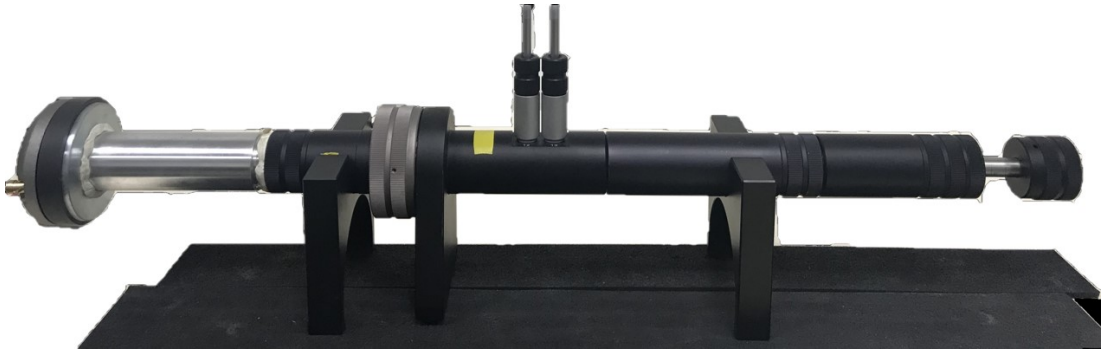

Figure 2.13: B&K impedance tube used for acoustic characterisation of the plates

For the acoustic characterisation at normal incidence, the B&K impedance tube shown in Figure 2.13 with a nominal diameter of 29 mm is used. The tube works in a frequency range of 50-6400 Hz. The setup consists of: a FANE CD125 compression driver, two B&K 1/4" pressure-field microphones surfacing the duct wall with their B&K preamplifiers connected to a B&K Conditioning amplifier and an adjustable piston connected to a rigid cavity termination disk. The compression chamber was substituted for the loudspeaker supplied by the manufacturer in order to achieve high acoustic levels without experiencing a nonlinear source response. The signal is provided by a B&K Power Amplifier. The signal output and input is provided by a NI compact DAQ chassi with four NI channels. Signal generation and control and data post-processing are made by a PC using codes developed in environment Matlab©.

A temperature and humidity sensor was placed next to the tube to assess the humidity and ambient temperature conditions. Various protocols were followed in order to keep the measurement parameters as constant as possible. The protocol for the ambient parameters, the acoustic parameters concerning the excitation signal and sound propagation, and the excited sound level are analysed below.

2.3.2 Thermodynamic characterisation

For each measurement, it was ensured that the temperature and humidity, and therefore the speed of sound, remained constant. In this respect, we briefly discuss the variation of the speed of sound c_0 as a function of temperature T and relative humidity r_h. The speed of sound can be expressed as a function

of the relative humidity by:

$$c_{0,r_h} = c_0[1 + r_h(a_0 + a_1 T + a_2 T^2 + a_3 T^3 + a_4 T^4)] \tag{2.1}$$

with $a_0 = 9.66 \times 10^{-4}$, $a_1 = 7.2 \times 10^{-5}$ K^{-1}, $a_2 = 1.8 \times 10^{-6}$ K^{-2}, $a_3 = 7.2 \times 10^{-8}$ K^{-3}, and $a_4 = 6.5 \times 10^{-11}$ K^{-4}, where r_h is the relative humidity and c_0 is the sound speed for dry air (r_h=0) [151].

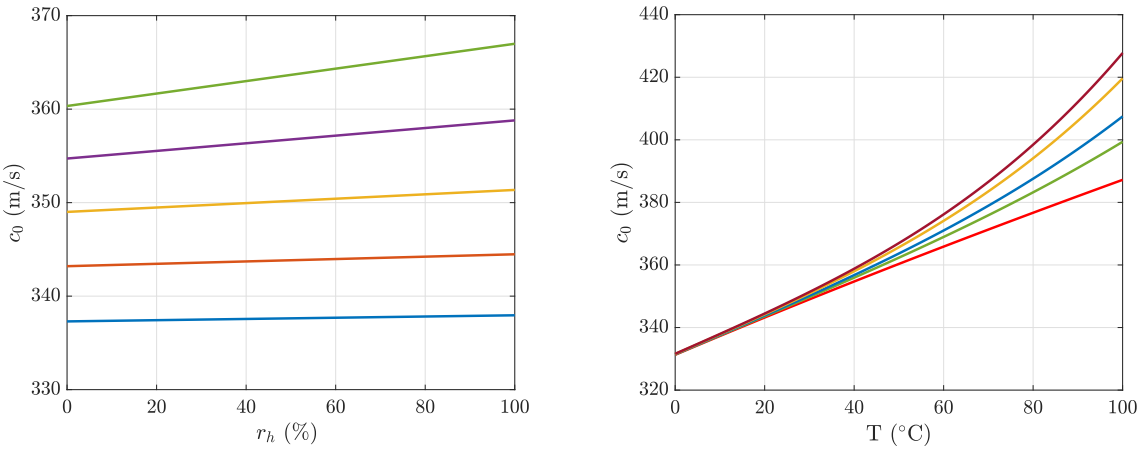

(a) (b)

Figure 2.14: Dependency of sound speed c_0 on (a) relative humidity at T = 10 °C(—), T = 20 °C (—), T = 30 °C (—), T = 40 °C (—), T = 50 °C (—) and ambient temperature (b) at r_h = 0% (—) , r_h = 30% (—), r_h = 50% (—), r_h = 80% (—), r_h = 100% (—)

Figure 2.14a shows the evolution of c_0 as a function of the relative humidity for several temperatures. Figure 2.14b shows the evolution of c_0 with the temperature for several values of the relative humidity. Although the room temperature is always within a range of 15 °C to 25 °C, in which the variations induced by the relative humidity on the sound speed are overall negligible, we ensure by monitoring both the temperature and the humidity a constant sound speed for each measurement set in order to reduce measurement uncertainties.

2.3.3 Acoustic characterisation of the impedance tube

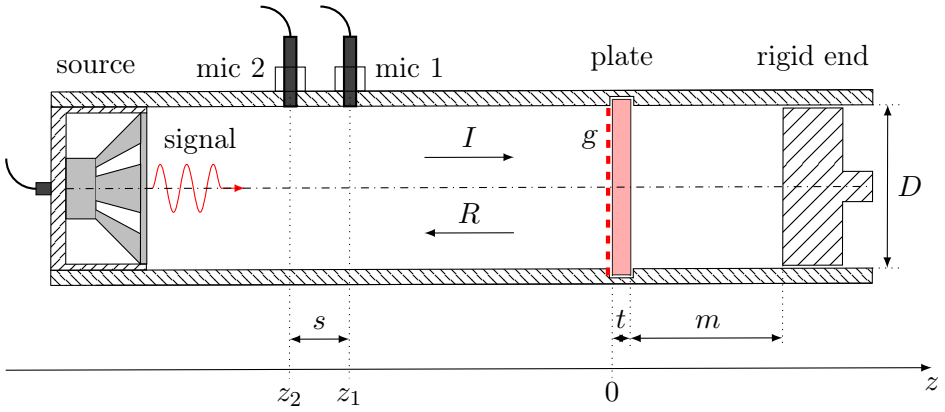

Figure 2.15: Schematic of the impedance tube in the configuration with transversal plate and resonant cavity

For the acoustic characterisation of the impedance tube, Figure 2.15 is taken as reference for the analysis. The two microphones are located at $z_1 = -0.06$ m and $z_2 = -0.08$ m, corresponding to a distance $s = 0.02$ m between the two microphones. For the plate dimensions, the plate thickness is $t = 0.001$ m and the air gap behind the plate is $m = 0.03$ m. On the external side of the plate (at $z = 0$), it is possible to define a global pressure value denoted p_g. Inside the tube, the pressure can be decomposed into an incident wave of amplitude I and a reflected wave of amplitude R. The pressures at the microphones and the global pressure can be defined as:

$$\begin{cases} p_1 = I\mathrm{e}^{-\mathrm{j}kz_1} + R\mathrm{e}^{\mathrm{j}kz_1} \\ p_2 = I\mathrm{e}^{-\mathrm{j}kz_2} + R\mathrm{e}^{\mathrm{j}kz_2} \\ p_g = p(z=0) = I + R \end{cases} \tag{2.2}$$

We can than obtain the global acoustic velocity at the plate from p_1 and p_2 as:

$$v_g = \frac{I - R}{\varrho_0 c_0} \tag{2.3}$$

and the velocity in the perforation from the POA as:

$$v = \frac{v_g}{\phi} \tag{2.4}$$

with its rms value as $v_{\mathrm{rms}} = v/\sqrt{2}$.

The transfer function between the two microphones is defined as:

$$h_{12} = \frac{S_{12}}{S_{11}} \tag{2.5}$$

where S_{12} is the cross power spectral density (CPSD) of the time-signals measured at the the two microphones and S_{11} is the power spectral density (PSD) of microphone 1. The Matlab© function cpsd is used for this calculation employing a Hamming type window.

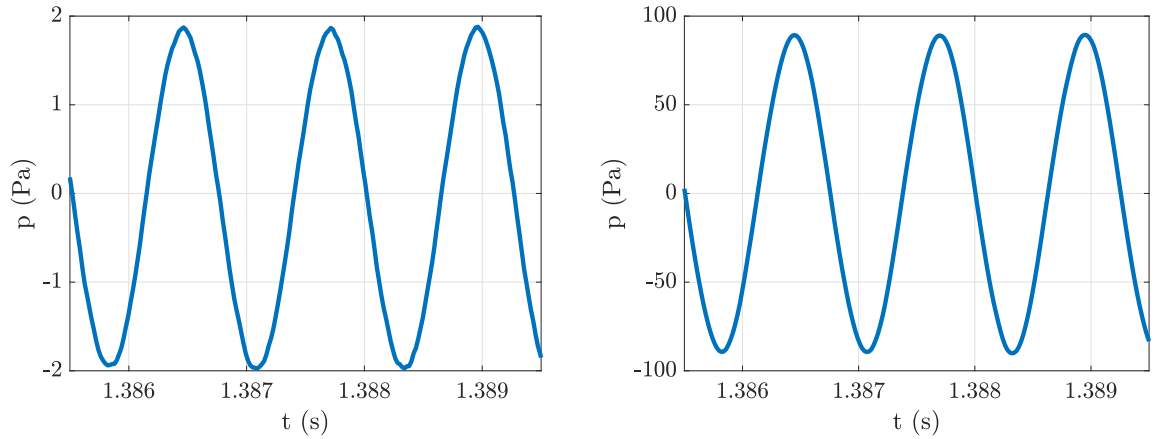

Figure 2.16: Time signal of an harmonic excitation in impedance tube at (a) 92 dB and (b) 130 dB at 1000 Hz

For the acoustic excitation, both a harmonic and broadband type of excitation are employed. Figure 2.16 presents the time signals at one of the two microphones in the impedance tube using an harmonic excitation at two incident SPL 92 dB and 130 dB. Even for a SPL of 130 dB, the signal remains sinusoidal, which shows that the compression chamber does not generate signal distortion. Further measurements show that up to incident SPL of 140 dB signal distortion is negligible.

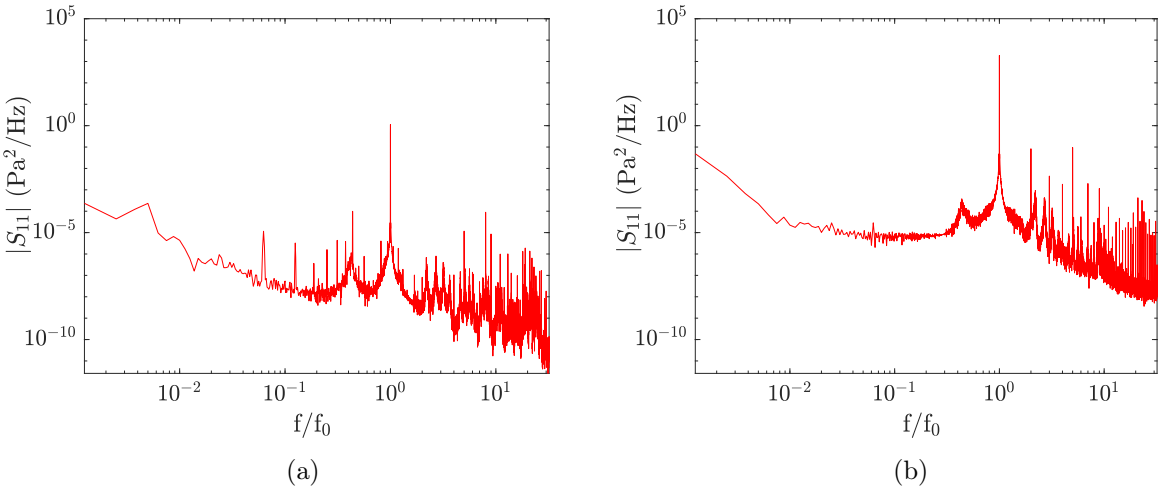

Figure 2.17: Power spectral densities of the incident pressure in impedance tube at (a) 92 dB and (b) 130 dB in harmonic excitation at 1000 Hz

In Figure 2.17 the power spectral density of the signals shown in Fig. 2.16 is presented for both linear and nonlinear cases. We note that the amplitude of the harmonics is several orders of magnitude lower than that of the fundamental.

2.3.3.1 Acoustic propagation

In order to isolate only the nonlinear behaviour of the material, propagation is always kept linear. The importance of nonlinear propagation effects can be estimated with the shock formation distance. It

represents the distance at which a sinusoidal plane wave of initial amplitude p and angular frequency $\omega = 2\pi f$ presents a shock. The shock formation distance is given by [126]:

$$\bar{x} = \frac{\varrho_0 c_0^2}{\beta k p} \tag{2.6}$$

with $\beta = 1.4$ for air, k is the wave number, and p is the initial amplitude of the signal.

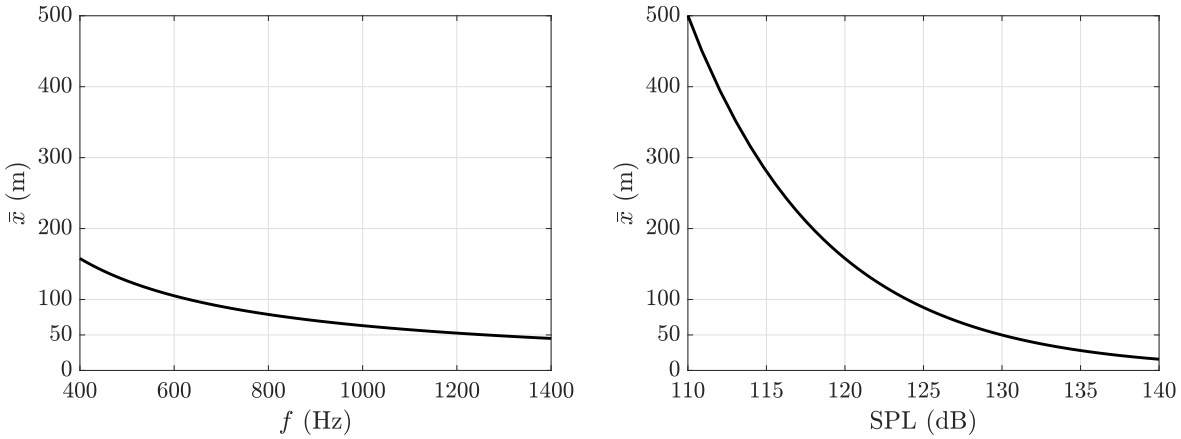

(a) (b)

Figure 2.18: Shock formation distance $\bar{x}$ varying with (a) the excitation frequency for a signal amplitude of 100 Pa and (b) the signal sound pressure level for a frequency of 700 Hz.

Figure 2.18a shows the shock formation distance for frequencies between 400 and 1400 Hz and for a signal amplitude of 100 Pa corresponding to a SPL of 134 dB. Figure 2.18b shows the shock formation distance at a frequency of 700 Hz for different incident pressure amplitudes. In both cases we can observe that the shock formation distance is significantly larger than the length of the impedance tube, assuring that nonlinear propagation effects are negligible.

2.3.3.2 Nonlinear experimental protocol

Preliminary remarks on the SPL

In the nonlinear acoustic regime, the material behaviour depends on both the excitation frequency and the amplitude of the acoustic velocity in the perforations. In this respect, it is necessary to control precisely the amplitude of the acoustic field in the measurements. The SPL can be defined as:

$$\mathrm{SPL} = 20 \log_{10} \left(\frac{p_{\mathrm{rms}}}{p_{\mathrm{ref}}} \right) \tag{2.7}$$

being p_{rms} the rms value of the pressure and $p_{\mathrm{ref}} = 2 \times 10^{-5}$Pa. Two different SPL are of interest for this study. The first one is the incident SPL, related to the amplitude of the incident wave pressure (I in Fig. 2.15). The second one is the global SPL on the material surface, corresponding to the pressure amplitude on the material surface (g in Fig. 2.15). Their SPL are defined as:

$$\mathrm{SPL_i} = 20 \log_{10} \left(\frac{I}{\sqrt{2} p_{\mathrm{ref}}} \right) \qquad \mathrm{SPL}_g = 20 \log_{10} \left(\frac{|p_g|}{\sqrt{2} p_{\mathrm{ref}}} \right) \tag{2.8}$$

The definition of I and R is detailed in Annex C.

In the literature, it is not always precised if the SPL used in the measurements corresponds to the incident SPL or to the global SPL on the plate. When studying the nonlinear regime, the control of the SPL is essential. The difference between these two SPL is significant, and controlling one or another changes the values of the acoustic velocity in the perforations, and the behaviour of the plate.

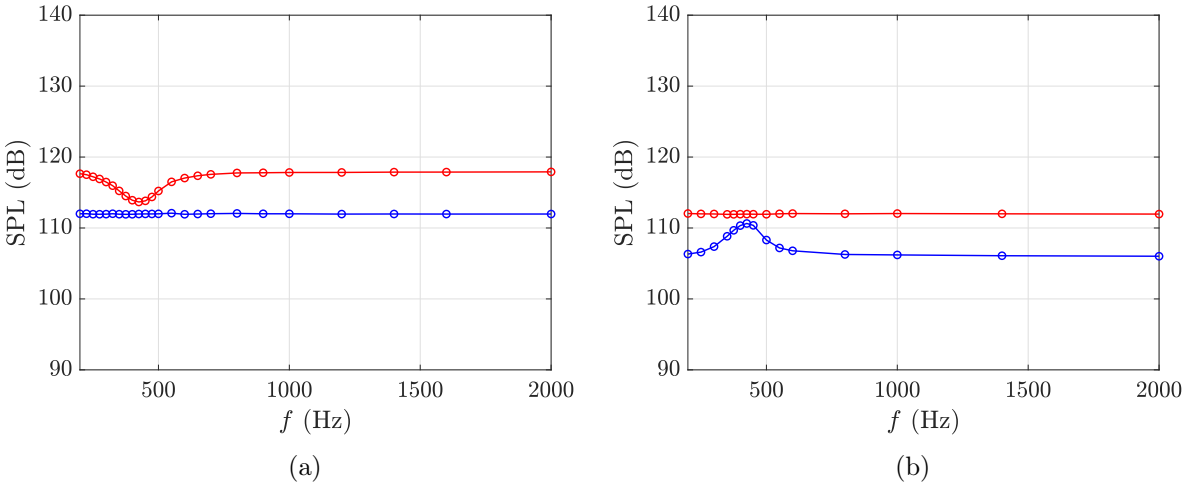

Figure 2.19: Incident $\mathrm{SPL_i}$ (—) and global SPL_g (—) when (a) $\mathrm{SPL_i}$ is costant at 112 dB and when (b) SPL_g tot is constant at 112 dB for sinusoidal excitation

Figure 2.19 shows a comparison between the global and the incident SPL for a plate with a single perforation, maintaining first the incident SPL constant and then the global SPL on the plate constant. It can be observed that the global SPL is higher than the incident SPL in this case. This is not a general rule, as the global SPL on the plate can be smaller than the incident SPL. Also one has $\mathrm{SPL}_g \leq \mathrm{SPL_i} + 6$ dB with the equality satisfied if the plate is perfectly reflecting. At the resonance, the incident SPL and the global SPL are almost equal, because the absorption by the plate is maximum and the reflected wave amplitude is small.

In the course of this study, the incident $\mathrm{SPL_i}$ will be taken as reference for the acoustic control (Chapters 2,3,4 and 6), since it is easier to impose in the experiments in the CAIMAN bench and in the numerical simulations. The global SPL_g will just be employed in Chapter 5 when considering the external global pressure at the plate.

Iterative procedure for controlling the SPL

In Kundt tube experiments (see Fig. 2.15), we can determine both $\mathrm{SPL_i}$ and $\mathrm{SPL_g}$ from the pressures measures at microphones 1 and 2. Indeed, from the system in Eq. (2.2), once p_1 and p_2 are known, I and p_g can be calculated.

The iterative procedure to obtain the target acoustic level at each frequency is presented in Fig. 2.20. The input to the loop are the target SPL value, an initial guess of the signal amplitude A and the error threshold err, e.g. 0.03 dB. Once a measurement has been taken, the measured SPL value is calculated using Eq. (2.7). A parameter "Cond" is defined as the difference between the target SPL and the measured SPL. If this difference is less than the error threshold, it can be concluded that the level obtained corresponds to the expected level. If not, a correction is made to the amplitude of the signal to be sent based on the difference in dB between the two pressure levels, the procedure is repeated until the condition is satisfied.

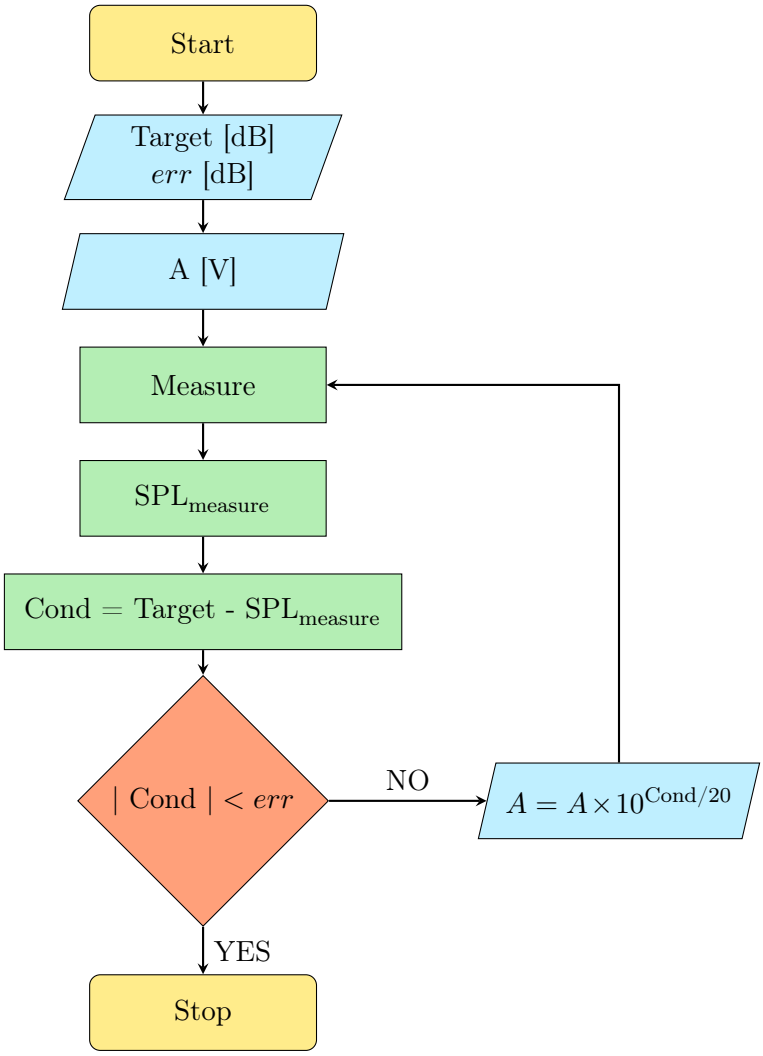

Figure 2.20: Iterative experimental procedure to assure a constant value of the SPL at each excitation frequency.

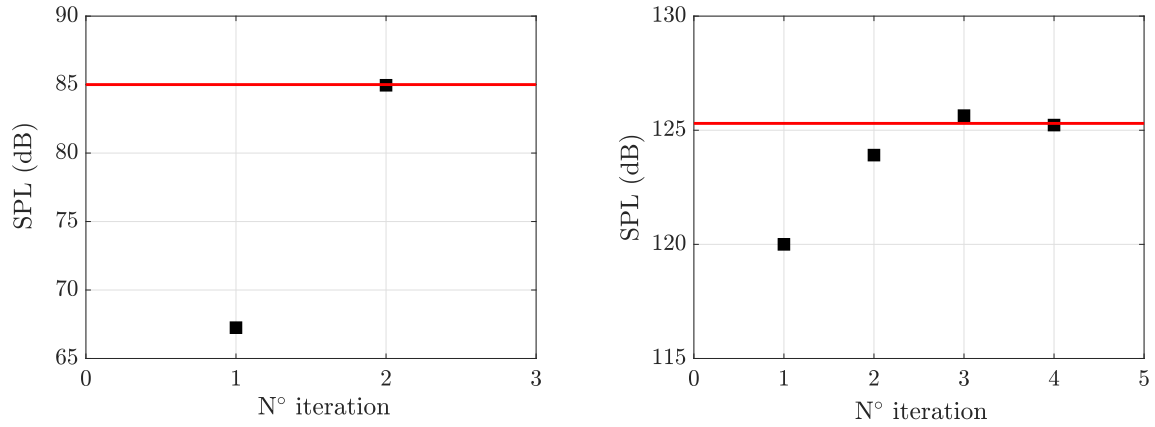

(a) (b)

Figure 2.21: Number of iterations (■) in order to arrive at the target SPL (—) (a) at SPL = 85 dB (b) and SPL = 125.3 dB

Figure 2.21 illustrates the iterative process for the SPL at 92 dB and 130 dB. It is noted that only two iterations are necessary to achieve the target SPL in the linear regime. In the nonlinear regime, convergence requires four iterations.

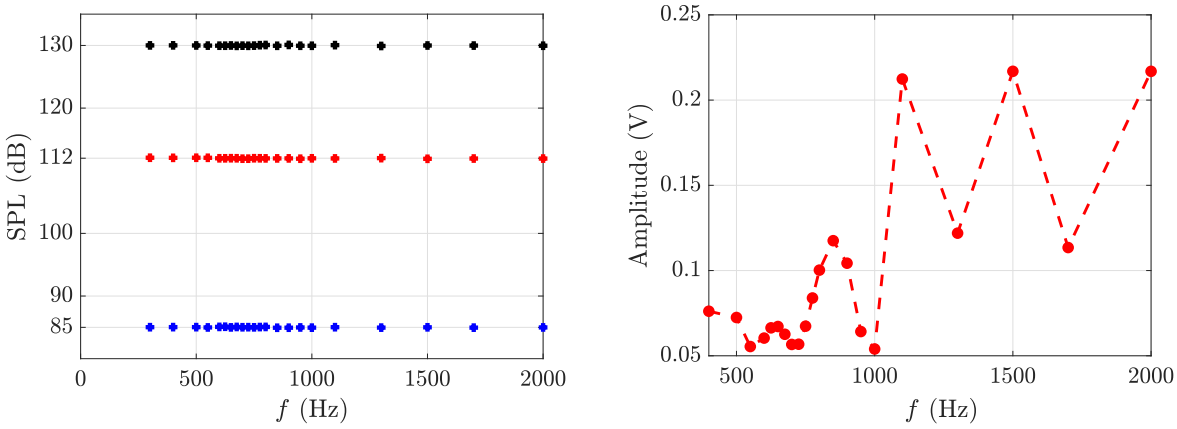

(a) (b)

Figure 2.22: (a) SPL at 85 dB, 112 dB and 130 dB operating the iterative procedure at each frequency and (b) the signal pressure amplitude values for a set of frequencies at a constant SPL = 112 db

Figure 2.33a shows different constant levels obtained for sinusoidal signals with several different frequencies. It can be seen that thanks to this procedure, a constant SPL level is obtained at each frequency, making it possible to evaluate the evolution of a given property with frequency at a constant SPL value. As shown in Figure 2.33b, the constancy of the SPL is granted by the variation of the amplitude of the signal acoustic pressure, which varies with the frequency.

2.3.3.3 Definition of the acoustic indicators

Once the pressure level is accurately controlled in the experiments, it is possible to proceed with the calculation of the plate surface impedance. In reference to Figure 2.15, we can define the surface impedance Z as:

$$Z = \mathrm{j}\frac{h_{12}\sin(kz_2) - \sin(kz_1)}{h_{12}\cos(kz_2) - \cos(kz_1)} \tag{2.9}$$

where h_{12} is the transfer function defined in Eq. (2.5) and $Z_0 = \varrho_0 c_0$. From the impedance value, the reflection coefficient can be derived as :

$$r = \frac{Z-1}{Z+1} \tag{2.10}$$

Finally, the absorption coefficient of the plate is defined as:

$$\alpha = 1 - |r|^2 \tag{2.11}$$

Further on in the course of the discussion, reference will be made the admittance Y given by:

$$Y = \frac{1}{Z} \tag{2.12}$$

Conclusion

In this section, the methodology employed for the acoustic characterisation of perforated plates under normal incidence has been presented. The experimental setup based on a two-microphone impedance tube was described, including details on the instrumentation and measurement protocols. Particular attention was paid to controlling environmental parameters, ensuring linear acoustic propagation, and defining consistent excitation levels for both linear and nonlinear regimes. A precise nonlinear protocol has been introduced to guarantee the constancy of the SPL in each measurement. These procedures ensure accurate and repeatable measurements of the surface impedance and absorption coefficients of the tested samples.

2.4 Experimental study in acoustic wind tunnel: The Caiman flow duct at ECL

2.4.1 Caiman description

Once the experimental procedure for the acoustic characterisation of perforated plates in the impedance tube has been described, the study is extended to the liner (Fig. 2.8) under grazing incidence and in the presence of flow. The bench used for this purpose is the 'Caiman' subsonic wind tunnel for the characterisation of wall acoustic treatments located at the LMFA laboratory of the Ecole Centrale de Lyon, presented in Figure 2.23.

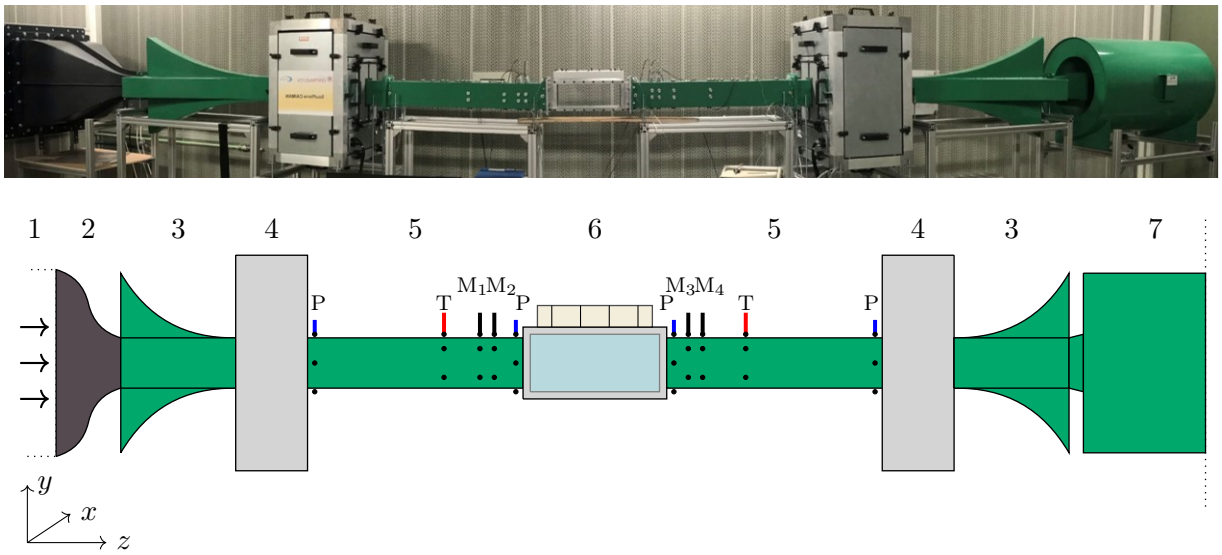

Figure 2.23: Photo and sketch of the acoustic wind tunnel Caiman at Ecole Centrale de Lyon

The wind tunnel is supplied by an ABB M2AA motor (1), with a nominal power of 30 kW, allowing a rotational speed of 3300 rpm. The Mach number based on the bulk velocity inside the duct can reach up 0.3. Through a flow-stabilising convergent (2), the flow is channelled into the duct. The duct presents a rectangular cross-section with a width of 7 cm and a height of 11 cm. The walls of the duct, which are made of steel, are 1 cm thick. The different sections of the duct are joined by mechanical joints protected by bearings to prevent external leakage. An absorbent acoustic horn (3) functions as an anechoic termination in order to reduce the acoustic reflection at the duct inlet. The first array of acoustic sources (4) is found, whose purpose is to produce an acoustic field in the direction of flow (downstream). The array consists of four BMS 2" M8Ω middle range drivers compression chambers, with an optimal frequency range between 300 and 5000 Hz, placed on the four walls of the duct. The sources can be excited individually or simultaneously. Immediately following the array the actual duct begins. The duct consists of three different parts: two rigid-walled sections (5), each 1 m long, and a central 0.3 m-long section (6) in which the liner is placed. Thereafter, mirroring the first part of the bench, is a second array of compression drivers (4) to excite the liner against the flow (upstream), an acoustic horn silencer (3) and finally a silencer (7) that serves as a second anechoic termination and that discharges into an outlet outside the room for proper evacuation of the air flow. The rigid walls of the duct (5) house the microphones for acoustic measurements (M_1,M_2,M_3,M_4), the thermocouples for measurements of the duct's internal temperature (T) and the static pressure tappings (P). The specifications of these

components will be detailed in the characterisations presented in the following paragraphs. The treated duct section is depicted in Figure (2.24).

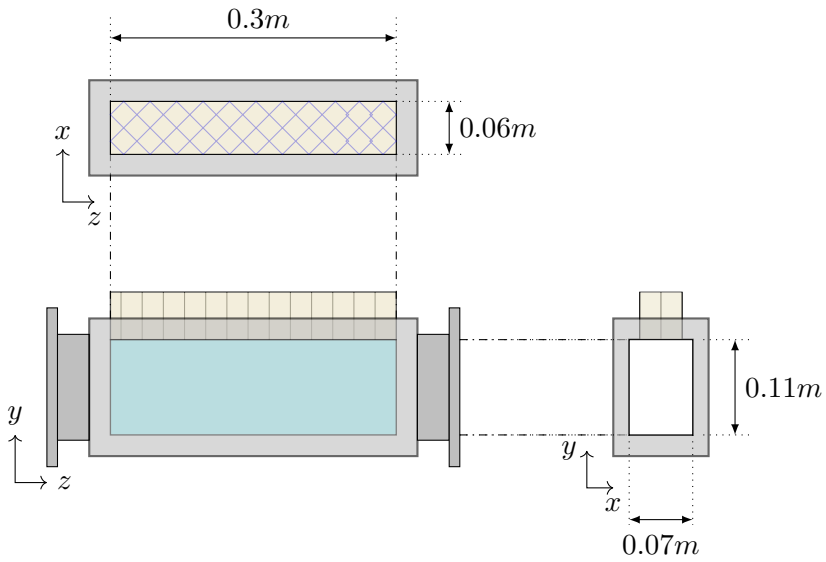

Figure 2.24: Liner placement in the central section of the duct: parametric views and dimensions

The liner is placed in the upper wall of the duct, to which it is anchored thanks to a dedicated resin 3D printed holder. The liner x-length is 0.01 m smaller than the the sample holder in order to guarantee the mounting with a proper clearance. A system of screws allows the perfect surfacing of the perforated liner in the inner wall of the duct. The remaining three walls of the section consist of a glass surface that allows not only to observe the bench inside, but also to carry out any optical inspections.

2.4.2 Caiman thermodynamic characterisation

Following the same procedure carried out in Section 2.3.2, a characterisation of the room and duct conditions is first performed. In order to monitor the characteristics of the incoming air, a hygrometer and thermocouple are placed at the inlet of the wind tunnel fan. A measurement station is also placed outside the duct in order to ensure constant conditions at the outer walls of the duct. Two K-type thermocouples are placed before and after the treated section of the duct in order to have the temperature conditions at the inlet and outlet of the liner in both directions of acoustic excitation. The thermocouples are inserted at a height of 5 cm from the edge in order not to be influenced by the thermal boundary layer. The thermocouple signal is processed via an Omega DP9800TC type control monitor. The measurement of these two temperatures and of humidity at the duct inlet are used to evaluate the sound speed.

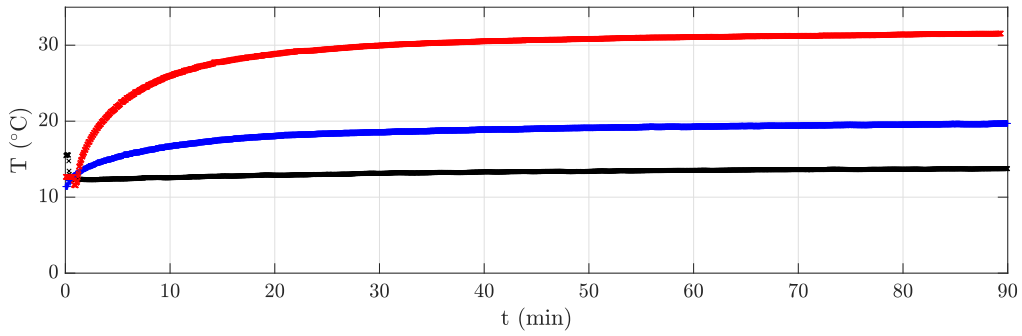

Figure 2.25: Temperatures transients for three different engine speeds: 1000 rpm (—), 2000 rpm (—) and 3000 rpm (—)

Considering the case with flow, it is necessary to ensure that the temperature inside the duct remains stable over time. To do this, the temperature transients presented in Figure 2.25 inside the duct are considered for different rotation speeds (in revolutions per minute, or rpm). The temperature depicted is an average of the two temperatures upstream and downstream of the liner. Each test performed on Caiman is preceded by a 90-minute transient to ensure that a steady-state temperature value is reached inside the duct. Especially for cases with flow, as in Figure 2.25, it can be seen that the temperature variation during the transient reaches up to 20 °C, directly influencing the sound speed value. As recalled in Figure 2.14b, having a temperature value that is as constant as possible allows for a constant sound speed and thus reduces errors on the measurements taken, especially during a single acoustic test. In this configuration it is even more essential to take into account the real value of the sound speed inside of the duct (see Eq. (2.1)), in order both to perform a correct measurement and later to operate a more realistic simulation.

2.4.3 Caiman aerodynamic characterisation

In order to assure a more precise experimental protocol and in order to enter more realistic parameters into the numerical simulation, a characterisation of the flow inside the bench is carried out. First, the static pressure evolution inside the duct is analysed. Secondly, the flow velocity profiles at different wind tunnel engine rotation regimes are measured with the aid of a Pitot tube.

As shown in Figure 2.23, there are sixteen static pressure intakes in four sections of the duct, two upstream of the liner and two downstream. Each outlet is located at the midpoint of a section's walls. The pressures are measured using a Furness Controls FCO510 digital manometer. The values reported below correspond to the average of the four measured pressures per section.

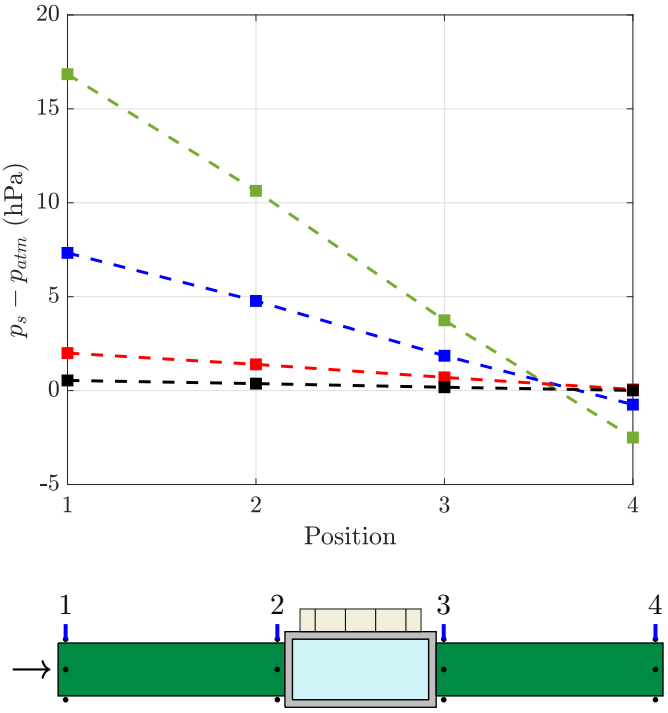

Figure 2.26: Evolution of static pressure change in different duct sections for different engine speeds: 500 rpm (—), 1000 rpm (—), 2000 rpm (—) and 3000 rpm (—)

The curve of the static pressure in the four sections is shown in Figure 2.26. If we take the position 1 as the reference, position 2 is at 0.76 m, position 3 at 1,22 m and position 4 at 1,98 m. Without flow, the pressure remains constant. In presence of flow, the pressure decreases along the duct. In the 3000 rpm case, a depression is observed at the end of the duct, downstream of the liner. For each case considered, the liner section is not affected by a negative pressure change, which would result in the liner being pulled into the duct. However, induced pressure differences could cause displacement and detachment of the liner, hence the need to produce a liner that is robust and resistant to continuous stress.

Once the pressure inside the duct has been assessed, the focus is placed on the flow velocity profile inside the duct. For the study, a rigid component with a perforation at its centre is inserted into the liner compartment to allow a Pitot tube to translate inside the duct. The Pitot tube is electronically controlled with a carriage that allows it to be moved and positioned remotely by a PC in a LabView© environment. For each speed considered, a stationary temperature regime was reached before the measurement was taken. Each profile consists of 18 points taken along the height of the duct measuring 0.11 m.

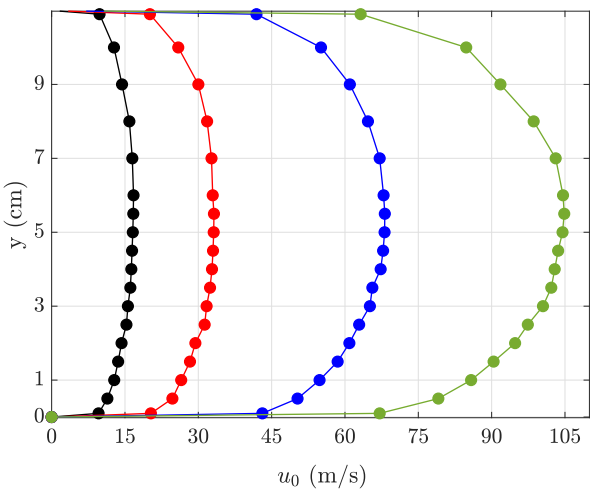

Figure 2.27: Flow velocity profiles at the central section of the liner at different engine speed regimes: — 500 rpm, — 1000 rpm, — 2000 rpm and — 3000 rpm

Figure 2.27 shows the profiles for different engine speeds. It can be observed that the profiles are symmetrical with respect to the centre of the duct and that the boundary layer is increasingly important as the engine speed increases. The Mach number associated with each speed is calculated from the average of the velocities in the section and the stationary temperature of each measurement.

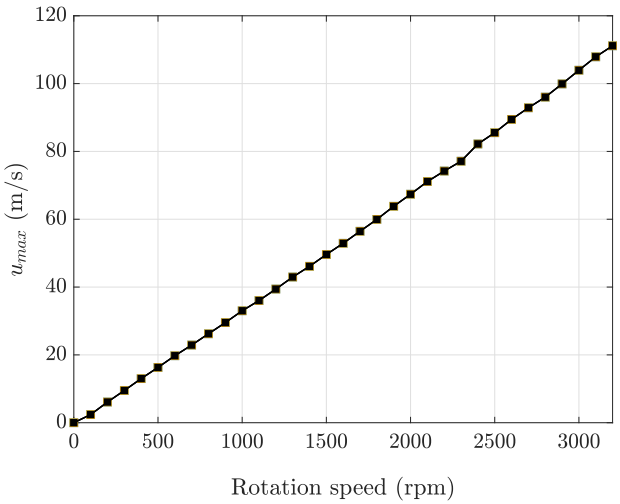

Figure 2.28: Maximum flow velocity u_{max} at the center of the duct cross-section as a function of the respective engine rotation regime

Figure 2.28 presents the evolution of the maximum flow velocity at the center of the duct cross-section as a function of the engine rotation regime. Density and viscosity were calculated from the actual temperature value in the vein. In Eq. (2.13) we define the Reynolds number as:

$$\mathrm{Re} = \frac{\varrho_0 u_0 D_h}{\mu} \tag{2.13}$$

where u_0 is the flow velocity, ϱ_0 the air density, μ the air dynamic viscosity and D_h the hydraulic radius for rectangular ducts defined as (2.14)

$$D_h = \frac{2L_xL_y}{L_x + L_y} \tag{2.14}$$

based on the x and y dimension of the duct (L_x and (L_y respectively).

	Wind tunnel rotation regime (rpm)					
	500	1000	1500	2000	2500	3000
$\bar{T}$ (°C)	25.5	26.6	28.6	31.4	35.8	41.4
u_{max} (m/s)	16.8	33.8	51.5	69.8	89.1	108.7
u_{av} (m/s)	14.8	30.1	46.1	62.5	79.7	97.4
M	0.05	0.1	0.15	0.2	0.26	0.3
M_{av}	0.04	0.09	0.14	0.18	0.23	0.29
$\mathrm{Re_{max}}$	8.9×10^4	1.76×10^5	2.66×10^5	3.55×10^5	4.41×10^5	5.20×10^5
$\mathrm{Re_{av}}$	7.8×10^4	1.56×10^5	2.38×10^5	3.18×10^5	3.94×10^5	4.66×10^5

Table 2.2: Flow aerodynamic properties for several wind tunnel engine speed regimes

Table 2.2 shows the different values of M and Re for different engine speeds, considering both an average value of the velocity taken from the profiles and the maximum value at the center of the vein, which is the maximum as well. For every Mach regime, the flow is fully turbulent.

In the course of the study, all the measurements and calculations will be made using the mean value of the Mach number, but for clearness of the exposition the value indicated in the text will be the maximum value at the center (e.g., a result presented for M = 0.1 refers to a measurement or a simulation performed at $M_{av} = 0.09$).

2.4.4 Caiman acoustic characterisation

The measurement of sound pressure in a duct with flow is particularly delicate, as the captor is subjected to the acoustic pressure and noise of the flow. Pressure standard microphones of the type GRAS 46DE-FV 1/8' CCP with a built-in grid to avoid flow-related perturbations and B&K preamplifiers are mounted as in Figure 2.23 on the inside wall of the duct on the upper wall. Four microphones were used, two upstream of the liner and two downstream, positioned symmetrically to the centre of the vein. Similar to the instrumentation employed in the impedance tube, a B&K Power Amplifier for each of the drivers and a NI PXI-1024Q acquisition-generation card were used. As for the impedance tubes, the generation, acquisition, and post-processing of the signals is made by a PC using codes developed in environment Matlab©. In order that the acoustic signal emerges from the flow noise floor, a sinusoidal type signal was used. Critical measurements results in linear acoustic regimes (below 100 dB), for flows with M > 0.1, for which the acoustic signal may have more difficulty emerging from the flow background noise. The excitation is within a frequency spectrum limited by the duct cutoff frequency, which equals 1550 Hz. This decreases when considering the presence of flow with the addition of the Mach number dependence in the wave number.

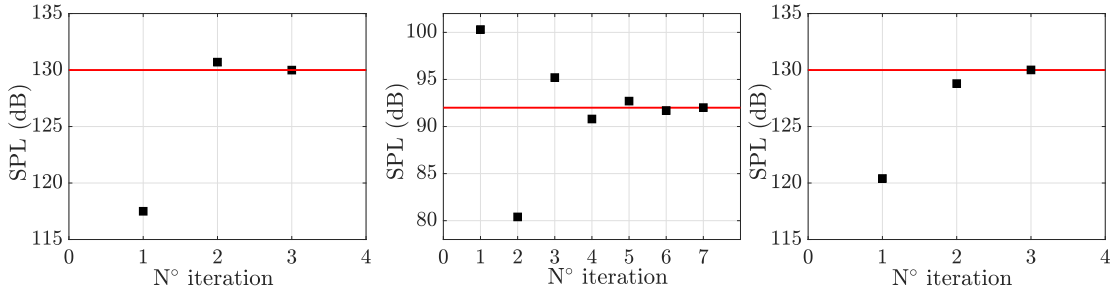

Figure 2.29: Number of iterations (■) in order to arrive at the target incident SPL (—) at (a) SPL = 130 dB, M = 0 (b) SPL = 92 dB, M = 0.1 and (c) SPL = 130 dB, M = 0.1

The incident pressure level SPL_i is controlled by means of the procedure described in Section 2.3.3.2. Figure 2.29 presents the iterative process to arrive at the target incident SPL. In the nonlinear regime at 130 dB, both with and without flow, only three iterations are necessary to get to the target. At 92 dB and $M = 0.1$, the process requires more iterations, indicating a more complex convergence towards the target SPL. This may be attributed to challenges in signal emergence in the presence of flow at low acoustic levels, or to difficulties in reaching a precise value due to fluctuations in the measurement conditions.

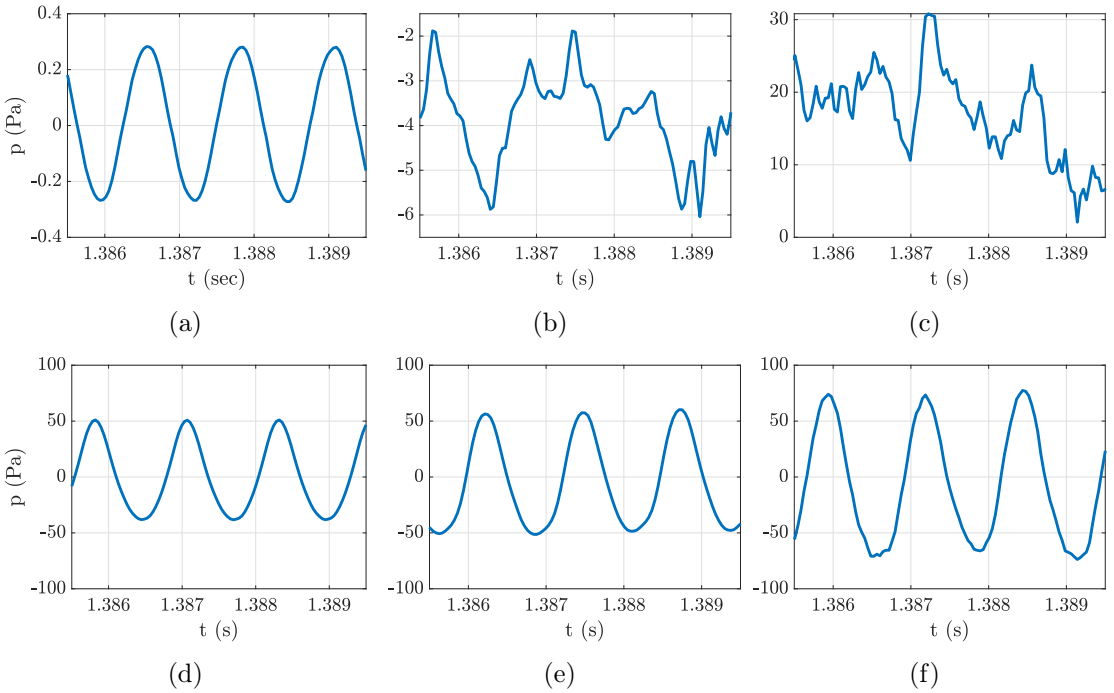

Figure 2.30: Time signal of an harmonic excitation in Caiman for different Mach regimes: $M = 0$ at (a) 92 dB and (d) 130 dB, $M = 0.05$ at (b) 92 dB and (e) 130 dB and $M = 0.1$ at (c) 92 dB and (f) 130 dB at 1000 Hz

An example of time signals measured at a microphone is presented in Figure 2.30. It can be seen that for a nonlinear regime, e.g. 130 dB, the signal appears to have a clean shape. For the linear case, at 92 dB, for regimes of $M = 0.05$ and 0.1, the signal does not look like a sinusoidal wave, due to the weak emergence with respect to the flow background noise. The use of compression chambers allows to keep a sinusoidal signal even in nonlinear regime. This aspect is also verified in nonlinear regime under flow. In linear regime under flow, even if the signal emerges, the form of the signal is disturbed.

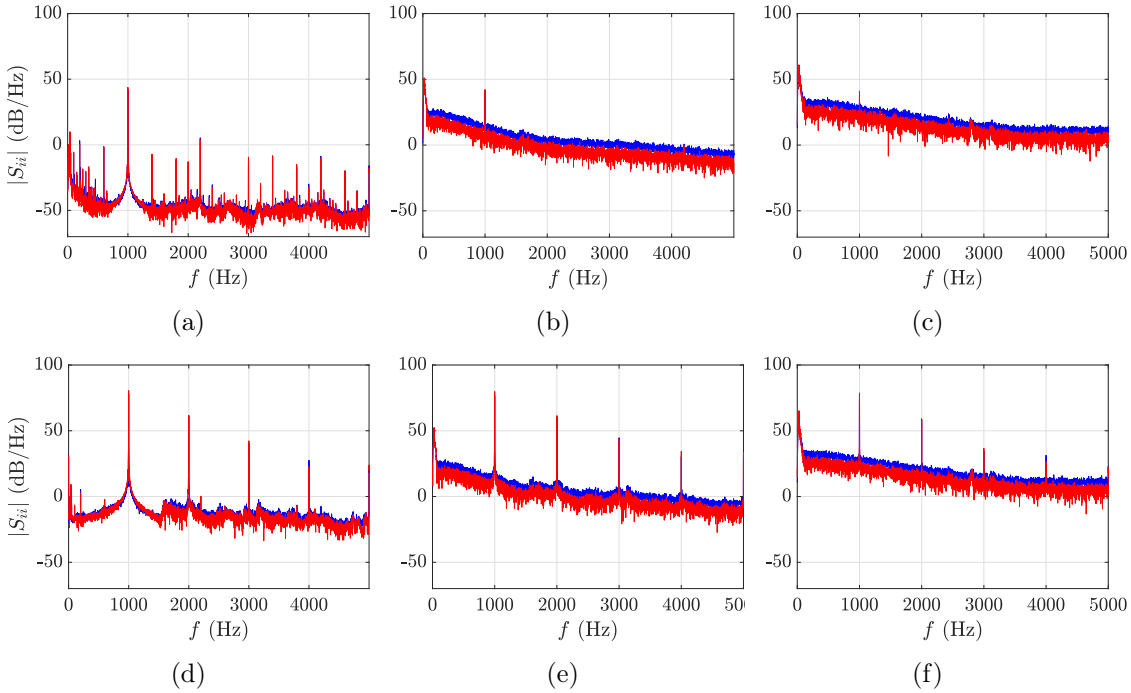

Figure 2.31: Power spectral densities of the incident pressure in Caiman for different Mach regimes: M = 0 at (a) 92dB and (d) 130dB, M=0.05 at (b) 92dB and (e) 130dB and M = 0.1 at (c) 92dB and (f) 130dB for microphones 1 (—) and 4 (—) at 1000 Hz

Figure 2.31 considers the power spectral density of the first (1) and last (4) microphone in the duct for a sinusoidal excitation at $f = 1000\ Hz$ in linear and nonlinear regime for the cases $M = 0$, 0.05 and 0.1. Without flow, the signal-to-noise ratio is excellent at the excitation frequency. The amplitude of the harmonics is significantly lower than that of the excitation frequency. With the flow, despite the increase of the background noise, the peak at the excitation frequency manages to emerge. This is particularly noticeable in the nonlinear case, where the wave contains more energy than in the linear case. The acoustic level at 1000 Hz dominates the spectrum irrespective of the flow velocity in the duct. The signal-to-noise ratio at 1000 Hz is about +14 dB when the wind tunnel is set to full regime. At lower levels, it can be seen that the signal-to-noise ratio gets weaker and weaker as the flow increases, which is why the evaluation of the liner's performance parameters at high flow regimes (M = 0.2, M = 0.3) is more complex.

2.4.4.0 Determination of the liner transmission loss TL

In order to evaluate the performance of a liner within a duct, it is necessary to evaluate the transmission and reflection coefficients, breaking down the acoustic field into incident, reflected and transmitted waves. Specifically, in this study, the transmission loss TL is chosen as the metric for evaluating the efficiency of the liner. The transmission loss is defined as the difference between the incident sound power level and the transmitted sound power level. It quantifies how much sound energy is attenuated as it passes through a lined duct. Higher TL means better sound attenuation.

With flow, the wavenumbers for a plane wave propagating downstream $k+$ and upstream k^- are given by:

$$k^+ = \frac{k}{1+M} \qquad k^- = \frac{k}{1-M} \tag{2.15}$$

with M the mean flow Mach number. The pressure at a microphone i can be expressed as

$$p_i = I\mathrm{e}^{-\mathrm{j}k^+ z_i} + R\mathrm{e}^{\mathrm{j}k^- z_i} \tag{2.16}$$

with I the incident wave amplitude and R the reflected wave amplitude.

Anechoicity of the terminations

If the termination is supposed perfectly anechoic, the transmission loss can be determined from the ratio of the amplitude of the transmitted wave to that of the incident wave. In a rigid wall duct, the transmitted wave is equal to the incident wave, and the wave amplitudes take the form as presented in Figure 2.32.

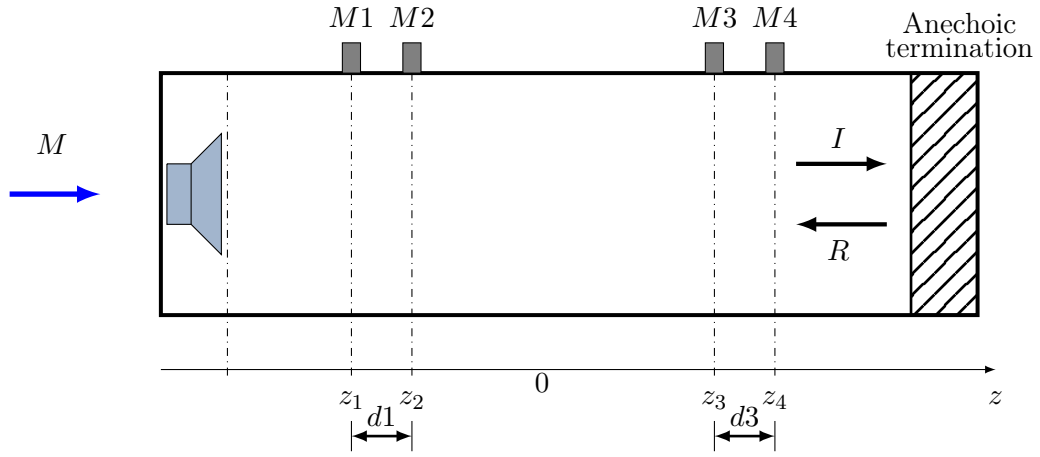

Figure 2.32: Schematic of the rigid wall duct in the case of anechoic termination

The reflection coefficient r is measured as the control parameter on anechoicity, and is defined as [131]:

$$r = \frac{p_3 e^{jk^+ z_3} - p_4 e^{jk^+ z_4}}{p_3 e^{-jk^- z_3} - p_4 e^{-jk^- z_4}} \frac{e^{-j\left(k^+ + k_0^-\right) z_3} - e^{-j\left(k^+ + k_0^-\right) z_4}}{e^{j\left(k^+ + k^-\right) z_3} - e^{j\left(k^+ + k_0^-\right) z_4}} \tag{2.17}$$

with p_1, p_2, p_3, p_4 the pressures measured at each microphone and z_1, z_2, z_3, z_4 the microphone positions from a fixed point 0. For the calculation, we operate by the frequency response function FRF between microphones to get the pressure amplitudes. Figure 2.32 refers to the downstream case. In the upstream case, the acoustic source and the anechoic termination switch position, but the calculation remain the same as in the downstream case.

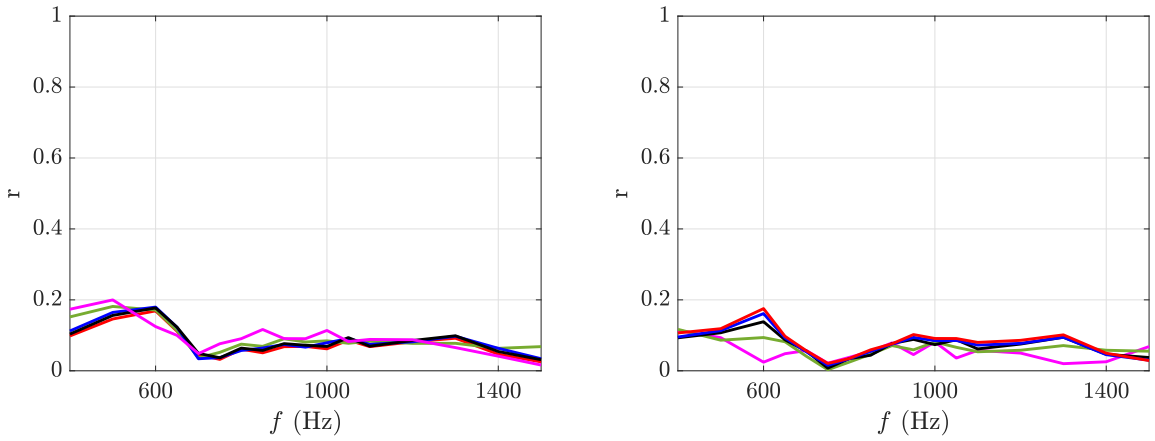

Figure 2.33: Reflection coefficients in Caiman in the rigid-wall case in (a) downstream and (b) upstream for M = 0 (—), M = 0.05 (—), M = 0.1 (—), M = 0.2 (—) and M = 0.3 (—) at 130 dB

In Figure 2.33 it can be noted that the condition of anechoicity is roughly respected for the case without flow. The fact that the reflection coefficient does not have a value exactly equal to zero may be due to dissymmetries in the duct and imperfections in the termination, and cannot be neglected. The results show a sufficiently small reflection coefficient, less than 0.2, over the full range of frequencies studied up to M = 0.3, both in downstream and upstream directions. Even if with relatively small values, reflection for M = 0.2 and M = 0.3 results higher than other cases. For a question of robustness of the results, it is interesting to consider measurement approach that does not rely on the hypothesis of perfectly anechoic termination, since even if low, a reflection coefficient is present and cannot be neglected, even without flow.

One source method with anechoic termination

In a duct treated with a liner, the transmission amplitude T becomes relevant, and the wave amplitudes take the form as presented in Figure 2.34:

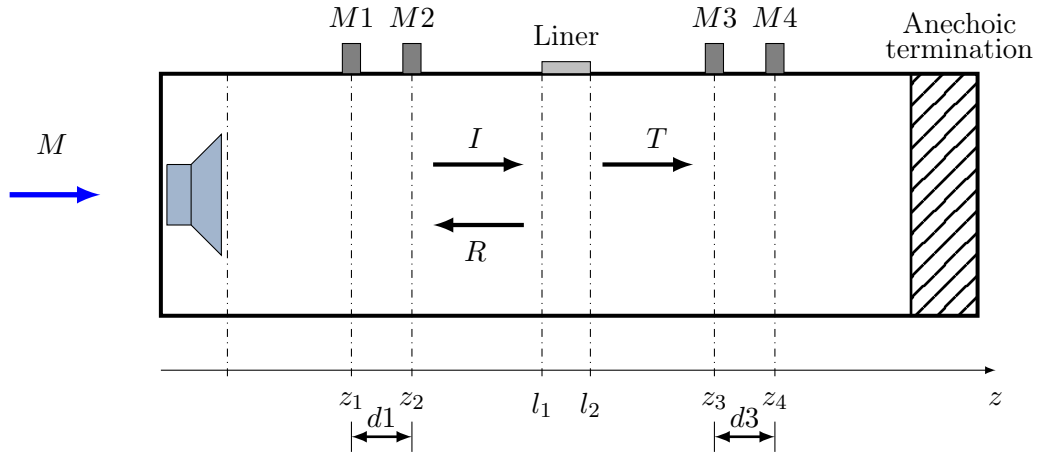

Figure 2.34: Schematic of the treated wall duct in the case of anechoic termination, downstream case

If the duct termination is supposed perfectly anechoic , the transmission loss TL in downstream direction can be written as [131]:

$$\mathrm{TL} = 20\log_{10}\left|[\mathrm{e}^{+\mathrm{j}(k^+ + k^-)z_1} - \mathrm{e}^{+\mathrm{j}(k^+ + k^-)z_2}]\frac{p_3\mathrm{e}^{-\mathrm{j}k^+ z_3}}{p_1\mathrm{e}^{-\mathrm{j}k^- z_1} - p_2\mathrm{e}^{-\mathrm{j}k^- z_2}}\right| \tag{2.18}$$

When considering the upstream case, it is just necessary to switch the source and the termination, and to consider $M < 0$.

A parallel one source method, developed by Bolton et al. [26], adds to the anechoic termination hypothesis the strong hypothesis of perfect symmetry and reciprocity of the duct [142]. For completeness, its description is presented in Annex A.1 for both downstream and upstream case. Nevertheless, the hypothesis of perfect symmetry is no longer respected as a flow is introduced in the duct, being the flow itself not symmetrical if considering downstream or upstream cases, making this method not applicable to our case.

Two-source method

In order to fully detach from the type of termination, a diffusion matrix is introduced to calculate the pressure coefficients using the defined two source method, first introduced by Abom [1]. In this method, the duct is first excited in the downstream direction of the flow and in a second time in the opposite direction. Without flow, the wave numbers are the same for the two configurations, and the difference between upstream and downstream source results should be minimal. With flow, the two wave numbers change, differentiating the upstream and downstream cases consistently. The cutoff frequency of the duct is taken as the maximum frequency (1550 Hz). For the measurement of the two-source method, reference is made to Figure 2.35. The details of the matrix calculation are described in Appendix A.2.

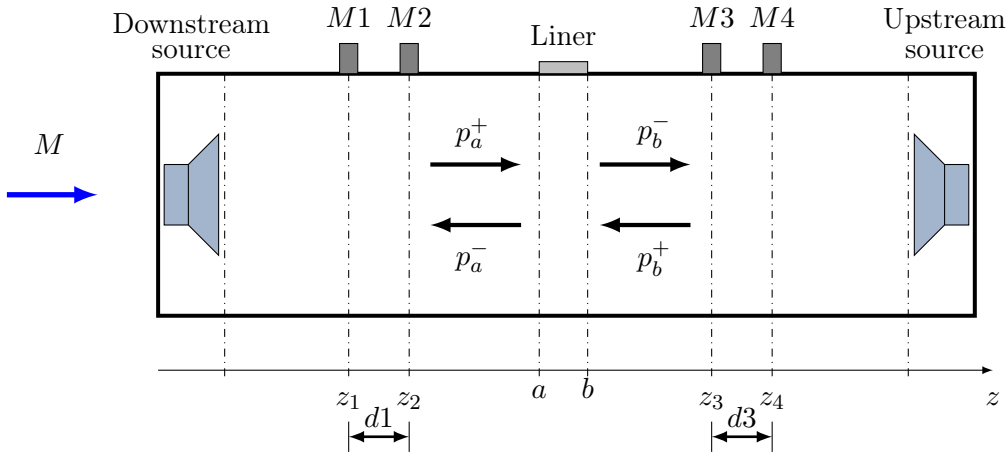

Figure 2.35: Schematic of the duct in the case of two-source method

From the evaluation of the pressure amplitudes in the upstream and downstream cases, the scattering matrix $\boldsymbol{D}$, which give linear relationship between incoming and outgoing pressure wave vectors, is introduced as :

$$\begin{pmatrix} p_a^- \\ p_b^- \end{pmatrix} = \boldsymbol{D} \begin{pmatrix} p_a^+ \\ p_b^+ \end{pmatrix} \tag{2.19}$$

As a result of mathematical manipulations, the matrix D can be defined as a matrix of 4 elements:

$$\boldsymbol{D} = \begin{pmatrix} D_{11} & D_{12} \\ D_{21} & D_{22} \end{pmatrix} \tag{2.20}$$

In particular, taking the downstream case M > 0 as the main direction, D_{11} is the reflection coefficient in the downstream case, D_{22} is the reflection coefficient in the upstream case, D_{12} is the transmission coefficient in the downstream case and D_{21} is the transmission coefficient in the upstream case. From here, the transmission loss in the downstream case TL^+ and upstream case TL^- can be defined as

$$\mathrm{TL}^+ = 20\log_{10}\left(\frac{1}{|D_{12}|}\right) \qquad \mathrm{TL}^- = 20\log_{10}\left(\frac{1}{|D_{21}|}\right) \tag{2.21}$$

Moreover, the two-source method allows to obtain the measures of the TL in both directions with just one procedure, making the measurement process faster.

Conclusion

The Caiman wind tunnel has been fully characterised from thermodynamic, aerodynamic, and acoustic perspectives to ensure reliable measurements of liner performance under grazing incidence and flow conditions. The thermodynamic analysis guarantees temperature stability during tests, while the aerodynamic characterisation provides accurate flow profiles and pressure distributions for different regimes. Finally, the acoustic analysis addresses the challenges of measuring sound fields in the presence of flow, allowing the determination of transmission loss with appropriate corrections for flow-induced effects. Due

to the limitations of assuming perfect anechoic terminations, especially in the presence of flow, the two-source method is employed to accurately determine the transmission loss of the liner. This comprehensive characterisation establishes a robust framework for subsequent liner performance evaluation.

2.5 Conclusions

This chapter describes the experimental protocol developed for the characterisation and testing of acoustic liners, focusing on material selection and performance under various conditions.

The liner design process began with a detailed analysis of materials and manufacturing methods. A modular design was chosen, combining a galvanized steel perforated plate with a separate resonant cavity. This ensured mechanical strength, resistance to stress, and precise perforation geometry, verified through optical and acoustic inspections. Galvanized steel was selected to be manufactured with laser cutting technique for its ability to maintain perforation quality in both macro- and micro-perforated forms.

Acoustic characterisation was performed in an impedance tube under normal incidence. Measurements included surface impedance, reflection coefficient, and absorption coefficient. An iterative procedure was implemented to control the acoustic pressure levels, ensuring consistent and reliable results, particularly for nonlinear acoustic behaviour. This method maintained stable sound levels across frequencies, reducing errors and enabling accurate characterisation under high sound pressures. In particular, the procedure of control of of the incident sound pressure level is particularly effective in Caiman duct, when considering nonlinear regimes in presence of flow.

A robust liner assembly was developed, combining the steel plate with a polycarbonate honeycomb cavity sealed by a silicone joint. This addressed issues such as sealing, prevention of transverse leaks, and proper alignment within the duct. The honeycomb structure was optimized to ensure structural integrity and uniform perforation distribution.

The Caiman wind tunnel was characterized to assess liner performance under flow conditions. This included aerodynamic profiling of pressure and velocity, and acoustic testing with grazing incidence, both with and without flow. To address this, a two-source method was implemented, allowing accurate transmission loss measurements even in high-speed flows. The use of compression chambers guarantee the signal to remain sinusoidal even in nonlinear regime. In presence of flow, the signal at linear regime results distorted, making more difficult to have a stable TL in such conditions.

Results confirmed that linear acoustic propagation was preserved in most cases, with nonlinear effects isolated when required. However, high Mach numbers reduced the signal-to-noise ratio, making measurements difficult under linear conditions. Despite this, harmonic excitation allowed the acoustic signal to remain above flow-induced noise, ensuring data accuracy.

This chapter offers a comprehensive methodology for acoustic liner testing, integrating material analysis, experimental design, and aerodynamic assessment.

3 Numerical methods for duct acoustic propagation

Contents

Abstract

This chapter presents the models used in this thesis to predict the propagation of sound waves in ducts. The focus is on ducts lined with acoustic absorbers and in presence of flow, which are commonly used in aerospace and industrial applications to reduce noise. Accurately modelling these systems is crucial for optimizing their performance and gaining a better understanding of the underlying physical phenomena. First, the chapter discusses the mode matching technique, a well-established semi-analytical method that is widely used for addressing acoustic wave propagation problems in duct systems. This technique is particularly helpful when dealing with ducts that have different acoustic properties in different segments, such as rigid walls and acoustically treated walls. Then, time-domain approaches based on the linearized Euler approaches are presented. They allow one to consider non-uniform grazing flow. In particular, a time-domain nonlinear admittance boundary condition is described. It has proven to be efficient in capturing nonlinear effects for perforated plate liners. The chapter concludes with a detailed evaluation of finite-difference methods for simulating sound propagation in both one-dimensional and two-dimensional duct configurations.

3.1 Mode-matching approach

The mode-matching method is an established analytical approach for studying acoustic wave propagation in ducts with piecewise varying acoustic properties, such as rigid and acoustically lined sections. The method decomposes the acoustic field into eigenmodes, which represent the natural solutions to the governing equations under specific boundary conditions. By enforcing continuity of pressure and velocity at the interfaces between different regions, the method allows for accurate and efficient prediction of the acoustic field. Its primary strength lies in its ability to handle higher-order modes, which is critical for predicting acoustic behaviour in lined ducts, particularly in scenarios where frequencies exceed the plane wave cutoff.

Historically, the method was developed to address simplified cases of plane wave propagation in uniform flow conditions. Early advancements included iterative techniques such as the Newton-Raphson and secant methods for finding eigenmodes, enabling the method to handle higher-order modes more effectively [12, 87]. These developments made the mode-matching method highly effective for studying idealized configurations. However, the introduction of acoustic liners added complexity, necessitating the development of impedance boundary conditions, such as the Ingard-Myers boundary condition, which models the interaction between sound waves and acoustic liners. Although this boundary condition is widely used, studies by Gabard et al. [56] and Deng et al. [49, 50] revealed its limitations, particularly in cases involving shear flows or boundary layers. Gabard showed that the Ingard-Myers boundary condition could overestimate sound attenuation, emphasizing the need for refined boundary conditions to better capture the effects of flow profiles and liner interactions.

In recent years, efforts have been made to extend the applicability of the mode-matching method to more complex and realistic scenarios. Pagneux et al. [20] introduced multimodal approaches that account for non-uniform flow profiles, broadening the method's relevance to practical engineering problems. Deng [49] utilized the mode-matching method alongside modal analysis to study higher-order modes in lined ducts with both uniform and shear flow conditions, demonstrating its effectiveness in analyzing sound propagation under more challenging configurations. Similarly, Betgen [19, 131] applied the method to hybrid active-passive acoustic liners for noise reduction in aerospace applications, showcasing its value in optimizing liner performance.

While the method's computational efficiency and accuracy make it indispensable for fundamental research and benchmarking, its reliance on simplified assumptions limits its application in complex geometries or scenarios involving nonlinear effects and flow. To address these limitations, hybrid approaches combining mode-matching with fully numerical methods, such as finite element or time-domain simulations, have been developed. These hybrid methods retain the efficiency of the mode-matching framework while allowing for the analysis of nonlinearities and transient phenomena, making them particularly useful for solving broadband noise problems or capturing detailed flow-acoustic interactions. Comparisons of the methods have been implemented by Deng et al. [49] and Gabard and al. [56]. Recently, Mangin et al. [102] proposed an extension of the multimodal methodology to account for an accurate flow description at high Mach numbers, after having proposed a multiple-scale flow extension accurate for low frequencies and low Mach numbers [101].

3.1.1 Theoretical calculation

For this study, it is made reference to the geometric dimensions of the CAIMAN bench at ECL's LMFA laboratory (Section 2.4). A duct with a rectangular cross-section is modeled, ideally divided into three sections, the first and last with rigid walls and the intermediate section with an upper wall characterised by an acoustic treatment, as shown in Fig. 3.1 .

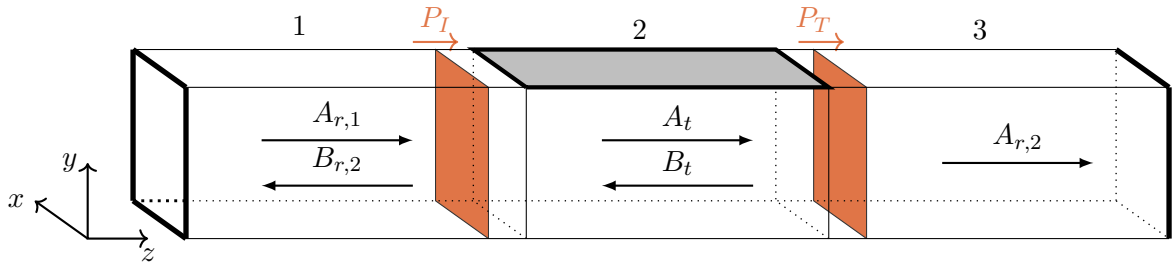

Figure 3.1: Sketch of the CAIMAN duct

Formulation

The quantities and equations considered in this section are dimensionless. $A_{r,1}$ and $A_{r,2}$ are the modal amplitudes of the outgoing waves in the first and second rigid sections, respectively. Reflected waves are produced at the boundary between the rigid and lined sections. $B_{r,1}$ and B_t represent the amplitudes of the reflected waves in the first rigid and lined sections. There are no reflected waves leaving the second rigid section, as it is assumed that the exit plane of the duct is anechoic. The modal characteristics of the source are determined by setting the values of $A_{r,1}$ in the first rigid section of the duct.

Considering an uniform flow, propagation of acoustic waves is governed by the convected wave equation:

$$\nabla^2 p - \frac{1}{c_0^2}\frac{D^2 p}{Dt^2} = 0 \tag{3.1}$$

with the convective derivative containing the Mach number M:

$$\frac{D^2}{Dt^2} = \left(\mathrm{j}\omega + c_0 M \frac{\partial}{\partial z}\right)^2 \tag{3.2}$$

For the boundary conditions, the walls along the z-axis are all rigid, yielding:

$$\left.\frac{\partial p}{\partial x}\right|_{x=0,L_x} = 0 \tag{3.3}$$

In the first and third parts of the duct, a rigid boundary condition is applied on the walls along the y-axis:

$$\left.\frac{\partial p}{\partial y}\right|_{y=0,L_y} = 0 \tag{3.4}$$

Finally, in the second part of the duct, the lower wall ($y = 0$) is rigid and the upper wall ($y = L_y$) is lined, which writes using the Ingard-Myers boundary condition:

$$\left.\frac{\partial p}{\partial y}\right|_{y=0} = 0 \qquad \left.\frac{\partial p}{\partial y}\right|_{y=L_y} = -\frac{D^2}{Dt^2}\left(\frac{p}{\mathrm{j}\omega Z}\right) \tag{3.5}$$

The pressure can be expressed as the following modal sum:

$$p(x,y,z) = \sum_{l,m} \left[A_{l,m}\psi^{+}_{l,m}(x,y)\mathrm{e}^{-\mathrm{j}k^{+}_{lm}z} + B_{l,m}\psi^{-}_{l,m}\mathrm{e}^{-\mathrm{j}k^{-}_{lm}z} \right] \tag{3.6}$$

where $\psi^{\pm}$ are the eigenfunctions associated to the rigid or treated section and k^{+} and k^{-} are the axial wavenumbers in the downstream and upstream directions, respectively.

The eigenfunctions of the duct can be expressed by:

$$\psi(x,y) = \Lambda \cos(\sigma x)\cos(\gamma y) \tag{3.7}$$

where the transverse wavenumbers σ and γ are related to the axial wavenumbers by the dispersion relation:

$$k^2 + \gamma^2 + \sigma^2 = (\omega - Mk)^2 \tag{3.8}$$

obtained with Eq. (3.1). Finally, Λ are defined in order to make the modes forming an orthonormal base (Annex A.2 of [19]).

Up to now, the wavenumbers and the modal amplitudes are not known. We detail in the next two sections how to get these values.

Wavenumbers

In the rigid sections, the transversal wavenumbers σ_l and γ_m are given by:

$$\sigma_l = \frac{l\pi}{l_x} \qquad \gamma_m = \frac{m\pi}{l_y} \tag{3.9}$$

Using the dispersion relation in Eq. (3.8), the axial wavenumbers $k^{\pm}_{lm}$ in the rigid section can be expressed as:

$$k^{\pm}_{lm} = \frac{-M\omega \pm \sqrt{\omega^2 - (1-M^2)(\gamma_m^2 + \sigma_l^2)}}{1-M^2} \tag{3.10}$$

For the treated section, the wavenumbers along the z-direction are still given by $\sigma_l = l\pi/l_x$. However, the wavenumbers γ and k cannot be obtained analytically and have to be determined numerically. For that, using the boundary condition in Eq. (3.5), one has:

$$\mathrm{j}\omega Z\gamma \sin(\gamma) + (\omega - Mk)^2 \cos(\gamma) = 0 \tag{3.11}$$

With the relation dispersion in Eq. (3.8), we can write:

$$\gamma = \sqrt{(\omega - Mk)^2 - k^2 - \sigma^2} \tag{3.12}$$

Combining Eqs. (3.11) and (3.12) leads to an equation under the form $f(k,\sigma) = 0$ with $\sigma_l = l\pi/l_x$. Following Rienstra [120], this equation is solved iteratively. At the first iteration, we consider a large value of $|\Im(Z)|$ using as initial guess for k the values given in the rigid case by Eq. (3.10). We then gradually decrease the value of $|\Im(Z)|$ towards its actual value, using as initial guess the values of k determined at the previous step. Once the values of $k^{\pm}_{lm}$ are obtained, one can get $\gamma^{\pm}_{lm}$ using Eq. (3.12).

3.1.2 Mode matching procedure

The matching of the modal expansions between the rigid (r) and the treated (t) part of the duct is based on the continuity of the pressure and the axial velocity at the interface between the two sections. We first express the axial velocity as a function of the acoustic pressure, using the linearized Euler equation:

$$\frac{\partial p}{\partial z} = -\frac{Du}{Dt} = -\left(\mathrm{j}\omega + M\frac{\partial}{\partial z}\right)u \tag{3.13}$$

This leads to:

$$u = \frac{k}{\omega - Mk_z}p \tag{3.14}$$

At the interface between two parts of the duct, we can write the continuity of the pressure:

$$\begin{cases} A_{r,1}\psi_r^+ + B_{r,1}\psi_r^- = A_t\psi_t^+ + B_t\psi_t^+\mathrm{e}^{\mathrm{j}k_z^- l_z} & \text{(3.15a)} \\ A_t\psi_t^+\mathrm{e}^{-\mathrm{j}k_z^+ l_z} + B_t\psi_t^- = A_{r,2}\psi_r^+ & \text{(3.15b)} \end{cases}$$

and the continuity of the velocity:

$$\begin{cases} A_{r,1}\dfrac{k_r^+}{\omega - Mk_r^+}\psi_r^+ + B_{r,1}\dfrac{k_r^-}{\omega - Mk_r^-}\psi_r^- = A_t\dfrac{k_t^+}{\omega - Mk_t^+}\psi_t^+ + B_t\mathrm{e}^{\mathrm{j}k_t^- L_x}\dfrac{k_t^+}{\omega - Mk_t^-}\psi_t^- & \text{(3.16a)} \\ A_t\mathrm{e}^{-\mathrm{j}k_t^+ L_x}\dfrac{k_t^+}{\omega - Mk_t^+}\psi_t^+ + B_t\dfrac{k_t^-}{\omega - Mk_t^-}\psi_t^- = A_{r,2}\dfrac{k_r^+}{\omega - Mk_r^+}\psi_r^+ & \text{(3.16b)} \end{cases}$$

Integrating Eqs. (3.15) and (3.16) over the section gives a relation between the modal amplitudes, which can be recast under a matrix form. We do not further detail the procedure to obtain the modal amplitudes. For interested readers, this is described in Sec. 1.3.1 of the thesis of Betgen [19] and in Sec. 2.2.1 of the thesis of Deng [49].

Transmission loss

Once we have determined the acoustic pressure in the different parts of the duct, we can determine the transmission loss. For that, we first introduce the acoustic intensity in the presence of flow [53]:

$$I(x,y,z) = \frac{1}{2}[(1+M^2)\Re(pv^*) + M\Re(pp^*) + M\Re(vv^*)] \tag{3.17}$$

By integration of the intensity in a section, it is possible to obtain the acoustic power as:

$$P(z) = \iint I(x,y,z)\,\mathrm{d}x\,\mathrm{d}y \tag{3.18}$$

Finally, we obtain the transmission loss TL:

$$\mathrm{TL} = 10\log_{10}\left(\frac{P_I}{P_T}\right) \tag{3.19}$$

where P_I is the incident power and P_T the transmitted power, as represented in Figure 3.1.

3.2 FDTD solution of the linearized Euler equations

3.2.1 Literature context

Numerical modeling of sound propagation in lined ducts requires the accurate solution of the linearized Euler equations, which describe the propagation of small-amplitude acoustic waves in moving, inhomogeneous media. Time-domain formulations offer the advantage of broadband simulations and allow for the inclusion of nonlinear effects, which are crucial in high-amplitude regimes such as aeroacoustic applications.

Time-domain solutions of the linearized Euler equations for duct acoustics have been widely developed since the work of Özyörük et al. [116]. Various numerical schemes have been applied, each offering specific advantages in handling complex geometries and flow configurations. Among these, finite element methods (FEM) are widely employed [30], owing to their adaptability in addressing complex geometries, as evidenced by the studies of Joly et al. [75, 76], Kampinga et al. [84, 85], and Tissot et al. [148]. In contrast, finite volume methods (FVM), which formulate conservation laws in their integral form, are particularly effective for applications involving diverse and complex flow configurations, as demonstrated in the works of Cockburn [39] and Carcione et al. [33]. Temporal discretization often employs Runge-Kutta methods, which strike a balance between stability and accuracy, as highlighted by Toulorge [149] in the context of wave propagation. Discontinuous Galerkin methods are another popular choice due to their flexibility and ability to handle discontinuities in solutions, although careful numerical scheme selection is required to ensure stability [64]. Validation remains a critical step in the development of numerical models, ensuring that simulations accurately replicate physical behaviour [103, 104, 154].

A critical challenge in time-domain simulations lies in the modeling of frequency-dependent dissipative effects, such as those occurring in porous liners or perforated plates. Translating frequency-domain impedance conditions into time-domain boundary conditions introduces convolution products that are computationally expensive to evaluate. To overcome this, time-domain impedance (TDIBC) and admittance (TDABC) boundary conditions have been developed over the past three decades [52, 116, 141, 150]. One approach is to treat the liner as a surface with a specific impedance, which is computationally efficient and widely used when the liner's geometry does not necessitate detailed modeling. This method has been extensively employed by Özyörük et al. [116], Tam et al. [141], Monteghetti [109], Billard [22], and Diab [51] to address both linear and nonlinear regimes. Among these, the Auxiliary Differential Equation (ADE) approach introduced by Troian et al. [150] approximates impedance or admittance using rational functions and recasts the convolution into a set of first-order differential equations, enabling efficient time integration. Alternative methods, such as equivalent fluid models presented by Alomar et al. [10, 11], also allow the representation of porous and perforated materials directly in the time domain, though at higher computational cost. Alternatively, liners can be modeled as equivalent porous media, allowing the propagation of acoustic waves within the material to be captured. Although computationally more demanding, this method provides a more detailed description of liner behaviour, particularly under nonlinear conditions. Recent works by Moufid et al. [112, 113] have demonstrated the efficacy of this approach, implementing time-domain models based on the Equivalent Fluid Model to study the nonlinear response of acoustic liners in detail.

More recently, nonlinear effects in perforated liners have been incorporated into time-domain models. These effects, including flow separation and vortex shedding at high sound pressure levels, lead to amplitude-dependent impedance characteristics. Diab et al. [51] proposed a nonlinear admittance boundary condition based on TDABC, while Moufid et al. [112, 113] modeled perforated plates as nonlinear equivalent fluids, introducing a Forchheimer correction to account for velocity-dependent resistance. Such approaches have demonstrated improved accuracy in simulating the nonlinear response of liners under realistic flow conditions.

Models are typically validated against experimental data obtained from impedance tube measurements or aeroacoustic bench tests, as illustrated in studies by Billard [22] and Diab [51], who explored the influence of excitation levels on sound propagation. Similarly, Jones et al. [78, 82] and Howerton et al. [65] investigated liner behaviour under grazing flow conditions, further advancing the understanding of acoustic liner performance in realistic environments.

In the present work, we use the TDABC formulation introduced by Diab et al. [51], following the ADE approach of Dragna [52] and Troian [150], to model the interaction of acoustic waves with perforated liners. The liner impedance model, detailed in Chapter 1, is implemented as a nonlinear boundary condition in both impedance tube and grazing flow duct simulations. This framework allows the investigation of liner behaviour under high-amplitude and flow conditions. Application are made both to an impedance tube and a lined flow duct.

3.2.2 Finite difference time domain method

In the study of sound propagation with small amplitude acoustic perturbations in a flow duct, the linearized two-dimensional Euler equations (LEE) govern the behaviour of the system. These equations can be written as follows:

$$\begin{cases} \dfrac{\partial u}{\partial t} + u_0 \dfrac{\partial u}{\partial z} + +w \dfrac{\partial u_0}{\partial y} + \dfrac{1}{\varrho_0} \dfrac{\partial p}{\partial z} = 0 \\ \dfrac{\partial w}{\partial t} + u_0 \dfrac{\partial w}{\partial z} + \dfrac{1}{\varrho_0} \dfrac{\partial p}{\partial y} = 0 \\ \dfrac{\partial p}{\partial t} + u_0 \dfrac{\partial p}{\partial z} + \varrho_0 c_0^2 \left(\dfrac{\partial u}{\partial z} + \dfrac{\partial w}{\partial y} \right) = Q \end{cases} \tag{3.20}$$

where u and w represent the acoustic axial and transverse velocity, respectively, u_0 is the axial component of the flow, p represents the acoustic pressure, and Q is a forcing term.

To solve these equations, high-order finite-difference time-domain (FDTD) methods are used. The spatial derivatives are calculated using optimized fourth-order finite difference schemes over 11 points [18, 24]. Time integration is carried out using an optimized six-stage, fourth-order Runge-Kutta algorithm [17]. In order to prevent numerical instabilities and eliminate grid-to-grid oscillations, selective filters are applied after each time iteration, as described by Bogey et al. [25].

3.2.3 Perforated plate modeling

In this section, the modeling of the perforated plate liner inside the duct is addressed. This can be done either by modeling it by a surface impedance (Section 3.2.3.1), or by explicitly calculating the propagation inside the cavity and modeling the perforated plate by an impedance discontinuity between the duct and the cavity (Section 3.2.3.2).

3.2.3.1 Time-Domain Admittance Boundary Condition (TDABC)

First, we consider the treated region as a surface with a specific impedance Z (or admittance $Y = 1/Z$). The system can be represented as shown in Figure 3.2.

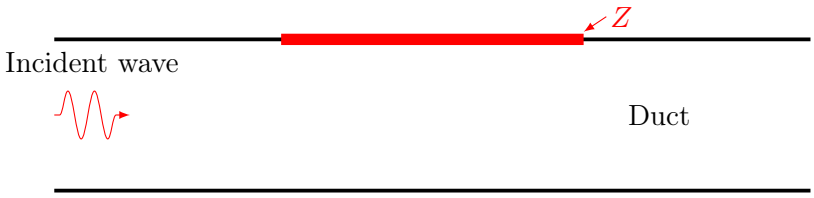

Figure 3.2: Sketch of the duct with surface impedance modelling

Linear regime

Before addressing the nonlinear case, we first briefly discuss the implementation of the time-domain admittance boundary condition in the linear regime. The admittance boundary condition is written in the frequency domain as $Z_0 U_n(\omega) = Y(\omega)P(\omega)$, where $U_n = \mathbf{U} \cdot \mathbf{n}$ represents the normal component of the velocity vector $\mathbf{U}$. $P(\omega)$ and $\mathbf{U}(\omega)$ are the Fourier transforms of the acoustic pressure and velocity on the liner surface, respectively. The time-domain version of the admittance boundary condition is derived by translating the frequency domain condition, yielding the convolution:

$$Z_0 u_n(t) = [y * p](t) \tag{3.21}$$

where $y(t)$ is the surface admittance in the time domain and $Z_0 = \varrho_0 c_0$.

The convolution appearing in Eq. (3.21) is computationally expensive, as it requires to store the history of the acoustic pressure on the liner and to evaluate an integral at every time step. To avoid its computation, we approximate the admittance in the frequency domain by a multipole model [150]:

$$Y(\omega) = Y_\infty + \sum_{k=1}^{P} \frac{A_k}{\lambda_k - \mathrm{j}\omega} \tag{3.22}$$

where λ_k are the poles of the admittance, and P denotes the number of poles. The poles and coefficients A_k can be real or come as complex conjugate pairs, and Y_∞ is a real-valued constant.

To approximate the broadband admittance, the vector fitting (VF) algorithm is employed to determine the poles and coefficients in the frequency range of interest, approach that will be later detailed. While this algorithm yields stable poles, it does not guarantee the passivity of the model, i.e. $\mathrm{Re}[Y(\omega)] \geq 0$ for $\omega > 0$. The passivity condition is checked, and if necessary, the coefficient Y_∞ is adjusted to enforce $\mathrm{Re}[Y] \geq 0$. The time-domain admittance boundary condition is then expressed in the time-domain as:

$$Z_0 u_n(t) = Y_\infty p(t) + \sum_{k=1}^{P} A_k \varphi_k(t) \tag{3.23}$$

where the temporal functions $\varphi_k(t)$ are governed by the system of ordinary differential equations (ODE):

$$\frac{\mathrm{d}\varphi_k}{\mathrm{d}t} + \lambda_k \varphi_k(t) = p(t) \tag{3.24}$$

This system is numerically solved using the same time scheme as for the LEE. Equations (3.23) and (3.24) constitute the TDABC. As in the study of Diab et al. [51], the accumulators φ_k are complex-valued, not subsisting an explicit distinction between the real poles and the pairs of complex conjugate poles.

Nonlinear regime

At higher acoustic levels, the surface impedance model of the perforated plate liner depends on the

velocity in the perforations. Following the work of Shur et al. [134], an extension of the TDABC has been proposed in Diab et al. [51] in the nonlinear regime. It is based on a quasi-steady approach to dynamically modify the surface admittance depending on the root mean square (rms) velocity in the perforations v_{rms}. Two methods for incorporating the variation of the admittance with v_{rms} are proposed in Diab et al. [51]. The first one, called the interpolation of the admittance method, involves interpolating the admittance for different values of v_{rms}. While this method is accurate, it significantly increases the number of poles in the model. The second, more efficient method, referred to as the interpolation of the admittance parameters (IAP) method [51], approximates the coefficients and poles of the multipole model as functions of v_{rms}. This latter method is adopted in this study.

The surface admittance is written as:

$$Y(\omega, v_{\text{rms}}) = Y_\infty(v_{\text{rms}}) + \sum_{k=1}^{P} \frac{A_k(v_{\text{rms}})}{\lambda_k(v_{\text{rms}}) - \mathrm{j}\omega} \tag{3.25}$$

allowing the coefficients and the poles to vary with v_{rms}. The parameters of the multipole admittance function are assumed to vary as a rational function of v_{rms}. For instance, the coefficient $Y_\infty(v_{\text{rms}})$ is given by:

$$Y_\infty(v_{\text{rms}}) = \frac{Y_\infty^{n,0} + Y_\infty^{n,1} v_{\text{rms}} + Y_\infty^{n,2} v_{\text{rms}}^2}{1 + Y_\infty^{d,1} v_{\text{rms}} + Y_\infty^{d,2} v_{\text{rms}}^2} \tag{3.26}$$

where the constants $Y_\infty^{n,0}, Y_\infty^{n,1}, Y_\infty^{n,2}, Y_\infty^{d,1}, Y_\infty^{d,2}$ are determined from curve fitting. A similar approximation holds for the real and imaginary parts of $A_k(v_{\text{rms}})$ and $\lambda_k(v_{\text{rms}})$.

The rational function approximation in Eq. (3.26) is determined using the curve fitting toolbox of MATLAB (with data points obtained with the VF algorithm for $0 \leq v_{\text{rms}} \leq 12$ m s^{-1} with a step of 1 m s^{-1}) employing a Levenberg-Marquardt algorithm [59]. An example of the fitting parameters are presented in Fig. 3.3:

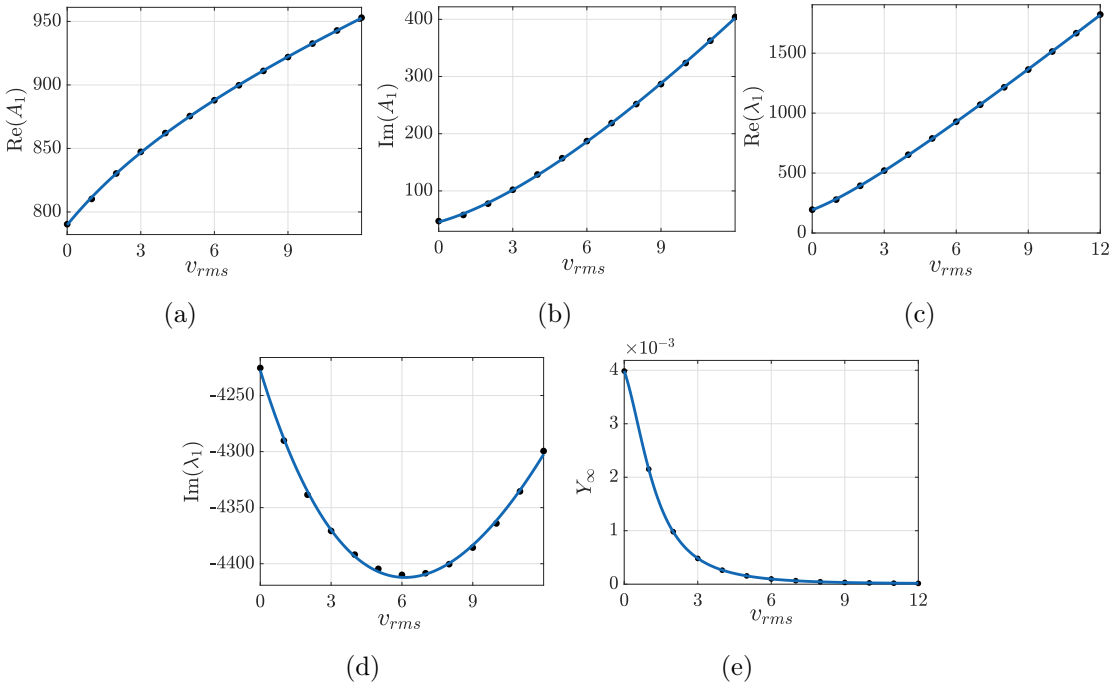

Figure 3.3: Evolution of the multipole coefficients with v_{rms} and fit using a rational function

We need also to evaluate v_{rms} from the numerical solution. First, we introduce the instantaneous

velocity in the perforations defined by $v(t) = u_n(t)/\phi$. We can then estimate the rms velocity in the perforations at a given time t with:

$$\tilde{v}^2_{\text{rms}}(t) = \frac{1}{t}\int_0^t v^2(t')\,\mathrm{d}t' \tag{3.27}$$

Assuming that u_n is constant over a time step, the value of $\tilde{v}_{\text{rms}}$ at the time iteration n is calculated from its value at iteration $n-1$ using the recursive expression:

$$\tilde{v}^2_{\text{rms}}(n\Delta t) = \left(1 - \frac{1}{n}\right)\tilde{v}^2_{\text{rms}}[(n-1)\Delta t] + \frac{1}{n}\frac{u_n^2(n\Delta t)}{\phi^2} \tag{3.28}$$

with Δt the time step.

Finally, the nonlinear TDABC is given by:

$$Z_0 u_n(t) = Y_\infty(\tilde{v}_{\text{rms}})p(t) + \sum_{k=1}^{P} A_k(\tilde{v}_{\text{rms}})\varphi_k(t) \tag{3.29}$$

where the functions $\varphi_k(t)$ satisfy the ODE:

$$\frac{\mathrm{d}\varphi_k}{\mathrm{d}t} + \lambda_k(\tilde{v}_{\text{rms}})\varphi_k(t) = p(t) \tag{3.30}$$

and $\tilde{v}_{\text{rms}}$ is determined using Eq. (3.28).

For Mach numbers above 0.2 and perforation velocities higher than 12 m s^{-1}, we observe that the poles of the surface admittance obtained from the vector fitting approach can shift from pairs of complex conjugate poles to real poles. In this case, it is no more possible to use Eq. (3.25) on the whole range of velocities. For this reason, in such a situation, it becomes necessary to consider an alternative method to model the perforated plate liner.

3.2.3.2 Alternative with explicit modeling of the cavity

The second method for modeling the perforated plate liner is based on Alomar et al. [10]. In this approach, propagation inside the cavity is explicitly modeled and the perforated plate is modeled by an impedance discontinuity. The duct-cavity system is represented in Figure 3.4.

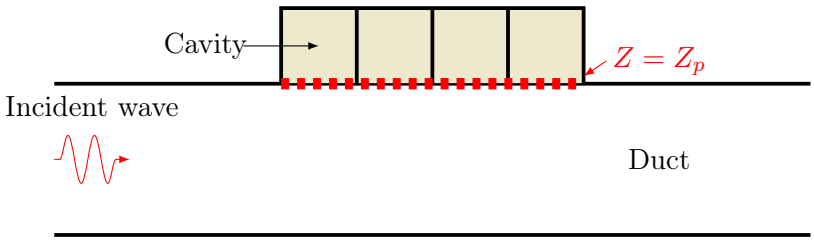

Figure 3.4: Sketch of the 2D duct with explicit cavity model

Because of the honeycomb structures, we consider that propagation within the cavity occurs only in the transverse direction. Consequently, the propagation inside the cavity is governed by the system of equations:

$$\begin{cases} \dfrac{\partial w}{\partial t} + \dfrac{1}{\varrho_0}\dfrac{\partial p}{\partial y} = 0 \\ \dfrac{\partial p}{\partial t} + \varrho_0 c_0^2 \dfrac{\partial w}{\partial y} = 0 \end{cases} \tag{3.31}$$

The perforated plate is modelled by a pressure jump between the duct and the cavity, which can be expressed as:

$$\Delta p = p_d - p_c = -Z(\omega)w \tag{3.32}$$

where p_c and p_d are the pressures on the plate from the cavity side and the duct side, respectively. The normal velocity w is continuous between the cavity and the duct. The transmission of information between the duct and the cavity is handled using the method of characteristics, see Alomar et al. [10] for details. Subsequently, the procedure is similar to that presented in the previous section, except that the transmission coefficients from the cavity to the duct and vice versa are considered, instead of the surface impedance. We observe that the poles of the transmission coefficients are real over the entire range of velocities in the perforations. Therefore, this method is applicable without the restrictions detailed above for the surface impedance.

The simulation methods presented in this section will be applied to two application cases: a one-dimensional case, to simulate the acoustic behaviour inside an impedance tube, and a two-dimensional case, to simulate the acoustic behaviour inside a treated duct, where the effect of a flow will be considered both in the impedance modeling and in the acoustic propagation.

3.2.4 1D application case

This section describes the numerical implementation of the impedance tube configuration, introduced in Sec. 2.3. Figure 3.5 illustrates the problem.

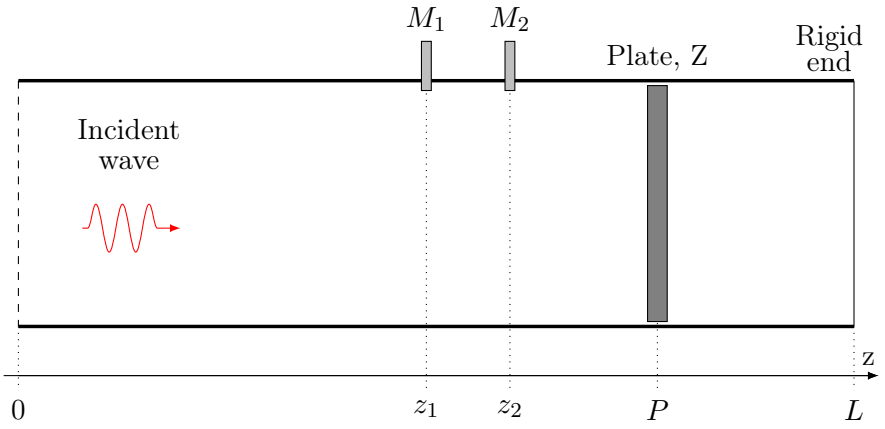

Figure 3.5: 1D schematic representation of the impedence tube

The incident wave $p_i(t)$ is prescribed using the method of characteristics, with the incoming and outgoing characteristics at the boundary $z = 0$, denoted by q_i and q_o, respectively, given by:

$$q_i(t) = \frac{1}{2}\left(p(z=0,t) + Z_0 u(z=0,t)\right) \quad q_o(t) = \frac{1}{2}\left(p(z=0,t) - Z_0 u(z=0,t)\right) \tag{3.33}$$

To ensure the correct incident wave and prevent reflections at the boundary, the method determines the outgoing characteristic from the numerical solution and imposes the incoming characteristic as $q_i(t) = p_i(t)$ after each stage of the Runge-Kutta algorithm. The pressure and velocity at the boundary are then corrected using the relations:

$$p(z=0,t) = q_i(t) + q_o(t) \quad u(z=0,t) = \frac{q_i(t) - q_o(t)}{Z_0} \tag{3.34}$$

All variables are initialized to zero at time $t = 0$.

The computational domain, spanning the interval ($0 \leq z \leq L$), is discretized into 101 grid points, corresponding to a uniform spatial resolution of $\Delta z = 0.0085$ m. The simulation time is set to a total duration of $t_{\max} = 0.3$ s. To ensure numerical stability, the Courant–Friedrichs–Lewy (CFL) number is fixed at 0.5, resulting in a temporal step size of $\Delta t = 1.25 \times 10^{-5}$ s.

Numerical simulations are conducted for two distinct types of incident acoustic waves: harmonic waves and broadband signals. For harmonic excitation, the incident pressure waveform is defined as:

$$p_i(t) = \sqrt{2}\, p_{i,\mathrm{rms}} \sin(2\pi f t) \tag{3.35}$$

where $p_{i,\mathrm{rms}}$ represents the root-mean-square value of the incident pressure. For broadband excitation, the waveform is expressed as:

$$p_i(t) = p_{i,\mathrm{rms}} s(t) \tag{3.36}$$

with $s(t)$ denoting a stationary broadband signal normalized to have a unitary rms value.

The SPL of the incident wave used to characterize the excitation is given by:

$$\mathrm{SPL}_i = 20 \log_{10} \left(\frac{p_{i,\mathrm{rms}}}{p_{\mathrm{ref}}} \right) \tag{3.37}$$

where the reference pressure is set to $p_{\mathrm{ref}} = 2 \times 10^{-5}$ Pa.

The surface impedance of the perforated plate is evaluated numerically using the two-microphone method as for the experimental case. The frequency response function H_{12} is obtained as the ratio of the Fourier transforms of the pressure signals at z_1 and z_2 for harmonic excitation. For broadband excitation, H_{12} is calculated as the ratio of the cross-power spectral density of the pressure signals at z_1 and z_2 to the power spectral density at z_2.

For the broadband excitation, a white noise signal filtered through a Butterworth bandpass filter with cutoff frequencies of 200 Hz and 2000 Hz is used. Concerning the harmonic excitation case, simulations are performed for incident waves with identical SPL values across a frequency range of 200–2000 Hz, in increments of 100 Hz.

The rms velocity is calculated from the numerical solution, and the surface admittance is updated iteratively until steady-state is reached. With more details, all variables, including the rms velocity ($\tilde{v}_{\mathrm{rms}}$), are initially set to zero. Upon the interaction of the incident wave with the liner, $\tilde{v}_{\mathrm{rms}}$ progressively increases, modifying the surface impedance, which in turn alters the acoustic field and further influences $\tilde{v}_{\mathrm{rms}}$. This iterative process continues until a steady-state is reached, which is confirmed by the convergence of $\tilde{v}_{\mathrm{rms}}$.

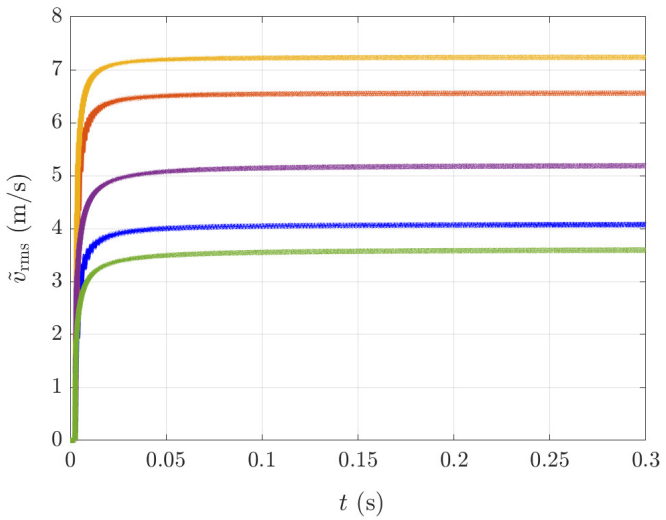

Figure 3.6: Time evolution of $\tilde{v}_{\mathrm{rms}}$ for different frequencies: (—) 300 Hz, (—) 500 Hz, (—) 1000 Hz, (—) 1500 Hz, and (—) 2000 Hz.

The time variations of $\tilde{v}_{\mathrm{rms}}$ are illustrated in Fig. 3.6 for a harmonic excitation with several frequencies. The results demonstrate a monotonic increase in $\tilde{v}_{\mathrm{rms}}$ over time, with convergence achieved by $t = 0.2$ s in all cases. Additionally, the rms velocity is observed to be strongly dependent on the excitation frequency.

3.2.5 2D application case

In this case, the properties of the Caiman duct are taken as reference. The computational domain under consideration consists of a two-dimensional duct with dimensions $L_z = 1.3$ m and $L_y = 0.1$ m, as illustrated in Fig. 3.7.

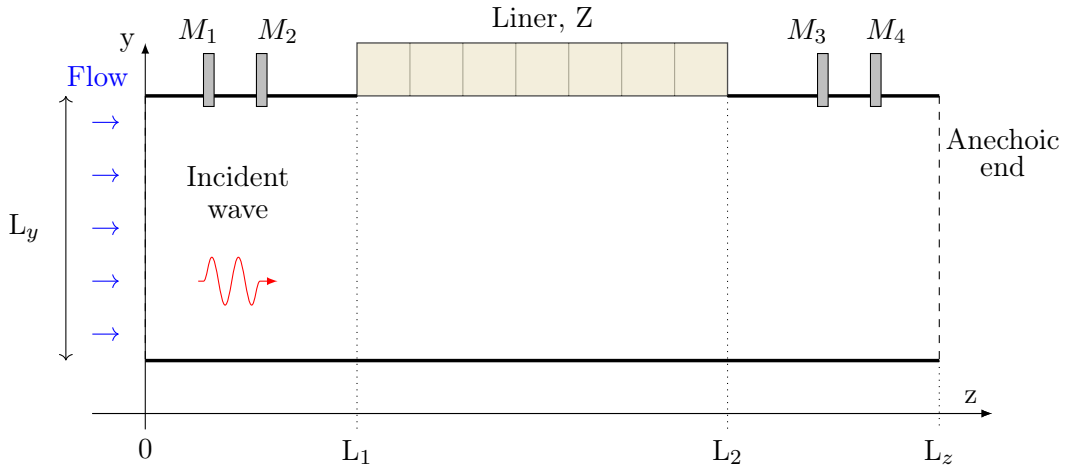

Figure 3.7: 2D schematic representation of the lined duct Caiman

A liner segment, measuring 0.3 m in length, is positioned on the lower wall of the duct between L_1 = 0.5 m and L_2 = 0.8 m. The remaining walls are rigid. Throughout the domain, the sound speed and the air density are constant. In this study, the performance of the absorber is analyzed, where the cavity depth is fixed at 30 mm. The frequency range of interest spans from 400 Hz to 1500 Hz, remaining below the duct's theoretical cutoff frequency of approximately 1550 Hz. Two types of incident waveforms are investigated: a harmonic pressure wave and a broadband pressure wave. The broadband signal is synthesized by filtering white noise with a Butterworth bandpass filter, configured with lower and upper cutoff frequencies of 200 Hz and 3000 Hz, respectively.

The numerical simulation is conducted by solving the 2D Linearized Euler Equations using methods previously detailed in Section 3.2.3. At the inlet ($z = 0$), a plane wave propagating in the z-direction is introduced using the method of characteristics. At the outlet boundary ($z = L$), non-reflecting boundary conditions are implemented by setting the incoming characteristic variable to zero, thus ensuring no wave reflections occur at this interface. Along the rigid walls of the duct, the normal velocity is constrained to zero. For the lined section, the Time-Domain Admittance Boundary Condition (TDABC) is applied.

The computational mesh is structured as follows. In the z-direction, the mesh is uniform with a grid spacing of $\Delta z = 1.110^{-3}$ m. Along the y-direction, the grid resolution varies, with progressively smaller mesh sizes near the lined wall achieved through a stretching factor of 0.99. The grid spacing at the duct centerline is $\Delta y = 1.110^{-3}$ m, reducing to $\Delta y = 8.1910^{-4}$ m at the wall boundaries.

Temporal discretization employs a time step of $\Delta t = 210^{-6}$ s, corresponding to a Courant-Friedrichs-Lewy (CFL) number of 0.84. To capture the steady-state behaviour, the total simulation time is set to 0.02 s for harmonic excitation. In order to asses the performance of the treatment, the transmission loss (TL) is calculated as:

$$\mathrm{TL} = 20 \log_{10} \left(\frac{p_{i,\mathrm{rms}}}{p_{t,\mathrm{rms}}} \right) \tag{3.38}$$

where $p_{t,\mathrm{rms}}$ represents the rms value of the transmitted pressure.

3.2.5.1 Numerical flow velocity profile modeling

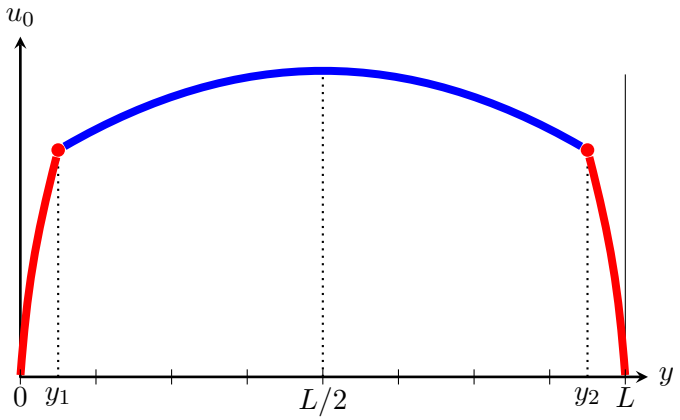

Figure 3.8: Analytical modeling of a velocity profile

The velocity profile included in the simulations is based on that measured on Caiman. As illustrated in Fig. 3.8, the profile is divided into three parts, one part at the center of the duct where the mean flow values match the Pitot tube measurements, and two parts near the wall, where the velocity at the wall is null and increases progressively to the first value measured by Pitot tube.

Analytically, the velocity profile is defined as a piecewise polynomial function:

$$u_0 = \begin{cases} Ay^2 + By & \text{y } \in [0, y_1] \\ ay^4 + by^3 + cy^2 + dy + e & \text{y } \in [y_1, y_2] \\ C(L-y)^2 + D(y-L) & \text{y } \in [y_2, L] \end{cases} \tag{3.39}$$

where the coefficients and the polynomial order are determined for each flow regime to fit the measured profile.

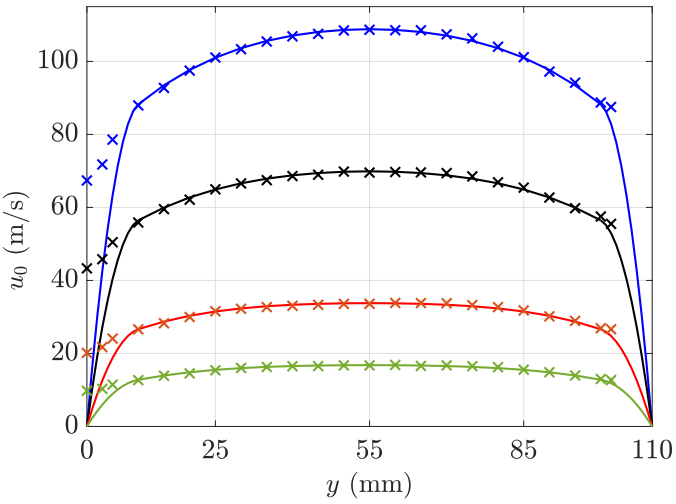

Figure 3.9: Comparison between the experimental (x) and analytical (line) flow profiles for $M = 0.05$ (—), $M = 0.1$ (—), $M = 0.2$ (—), and $M = 0.3$ (—)

Comparison of the analytical and the experimental profiles is presented in Fig. 3.9. It can be seen that for all flow regimes an excellent agreement is obtained. Finally, note that for propagation along the flow a positive velocity profile is considered and for propagation against the flow a negative velocity profile is considered.

3.3 Conclusion

This chapter outlines the numerical models used for sound wave propagation in flow ducts, with a focus on configurations including acoustic liners in nonlinear acoustic regimes.

After a review on the mode-matching method, the chapter delves into the time domain approaches. A key contribution is the development and application of Time-Domain Admittance Boundary Conditions (TDABC), which accurately model the interaction between sound waves and acoustic liners. These methods, based on multipole approximations, capture both linear and nonlinear acoustic effects, extending traditional models to account for behaviour under high-pressure and high-speed conditions. The Interpolation of Admittance Parameters (IAP) method further enhances the framework, enabling efficient time-domain analyses without sacrificing accuracy.

High-order finite-difference and finite-element methods are employed to simulate complex geometries and transient phenomena, effectively capturing aspects like grazing flow effects and nonlinear acoustic regimes.

By combining analytical and numerical methods, this chapter provides a comprehensive methodology for addressing duct acoustics modelling. Comparison with experimental benchmarks, such as the CAIMAN duct or impedance tube, will further strengthen these models in the next chapters.

4 Study of the acoustic behaviours of a reference liner

Contents

Abstract

The study of nonlinear acoustic behaviour in perforated plates and acoustic liners is essential for advancing noise reduction technologies. Traditional linear models are often inadequate for predicting the behaviour of these materials at high sound pressure levels or under flow conditions, necessitating a more detailed investigation of nonlinear effects. This chapter examines the response of the perforated plate and acoustic liner presented in Chapter 2 through experimental measurements, analytical models, and numerical simulations.

The first Section (4.1) focuses on normal incidence, evaluating the effects of increasing SPL on acoustic indicators such as absorption coefficient, impedance, and admittance, while comparing experimental results with theoretical predictions. The second Section (4.2) investigates the perforated plate liner behaviour in the CAIMAN duct under various flow conditions and incident sound pressure levels SPL_i.

4.1 Acoustic behaviours of a perforated plate in normal incidence

In this section, the results of the acoustic indicators determined under normal incidence are presented. First, the results from experimental observation are presented. A comparison is made between the results obtained from a harmonic excitation and a white noise excitation. These results are then compared with an analytical and numerical predictions. The perforated plate analytical reference model is the Guess impedance model (Section 1.3.3). A comparison between different approaches to perforated plate model is also presented.

4.1.1 Experimental observations

For the experimental study, reference is made to the setup presented in Section 2.3, in which the perforated plate depicted in Figure 2.7 is tested. First of all, the case of harmonic excitation is studied in a frequency range of 300 Hz - 2000 Hz. For each incident level specified in the procedure, the measured incident level is monitored to ensure that it corresponds to the target.

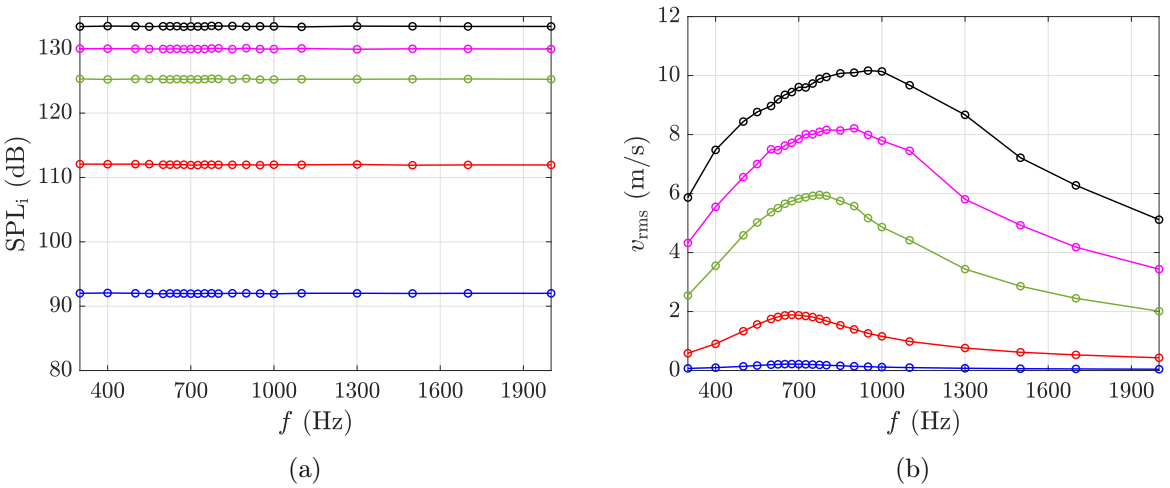

Figure 4.1: Control of SPL (a) and evolution of perforation acoustic velocities (b) measured at 92 dB, 112 dB, 125.3 dB, 130 dB, 133.5 dB

In Figure 4.1, the results deriving from the control performed on the SPL are presented, following the iterative scheme introduced in Section 2.3.3.2. For every acoustic level considered, a constant acoustic level is maintained at every frequency in the range. This control is as well performed for the thermodynamic properties (room temperature and humidity) for a given acoustic regime. The rms value of the acoustic velocity in the perforation is derived, as shown in Figure 4.1b. For a level of 92 dB, the velocity is small, below 0.2 m/s, over the entire frequency range. At 112 dB, it is observed that the velocity increases in value, presenting a peak at the plate resonance frequency. As the level increases, the peak amplitude and width increase accordingly. We can also observe that the peak frequency shifts towards higher frequencies.

Following Section 2.3.3.3, it is possible to determine the absorption coefficient α, the impedance Z and the admittance Y of the plate.

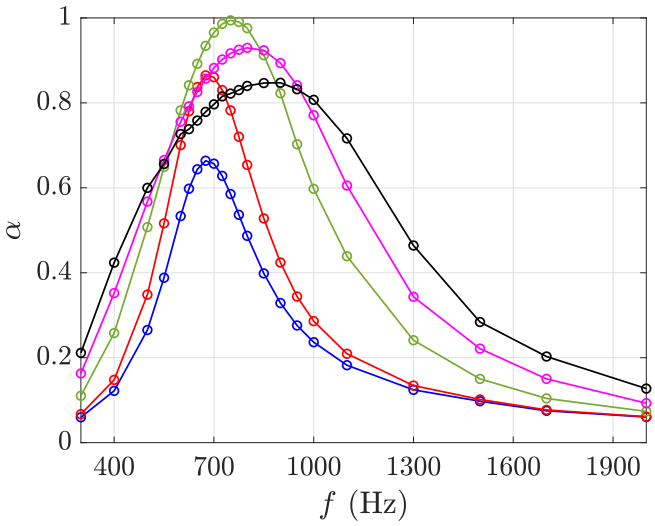

Figure 4.2: Nonlinear behaviour of the plate absorption coefficient α for 92 dB, 112 dB, 125.3 dB, 130 dB, 133.5 dB

Figure 4.2 shows the trend of the absorption coefficient α as the SPL varies. For an incident level of 92 dB, corresponding to the linear regime, an absorption peak of 0.6 can be noticed at the plate resonance frequency of 690 Hz. For the nonlinear regime, four different acoustic levels were analysed. For the 112 dB case, it is noticeable that the peak amplitude increases, while maintaining the peak at the resonance frequency. A broadening of the peak can also already be observed. For 125.3 dB, it can be noted that the peak amplitude is nearly one and that the peak is shifted towards higher frequencies. Once the absorption coefficient has reached its maximum value (equal to one), it tends to decrease with an increase in the incident sound pressure level. Simultaneously, the peak frequency keeps increasing.

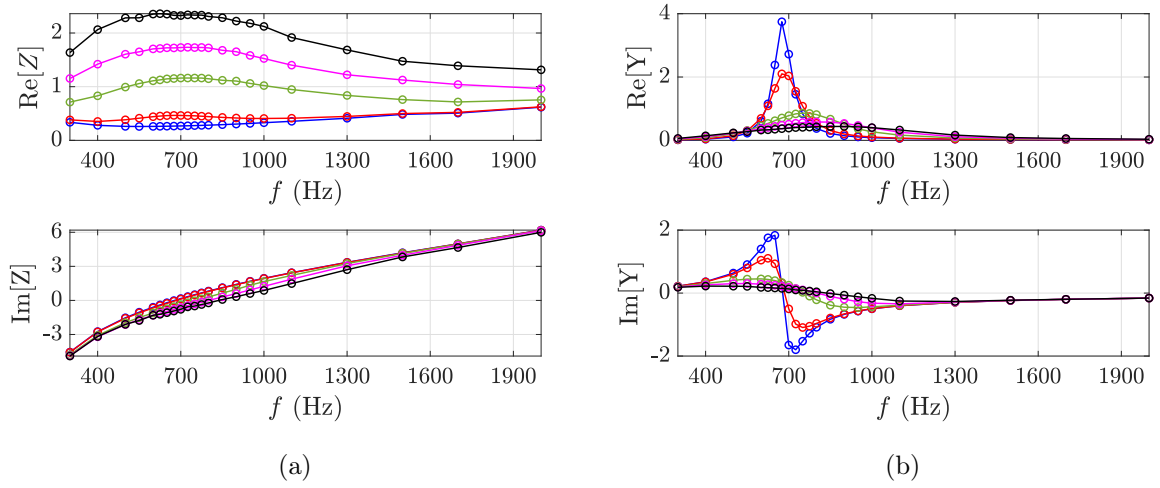

Figure 4.3: Nonlinear behaviour of the plate impedance (a) and admittance (b) at 92 dB, 112 dB, 125.3 dB, 130 dB, 133.5 dB

This behaviour is further observed by analysing the impedance and admittance in Figure 4.3, which will be divided into real and imaginary parts. As far as impedance is concerned, the zero value of the imaginary part represents the resonance frequency at that given level. This value coincides with the frequency of the absorption peak. In accordance with the comments on Figure 4.2, we can observe in Figure 4.3 that this frequency increases with the incident level. The real part increases with the incident

sound pressure level, in line with the velocity trend in the plate holes. In particular, the real part of the normalized impedance around the resonant frequency is equal to 1 for 125.3 dB and then exceeds one as the level increases. This corresponds to a maximum of the absorption coefficient seen in Figure 4.2 for 125.3 dB. Considering the resistance, this results in a flattening of the real part, when for the linear case a sharp peak could be observed at the resonance frequency. Unlike impedance, the frequencies of the maximum value of the admittance increase with SPL, consistently to the frequency value at the zero of the admittance imaginary part. Similar behaviour was observed by Diab [51] in his study for a plate with similar characteristics to the one examined in this chapter.

4.1.2 Comparison with Guess analytical and numerical approaches

For comparison with theoretical approaches, reference is made to the semi-empirical Guess impedance model. For the analytical model, the rms velocities obtained from the measurements are taken as the reference value. In the numerical case, the velocity is a result of the simulation. The incident sound level is the only input parameter for the numerical approach.

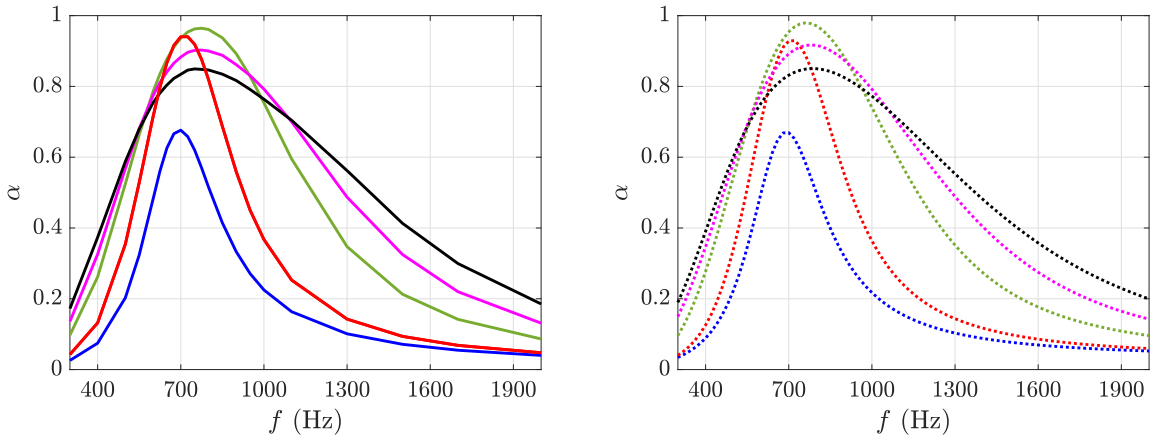

(a) Analytical

(b) Numerical

Figure 4.4: Absorption coefficients obtained by analytical (a) and numerical (b) approach for — 92 dB, — 112 dB, — 125.3 dB, — 130 dB, — 133.5 dB

Figure 4.4 presents the absorption coefficient determined with the analytical model and with the numerical simulation. It can be seen that both approaches positively predict the same evolution of the absorption coefficient with the frequency for the different incident levels.

The perfect agreement between the analytical case and the numerical case derives from the fact that in the numerical case we have based ourselves on the same analytical model as Guess in order to be able to carry out the simulation. The difference between the two approaches lies in the estimation of the velocity point, since in the analytical case we consider the drilling velocities measured experimentally, while in the numerical case we arrive at a velocity value following the stationary of the interpolation of the poles.

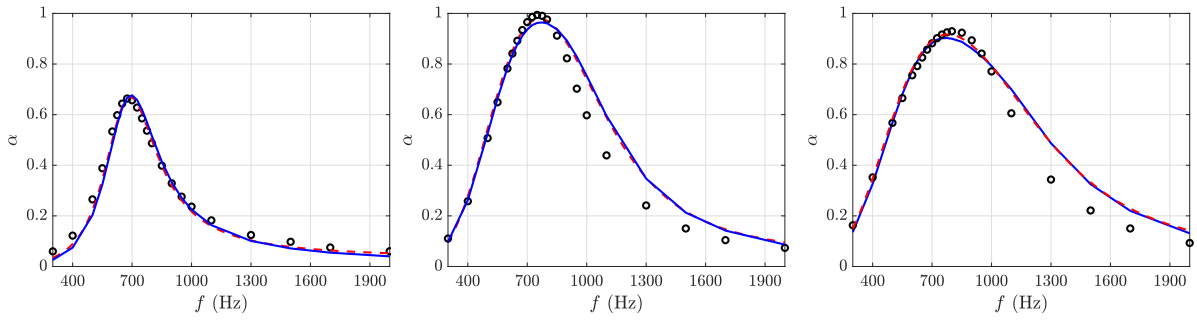

Figure 4.5: Absorption coefficient comparison between experimental (○), analytic (—) and numerical (- - -) approaches at (a) 92 dB, (b) 125.3 dB, (c) 130 dB

A direct comparison between the two theoretical approaches and the experimental case is proposed in Figure 4.5. Three different acoustic levels are considered: the linear at 92 dB and two nonlinear at 125.3 dB and 130 dB. It is observed that the absorption peak at a linear value estimated in the numerical and analytical approach corresponds to the frequency and value of that observed experimentally.

As far as the nonlinear effects are concerned, both the numerical and analytical approaches present a higher absorption peak width than the experimental case. In particular, a slight over-estimation of the resonance frequency at the peak in the nonlinear cases can be noted, as can be seen in the null value of the imaginary part of the admittance. This translates into the fact that the theoretical models, with the same acoustic level, estimate a stronger nonlinear effect than that observed experimentally.

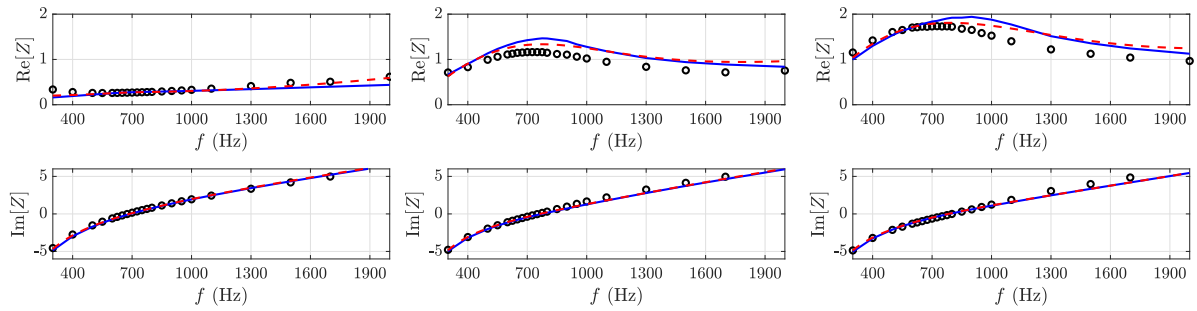

Figure 4.6: Impedance comparison between experimental (○), analytic (—) and numerical (- - -) approaches at (a) 92 dB (b) 125.3 dB (c) 130 dB

The second indicator investigated for the comparison is the impedance, as presented in Figure 4.6. It can be seen that the reactance turns out to be correctly predicted for all conditioned cases, especially with regard to the frequency of the null value. As far as resistance is concerned, in the linear case it is correctly predicted by the theoretical models, especially at values around resonance. The higher the sound level, the more the theoretical models overestimate the plate resistance, all without the presence of a grazing flow. However, at 130 dB, it can be seen that although the theoretical peak frequency is more detached from the experimental values, the deviation in the prediction of the resistance value is less consistent.

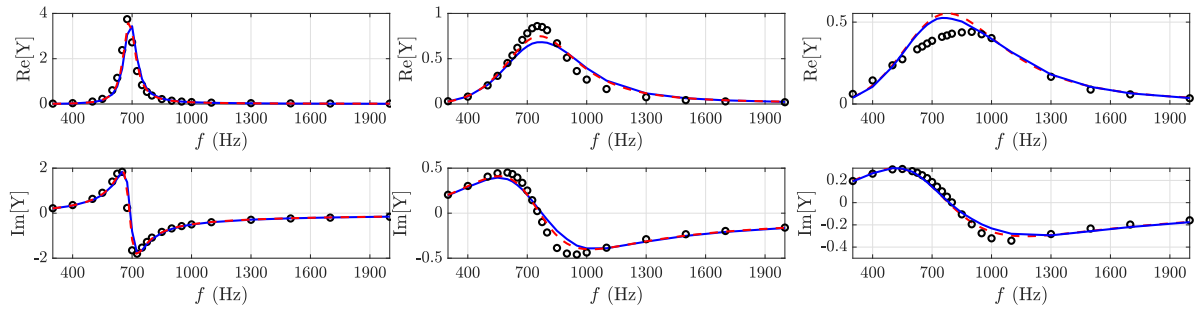

(a) (b) (c)

Figure 4.7: Admittance comparison between experimental (○), analytic (—) and numerical (- - -) approaches at (a) 92 dB (b) 125.3 dB (c) 130 dB

The comparison of the admittance is presented in Figure 4.7. Even in this case, there is a satisfactory coincidence between the three approaches, maintaining a slight underestimation of the theoretical real part of the admittance with a shift to overestimated theoretical values at 130 dB.

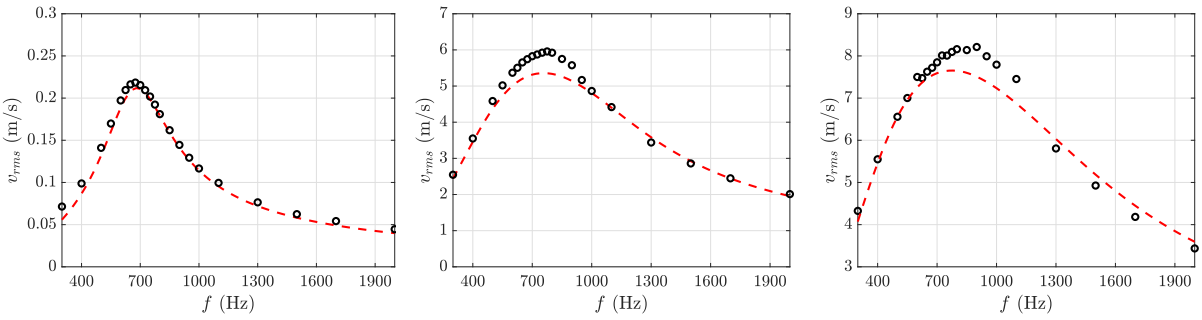

(a) (b) (c)

Figure 4.8: Comparison of the rms velocity in the perforations between experimental (○) and numerical (- - -) approaches at (a) 92 dB (b) 125.3 dB (c) 130 dB

Figure 4.8 shows a comparison between the velocity obtained experimentally and that predicted numerically. It can be observed that in the linear case, the two approaches coincide. In the nonlinear case, at both 125.3 dB and 130 dB, numerical stimulation has a tendency to underestimate the velocity value compared to that measured experimentally.

In general, it can be concluded that the analytical and numerical approaches are able to satisfactorily reflect the nonlinear plate acoustic behaviour observed experimentally in sinusoidal excitation.

4.1.3 Comparison between perforated plates models

In this section a comparison between different approaches to perforated plate model in normal incidence is presented. In particular, we will compare the Guess model with the equivalent fluid model (EFM) approach described in Section 1.4. The approach proposed by Rice and Cummings described in Section 1.5 will be largely developed and detailed in Chapter 5. An extension of the equivalent fluid approach, modified to better fit the macro-perforated case with experimental values, is presented in Annex B. In particular, focus is made on the different approaches to the nonlinear regime. For the determination of the rms velocity in the perforation, the equivalent fluid impedance model is taken as reference for a 1D FDTD numerical simulation.

Firstly, we are defining the parameters of the equivalent fluid model according to the characteristic of our plate. The choice is for a constant β=1.6, a discharge coefficient $C_D = 0.76$ and a Fok function $\Psi = 4/3$. These parameters have been selected following the study of Diab et al. [51], who provided similar plates to the one considered in this chapter.

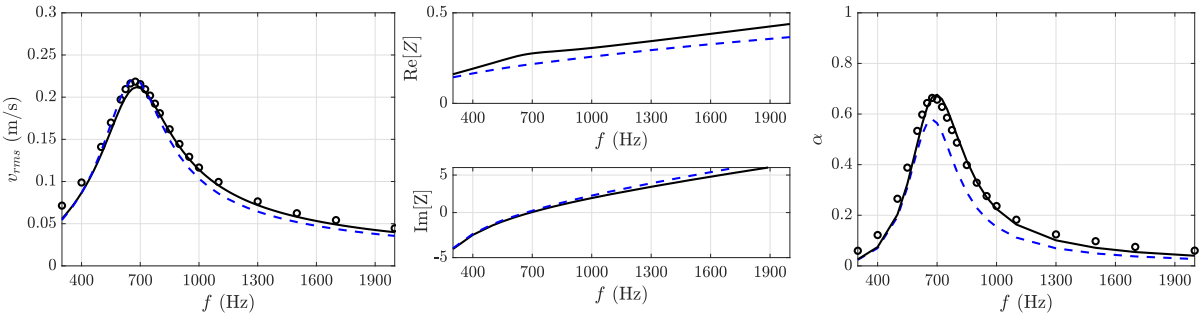

Figure 4.9: Comparison between experimental (○) and Guess (—) and equivalent fluid (- - -) models for (a) rms acoustic velocity, (b) impedance and (c) absorption coefficient at 92 dB

Figure 4.9 presents the comparison at a linear regime, 92 dB. The prediction of absorption coefficient with the EFM results less accurate in comparison to the Guess model with respect to experimental results. In particular, the prediction exhibits a smaller absorption coefficient with a peak slightly shifted toward lower frequencies. This behaviour is explained by the analysis of the impedance. In the EFM, the resistance is slightly underestimated in comparison to the Guess model, influencing directly the lower value of absorption. The reactance has its zero value at a slightly lower frequency rather than the Guess model, explaining the shift of the absorption peak. In linear regime, the rms acoustic velocity results well predicted in both models in comparison to experimental. The discrepancies of the values can be due to the fact that the parameters chosen for this model follow the study of Laly et al. [92], in which the model resulted more accurate for microperforated plate.

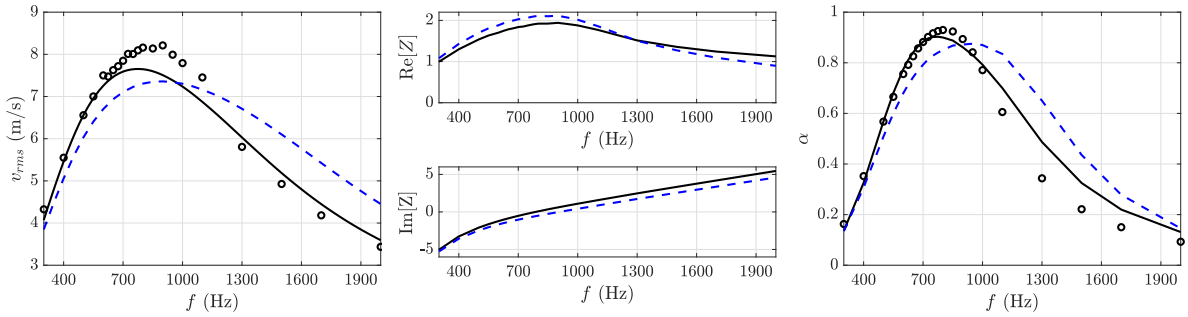

Figure 4.10: Comparison between experimental (○) and Guess (—) and equivalent fluid (- - -) models for (a) rms acoustic velocity, (b) impedance and (c) absorption coefficient at 130 dB

In Figure 4.10 the comparison of acoustic indicators in nonlinear regime, at 130 dB, is presented. Globally, the EFM correctly predicts the nonlinear effects on the plate, having a higher value of absorption, a wider peak and a consistent shift towards higher frequencies. More precisely, the model overestimate the influence of the nonlinear regime, by predicting both a higher resistance and reactance of the plate. This results in lower value of absorption and a significant shift toward higher frequencies, much higher than the experimental values and the Guess model predictions. For what concern the rms velocity, this appears to

be underestimated with respect to experimental, presenting a broader peak at a higher frequency range.

In conclusion, the EFM results to be less accurate compared to the Guess model to predict the experimental behaviours in normal incidence for macroperforated plates. The linear regime appears to be underestimated while the nonlinear effects are largely overestimated. For these reasons, the Guess model has been chosen as the reference for the theoretical study of the perforated plate. In order to take into account the differences induced by considering a macroperforation, a modified EFM is proposed in Annex B, set on the coincidence in linear regime to the experimental values.

4.1.4 Study under broadband excitation

In this section, the acoustic indicators of the plate under broadband excitation are analysed. A comparison with analytical modelling and numerical broadband simulation is presented.

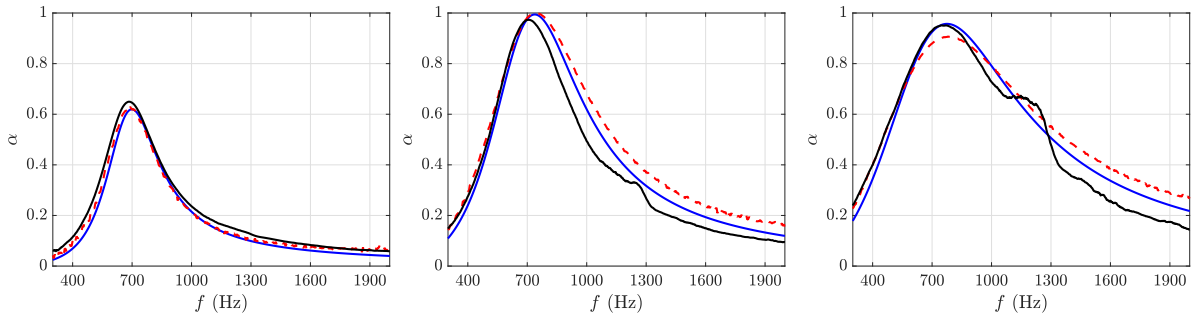

(a) (b) (c)

Figure 4.11: Absorption coefficient comparison in broadband excitation between experimental (—), analytic (—) and numerical (- - -) approaches at (a) 92 dB (b) 125.3 dB (c) 130 dB

The behaviour of the absorption coefficient for one linear and two nonlinear cases is exemplified in Figure 4.11. In analogy to harmonic excitation, the nonlinear case presents an increase in the absorption peak with a widening of the peak width and a shift towards higher frequencies. As far as the experimental curves are concerned, the secondary peak observed around 1250 Hz is due to the duct characteristic, notably imperfection in the assembly of the tube and parasite plate vibrations. Similar phenomena have been observed in the results of Diab et al. [51]. These defects appears to be more relevant with a broadband excitation rather than an harmonic one. The rms velocity in the perforations is calculated over the entire signal spectrum, indicating a single velocity value for each acoustic level considered. This value is then employed in the analytical simulation using the Guess impedance model. With regard to the numerical model given the input impedance model, a velocity value is obtained once convergence is reached for each acoustic level considered. It can be remarked that for the linear case the three approaches are comparable in all respects, with a slight underestimation of the peak in the numerical and analytical case. With regard to the nonlinear cases, the peak width is overestimated in the simulation cases, while still maintaining a comparable value of peak amplitude and frequency.

SPL	Experimental	Numerical
85 dB	0.029 m/s	0.0465 m/s
125.3 dB	3.029 m/s	3.8458 m/s
130 dB	6.244 m/s	8.0762 m/s

Table 4.1: Perforation acoustic velocities in broadband excitation from experimental and numerical approaches at different SPL

From a numerical point of view, it can be seen that for the case at 125.3 dB and at 133.5 dB we slightly overestimate the nonlinear effect compared to the experimental results. This is due to an an overestimation of the numerical velocity compared to the experimental one, as can be seen from the values presented in table 4.1.

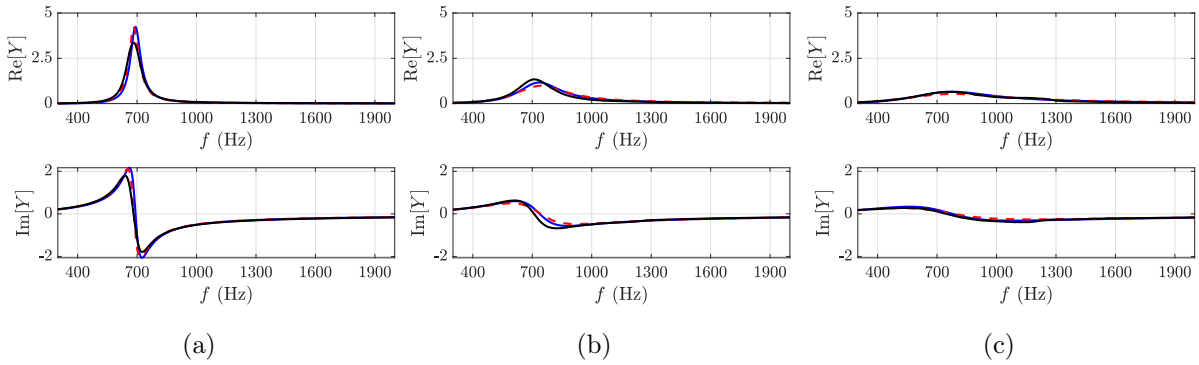

Figure 4.12: Admittance comparison in broadband excitation between experimental (—), analytic (—) and numerical (- - -) approaches at (a) 92 dB (b) 125.3 dB (c) 130 dB

Figure 4.12 shows the admittance for the three levels considered. It is noticeable how for the 133.5 dB case, the differences are smaller than for the other two cases. The three approaches give anyway comparable and close results.

4.1.5 Comparison between harmonic and broadband excitations

A comparison between experimental values obtained by harmonic and broadband excitation at a same acoustic level is now presented.

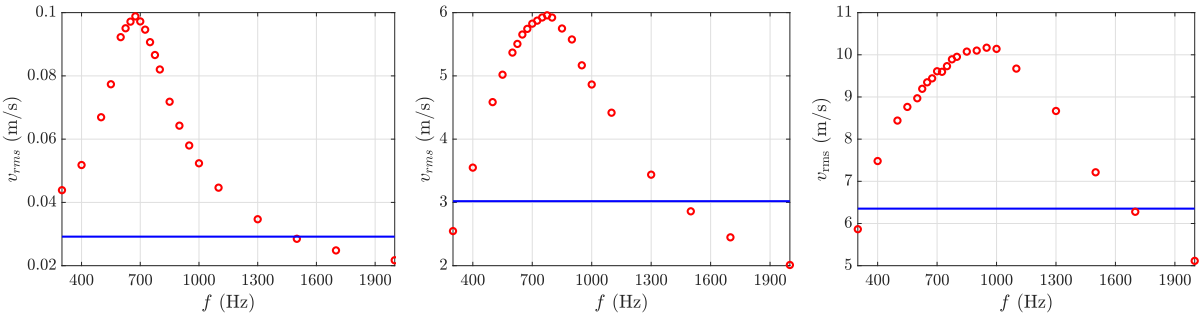

Figure 4.13: Comparison of perforations acoustic velocities obtained in harmonic (○) and broadband (—) excitations at (a) 85 dB (b) 125.3 dB (c) 133.5 dB

In Figure 4.13, a comparison is made of the measured acoustic velocity level for three different acoustic levels: a linear case at 85 dB, a nonlinear case at 125.3 dB, and a strongly nonlinear case at 133.5 dB. For harmonic excitation, the velocity exhibits a peaking pattern with a maximum at the resonance frequency. For all the cases considered, it can be observed that the value obtained from broadband excitation is lower than the average value obtained at the peak of sinusoidal excitation. Underestimating the velocity value especially at peak values and especially for nonlinear levels has a direct effect on the absorption and admittance values observed in Figure 4.14 and Figure 4.15.

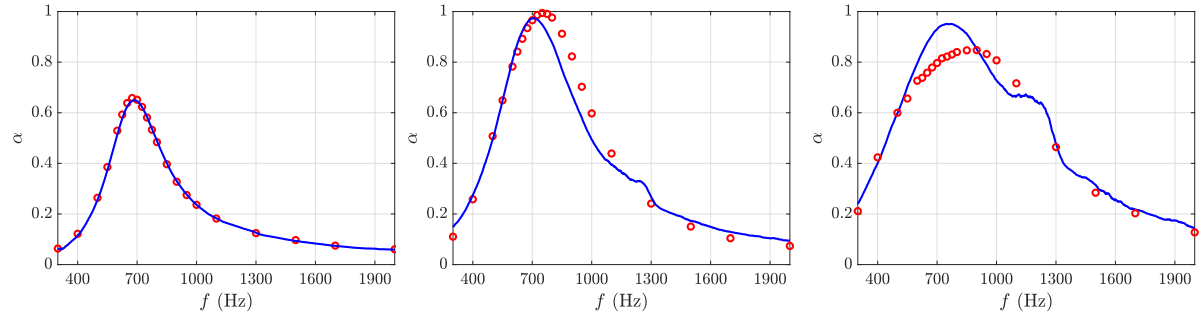

Figure 4.14: Comparison of absorption coefficients obtained in harmonic (○) and broadband (—) excitations at (a) 85 dB (b) 125.3 dB (c) 133.5 dB

With regard to the linear case, both the absorption coefficient and the imaginary real part of the admittance coincide in the two cases, with only a slight increase in the peak of the real part in the case of sinusoidal excitation. In the cases at 125.3 dB and 130 dB cases, the shape of the absorption peak is respected as well as the width, but the reduced velocity in the broadband configuration leads to absorption values corresponding to that for weaker sinusoidal excitation. For example, for the 133.5 dB case, the velocity value observed in the broadband case corresponds to the peak value observed in the sinusoidal case at 125.3 dB, which results in an absorption curve at 130 dB for the broadband case that is closer to the values of the sinusoidal case for a level of 125.3 dB. Similarly, the same consideration can be made for the 125.3 dB case where the broadband velocity corresponds to observed absorption values in harmonic

excitation that can be thought of as intermediate between 112 dB and 125.3 dB.

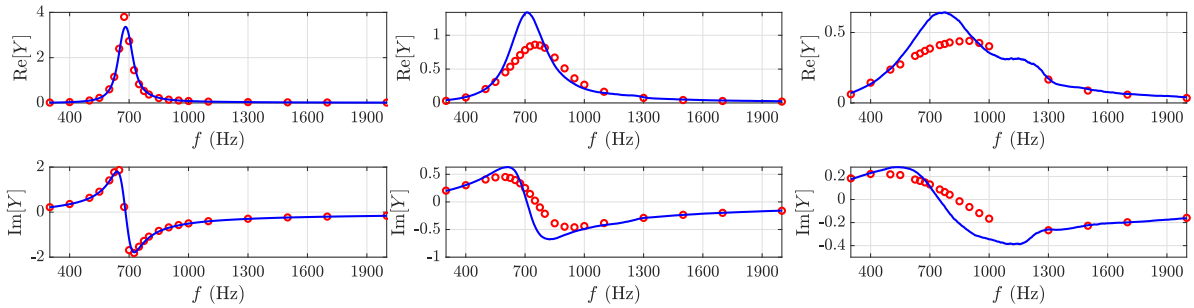

(a) (b) (c)

Figure 4.15: Comparison of admittances obtained in harmonic (○) and broadband (—) excitations at (a) 85 dB (b) 125.3 dB (c) 133.5 dB

Such observations are equally evident with regard to the peak of the real part of the admittance. With regard to the imaginary part, the intercept with zero obviously falls at different values since the peak frequencies in the two cases are shifted.

It is concluded that at the same measured acoustic level, broadband excitation produces a similar nonlinear effect than in the case of harmonic excitation, with the exception of the values at the peak, where the acoustic velocity in harmonic case is well superior to the one measured in broadband.

4.2 Acoustic behaviours of a perforated liner in Caiman wind tunnel

In this section the nonlinear behaviour of the liner described in Section 2.2.2 placed in Caiman wind tunnel is analysed. The perforation ratio considered in this study corresponds to that determined from the internal side of the plate, namely $\phi = 1.99\%$. In addition to the nonlinear acoustic behaviour in grazing incidence, the effect of the flow on the nonlinearity of the perforated plates is also assessed. Firstly, the experimental results are analysed by comparing different measurement methods, and then a comparison with numerical simulation described in Section 3.2 is carried out. Finally, a comparison between different numerical approaches is presented as a validation of the results found.

4.2.1 Experimental results

For the experimental study, the chosen performance indicator for analysing liner performance is the transmission loss (TL). Two cases will be analysed: the downstream case with acoustic excitation in the direction of the flow, and the upstream case with acoustic excitation opposite to the flow .

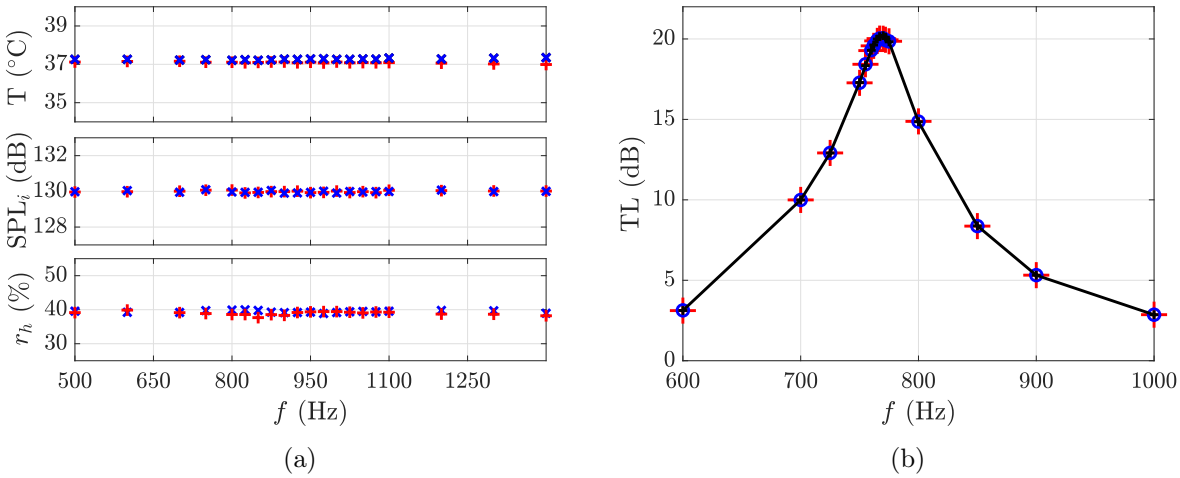

Figure 4.16: (a) Evolution of temperature, SPL and relative humidity in upstream (+) and downstream (X) configurations for a single measurement; (b) Validation of the linear regime for TL at 70 dB (○), 80 dB (+) and 92 dB (—) at M = 0

As a validation of the experimental procedure, in Figure 4.16, the procedure of control on the main parameters analysed in the study is presented. In Figure 4.16a it can be observed for the entire range of frequencies considered in the sinusoidal excitation, the temperature, the incident acoustic level and the relative humidity have been kept constant. Figure 4.16b shows an example of transmission loss obtained without flow and, for three weak acoustic levels. The same transmission loss obtained for the three levels, indicating that up to 92 dB the linear acoustic regime is present; in other words, the properties of the liner do not change with the excitation level. For the nonlinear study, we will therefore proceed to analyse levels above 92 dB: 112 dB, 125.3 dB and 130 dB.

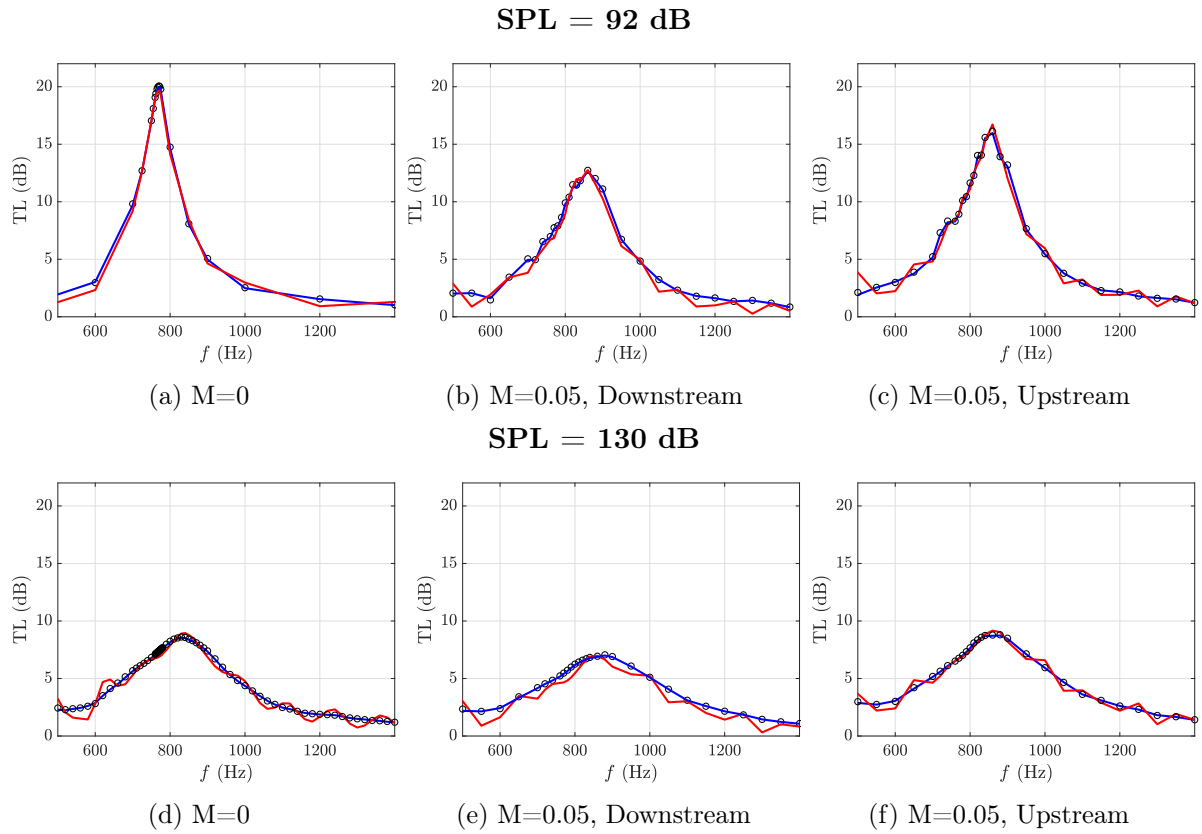

(a) M=0 (b) M=0.05, Downstream (c) M=0.05, Upstream

(d) M=0 (e) M=0.05, Downstream (f) M=0.05, Upstream

Figure 4.17: TL obtained by 1 source method with anechoic termination (—) and 2 sources method with diffusion matrix (-o-) at several flow and acoustic regimes in downstream and upstream configurations

The measurement methods introduced in Section 2.4.4 are compared in Figure 4.17. Firstly, the transmission loss is evaluated for the case under the assumption of anechoic termination. Then, the diffusion matrix approach with two-sources is considered for the calculation of transmission loss. The results are presented for two acoustic levels, a linear one at 92 dB and a strongly nonlinear one at 130 dB, both without flow and with a flow of M = 0.05, in downstream and upstream configurations. Without flow, in a linear acoustic configuration, it can be observed that the two approaches yield similar results. At low and high frequencies, only slight variations are observed for the one source case with anechoic termination. When examining the nonlinear case without flow, considering anechoic termination leads to fluctuations in terms of TL over the entire frequency range. For the cases with flow, significant fluctuations in transmission loss are observed for both the linear and nonlinear cases. In particular, in the downstream case these oscillations are more important, causing some values to approach the null value. In contrast, for the two sources method, both with and without flow, the transmission loss results are smooth, with minor local oscillations. In the course of this discussion, all transmission losses that will be presented will be estimated using the two-sources method.

4.2.1.1 Study at constant flow regimes

In this section, the influence of the nonlinear acoustic regimes on the experimental TL is analysed for four Mach numbers for the downstream and upstream case: M = 0, M = 0.05, M = 0.1, M = 0.2 and M = 0.3. As detailed in table 2.2, the Mach number based on the mean flow values considered in the experimental measurements and in the simulations are slightly different (0.04, 0.09, 0.18 and 0.29), but for concision and clearness of the exposition, reference is made to the Mach number on the experiments. It is examined

a linear acoustic regime at 92 dB and three nonlinear regimes at 112 dB, 125.3 dB and 130 dB.

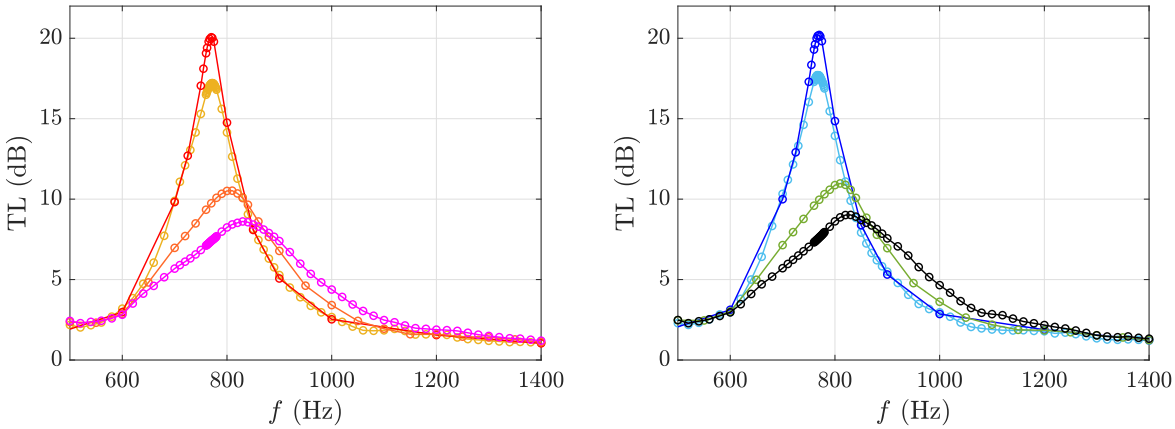

(a) Downstream (b) Upstream

Figure 4.18: Experimental TL at M=0 in (a) downstream configuration at 92 dB, 112 dB, 125.3 dB, 130 dB and (b) upstream configuration at 92 dB, 112 dB, 125.3 dB and 130 dB

In Figure 4.18, the case without flow is considered. At first instance, despite the division between the downstream and upstream case being presented, the two cases are coincident. The slight differences that are observed in terms of peak value, notably variations of a maximum of one decibel, are linked to the differences in the two measurement conditions, notably for slight changes in temperature and humidity that influences the repeatability of a measurement. For the linear case, a maximum absorption of the liner is observed at the liner resonance frequency of 780 Hz, as derived from analytical calculations. The nonlinear acoustic effect results firstly in a lowering of the TL peak to the same frequency value as in the linear case. In stronger nonlinear regimes, at 125.3 dB and 130 dB, the TL continues to lower its value, with a consistent shift towards higher frequencies. In addition the TL for these two incident levels presents a wider peak width.

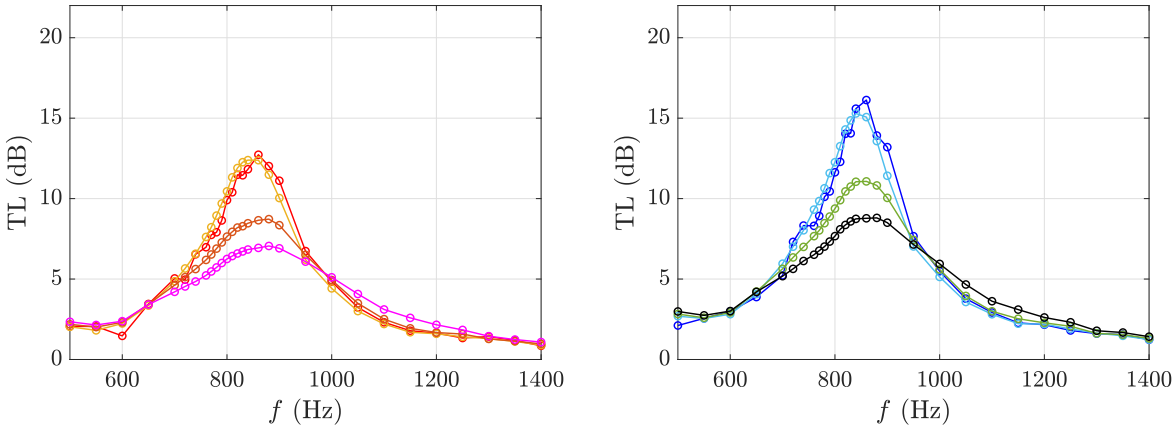

(a) Downstream (b) Upstream

Figure 4.19: Experimental TL at $M = 0.05$ for: (a) downstream case at 92 dB, 112 dB, 125.3 dB, and 130 dB and (b) upstream case at 92 dB, 112 dB, 125.3 dB and 130 dB.

In Figure 4.19, the M = 0.05 flow case is considered. First, it is appreciated that the TL values in the upstream case are higher than those observed in the downstream case. This means that attenuation with acoustic excitation contrary to the direction of flow is larger than that in the direction of flow. For the latter case, the maximum TL occurs in the linear acoustic case, to decrement in the nonlinear case until 130 dB. At 112 dB, the TL does not undergo consistent changes compared to the linear case, indicating a probable increase in the spectrum of the linear acoustic regime. The TL at 125.3 dB and 130 dB show differences with respect to the TL at 92 dB. In contrast, the peak frequency appears to be roughly constant, with a slight shift to higher frequencies reaching a few tens of Hz for 130 dB. This behaviour is observed for both the downstream and upstream configurations. In general, the plate resonance frequency appears to be shifted by about 100 Hz compared to the case without flow. This could be due to a shift of the zero value of the reactance in presence of flow. The frequency of the TL peak is the same for both downstream and upstream configurations.

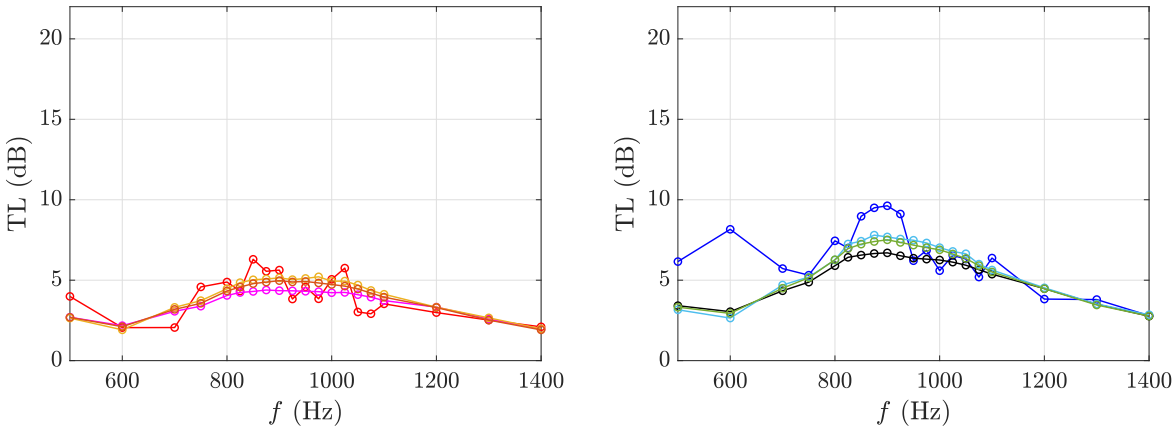

(a) Downstream (b) Upstream

Figure 4.20: Experimental TL at M = 0.1 in (a) downstream configuration at 92 dB, 112 dB, 125.3 dB, 130 dB and (b) upstream configuration at 92 dB, 112 dB, 125.3 dB, 130 dB

The configuration at M = 0.1 is considered in Figure 4.20. As before, it is observed that the TL in the upstream case is higher than in the downstream case. In contrast to the results at M = 0.05 , it can be seen that the TL does not vary much with the incident pressure level. A further shift towards higher frequencies is observed. The TL curve is considerably flattened with a broad plateau over the entire range of frequencies considered, with no real attenuation at a specific frequency. The TL at 92 B varies erratically with the frequency, due to the difficulty of the measurement caused by low noise levels coupled with a strong background noise due to the flow. The differences between linear and nonlinear levels appear to be minimal, especially with maximum TL levels measured around 10 dB. The liner does not appear to perform efficiently at high flow regimes.

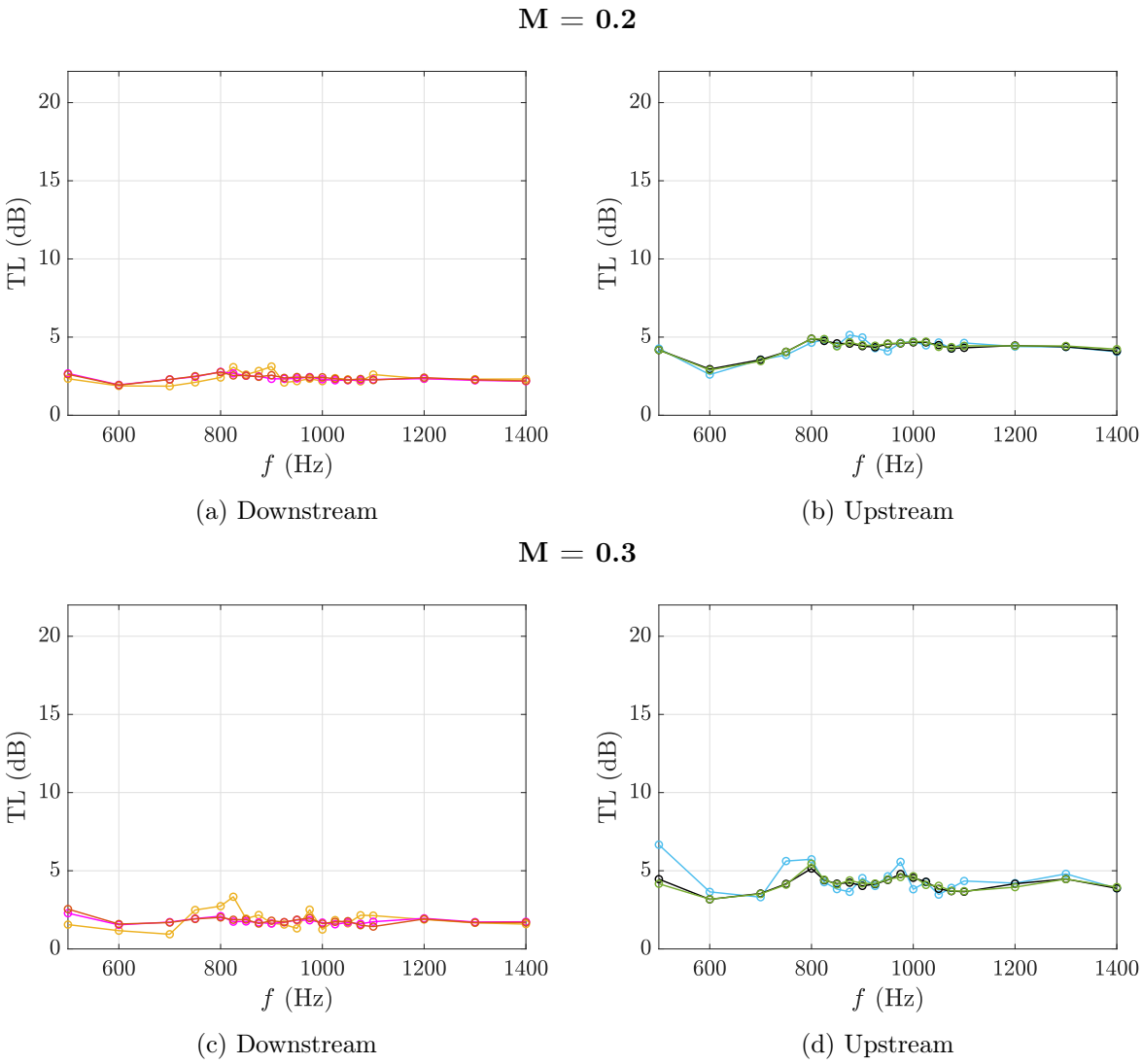

Figure 4.21: Experimental TL at M = 0.2 and M = 0.3 in (a) downstream configuration at 112 dB, 125.3 dB, 130 dB and (b) upstream configuration at 112 dB, 125.3 dB, 130 dB

For higher flow regimes, Figure 4.21 groups together the L for M = 0.2 and M = 0.3, since the TL values observed are relatively weak and uniform over the frequency range considered. For both cases, consistently with the cases analysed so far, the upstream case presents higher TL values than the downstream case. It is observed that for this liner configuration, at the considered flow regimes, the acoustic nonlinearity no longer affects the behaviour of the liner, presenting no difference between the 112 dB and 130 dB cases. The TL at 92 dB are not presented due to the difficulty of carrying out measurements.

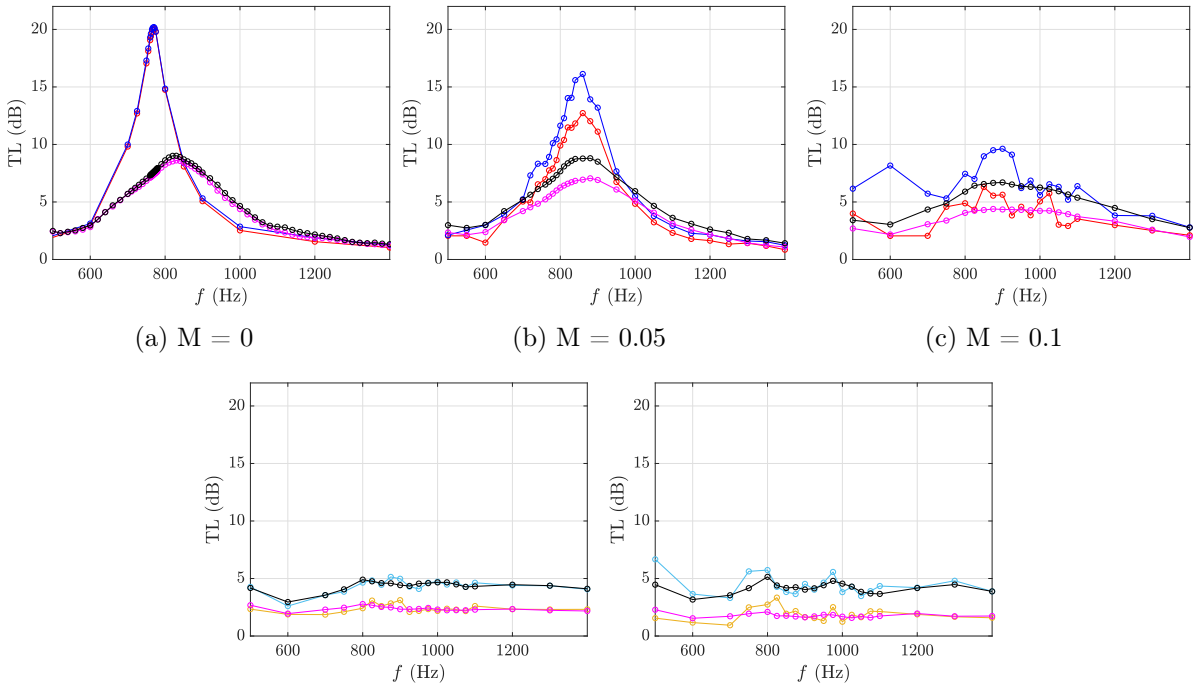

(a) M = 0 (b) M = 0.05 (c) M = 0.1

(d) M = 0.2 (e) M = 0.3

Figure 4.22: Comparison between the configuration downstream at 92 dB, 112 dB, 130 dB and upstream at 92 dB, 112 dB, 130 dB for several flow regimes

In Figure 4.22 we re-plot the TL in the upstream and downstream configurations for both the linear case and the strongly nonlinear case at 130 dB and for different Mach numbers to better analyse the effect of the flow direction on TL. It can be appreciated that for the case at M = 0, the two configurations present no differences. With flow, in all cases considered, for both the linear and nonlinear regimes, the upstream case presents a higher transmission loss than the downstream case.

4.2.1.2 Study at constant acoustic regimes

In this paragraph a study on the influence of the flow at constant incident SPL is presented.

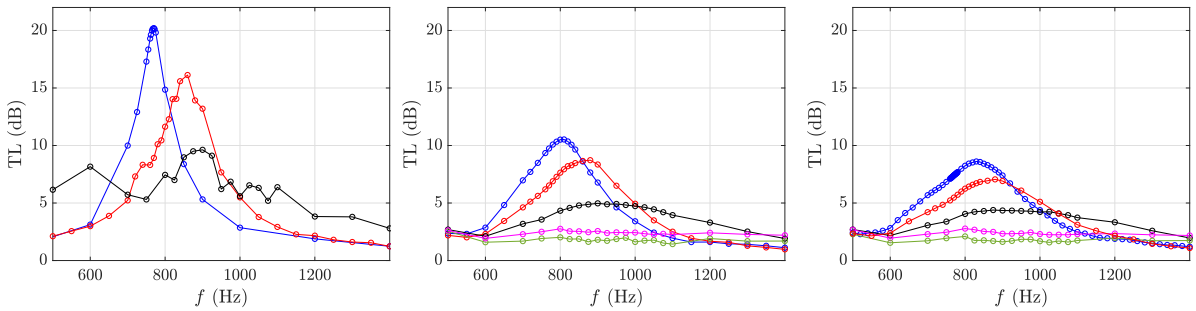

(a) 92 dB (b) 125.3 dB (c) 130 dB

Figure 4.23: Comparison of TL at constant SPL values at M = 0, M = 0.05, M = 0.1, M = 0.2 and M = 0.3

As depicted in Figure 4.23 for the linear case at 92 dB, it can be observed that increasing the Mach

number causes a lowering of the TL and a shift of the TL peak about 200 Hz towards higher frequencies. Such a phenomenon is as well found in nonlinear cases at 125.3 dB and 130 dB. The flow reduces transmission loss due to the liner, making the TL curve flatter and flatter with smaller values.

4.2.1.3 Conclusions

In conclusion, two distinct behaviours are observed and distinguished: the nonlinear effect associated with stronger incident sound pressure levels, which results in a lowering and shifting of the transmission peak towards higher frequencies, and the effect associated with the flow, which similarly results in a lowering and widening of the TL values and a shift towards higher frequencies. As the Mach number increases, the influence of the flow on the TL becomes dominant over that of high sound pressure levels.

4.2.2 Comparison with numerical simulation

We now present the comparison between the experimental study and the results obtained from numerical simulation. For most of the cases considered, the plate is modeled using the full TDABC including the cavity, as presented in Section 3.2.3.1. For M = 0.2 and M = 0.3, the poles of the admittance switch for a given value of the rms velocity in the perforations from a pair of complex conjugate poles to two real poles. For these two cases, the propagation inside the cavity is explicitly simulated and the TDABC is used only for the plate modeling, as presented in Section 3.2.3.2. The results for the TL is first presented. The focus is then made on the numerical evolution of the acoustic velocity and impedance both spatially along the liner and over the frequency range considered, in the linear and nonlinear case without and with flow.

4.2.2.1 Transmission loss

In this section the comparison of transmission loss in measurements and numerical predictions is presented. The impedance model employed in this section is the Guess model.

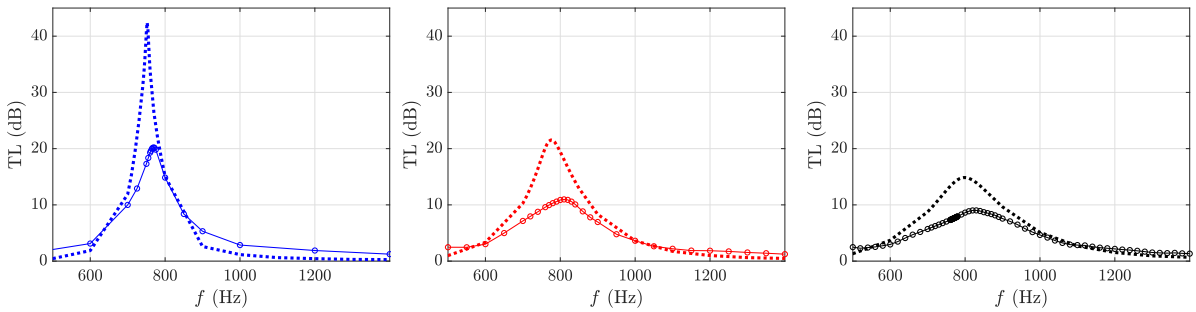

(a) 92 dB (b) 125.3 dB (c) 130 dB

Figure 4.24: TL comparison obtained by experimental (o) and numerical (- - -) approaches for different acoustic regimes at M = 0

Figure 4.24 presents the TL comparison without flow. For the case at 92 dB , the peak resonance frequency match the measure one by a few Hertz. This could be due to flaws in the experimental assembly that were not taken into account in the simulation. Thus, having experimental values that coincide with a higher resonance peak than the numerical one, could suggest that the liner actually has a slightly higher perforation rate, due to leaks, imperfections in the hole making. The transmission peak, in the numerical

simulations is vastly overestimated compared to that observed experimentally. This fact may also be linked to experimental imperfections which would reduce the liner performance. In the nonlinear regime, it can be seen that the shift of the TL peak towards higher frequencies and the widening of the peak with the increase in the incident pressure level is reproduced in the numerical simulation. As in the linear case, the slight difference in the peak frequency and the overestimation of the maximum TL value persist.

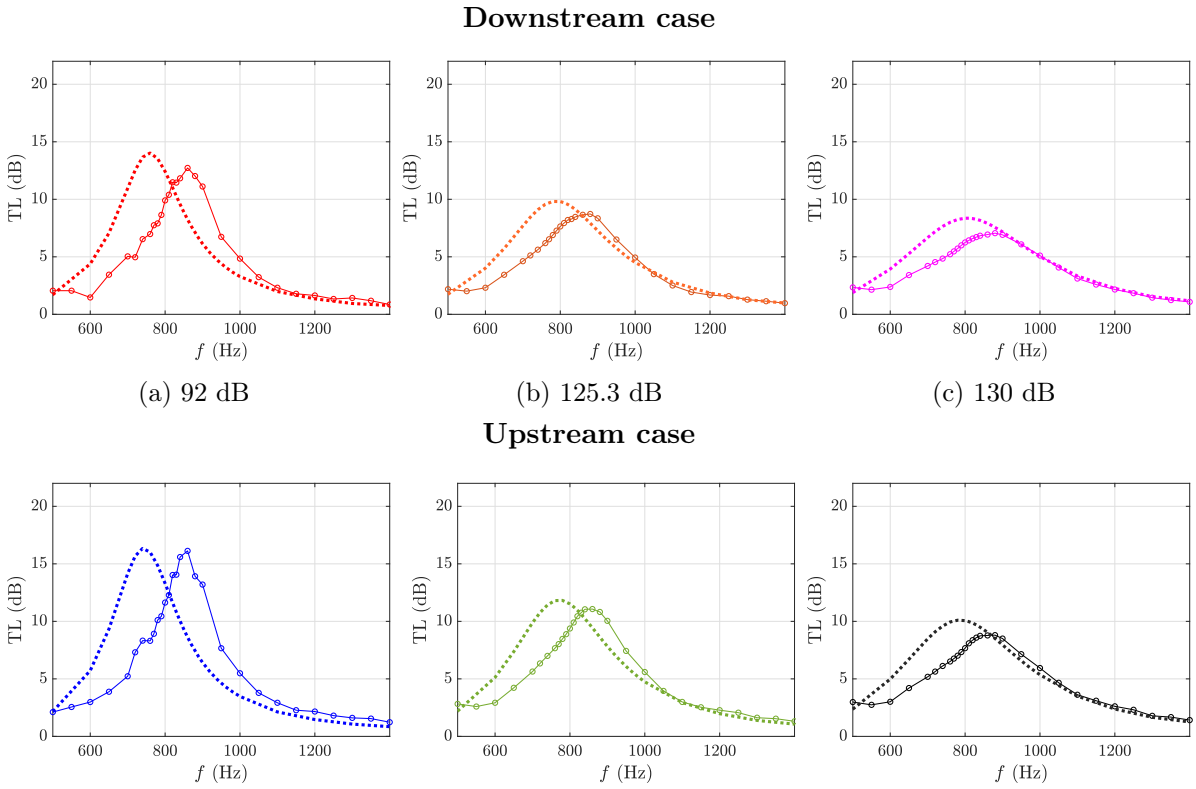

(a) 92 dB (b) 125.3 dB (c) 130 dB

(d) 92 dB (e) 125.3 dB (f) 130 dB

Figure 4.25: TL comparison obtained by experimental (⊖) and numerical (- - -) approaches for different acoustic regimes at M = 0.05 in downstream and upstream configurations

Figure 4.25 shows the comparison for the case M = 0.05, respectively in the downstream and upstream cases for linear and nonlinear regimes. Experimentally, it is noticed that the downstream case perform a slightly higher peak resonance frequency than the upstream case. This phenomenon is also found in numerical simulations. For the linear case, in comparison with the case M = 0 , the peak is at a comparable level to the value found experimentally. A difference is noted with respect to the frequency value at the peak. Compared to the case without flow, this frequency appears to have increased slightly, in concordance with what was observed. However, this shift appears to be small compared to the experimental case. As far as the nonlinear regimes are concerned, the numerical simulation correctly predicts the evolution of TL, with a reduction and a widening of the TL peak. It can also be seen that the TL slightly shifts towards the high frequencies as the sound level increases, which is in any case lower than that observed experimentally. The difference of a few decibels from the experimental case could be related to measurement uncertainty. Again, the numerical model succeeds in satisfactorily predicting the nonlinear behaviour in the presence of flow, albeit with some inaccuracies.

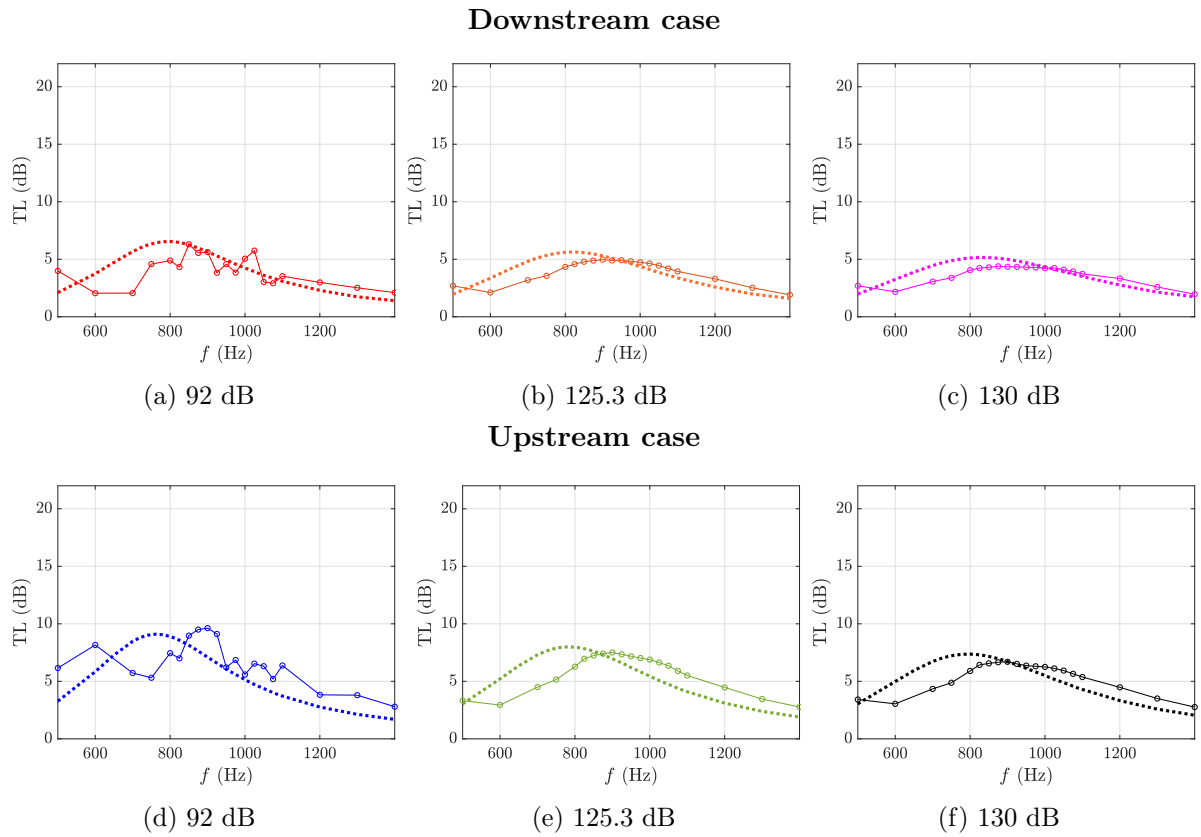

(a) 92 dB (b) 125.3 dB (c) 130 dB

(d) 92 dB (e) 125.3 dB (f) 130 dB

Figure 4.26: TL comparison obtained by experimental (⊖) and numerical (- - -) approaches for different acoustic regimes at M = 0.1 in downstream and upstream configurations

In Figure 4.26 the case at M = 0.1 is considered. In this case, it is empirically observed that the peak was considerably flattened and that the nonlinear acoustic effect was significantly reduced compared to the flow effect. It was also noted that the upstream configuration had higher values than that in the downstream case. It is remarked that the numerical simulations correctly predicts the amplitude and width of the TL peak in both downstream and upstream configurations. As in the case M = 0.05 , a difference in peak frequency of approximately 100 Hz is found. In spite of these differences, compared to the numerical case M = 0.05, the peak is shifted more towards higher frequencies. Also for the numerical approach, the TL in the upstream case turns out to be higher than that in the downstream case effectively taking into account both the effect of flow and high sound pressure levels. In fact, for each case it can be observed that the highest TL is that at the linear acoustic regime, then gradually decreasing to the strongest case at 130 dB.

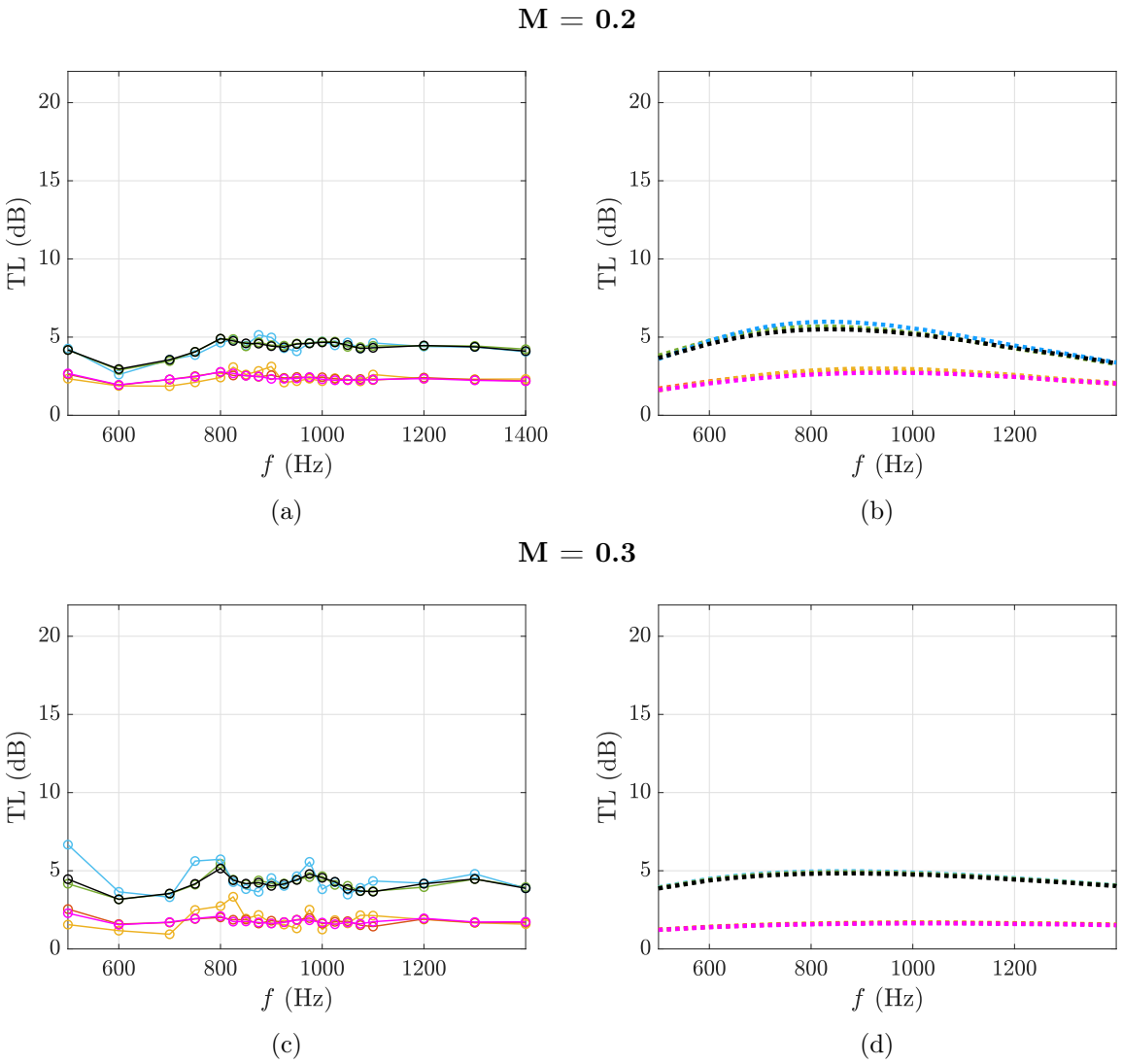

Figure 4.27: TL comparison obtained by (a),(c) experimental and (b),(d) numerical approaches for M = 0.2 and M = 0.3 in downstream configuration at 112 dB, 125.3 dB, 130 dB and upstream configuration at 112 dB, 125.3 dB, 130 dB

In Figure 4.27, the cases at M = 0.2 and M = 0.3 are presented. Experimentally, these cases presented a relatively weak TL, below 10 dB, and with almost no influence of high sound pressure levels. For both cases, it was observed that the upstream case presented higher values than the downstream case. It is apparent that from numerical simulations as well, the TL values are correctly predicted, presenting a weak influence of the nonlinear acoustic regime, and presenting in both cases a higher value in the upstream case than in the downstream case. From a numerical point of view, since there are no fluctuations and inaccuracies associated with the experimental measurements, a bell-shaped trend can be observed, albeit with a very wide peak width, taking in the entire range of frequencies considered. It can be seen how, albeit weakly, the linear case presents a higher TL than the nonlinear cases, both at M = 0.2 and at M = 0.3. The small maximum TL value occurs at higher frequencies than in the cases considered above, confirming the trend of the flow effect to increase the TL peak frequency.

4.2.2.2 Numerical evolution of the liner acoustic properties

In this section, numerical results are presented and analysed concerning the evolution of velocity and impedance, first spatially along the liner, at constant frequency, and then with respect to the whole spectrum of frequencies examined. The simulation allows us to study the evolution of these two properties on the surface of the liner. Experimentally, these could be measured by various methods, such as with the in situ microphone methods [29, 100], with microphones placed in the backup cavity or with microphones placed spatially on the side opposite the liner [138], and by impedance eduction method [15, 28, 80, 91, 118] and by means of optical methods [91, 96].

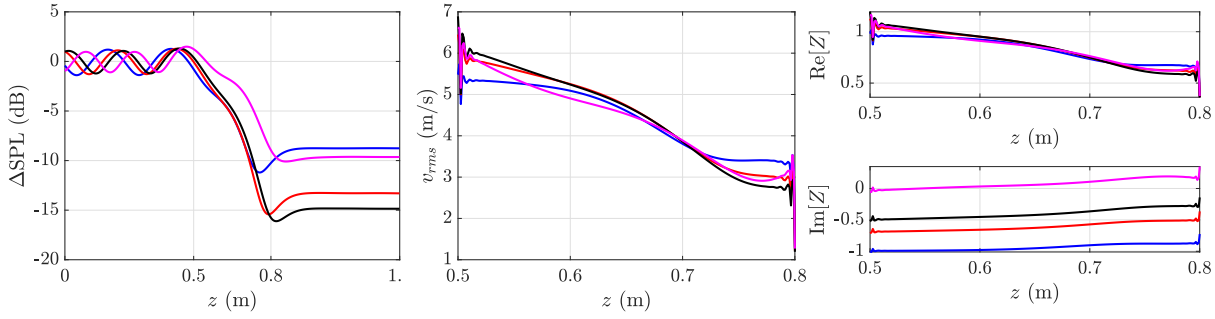

(a) (b) (c)

Figure 4.28: Numerical predictions of (a) SPL, (b) acoustic velocity and (c) impedance along the liner surface at — 700 Hz, — 750 Hz, — 800 Hz, — 900 Hz for 130 dB and M = 0

In Figure 4.28 a case with constant flow M = 0 and constant sound level at 130 dB , is presented to assess the influence of the excitation frequency on the liner behaviour. Four frequencies close to the resonance are considered. It was observed that for M = 0 at 130 dB, the TL peak was at 780 Hz. For all cases considered, the velocity is highest at the inlet of the liner and then decreases along the liner to the outlet section. The highest TL shown in this comparison presented in the figure is that at 800 Hz. It appears to be the one with the highest average speed along the liner. The influence of frequency appears to have little impact on the real part of the impedance, while for the imaginary part, gradually increases in values along the liner as frequency increases.

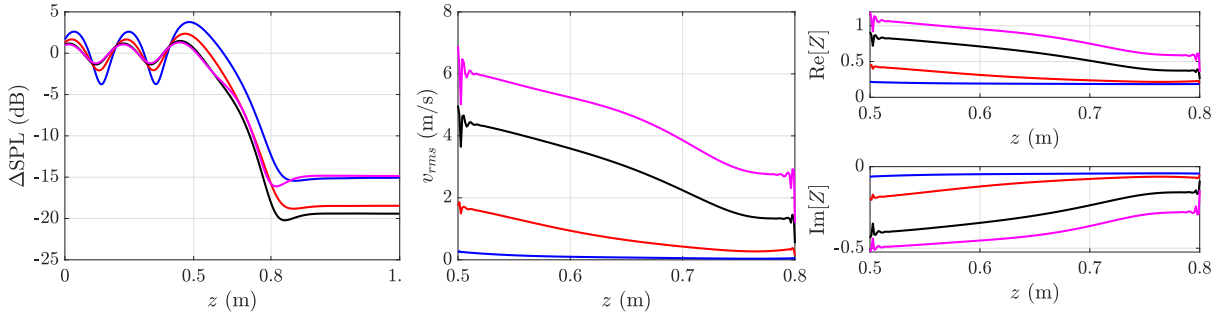

(a) (b) (c)

Figure 4.29: Numerical predictions of (a) SPL, (b) acoustic velocity and (c) impedance along the liner surface at — 92 dB, — 112 dB, — 125.3 dB and — 130 dB for M = 0 at 800 Hz

In Figure 4.29 the influence of the nonlinear sound level on the behaviour of the liner is discussed, at Mach M = 0 and at a frequency of 800 Hz. The behaviour at 800 Hz is not the same for all the acoustic levels, since the TL peak shifts towards higher frequencies with increasing acoustic level. For example,

at 130 dB the behaviour at 800 Hz does not correspond to the maximum of the TL. It is noticeable that the rms velocity in the perforations increases considerably with the incident SPL along the entire liner. For the linear regime at 92 dB, the rms velocity is small, below 0.1 m/s, to a strongly nonlinear case at 130 dB where a maximum speed of 6 m/s is reached. This behaviour is observable as well for the value of the imaginary and real part of the impedance. It can be seen that for the linear value, both are almost constant along the entire liner and close to zero. As the sound level increases, the resistance of both is increasingly stronger and the reactance weaker, moving towards values close to zero for the end of the liner. Although there is a consistent difference in impedance, the influence on the sound pressure difference is not particularly significant in the range of 5 dB.

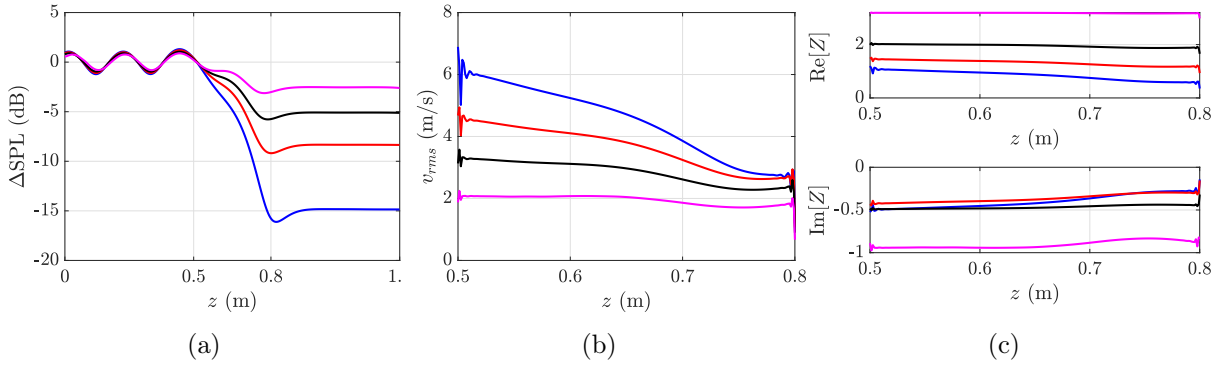

(a) (b) (c)

Figure 4.30: Numerical predictions of (a) SPL, (b) acoustic velocity and (c) impedance along the liner surface at — M = 0, — M = 0.05, — M = 0.1, — M = 0.2 for 130 dB at 800 Hz in downstream case

Finally, in Figure 4.30 the influence of flow at different Mach regimes is presented for a constant sound level at 130 dB and a constant frequency of 800 Hz. Again, the behaviour at 800 Hz is not the same for all the flow levels, since the TL peak shifts towards higher frequencies with increasing Mach regime. It is noted that the acoustic velocity is higher without flow, and then gradually decreases with increasing flow velocity. This fact explains why the effect of flow is finally preponderant over that due to high SPL at a sufficiently high Mach number. As observed in the previous paragraphs, and that the TL is lower and lower as flow velocity increases. With regard to impedance, a flattening of the curves can be and again it can be seen that the real part of the impedance increases as the number of Mach.

As considered in the previous paragraph, a maximum value, a minimum value and an average mean value can be calculated for each spatial evolution of velocity and impedance. Taking these three values, it is possible to represent the velocity and impedance trends as the frequency varies, for the different cases of acoustic regime and flow, in the range of the values considered.

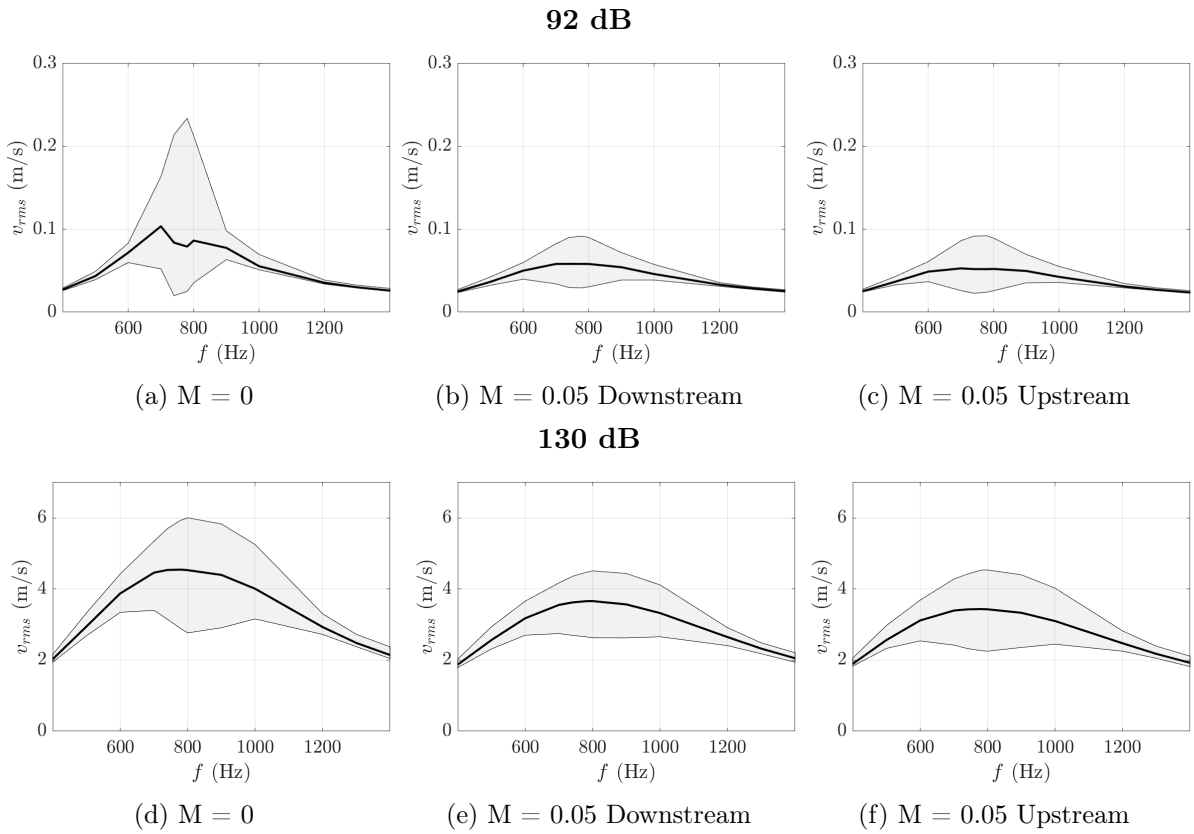

(a) M = 0 (b) M = 0.05 Downstream (c) M = 0.05 Upstream

(d) M = 0 (e) M = 0.05 Downstream (f) M = 0.05 Upstream

Figure 4.31: Numerical evolution of the rms acoustic velocity as a function of the frequencies considered for different sound levels and Mach numbers

Figure 4.31 shows the trend of the rms velocity on the liner as the frequency changes, in acoustic linear and nonlinear regimes with and without flow. The black line is the mean value, while the grey zone represents the range of the values between the maxima and the minima at each frequency. It is evident that for the linear regime, the velocity is at weaker values, less than 1 m/s. For the case without flow, the maximum value is found near the resonance frequency , and then falls in the cases at M = 0.05, both downstream and upstream. At 130 dB, this velocity value increased considerably, presenting a maximum where the TL is maximum. As far as the difference between the upstream and downstream cases is concerned, it can be seen that the upstream case has slightly higher error ranges than the downstream case, but with minimal differences between the two cases.

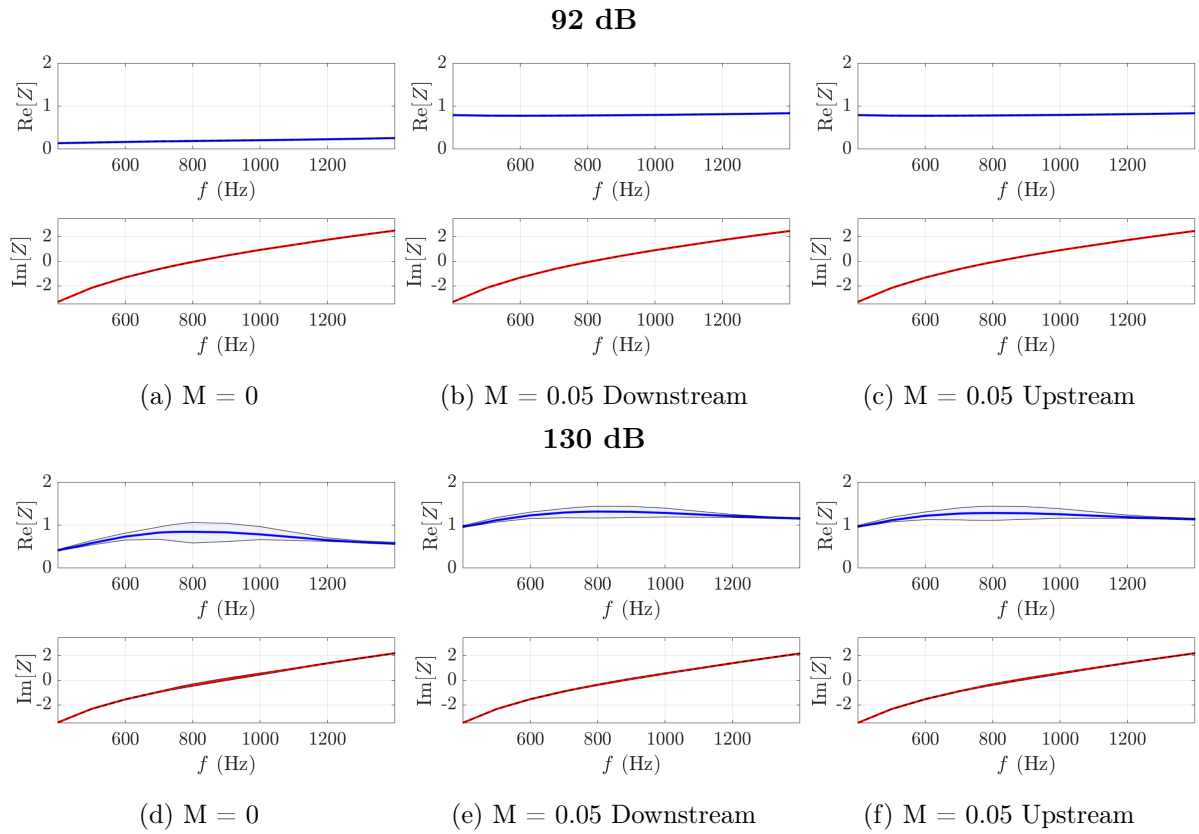

(a) M = 0 (b) M = 0.05 Downstream (c) M = 0.05 Upstream

(d) M = 0 (e) M = 0.05 Downstream (f) M = 0.05 Upstream

Figure 4.32: Numerical evolution of the average real and imaginary parts of impedance as a function of the frequencies considered for different sound level and Mach number configurations

Similarly, Figure 4.32 presents the impedance behaviour as the frequency varies in all the range values. For the linear regime it is noticeable that the real part of the impedance remains constant over the entire frequency spectrum considered. The imaginary part also appears to be constant. It can be seen that the real part has a bell-shaped evolution for the 130 dB case, presenting a greater deviation from the maximum and minimum at the resonance frequency. The resistance slightly increases between the case without flow and the cases with flow. It is noticeable how, with the increase of flow regime, the impedance has the tendency to flatten and to become more uniform along the liner, both in reference to the length and to the frequencies.

4.2.3 Comparison between perforated plates models

In this section a comparison between perforated plates models under grazing incidence is presented. Focus is particularly made on the influence of nonlinear acoustic and of flow. The experimental results and the Guess model simulation are compared to the predictions of simulations based on the EFM (Section 1.4) and on the Rice-Cummings approach (Section 1.5). The differential equations of the Rice-Cummings model are directly integrated in time domain by using the same Runge-Kutta algorithm used for the linearised Euler equations. Comparisons are made for TL and for numerical behaviours of impedance and rms velocity along the liner surface. All simulations have been implemented with the FDTD approach presented in Chapter 3.

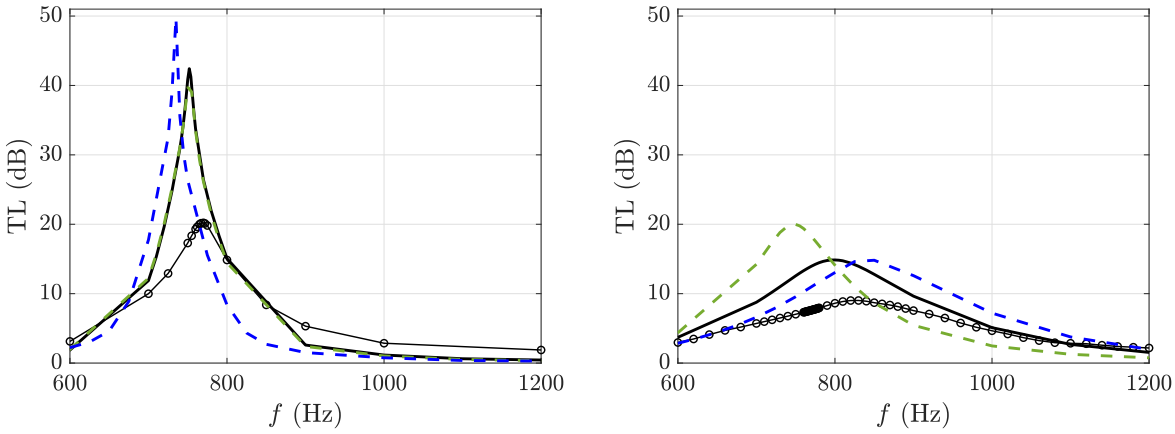

(a) 92 dB (b) 130 dB

Figure 4.33: TL comparison obtained at M = 0 from Experimental, Guess, Rice-Cummings and EFM approaches at 92 dB and 130 dB

Figure 4.33 presents a TL comparison at M = 0 for a linear regime at 92 dB and a nonlinear regime at 130 dB. In the linear case, the Rice-Cummings model prediction results in excellent agreement with the Guess mode, both in value and in peak. Even in this approach based on the direct resolution of governing conservation equations, the TL results overestimated in comparison to experimental. The transmission loss from EFM simulation presents a higher peak with a maximum shifted approximately 50 Hz to lower frequencies compared to the Guess approach. In nonlinear regime, the Rice-Cummings approach takes into account the TL reduction induced by the nonlinearity, but not the peak shift towards higher frequencies. The EFM follows the Guess prediction in term of level reduction, but overestimates the nonlinear effect on the peak shift. The shift from the linear regime case results too high in comparison to the difference observed both in experimental and in the Guess approach. In the latter, even if at lower frequencies, the peak difference between linear and nonlinear is correctly predicted. The EFM seems to predict too much the influence of nonlinearities on the behaviour of the plate. Differences between the Guess and the EFM have already been noticed in normal incidence.

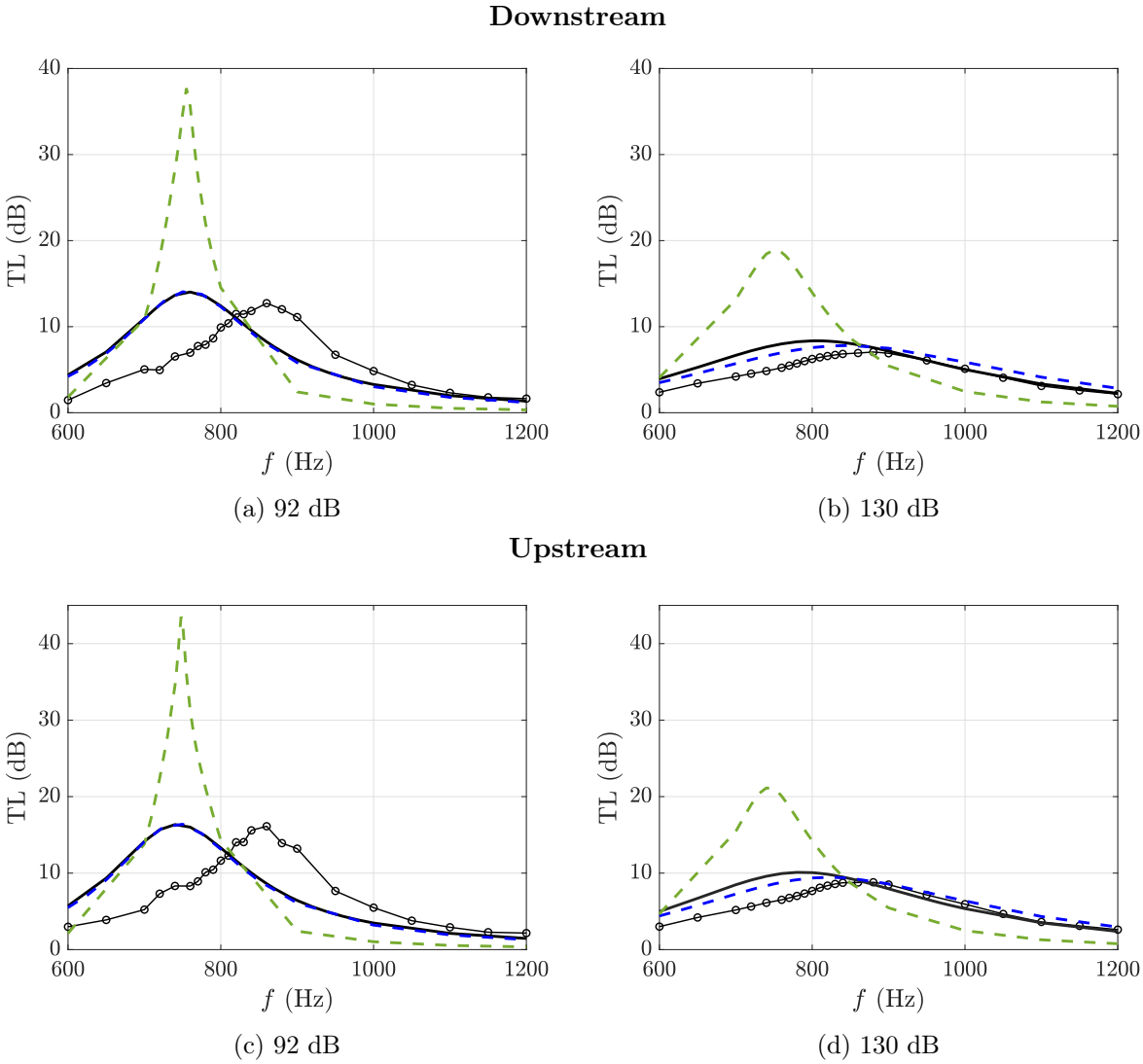

(a) 92 dB (b) 130 dB

(c) 92 dB (d) 130 dB

Figure 4.34: TL comparison obtained by downstream and upstream approaches at M = 0.05 from Experimental, Guess, Rice-Cummings and EFM approaches at 92 dB and 130 dB

Figure 4.34 presents the TL comparison with a flow of M = 0.05 in linear and nonlinear regime, both downstream and upstream. The Rice-Cummings model shows no relevant difference when adding flow to the propagation, since the presence of flow is not included in the differential equation formulation. Similar to the case without flow, the TL peak frequency remain unchanged and only a reduction of TL in nonlinear regime is observed. Nevertheless, this reduction is insufficient to correctly predict the experimental behaviour, demonstrating the inaccuracy of this approach when considering the presence of a flow. The EFM presents an excellent alignment with the Guess model in linear regime. In presence of flow, both the value of the TL peak and its frequency are in agreement with Guess model, suggesting a similar approach to the presence of flow in the two methods. In nonlinear regime, the EFM presents a slight shift in peak towards higher frequencies, coherently to what observed without flow.

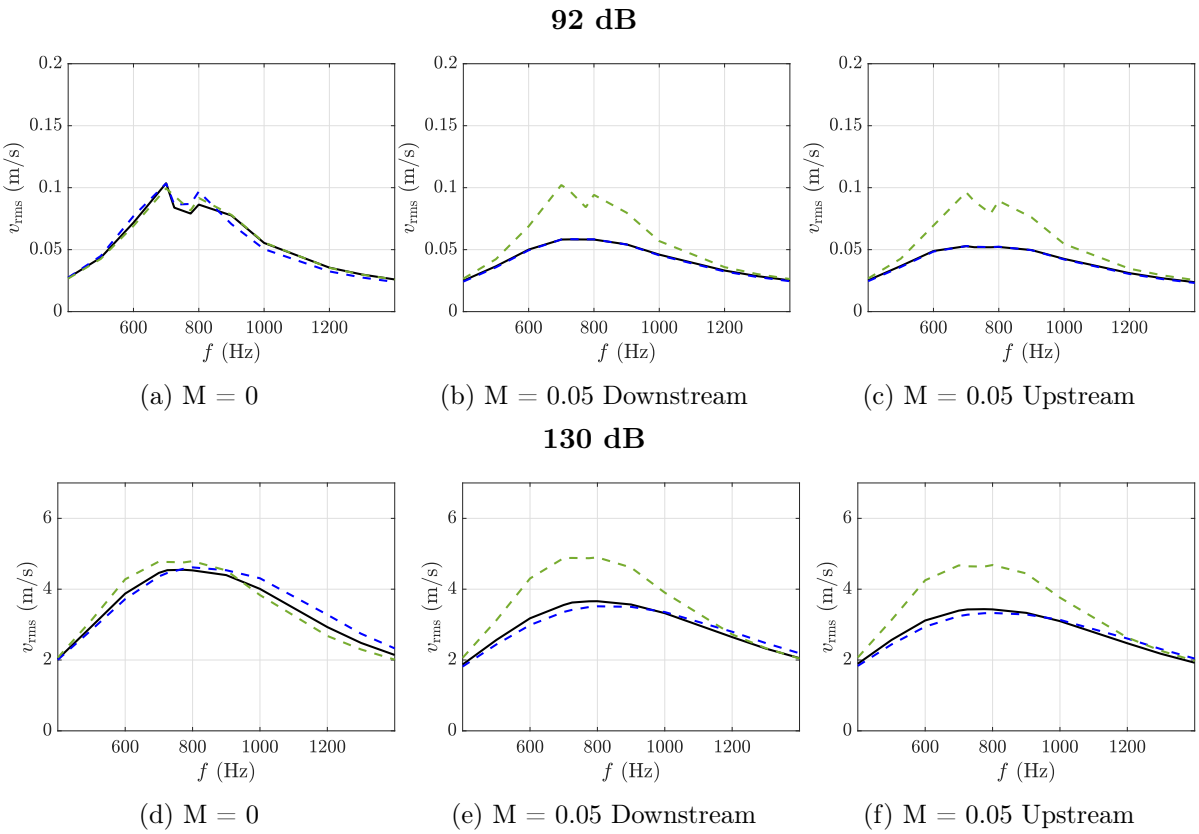

(a) M = 0 (b) M = 0.05 Downstream (c) M = 0.05 Upstream

(d) M = 0 (e) M = 0.05 Downstream (f) M = 0.05 Upstream

Figure 4.35: Numerical evolution of the mean rms acoustic velocity as a function of the frequencies considered for different sound levels and Mach numbers for — Guess, - - - EFM and - - - Rice-Cummings approaches

The numerical evolution of mean rms acoustic velocity is presented in Figure 4.35, for several Mach numbers and two SPL values. Without flow, the three approaches are in good agreement, in both linear and nonlinear case. With flow, the EFM and the Guess model remain consistent with each other, whereas the Rice-Cummings model exhibits minimal variation compared to the no-flow case, confirming the results previously found.

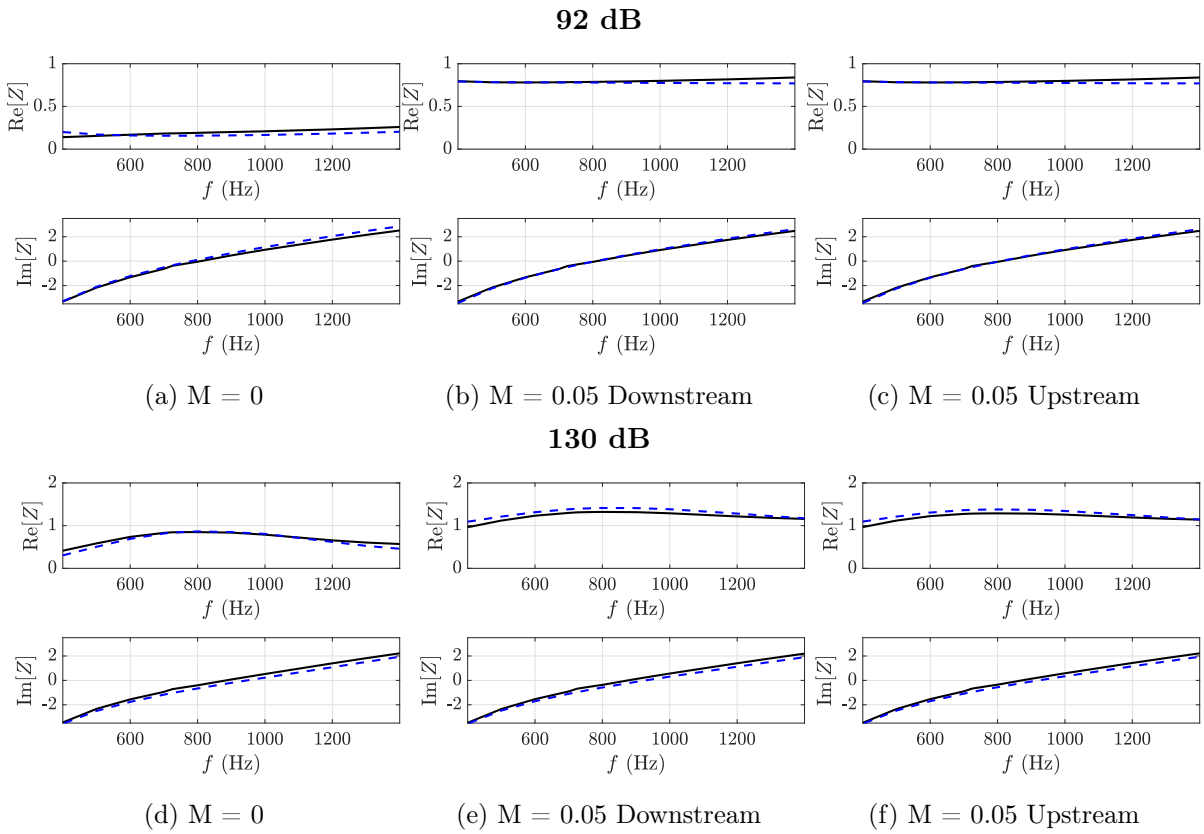

(a) M = 0 (b) M = 0.05 Downstream (c) M = 0.05 Upstream

(d) M = 0 (e) M = 0.05 Downstream (f) M = 0.05 Upstream

Figure 4.36: Numerical evolution of the impedance as a function of the frequencies considered for different sound levels and Mach numbers for — Guess and - - - EFM approaches

Finally, Figure 4.36 compares the mean impedance along the liner. Without flow in linear regime, the EFM gives lower values of resistance and higher values of reactance compared to the Guess model. In the nonlinear regime and with flow, the resistance tends to be higher than that predicted by the Guess model, while the reactance is generally lower. These differences directly impact the TL values discussed earlier in this chapter.

Conclusion

In conclusion, two different approaches have been compared to the Guess model for perforated plates under grazing incidence with flow. The EFM present good agreements in the Guess model, even if in linear regime it underestimates the TL and in contrary tends to overestimate the nonlinear effects on the liner. The presence of flow is correctly considered, due to flow modeling similar to the Guess approach. The Rice-Cummings approach results efficient in the case without flow, in particular in linear regime, and in nonlinear regime it correctly predicts the trend of the effect of nonlinearities, but not in good precision as the Guess model and the EFM. When introducing a flow, the Rice-Cummings model does not predict correctly the effect on the liner. However, this result was expected, since the presented approach does not directly take into account the effect of a mean flow as the Guess impedance model and the EFM. The fact of not considering some parameters and coefficients in the Rice-Cummings approach is surely to be improved and implemented in future studies. In this approach, the fact of not considering the flow effect directly in the modeling of the impedance but only in the propagation reveals to be not sufficient to correctly predict the behaviour in flow environments.

4.3 Conclusions

This study provides an analysis of experimental, analytical and numerical results concerning of a specific reference perforated plate liner, emphasizing its response to acoustic excitations under different flow conditions. The combined experimental, analytical, and numerical investigations demonstrate the significant impact of nonlinearity on key acoustic indicators such as absorption coefficient, impedance, admittance, and transmission loss (TL). The objective of the chapter was to validate the theoretical prediction using the developed models against experimental results.

For the perforated plate in impedance tube, increasing SPL leads to a broadening and a shift toward high frequencies of absorption peak. Impedance measurements confirm that resonance frequency shifts correlate with SPL, with higher acoustic levels amplifying velocity effects within the perforations. Analytical and numerical models, based on the Guess model, effectively predict the trends observed, though minor discrepancies arise from overestimated velocity evaluations.

For the liner tested in Caiman wind tunnel, the study extends the analysis to flow effects, showing that the presence of flow mitigates the impact of high sound pressure levels. In the absence of flow, TL decreases with increasing SPL. The TL peak shifts towards higher frequencies and broadens accordingly. At moderate flow levels ($M = 0.05$), resonance shifts are less pronounced. As the Mach number increases ($M \geq 0.1$), the flow effect becomes predominant, reducing TL and flattening the frequency response. The upstream configuration consistently exhibits higher TL values than the downstream case, confirming the directional dependence of liner performance due to flow-acoustic interactions. Numerical simulations align well with experimental data, accurately predicting TL behaviour and impedance variations. The velocity and impedance distributions further confirm that nonlinearity is dominant at low flow conditions but diminishes as the flow velocity increases. With an increasing flow, the tendency of velocity and impedance along the liner is to become more and more uniform. Moreover, experimental data collected in this study presents a solid and important database for future studies.

For the perforated plate studied, we observed that the TL of the liner strongly decreased in presence of flow, even at low Mach. For this reason, the aim is to design a liner that could perform efficiently in the presence of flow and in nonlinear regimes. This study will be presented and analysed in Chapter 6 of this thesis. The conclusions presented in the chapter are valid for the geometry considered for this specific liner, but are not necessarily applicable to other liners. It is also for this reason the necessity of developing a second liner.

5 Nonlinear dynamic approach to the study of perforated plates

Contents

Abstract

Starting from the differential equations presenting in the Rice-Cummings approach in Chapter 1, a dynamic approach is presented in this chapter in order to characterise the nonlinear impedance of perforated plates. To do so, a Multiple Scale Method will be employed. The details of the analytical procedures are presented in Section 5.2. The extension of this approach to perforated plates represents an innovative application of this method. In Section 5.3, experimental observations will validate the results obtained from this approach for a one perforation plate, more close to a classic Helmholtz resonator, and to a three perforation plate, more close to the liners we consider in this thesis. Comparisons will be made between different models and numerical simulation by directly implementing the differential equations in a time domain model.

5.1 Introduction

Helmholtz resonators have been a fundamental tool in noise control, recognized for their effectiveness in absorbing sound energy at targeted frequencies. Traditional impedance models are based on the assumption of linear behaviour, which holds true for low-amplitude acoustic fields. However, in real-world applications, resonators often operate under high-intensity conditions where nonlinear phenomena, such as jet formation and vortex shedding, significantly impact their performance. Singh and Rienstra [135] addressed this issue by developing a nonlinear impedance model for Helmholtz resonators, accounting for the complex interactions between damping mechanisms and nonlinear effects.

Research into the nonlinear behaviour of Helmholtz resonators dates back to early studies by Ingard [69] and Ingard and Ising [70], which identified transitions from linear to nonlinear regimes. These studies showed that under low excitation, the flow through the resonator neck remains irrotational, resulting in a linear relationship between acoustic pressure and velocity. However, at higher excitation levels, phenomena such as vortex shedding and jet losses introduce significant nonlinear damping effects, necessitating extensions to traditional linear models.

Förner et al. [55] explored the impact of geometric features on nonlinear dissipation, focusing on the neck region of the resonator. Their findings revealed that changes to the edge geometry could reduce vortex-induced losses, thereby modifying the resonator's impedance. This aligns with Singh and Rienstra's framework, which attributes nonlinear damping primarily to jet loss mechanisms, a dominant factor under high-amplitude acoustic conditions.

Beyond damping effects, the compressibility of air within the resonator cavity contributes nonlinear restoring forces. Research by Yu [155] and Meissner [106] examined quadratic and cubic restoring force terms, showing their role in shaping the frequency response under large displacements. Gourdon et al. [4] extended this work by demonstrating how tailored neck designs can reduce vortex shedding, allowing cubic nonlinearities to dominate and result in hardening behaviour at high amplitudes.

Nonlinear acoustic effects have also been studied in broader contexts, such as porous materials and viscoelastic systems, where they facilitate energy transfer. Studies by Cochelin et al. [38] and Bellet et al. [16] applied these principles to vibro-acoustic systems, showing that coupling acoustic mode with nonlinear absorbers enhances energy dissipation. These findings underscore the potential for designing resonators that leverage nonlinear effects to achieve improved broadband performance.

Singh and Rienstra's work represents a key advancement in understanding and modeling the nonlinear dynamics of Helmholtz resonators. Their impedance model captures nonlinear jet losses while maintaining practical simplicity. While their approach partially incorporates the method of multiple scales by considering limited scales, the method presented in this chapter aims for a comprehensive application of the multiple scales method [115]. This includes both time scales and small parameter considerations, ensuring a constant small value of ε for all external pressure conditions analyzed, which was not the case in the work of Singh and Rienstra.

5.2 Analytical model

5.2.1 Physical phenomena and analytical approach

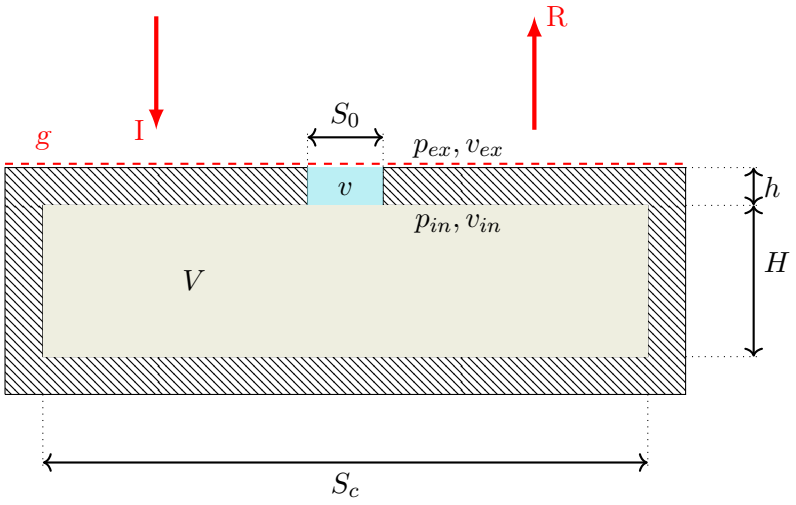

Figure 5.1: Schematic representation of a Helmholtz resonator under acoustic excitation

A schematic representation of the Helmholtz resonator under consideration is shown in Figure 5.1. This dissertation is based on the governing equations of the Rice-Cummings model presented in Section 1.5. Combining the momentum equation and the mass conservation law, we obtain:

$$\varrho_0 \ell \frac{\mathrm{d}}{\mathrm{d}t} v + \frac{1}{2} \varrho_0 v \left| v \right| + R v = p_{\mathrm{in}} - p_{\mathrm{ex}} \tag{5.1}$$

where v is the normal acoustic velocity in the perforation, R the resistance factor, p_{in} the cavity-side perforation pressure and p_{ex} the pressure just outside of the perforation, and r_p the perforation radius. The corrected length is defined as $\ell = h + 2r_p$. This definition of corrected length has been chosen according to the definition of the linear Guess model.

Elimination of v from Eq.(5.1) leads to the classic equation of the nonlinear Helmholtz resonator:

$$p_{ex} = p_{in} + \frac{\ell V}{c_0^2 S_0} \frac{\mathrm{d}^2 p_{in}}{\mathrm{d}t^2} + \frac{V^2}{2\varrho_0 c_0^4 S_0^2} \frac{\mathrm{d}p_{in}}{\mathrm{d}t} \left| \frac{\mathrm{d}p_{in}}{\mathrm{d}t} \right| + R \frac{V}{\varrho_0 c_0^2 S_0} \frac{\mathrm{d}p_{in}}{\mathrm{d}t} \tag{5.2}$$

The nonlinear term is related to the jet phenomenon inside of the perforation. Dividing by $\ell V/(c_0 S_0)$, we obtain:

$$p_{ex} \frac{c_0^2 S_0}{\ell V} = \frac{\mathrm{d}^2 p_{in}}{\mathrm{d}t^2} + \underbrace{\frac{V}{2\varrho_0 \ell c_0^2 S_0} \frac{\mathrm{d}p_{in}}{\mathrm{d}t} \left| \frac{\mathrm{d}p_{in}}{\mathrm{d}t} \right|}_{\text{non linear damping}} + \underbrace{\frac{R}{\varrho_0 \ell} \frac{\mathrm{d}p_{in}}{\mathrm{d}t}}_{\text{linear damping}} + \underbrace{\frac{c_0^2 S_0}{\ell V}}_{=\omega_0^2} p_{in} \tag{5.3}$$

It turns out that $\frac{c_0^2 S_0}{\ell V} = \omega_0^2 = (2\pi f_h)^2$ is linked the resonance frequency of the resonator also referred to as the Helmholtz frequency.

It is convenient to use dimensionless variables by changing the time scales. Having $\tau = \omega_0 t$ to

adimensionalise the time, the time derivative of a generic variable $\cdot$ is defined as:

$$\begin{cases} \dfrac{\mathrm{d}\cdot}{\mathrm{d}t} = \dfrac{\mathrm{d}\tau}{\mathrm{d}t}\dfrac{\mathrm{d}\cdot}{\mathrm{d}\tau} = \omega_0 \dfrac{\mathrm{d}}{\mathrm{d}\tau} \\ \dfrac{\mathrm{d}^2\cdot}{\mathrm{d}t^2} = \dfrac{\mathrm{d}}{\mathrm{d}t}\left(\dfrac{\mathrm{d}\cdot}{\mathrm{d}t}\right) = \dfrac{\mathrm{d}\tau}{\mathrm{d}t}\dfrac{\mathrm{d}\cdot}{\mathrm{d}\tau}\left(\omega_0 \dfrac{\mathrm{d}\cdot}{\mathrm{d}\tau}\right) = \omega_0^2 \dfrac{\mathrm{d}^2\cdot}{\mathrm{d}\tau^2} \end{cases} \tag{5.4}$$

From this system we can express Eq. (5.3) as:

$$\omega_0^2 \frac{\mathrm{d}^2 p_{in}}{\mathrm{d}\tau^2} + \frac{V\omega_0^2}{2\varrho_0 \ell c_0^2 S_0} \frac{\mathrm{d}p_{in}}{\mathrm{d}\tau}\left|\frac{\mathrm{d}p_{in}}{\mathrm{d}\tau}\right| + R\frac{\omega_0}{\varrho_0 \ell}\frac{\mathrm{d}p_{in}}{\mathrm{d}\tau} + \omega_0^2 p_{in} = p_{\mathrm{ex}}\,\frac{c_0^2 S_0}{\ell V} \tag{5.5}$$

Dividing for ${\omega_0}^2$ we obtain:

$$\frac{\mathrm{d}^2 p_{in}}{\mathrm{d}\tau^2} + p_{in} + \underbrace{\frac{V}{2\varrho_0 \ell c_0^2 S_0}\frac{\mathrm{d}p_{in}}{\mathrm{d}\tau}\left|\frac{\mathrm{d}p_{in}}{\mathrm{d}\tau}\right|}_{\text{Nonlinear damping}} + \underbrace{\frac{R}{\varrho_0 \ell c_0}\sqrt{\frac{\ell V}{S_0}}\frac{\mathrm{d}p_{in}}{\mathrm{d}\tau}}_{\text{Linear damping}} = p_{ex} \tag{5.6}$$

It is to be noted that it is already possible to find an analytical approximation for equation (5.6), but it is preferable to arrive at eq. (5.14) to have a decomposition in the terms of order near the resonance. Moreover, it is already evident that the resonance frequency will not change with the SPL, since we chose a corrected length that does not depend on v. Also, in eq. (5.6) we do not consider quadratic and cubic terms in the nonlinear component of p_{in} as in previous works from Vargas et al. [5]

5.2.2 Application of the Multiple Scales Method (MSM)

The linear and nonlinear damping are assumed weak. We define the dimensionless internal pressure y with:

$$p_{in} = C\varepsilon y \quad (\varepsilon \ll 1) \tag{5.7}$$

The parameter ε is introduced to assess the smallness of the various parameters and variables. The constant C given by:

$$C = 2\varrho_0 c_0^2 \frac{\ell S_0}{V} \tag{5.8}$$

is chosen so that the linear and nonlinear damping are both of order ε. We introduce also r_1:

$$r_1 \varepsilon = \frac{R}{\varrho_0 \ell c_0}\sqrt{\frac{V\ell}{S_0}} \tag{5.9}$$

corresponding to a dimensionless hydraulic resistance. Finally, we add in front of the nonlinear damping term a dimensionless constant r_2, with default value $r_2 = 1$, allowing us to tune and identify the nonlinear damping term.

Let us concentrate on the external pressure p_{ex}, that we can define as:

$$p_{ex} = P\cos(\omega t) \tag{5.10}$$

The amplitude P can be deduced from the global SPL on the plate with:

$$P = \sqrt{2} p_{\mathrm{ref}} 10^{\mathrm{SPL_g}/20} \tag{5.11}$$

with $p_{\mathrm{ref}} = 2 \times 10^{-5}$ Pa. Introducing $\tau = \omega_0 t$, $\Omega = \omega/\omega_0$, and P_0 such that $P = \varepsilon^2 P_0$, the external

pressure can be written as:

$$p_{ex} = \varepsilon^2 P_0 \cos(\Omega\tau) \tag{5.12}$$

Equation (5.6) becomes:

$$C\varepsilon\frac{\mathrm{d}^2y}{\mathrm{d}\tau^2} + C\varepsilon y + r_2 C\varepsilon^2\frac{\mathrm{d}y}{\mathrm{d}\tau}\left|\frac{\mathrm{d}y}{\mathrm{d}\tau}\right| + r_1\varepsilon^2 C\frac{\mathrm{d}y}{\mathrm{d}\tau} = \varepsilon^2 P_0\cos(\Omega\tau) \tag{5.13}$$

We then divide by $C\varepsilon$ to obtain:

$$\frac{\mathrm{d}^2y}{\mathrm{d}\tau^2} + y + \underbrace{\varepsilon r_2\frac{\mathrm{d}y}{\mathrm{d}\tau}\left|\frac{\mathrm{d}y}{\mathrm{d}\tau}\right|}_{\text{Nonlinear damping}} + \underbrace{\varepsilon r_1\frac{\mathrm{d}y}{\mathrm{d}\tau}}_{\text{Linear damping}} = \varepsilon F_0\cos(\Omega\tau) \tag{5.14}$$

with F_0 is an external forcing term defined by:

$$F_0 = \frac{P_0}{C} = \frac{PV}{2\varrho_0 c_0^2 \ell S_0 \varepsilon^2} \tag{5.15}$$

We note that the linear and nonlinear damping and external forcing in Eq. (5.14) are of order ε.

We consider the method of multiple scales, in order to analyse the different physical phenomena according to ε scales [115]. The fast and slow time scales are developed using the multiple time scale expansion with an expansion of y of the time scale:

$$\begin{aligned} y &= \sum_{i=0}^{N}\varepsilon^i y_i, \quad \tau_i = \varepsilon^i\tau \\ y &= y_0 + \varepsilon y_1 + ... \\ \tau_0 &= \tau, \quad \tau_1 = \varepsilon\tau, \quad ... \end{aligned} \tag{5.16}$$

where τ_0 correspond to fast scales and τ_1 to slow scale.

We are looking for solutions near the resonance. For that, we introduce the relation $\Omega = 1 + \zeta\varepsilon$ where ζ is the tuning related to the excitation frequency. The external forcing modifies as:

$$F_0\cos(\Omega\tau) = \frac{F_0}{2}\left(\mathrm{e}^{\mathrm{j}\Omega\tau} + \mathrm{e}^{-\mathrm{j}\Omega\tau}\right) = \frac{F_0}{2}\left(\mathrm{e}^{\mathrm{j}(\tau_0+\zeta\tau_1)} + \mathrm{e}^{-\mathrm{j}(\tau_0+\zeta\tau_1)}\right) \tag{5.17}$$

By injecting the solution y with just the first values of the series of Eq. (5.16) in Eq. (5.14), and just considering the the first order of ε it is obtained:

$$\frac{\partial^2 y_0}{\partial\tau_0^2} + 2\varepsilon\frac{\partial^2 y_0}{\partial\tau_0\partial\tau_1} + \varepsilon\frac{\partial^2 y_1}{\partial\tau_0^2} + r_2\varepsilon\frac{\partial y_0}{\partial\tau_0}\left|\frac{\partial y_0}{\partial\tau_0}\right| + \varepsilon r_1\frac{\partial y_0}{\partial\tau_0} + y_0 + \varepsilon y_1 = \varepsilon\frac{F_0}{2}\left(\mathrm{e}^{\mathrm{j}(\tau_0+\zeta\tau_1)} + \mathrm{e}^{-\mathrm{j}(\tau_0+\zeta\tau_1)}\right) \tag{5.18}$$

Let us consider this equation by orders.

5.2.2.1 Zeroth order in ε

When considering the zeroth order $O\left(\varepsilon^0\right) = O(1)$ of Eq. (5.18), we get:

$$\frac{\partial^2 y_0}{\partial\tau_0^2} + y_0 = 0 \tag{5.19}$$

which has for solution:

$$\begin{cases} y_0 = A\mathrm{e}^{\mathrm{j}\tau_0} + A^*\mathrm{e}^{-\mathrm{j}\tau_0} \\ \dfrac{\partial y_0}{\partial \tau_0} = A\mathrm{j}\mathrm{e}^{\mathrm{j}\tau_0} - A^*\mathrm{j}\mathrm{e}^{-\mathrm{j}\tau_0} \end{cases} \tag{5.20}$$

with $A = A(\tau_1, \tau_2...) \in \mathbb{C}$ the amplitude. If we consider polar coordinates, we have:

$$\begin{cases} A = m\,\mathrm{e}^{\mathrm{j}\theta} = m(\cos\theta + \mathrm{j}\sin\theta) \\ A^* = m\,\mathrm{e}^{-\mathrm{j}\theta} = m(\cos\theta - \mathrm{j}\sin\theta) \end{cases} \tag{5.21}$$

with m the modulus and θ the phase of the amplitude A. Note that m represents the normalized amplitude of the internal pressure in the perforation. We can derive the polar form of the solution y_0 as:

$$\begin{cases} y_0 = 2m\cos(\tau_0 + \theta) \\ \dfrac{\partial y_0}{\partial \tau_0} = -2m\sin(\tau_0 + \theta) \end{cases} \tag{5.22}$$

5.2.2.2 First order in ε

In order to calculate the amplitude A (or the modulus m and the phase θ), we consider the first order $O\left(\varepsilon^1\right) = O(\varepsilon)$ of Eq. (5.18):

$$\frac{\partial^2 y_1}{\partial \tau_0^2} + y_1 = -2\frac{\partial^2 y_0}{\partial \tau_0 \partial \tau_1} - r_2\frac{\partial y_0}{\partial \tau_0}\left|\frac{\partial y_0}{\partial \tau_0}\right| - r_1\frac{\partial y_0}{\partial \tau_0} + \frac{F_0}{2}\left(\mathrm{e}^{\mathrm{j}(\tau_0+\zeta\tau_1)} + \mathrm{e}^{-\mathrm{j}(\tau_0+\zeta\tau_1)}\right) \tag{5.23}$$

Now by injecting the solution in Eq. (5.20) into Eq. (5.23) we obtain:

$$\begin{aligned} \frac{\partial^2 y_1}{\partial \tau_0^2} + y_1 = &-2\mathrm{j}\frac{\partial A}{\partial \tau_1}\mathrm{e}^{\mathrm{j}\tau_0} + 2\mathrm{j}\frac{\partial A^*}{\partial \tau_1}\mathrm{e}^{-\mathrm{j}\tau_0} - r_2\left(A\mathrm{j}\mathrm{e}^{\mathrm{j}\tau_0} - A^*\mathrm{j}\mathrm{e}^{-\mathrm{j}\tau_0}\right)\left|A\mathrm{j}\mathrm{e}^{\mathrm{j}\tau_0} - A^*\mathrm{j}\mathrm{e}^{-\mathrm{j}\tau_0}\right| - \\ &-r_1\left(A\mathrm{j}\mathrm{e}^{\mathrm{j}\tau_0} - A^*\mathrm{j}\mathrm{e}^{-\mathrm{j}\tau_0}\right) + \frac{F_0}{2}\left(\mathrm{e}^{\mathrm{j}(\tau_0+\zeta\tau_1)} + \mathrm{e}^{-\mathrm{j}(\tau_0+\zeta\tau_1)}\right) \end{aligned} \tag{5.24}$$

In general, the solution of the homogeneous equation of Eq. (5.24) (i.e. by not taking into account the right hand side having $\frac{\partial^2 y_1}{\partial \tau_0^2} + y_1 = 0$) takes the form:

$$y_1 = B\mathrm{e}^{\mathrm{j}\tau_0} + B^*\mathrm{e}^{-\mathrm{j}\tau_0} \tag{5.25}$$

In order to find B, it would be necessary to consider the second order of ε, which is not done in this study. The right hand side of Eq. (5.24) contains the so-called secular terms, which depend on $\mathrm{e}^{\mathrm{j}\tau_0}$, and their complex conjugates. In order to obtain periodical and non divergent solutions, the sum of these secular terms in $\mathrm{e}^{\mathrm{j}\tau_0}$ must be equal to zero [4, 115]. We get:

$$\begin{aligned} &\underbrace{-2\mathrm{j}\frac{\partial A}{\partial \tau_1}\mathrm{e}^{\mathrm{j}\tau_0}}_{\mathrm{T}_1} + 2\mathrm{j}\frac{\partial A^*}{\partial \tau_1}\mathrm{e}^{-\mathrm{j}\tau_0} - \underbrace{r_2\left(A\mathrm{j}\mathrm{e}^{\mathrm{j}\tau_0} - A^*\mathrm{j}\mathrm{e}^{-\mathrm{j}\tau_0}\right)\left|A\mathrm{j}\mathrm{e}^{\mathrm{j}\tau_0} - A^*\mathrm{j}\mathrm{e}^{-\mathrm{j}\tau_0}\right|}_{\mathrm{T}_2} \\ &\underbrace{-r_1 A\mathrm{j}\mathrm{e}^{\mathrm{j}\tau_0}}_{\mathrm{T}_3} + r_1 A^*\mathrm{j}\mathrm{e}^{-\mathrm{j}\tau_0} + \underbrace{\frac{F_0}{2}\mathrm{e}^{\mathrm{j}(\tau_0+\zeta\tau_1)}}_{\mathrm{T}_4} + \frac{F_0}{2}\mathrm{e}^{-\mathrm{j}(\tau_0+\zeta\tau_1)} = 0 \end{aligned} \tag{5.26}$$

We proceed with the identification of the secular terms, that we will call T_1, T_2, T_3 and T_4.

- T_1: Since in polar coordinates we can express:

$$\frac{\partial A}{\partial \tau_1} = \frac{\partial m}{\partial \tau_1} e^{j\theta} + m j \frac{\partial \theta}{\partial \tau_1} e^{j\theta} \tag{5.27}$$

It is possible to calculate:

$$\begin{aligned} T_1 &= -2j\frac{\partial A}{\partial \tau_1} e^{j\tau_0} = -2j\frac{\partial m}{\partial \tau_1} e^{j\theta} e^{j\tau_0} - 2j^2 m \frac{\partial \theta}{\tau_1} e^{j\theta} e^{j\tau_0} = -2j\frac{\partial m}{\partial \tau_1} e^{j\theta} e^{j\tau_0} + 2m\frac{\partial \theta}{\tau_1} e^{j\theta} e^{j\tau_0} \\ &= \left(-2j\frac{\partial m}{\partial \tau_1}\cos\theta + 2\frac{\partial m}{\partial \tau_1}\sin\theta + 2m\frac{\partial \theta}{\partial \tau_1}\cos\theta + 2mj\frac{\partial \theta}{\partial \tau_1}\sin\theta \right) e^{j\tau_0} \end{aligned} \tag{5.28}$$

- T_2: It is possible to rewrite:

$$T_2 = r_2 \left(A j e^{j\tau_0} - A^* j e^{-j\tau_0} \right) \left| A j e^{j\tau_0} - A^* j e^{-j\tau_0} \right| = -4 r_2 m^2 \sin(\tau_0 + \theta) \left| \sin(\tau_0 + \theta) \right| \tag{5.29}$$

In order to isolate the secular term in $e^{j\tau_0}$, we use the following development in Fourier series of a generic argument α [32]:

$$\sin(\alpha)\left|\sin(\alpha)\right| = -\frac{1}{\pi}\sum_{n=0}^{\infty} \frac{\sin\left[(2n+1)\alpha\right]}{\left(n^2 - \frac{1}{4}\right)\left(n + \frac{3}{2}\right)} = \frac{8}{3\pi}\sin\alpha - \frac{8}{15}\pi\sin(3\alpha) - \frac{8}{49}\pi\sin(5\alpha)\ldots \tag{5.30}$$

Given the exponential form of the sinus:

$$\sin(\tau_0 + \theta) = \frac{e^{j(\tau_0+\theta)} - e^{-j(\tau_0+\theta)}}{2j} = -\frac{j}{2}(e^{j\tau_0}e^{j\theta} + e^{-j\tau_0}e^{-j\theta}) \tag{5.31}$$

We limit to the first order of the Fourier series of T_2, since being at resonance just the first harmonic is considered. By considering only the secular term in $e^{j\tau_0}$, we obtain from eq. 5.29:

$$T_2 = -r_2\frac{32}{3\pi}m^2\sin(\tau_0+\theta) = r_2\frac{16}{3\pi}jm^2\left(\cos(\theta) + j\sin(\theta)\right)e^{j\tau_0} = \left(r_2\frac{16}{3\pi}jm^2\cos(\theta) - r_2\frac{16}{3\pi}m^2\sin(\theta)\right)e^{j\tau_0} \tag{5.32}$$

- T_3: We obtain:

$$T_3 = r_1 A j e^{j\tau_0} = r_1 m j(\cos(\theta) + j\sin(\theta))e^{j\tau_0} = \left(r_1 jm\cos(\theta) - r_1 m\sin(\theta)\right)e^{j\tau_0} \tag{5.33}$$

- T_4: We find

$$T_4 = \frac{F_0}{2}e^{j(\tau_0+\zeta\tau_1)} = \frac{F_0}{2}e^{j\zeta\tau_1}e^{j\tau_0} = \left(\frac{F_0}{2}\cos(\zeta\tau_1) + j\frac{F_0}{2}\sin(\zeta\tau_1)\right)e^{j\tau_0} \tag{5.34}$$

So by cancelling all the secular terms in $e^{j\tau_0}$ and substituting in (5.24) we obtain:

$$\begin{aligned} &-2j\frac{\partial m}{\partial \tau_1}\cos(\theta) + 2\frac{\partial m}{\partial \tau_1}\sin(\theta) + 2m\frac{\partial \theta}{\partial \tau_1}\cos(\theta) + 2mj\frac{\partial \theta}{\partial \tau_1}\sin(\theta) - r_2\frac{16}{3\pi}m^2 j\cos(\theta) + r_2\frac{16}{3\pi}m^2\sin(\theta) - \\ &-r_1 mj\cos(\theta) + r_1 m\sin(\theta) + \frac{F_0}{2}\cos(\zeta\tau_1) + j\frac{F_0}{2}\sin(\zeta\tau_1) = 0 \end{aligned} \tag{5.35}$$

The resolution of equation (5.35) gives the relation between the phase θ and the modulus m of the amplitude A.

5.2.3 Derivation of the governing equation

In order to simplify the calculation, we decompose the terms in Eq.(5.35) into real part and imaginary parts, which must be both equal to zero. We obtain:

$$\begin{cases} 2\dfrac{\partial m}{\partial \tau_1}\sin(\theta) + 2m\dfrac{\partial \theta}{\partial \tau_1}\cos(\theta) + r_2\dfrac{16}{3\pi}m^2\sin(\theta) + r_1 m\sin(\theta) + \dfrac{F_0}{2}\cos(\zeta\tau_1) = 0 & \text{(5.36a)} \\ -2\dfrac{\partial m}{\partial \tau_1}\cos(\theta) + 2m\dfrac{\partial \theta}{\partial \tau_1}\sin(\theta) - r_2\dfrac{16}{3\pi}m^2\cos(\theta) - r_1 m\cos(\theta) + \dfrac{F_0}{2}\sin(\zeta\tau_1) = 0 & \text{(5.36b)} \end{cases}$$

We now proceed with the following mathematical manipulation to find the first equation: Eq. (5.36*a*)$\times$ $\sin(\theta)$ − Eq. (5.36*b*) $\times$ $\cos(\theta)$. This gives:

$$\begin{aligned} &2\frac{\partial m}{\partial \tau_1}\sin^2(\theta) + 2m\frac{\partial \theta}{\partial \tau_1}\cos(\theta)\sin(\theta) + r_2\frac{16}{3\pi}m^2\sin^2(\theta) + r_1 m\sin^2(\theta) + \frac{F_0}{2}\cos(\zeta\tau_1)\sin(\theta) + \\ &- 2m\frac{\partial \theta}{\partial \tau_1}\sin(\theta)\cos(\theta) + 2\frac{\partial m}{\partial \tau_1}\cos^2(\theta) + r_2\frac{16}{3\pi}m^2\cos^2(\theta) + r_1 m\cos^2(\theta) - \frac{F_0}{2}\sin(\zeta\tau_1)\cos(\theta) = \\ &= 2\frac{\partial m}{\partial \tau_1} + r_2\frac{16}{3\pi}m^2 + r_1 m - \frac{F_0}{2}\sin(\zeta\tau_1 - \theta) = 0 \end{aligned} \tag{5.37}$$

Introducing the parameter Δ which corresponds to a deflection linked to the amplitude phase:

$$\Delta = \zeta\tau_1 - \theta, \tag{5.38}$$

we arrive at the first equation describing the evolution of m:

$$\frac{\partial m}{\partial \tau_1} = \frac{F_0}{4}\sin(\Delta) - r_2\frac{8}{3\pi}m^2 - \frac{r_1}{2}m \tag{5.39}$$

Now we proceed with the following mathematical manipulation to find the second equation: Eq. (5.36*a*)$\times$ $\cos(\theta)$ + Eq. (5.36*b*) $\times$ $\sin(\theta)$. This gives:

$$\begin{aligned} &2\frac{\partial m}{\partial \tau_1}\sin(\theta)\cos(\theta) + 2m\frac{\partial \theta}{\partial \tau_1}\cos^2(\theta) + r_2\frac{16}{3\pi}m^2\sin(\theta)\cos(\theta) + r_1 m\cos(\theta)\sin(\theta) + \frac{F_0}{2}\cos(\zeta\tau_1)\cos(\theta) + \\ &- 2\frac{\partial m}{\partial \tau_1}\sin(\theta)\cos(\theta) + 2m\frac{\partial \theta}{\partial \tau_1}\sin^2(\theta) - r_2\frac{16}{3\pi}m^2\sin(\theta)\cos(\theta) - r_1 m\cos(\theta)\sin(\theta) + \frac{F_0}{2}\sin(\zeta\tau_1)\sin(\theta) = \\ &= 2m\frac{\partial \theta}{\partial \tau_1} + \frac{F_0}{2}\cos(\Delta) = 0 \end{aligned} \tag{5.40}$$

With $\theta = \zeta\tau_1 - \Delta$, we note:

$$m\frac{\partial \theta}{\partial \tau_1} = m\frac{\partial}{\partial \tau_1}(\zeta\tau_1 - \Delta) = \zeta m - m\frac{\partial \Delta}{\partial \tau_1} \tag{5.41}$$

Eq. (5.40) can then we rewritten as:

$$m\frac{\partial \Delta}{\partial \tau_1} = \zeta m + \frac{F_0}{4}\cos(\Delta) \tag{5.42}$$

which gives a second equation relating m and Δ.

To sum up, the governing equations for m and Δ are:

$$\begin{cases} \dfrac{\partial m}{\partial \tau_1} = \dfrac{F_0}{4}\sin(\Delta) - r_2\dfrac{8}{3\pi}m^2 - \dfrac{r_1}{2}m & \text{(5.43a)} \\ m\dfrac{\partial \Delta}{\partial \tau_1} = \zeta m + \dfrac{F_0}{4}\cos(\Delta) & \text{(5.43b)} \end{cases}$$

We can find analytical approximate solutions of this system [5], but in this dissertation we are interested in computing the fixed points in order to have stationary solutions. So to find the periodical solutions we must have:

$$\frac{\partial \Delta}{\partial \tau_1} = \frac{\partial m}{\partial \tau_1} = 0 \tag{5.44}$$

We deduce from Eqs. (5.43a) and (5.43b):

$$\begin{cases} \dfrac{F_0}{4}\cos(\Delta) = -\zeta m & \text{(5.45a)} \\ \dfrac{F_0}{4}\sin(\Delta) = r_2\dfrac{8}{3\pi}m^2 + \dfrac{r_1}{2}m & \text{(5.45b)} \end{cases}$$

Calculating Eq. (5.45a)^2+Eq. (5.45b)^2:

$$\frac{F_0^2}{16} = \zeta^2 m^2 + \left(r_2\frac{8}{3\pi}m^2 + \frac{r_1}{2}m\right)^2 \tag{5.46}$$

leads to:

$$\frac{64}{9\pi^2}r_2^2 m^4 + \frac{8}{3\pi}r_1 r_2 m^3 + \left(\frac{r_1^2}{4} + \zeta^2\right)m^2 - \frac{F_0^2}{16} = 0 \tag{5.47}$$

We finally have an analytical approximation relating the frequency (through ζ) and the amplitude of the internal pressure (through m). This polynomial equation of fourth degree can be solved analytically using the Ferrari method [34, 140], or numerically, for example using the nonlinear system solver *fsolve* of Matlab©.

5.2.4 Impedance calculation

5.2.4.1 Formulation

We can define the impedance at a given frequency ω by:

$$Z(\omega) = -\frac{\hat{p}_{ex}(\omega)}{\hat{v}_{ex}(\omega)} \tag{5.48}$$

where $\hat{p}_{ex}$ is the Fourier transform of the external pressure p_{ex} on the plate and $\hat{v}_{ex}$ the Fourier transform of the external acoustic velocity v_{ex} on the plate. We first remind the relations:

$$\tau = \tau_0 = \omega_0 t \qquad \Delta = \zeta\tau_1 - \theta \qquad \tau_1 = \tau\varepsilon = \omega_0\varepsilon t \qquad \Omega = \frac{\omega}{\omega_0} = 1 + \varepsilon\zeta \tag{5.49}$$

We first consider the pressure $\hat{p}_{ex}$. From Eqs. (5.8) and (5.10), we have:

$$p_{ex} = P\cos(\omega t) = 2\varepsilon^2\varrho_0 c_0^2 \ell\frac{S_0}{V}F_0\cos(\omega t) \tag{5.50}$$

By definition, $\hat{p}_{ex}$ is the Fourier transform of p_{ex} given by:

$$\hat{p}_{ex}(\eta) = \int_{-\infty}^{+\infty} p_{ex}(t)\mathrm{e}^{-\mathrm{j}\eta t}\mathrm{d}t \tag{5.51}$$

from which, we get:

$$\hat{p}_{ex}(\eta) = 2\varepsilon^2\varrho_0 c_0^2 \ell \frac{S_0}{V} F_0 \underbrace{\int_{-\infty}^{+\infty} \cos(\omega t)\mathrm{e}^{-\mathrm{j}\eta t}\mathrm{d}t}_{\frac{1}{2}(\delta(\eta-\omega)+\delta(\eta+\omega))} \tag{5.52}$$

with δ the Dirac delta function. Finally, we obtain:

$$\hat{p}_{\mathrm{ex}}\ (\eta) = \varepsilon^2\varrho_0 c_0^2 \ell \frac{S_0}{V} F_0[\delta(\eta-\omega)+\delta(\eta+\omega)] \tag{5.53}$$

Let us now consider the external velocity $\hat{v}_{ex}$. It is related to the perforation velocity v by the relation:

$$v_{ex} = \frac{S_0}{S_c} v \tag{5.54}$$

The perforation velocity can be written as a function of the internal pressure, using Eq. (1.25):

$$v = -\frac{V}{c_0^2\varrho_0 S_0}\frac{\mathrm{d}p_{in}}{\mathrm{d}t} = -\frac{V}{c_0^2\varrho_0 S_0} C\varepsilon \frac{\mathrm{d}y_0}{\mathrm{d}t} = -2\ell\varepsilon\frac{\mathrm{d}y_0}{\mathrm{d}t} \tag{5.55}$$

By operating a variable change, the solution argument is modified as:

$$\begin{aligned}(\theta+\tau_0) = (\theta+\omega_0 t) = (\zeta\tau\varepsilon - \Delta + \omega_0 t) = \big((1+\zeta\varepsilon)\tau - \tau - \Delta + \omega_0 t\big) = \\ = \left(\frac{\omega}{\omega_0}\omega_0 t - \omega_0 t - \Delta + \omega_0 t\right) = (\omega t - \Delta)\end{aligned} \tag{5.56}$$

We recall the general solution, which is the first analytical approximation $y \approx y_0$:

$$\begin{cases} y_0 = 2m\cos(\theta+\tau_0) \\ \dfrac{\mathrm{d}y_0}{\mathrm{d}t} = -2m\omega_0\sin(\theta+\tau_0) \end{cases} \tag{5.57}$$

Hence, we obtain from Eq. (5.55):

$$v = 4\ell\varepsilon m\omega_0\sin(\omega t - \Delta) \tag{5.58}$$

The external velocity is then expressed as:

$$v_{ex} = \frac{S_0}{S_c}v = 4\omega_0\frac{S_0}{S_c}\ell\varepsilon m\sin(\omega t - \Delta) \tag{5.59}$$

Now, similarly to pressure, we can define the Fourier transform of velocity as:

$$\hat{v}_{ex}(\eta) = \int_{-\infty}^{+\infty} v_{ex}\mathrm{e}^{-\mathrm{j}\eta t}\mathrm{d}t = 4\omega_0\frac{S_0}{S_c}\ell\varepsilon m \underbrace{\int_{-\infty}^{+\infty}\sin(\omega t-\Delta)\mathrm{e}^{-\mathrm{j}\eta t}\mathrm{d}t}_{\frac{1}{2\mathrm{j}}(\delta(\eta-\omega)\mathrm{e}^{-\mathrm{j}\Delta}-\delta(\eta+\omega)\mathrm{e}^{\mathrm{j}\Delta})} \tag{5.60}$$

which leads to:

$$\hat{v}_{ex}(\eta) = -2\omega_0 m \frac{S_0}{S_c} \mathrm{j}\ell\varepsilon[\mathrm{e}^{-\mathrm{j}\Delta}\delta(\eta-\omega) - \mathrm{e}^{\mathrm{j}\Delta}\delta(\eta+\omega)] \tag{5.61}$$

At the excitation frequency $\eta = \omega$, we can then calculate the surface impedance $Z(\omega)$ by:

$$Z(\omega) = -\frac{\hat{p}_{ex}(\omega)}{\hat{v}_{ex}(\omega)} = \frac{\varepsilon\varrho_0 S_c c_0^2 F_0}{V\omega_0} \frac{-\mathrm{j}\mathrm{e}^{\mathrm{j}\Delta}}{2m} \tag{5.62}$$

5.2.4.2 Expression of the surface impedance with MSM

We can write the surface impedance in a simpler form. Indeed, from Eq. (5.45), we obtain:

$$\mathrm{e}^{\mathrm{j}\Delta} = -\frac{4\zeta m}{F_0} + \mathrm{j}\frac{4}{F_0}\left(\frac{8}{3\pi}m^2 + \frac{r_1}{2}m\right) \tag{5.63}$$

We can then write:

$$Z(\omega) = -\frac{S_c\varepsilon\varrho_0 c_0^2}{V\mathrm{j}\omega_0}\left[2\zeta - 2\mathrm{j}\left(r_2\frac{8}{3\pi}m + \frac{r_1}{2}\right)\right] = \frac{S_c\varepsilon\varrho_0 c_0^2}{V\omega_0}\left(r_1 + \frac{16}{3\pi}r_2 m\right) + \mathrm{j}\frac{2S_c\varepsilon\varrho_0 c_0^2}{V\omega_0}\zeta \tag{5.64}$$

After replacing ϵr_1 and $\epsilon\zeta$ by their expressions, we have:

$$Z(\omega) = \frac{S_c c_0^2 R}{V\ell\omega_0^2} + \frac{S_c\varepsilon\varrho_0 c_0^2}{V\omega_0}\frac{16}{3\pi}r_2 m + \mathrm{j}\frac{2S_c\varrho_0 c_0^2}{V\omega_0}\left(\frac{\omega}{\omega_0} - 1\right) \tag{5.65}$$

Introducing $||v||$ the amplitude of v related to m by the relation $||v|| = 4m\omega_0\ell\varepsilon$ and using the relation $\omega_0^2 = S_c c_0^2\phi/(V\ell)$, we finally have:

$$Z(\omega) = \frac{R}{\phi} + \frac{\varrho_0}{\phi}\frac{4}{3\pi}||v|| + \mathrm{j}\frac{2S_c\varrho_0 c_0^2}{V\omega_0}\left(\frac{\omega}{\omega_0} - 1\right) \tag{5.66}$$

The formula is comparable to that given in Eq. (51) in Singh and Rienstra [135] but it is slightly simpler. Near the resonance ($\omega \approx \omega_0$), both formula give the same result. According to Melling, the resistance factor R is defined as $R = \varrho_0 c_0(a + b|v|)$, where a and b values found experimentally, and depend on the velocity [110, 135]. In our case, the coefficient R has been chosen to be kept constant for all regimes, eliminating its the dependency on v. Nevertheless, we note that the real part of the impedance varies linearly with $||v||$, as it is the case for empirical models for perforated plate liners (such as the Guess model). In addition, the imaginary part of the impedance does not depend on the acoustic excitation amplitude. It could also be shown that it corresponds to that obtained by doing a Taylor expansion around ω_0 at the first order of the imaginary part of the exact impedance given in Eq. (1.35).

5.2.5 Comparison with the exact analytical solution in the linear regime

5.2.5.1 Exact relation m-ζ from Rice-Cummings equations

In the linear regime, we can obtain an analytical relation between m and ζ. From equations (1.32a) and (1.32b), we can write:

$$-\frac{V\ell}{S_c c_0^2\phi}(\mathrm{j}\omega)^2 P_{\mathrm{in}} - (\mathrm{j}\omega)\frac{RV}{S_c\varrho_0 c_0^2\phi}P_{\mathrm{in}} = P_{\mathrm{in}} - P_{\mathrm{ex}} \tag{5.67}$$

or equivalently:

$$-\omega^2 P_{\mathrm{in}} + (\mathrm{j}\omega)\omega_R P_{\mathrm{in}} + \omega_0^2 P_{\mathrm{in}} = \omega_0^2 P_{\mathrm{ex}} \tag{5.68}$$

with $\omega_0 = c_0\sqrt{S_c\phi/(V\ell)}$ and $\omega_R = R/(\varrho_0\ell)$.

From this, we deduce:

$$P_{\text{in}} = \frac{\omega_0^2}{\omega_0^2 - \omega^2 + (\mathrm{j}\omega)\omega_R} P_{\text{ex}} \tag{5.69}$$

which gives:

$$|P_{\text{in}}| = \frac{\omega_0^2}{\sqrt{(\omega_0^2 - \omega^2)^2 + \omega^2\omega_R^2}} |P_{\text{ex}}| \tag{5.70}$$

We introduce the normalized variables $y = p_{\text{in}}V/(S_c\varepsilon 2\varrho_0 c_0^2 l'\phi)$ and $F_0 = |P_{\text{ex}}|V/(S_c\varepsilon^2 2\varrho_0 c_0^2 l'\phi)$. With $m = |y|/2$, we obtain:

$$m = \frac{\omega_0^2}{\sqrt{(\omega_0^2 - \omega^2)^2 + \omega^2\omega_R^2}} \frac{\varepsilon F_0}{2} \tag{5.71}$$

Finally, we introduce $\zeta = (\omega/\omega_0 - 1)/\epsilon$ and $r_1 = \omega_R/(\varepsilon\omega_0)$, which allows us to write:

$$m = \frac{1}{\sqrt{\left(1 - \frac{\omega}{\omega_0}\right)^2 \left(1 + \frac{\omega}{\omega_0}\right)^2 + \frac{\omega^2}{\omega_0^2}\frac{\omega_R^2}{\omega_0^2}}} \frac{\varepsilon F_0}{2} = \frac{1}{\sqrt{\varepsilon^2\zeta^2\left(2 + \epsilon\zeta\right)^2 + \varepsilon^2 r_1^2(1 + \varepsilon\zeta)^2}} \frac{\varepsilon F_0}{2} \tag{5.72}$$

which finally leads to:

$$m = \frac{1}{\sqrt{\zeta^2\left(1 + \varepsilon\frac{\zeta}{2}\right)^2 + \frac{r_1^2}{4}(1 + \varepsilon\zeta)^2}} \frac{F_0}{4} \tag{5.73}$$

5.2.5.2 Analytical relation m-ζ with MSM

Using the multiple scales method, we obtain the relationship between m and ζ:

$$\zeta^2 m^2 + \frac{64}{9\pi^2} m^4 + \frac{8}{3\pi} r_1 m^3 + \frac{r_1^2}{4} m^2 - \frac{F_0^2}{16} = 0 \tag{5.74}$$

In the linear approach, m is proportional to F_0 (the pressure on the plate on the cavity side is proportional to the excitation pressure). From the normalized amplitude $m_n = m/F_0$, we can write the relation as:

$$\zeta^2 m_n^2 F_0^2 + \frac{64}{9\pi^2} m_n^4 F_0^4 + \frac{8}{3\pi} r_1 m_n^3 F_0^3 + \frac{r_1^2}{4} m_n^2 F_0^2 - \frac{F_0^2}{16} = 0 \tag{5.75}$$

Dividing the previous equation by F_0^2 and then taking the limit as $F_0 \to 0$ to remain in the linear regime, we obtain:

$$\zeta^2 m_n^2 + \frac{r_1^2}{4} m_n^2 - \frac{1}{16} = 0 \tag{5.76}$$

From this, we deduce:

$$m = \frac{1}{\sqrt{\zeta^2 + \frac{r_1^2}{4}}} \frac{F_0}{4} \tag{5.77}$$

Comparing this with the exact linear solution given by equation (5.73), we note that the multiple scales approach is valid if $|\varepsilon\zeta| \ll 1$, meaning for $|\omega/\omega_0 - 1| \ll 1$.

5.2.5.3 Comparison of the relation m-ζ from the two approaches

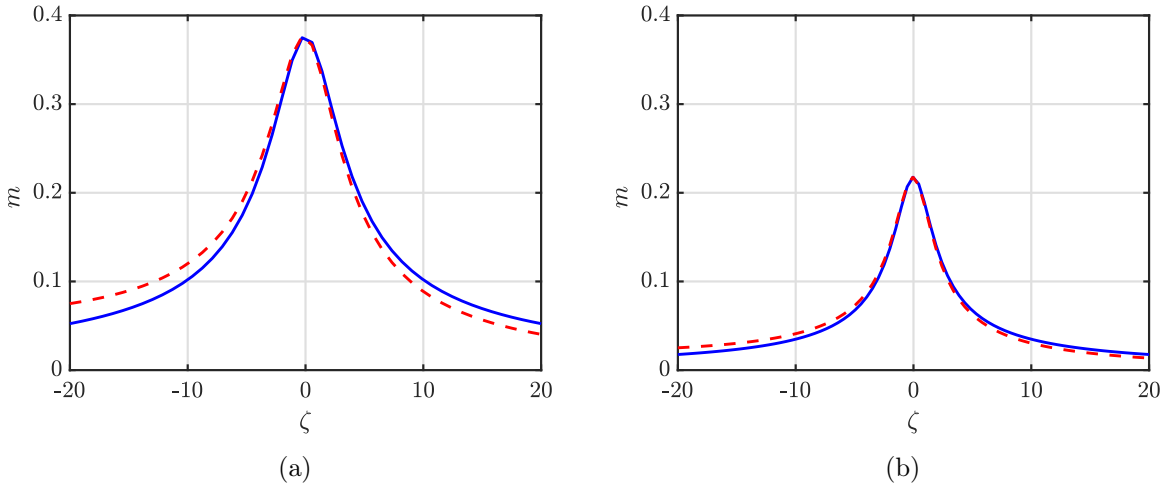

Figure 5.2: Reduced amplitude of the pressure m as a function of the reduced frequency ζ obtained with - - - the exact solution of the Rice-Cummings model in the linear regime (85 dB) and — its approximation with the multiple scale approach for a plate with (a) one single perforation and (b) three perforations

Figure 5.2 presents the evolution of the reduced pressure amplitude m as a function of the reduced frequency ζ obtained from the exact analytical solution and from the multiple scale approach in linear regime. Two plates are considered with one and three perforations. It is noted that in both cases the two approaches perfectly match at resonance ($\zeta = 0$), which is expected from the multiple scale approach. When $|\zeta| \gg 1$, the two approaches slightly differ. This validation allows us to proceed with the presentation of the results.

5.3 Results

In this section, the model presented in Section 5.2 is applied to perforated plates and compared with experiments on such plates in impedance tube. In particular, a first application is made to a single perforation plate in Section 5.3.1 and to a multi perforated plate in Section 5.3.2. The impedance formulation introduced in eq.(5.62) is found for a Helmholtz resonator. In this part, the objective is to assess the validity of this theory to a perforated plate. For such materials, it is possible to define a POA or perforation ratio ϕ, as defined in Section 1.2, that in application to Figure 5.1 can be defined as:

$$\phi = \frac{n_p S_p}{S_c} \tag{5.78}$$

with n_p the number of perforations in the plate, S_p the surface of each perforation, and S_c the surface of the cavity. If the perforations are well distanced and no interaction is present between them, it is possible to consider a parallel model. Here, the perforated plate is a sum of simple resonators with one perforation and a reduced volume V' defined as:

$$V' = \frac{V}{n_p} \tag{5.79}$$

In other words, under these hypotheses, it is possible to consider the described model by using:

$$S'_c = \frac{S_c}{n_p} \tag{5.80}$$

Experimentally, the plates have been tested at different acoustic pressure levels. The iterative procedure explained in Section 2.20 has been adopted in reference to the global level SPL_g at the plate, which in the model is noted as p_{ex}. An harmonic excitation is employed. Four different SPL have been considered, starting from a linear acoustic regime at 85 dB to a nonlinear evolution at 112 dB, 125.3 dB and 130 dB. In the MSM approach, ε should remain small for all the regimes considered in order to remain in the hypothesis of applicability of the method. For the case considered, it is arbitrarily set to $\varepsilon = 0.03$. Finally, the resistance factor R has been set to $R = 1.5$ in order to obtain a good fit of the absorption coefficient in the linear case for all the plates considered. This parameter leads to a real part of impedance value that is near to the values found in the Guess model, that stand in a range from 0.2 to 2.

5.3.1 Plate with a single perforation

A perforated plate with a single perforation backed up by an air cavity corresponds to a Helmholtz resonator. The plate considered is depicted in Fig. 5.3. In this case, according to Eq.(5.80) the effective surface is equal to the total surface of the plate. The circular plate presents a perforation radius of 1 mm and a perforation neck length of 1 mm. The length of the cavity is 30 mm and the diameter of the cavity is 29 mm.

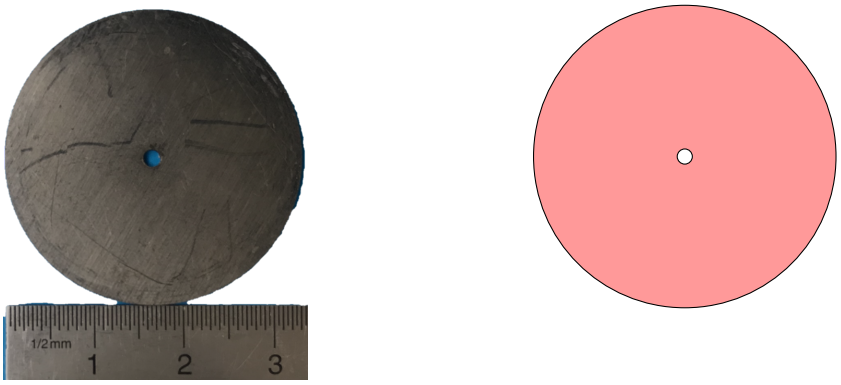

Figure 5.3: Plate with a single perforation used in the experiments and corresponding sketch.

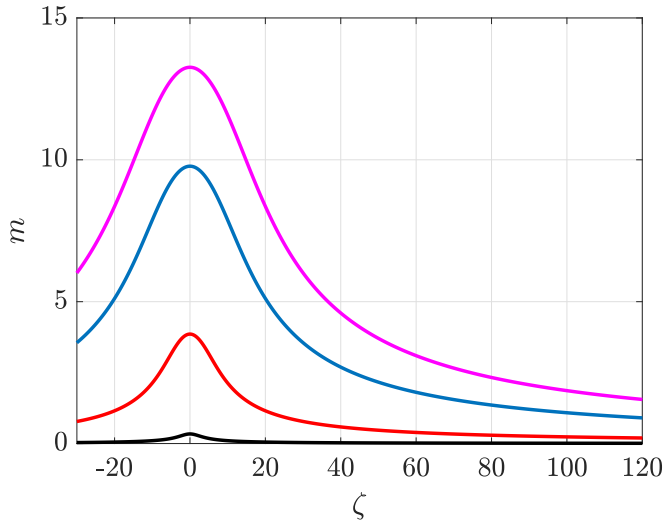

Figure 5.4: m as a function of ζ for different SPL: — 85 dB, — 112 dB, — 125.3 dB, and —130 dB

Figure 5.4 shows m as a function of ζ, for the single-perforation plate at several nonlinear acoustic levels. It was shown in Sec. 5.2.5 that the MSM solution is accurate around the peak (ζ=0) and that m increases proportionally to the pressure amplitude on the plate in the linear regime. We observe that m increases also with the pressure amplitude in the nonlinear regime, but not in a proportional way. Thus, from 125.3 dB to 130 dB, the pressure amplitude increases by a factor of 1.7, while the peak value of m increases by a factor of 1.4.

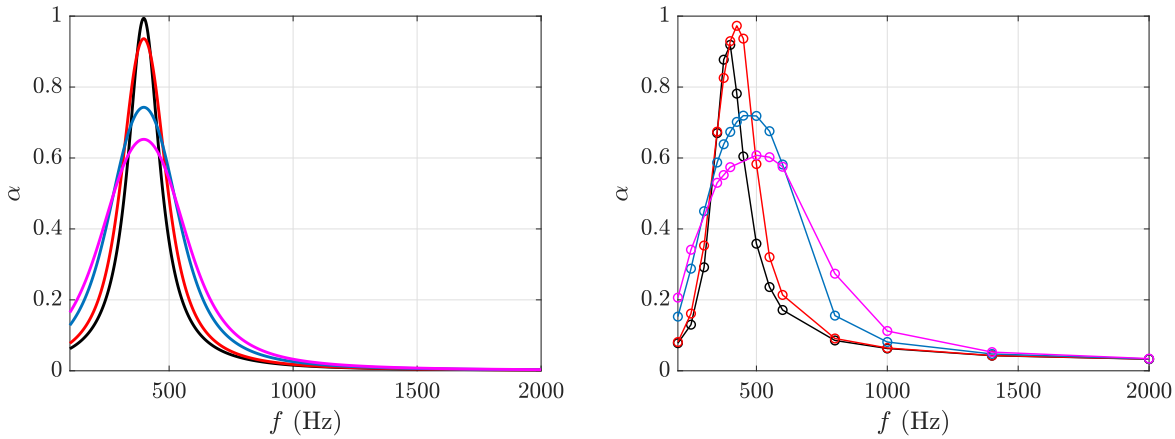

Figure 5.5: Absorption coefficient behaviour at different SPL —85 dB, —112 dB, —125.3 dB and —130 dB in (a) analytical and (b) Experimental case

We now investigate the acoustic properties of the plate, following the results presented in Chapter 4. Figure 5.5(a) shows the absorption coefficient found with the MSM methods at the SPL considered. We note that the general behaviour is well respected in comparison to the experimental values in Figure 5.5(b). Starting at a linear regime of 85 dB at which the plate is almost fully absorbent, a coherent widening of the peak is observed in both cases. As predicted, the resonance frequency does not shift in the analytical approach since the corrected length does not take into account the effect of v and because of the absence of quadratic and cubic terms in p_{in}. The fact that the widening is less consistent in the analytical case is due to the fact that the solution is, for hypothesis of the analytical calculation, precise near resonance, and since the nonlinear values presents a larger peak, the correctness of the solution is less precise but still acceptable as far as we get away from resonance. The shift in peak frequency observable in nonlinear regime is given by the Fourier development from equation (5.30) of the nonlinear damping term of equation (5.14).

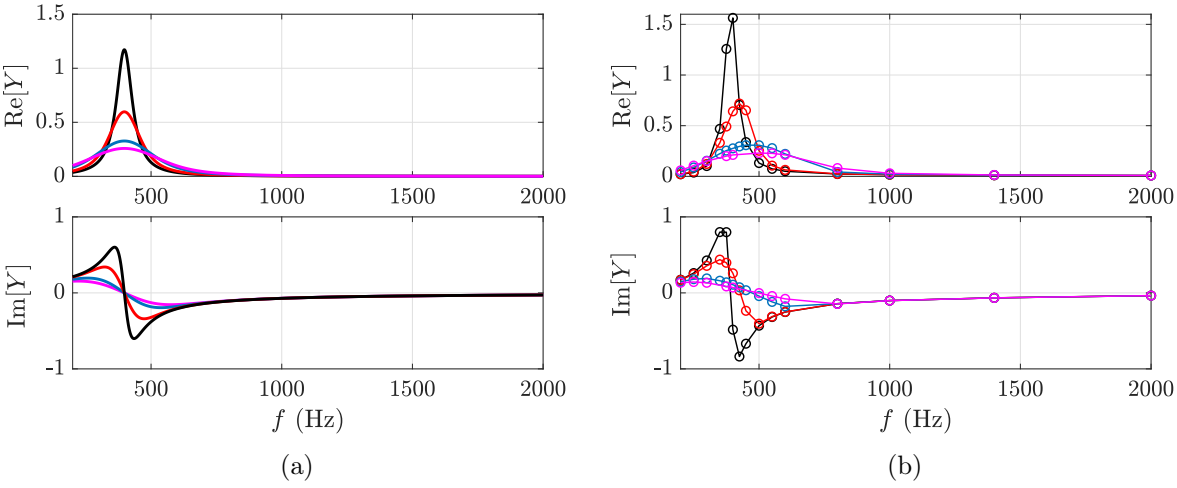

Figure 5.6: Admittance behaviour at different SPL —85 dB, —112 dB, —125.3 dB and —130 dB in (a) analytical and (b) Experimental case

Figure 5.6 shows the surface admittance of the plate. The experimental admittance variations with increasing global SPL in Figure 5.6(b) resemble those discussed in Chapter 4. Specifically, the amplitude

of both the real and imaginary components of Y decreases, while the peak of the real part becomes broader as the incident SPL increases. Analytical results for surface admittance are also shown in Figure 5.6(a). Although not identical to the measured data, they exhibit a close correspondence, particularly in capturing the trend of admittance changes with varying incident SPL.

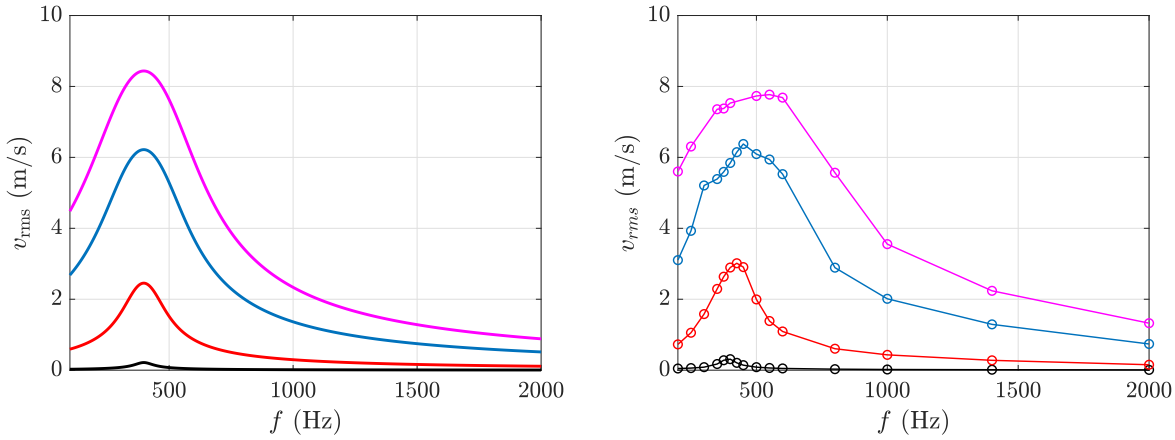

Figure 5.7: Perforation velocity at different SPL —85 dB, —112 dB, —125.3 dB and —130 dB in (a) analytical and (b) Experimental case

Figure 5.7 shows the trend of the rms velocity inside the perforation u_{rms}. In particular, analytically this velocity is derived as:

$$v_{\text{rms}} = \frac{||v||}{\sqrt{2}} = \frac{4}{\sqrt{2}} m\omega\ell\varepsilon \tag{5.81}$$

in order to be compared to the experimental rms velocity v_{rms} measured in impedance tube. For a linear case, it is consistently observed that the velocity value is approximately zero, and that for higher SPL it increases, making the effects of nonlinear damping negligible. Compared to the results found experimentally, it is observed that the values obtained analytically are similar, even slightly higher. This results in an overestimation of the viscous and jet effects developing in the cavity. However, this fact is consistent with the absorption levels found analytically, which for the same value seem to correspond to weaker experimental acoustic levels.

5.3.1.1 Comparison between approaches

In this section, a comparison is made between the results obtained with the nonlinear dynamics analytical approach, the experimental and the semi-analytical approach of the Guess surface impedance model, introduced in Chapter 1. A comparison with the numerical Rice-Cummings approach is also presented, being the direct resolution of the baseline equations employed in the dissertation of this chapter. The numerical simulation derives from a standard Runge-Kutta scheme implemented in a FDTD simulation. For the Guess model, the rms velocity values derived from a controlled measurement on the global SPL_{g} are considered for consistency with the other two cases.

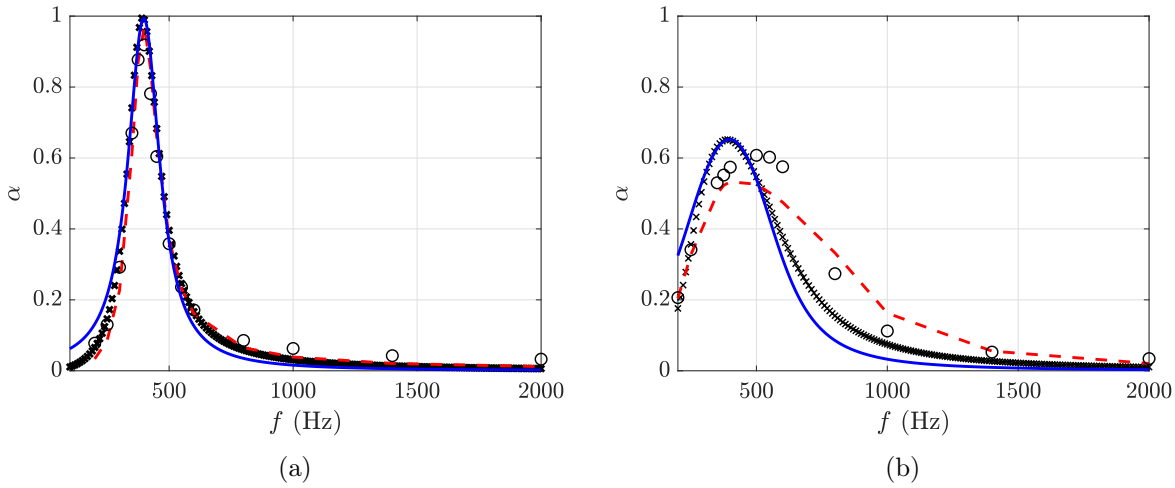

Figure 5.8: Comparison of the absorption coefficient in analytical MSM (—), experimental (○), numerical Cummings (X), and semi-analytical Guess (- - -) at (a) 85 dB (b) 130 dB

Figure 5.8 compares the absorption coefficient for a linear case at 85 dB and for a nonlinear case at 130 dB. For the linear case, the three approaches agree, showing similar results for resonance frequency, peak width and absorption rate. For the nonlinear case, it can be seen that the Guess model is more aligned with the resonance peak to the experimental case, but underestimates plaque absorption. The experimental case appears to fall somewhere between the analytical and semi-analytical approaches. In addition, there is more consistency between the three approaches in the area at frequencies below resonance, whereas for higher frequencies there are lower values for the analytical model and a flattening of the curve for the semi-analytical approach. The Rice-Cummings predictions reveals exact in the linear case, while in the nonlinear case the exact match is obtained at resonance, in accordance to the hypothesis of the model. Nevertheless, the model manages to correctly reproduce the behaviour of the absorption. No shift of frequency is observed when introducing the nonlinear regime, consistent to what observed for the Rice-Cummings TL prediction in Chapter 4.

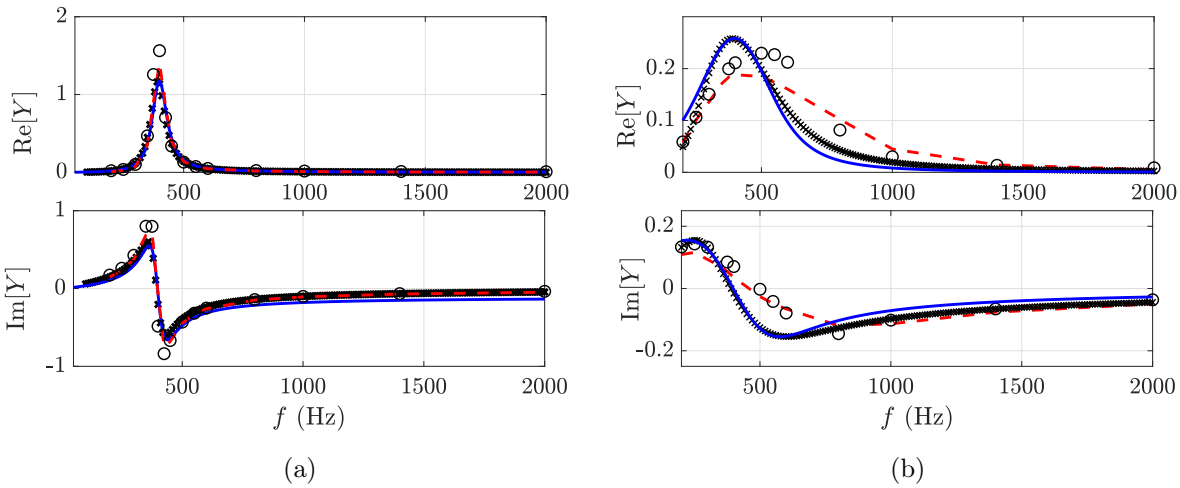

Figure 5.9: Comparison of the admittance in analytical MSM (—), experimental (○), numerical Cummings (X), and semi-analytical Guess (- - -) at (a) 85 dB (b) 130 dB

A comparison of the admittance values for a linear and nonlinear case is presented in Figure 5.9. Similarly to what was observed for absorption, the comparison between the models in the linear case

turns out to be more accurate, with an underestimation of the peak of the real part of the admittance for both the analytical and the semi-analytical model. With regard to the nonlinear case, it can be seen that for the imaginary part, the analytical model is underestimated over the entire frequency spectrum compared to the semi-analytical model, which finds good agreement with the experimental. As far as the real part is concerned, the peak value is more consistent between the experimental and the analytical, while in terms of peak width the semi-analytical model seems to reflect the experimental better. Also for this property, the experimental case lies somewhere between the analytical and the semi-analytical model. Once again, the Rice-Cummings model is close to the other predictions, and has an exact value to the multiple scale approach at resonance.

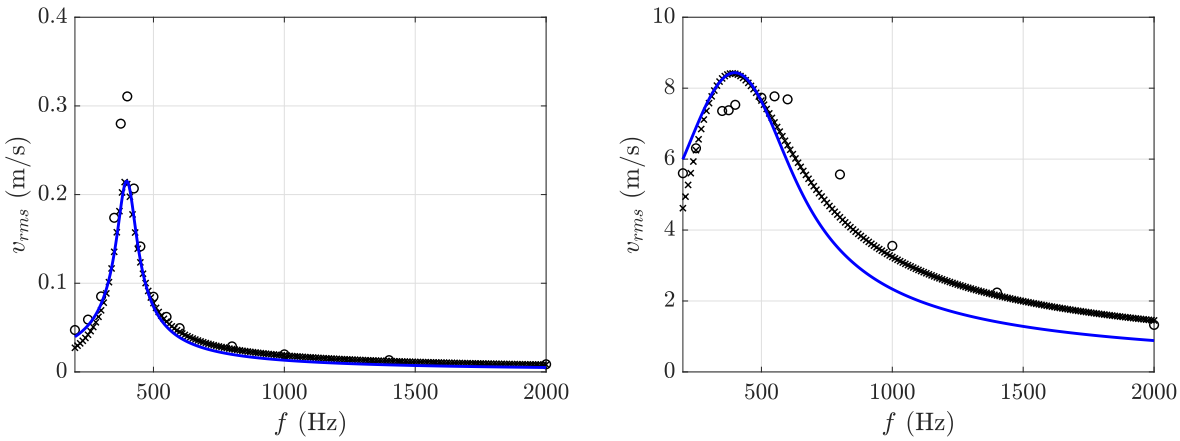

Figure 5.10: Comparison of the rms acoustic velocity in analytical MSM (—), experimental (○), numerical Cummings (X), and semi-analytical Guess (- - -) at (a) 85 dB (b) 130 dB

Figure 5.10 presents the comparison of the rms acoustic velocity. The Rice-Cummings approach is consistent with the MSM in linear case, and in nonlinear case in exact at resonance. The general behaviour is respected, but this approach tends to overestimate the evolution of the velocity compared to experimental.

5.3.2 Extension to a multiperforated plate

In this paragraph, we consider the perforated plate shown in Figure 5.11, which is the plate considered in Chapter 4.

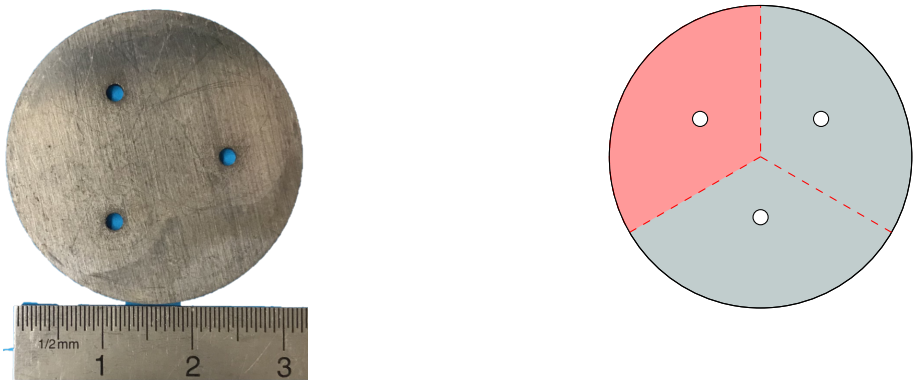

Figure 5.11: Three perforations plate in experiments and in sketch

The plate has three perforations of radius r =1 mm, perforation neck length of 1 mm and a POA of $\phi = 1.42\%$. As the perforations are sufficiently spaced to have no interaction effects between them, the plate can be considered as three symmetrical parts. Following equation (5.80), this case is equivalent to considering a one-perforation plate in an area of one third of the total area. Also for this case, experimental results from impedance tube tests are considered. The air gap back to plate is always 30 mm and the cavity diameter of 29 mm.

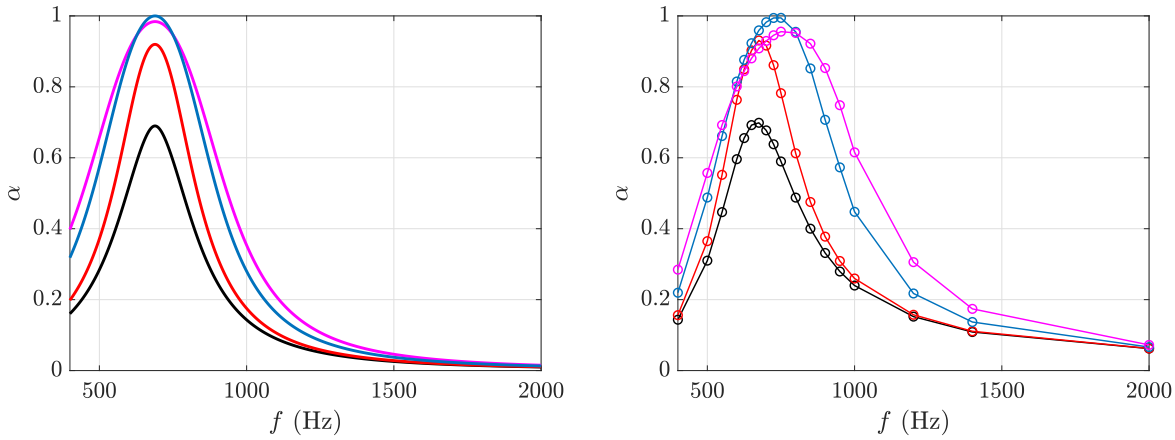

Figure 5.12: Absorption coefficient behaviour at different SPL in (a) analytical and (b) Experimental case: —85 dB, —112 dB, —125.3 dB and —130 dB

Figure 5.12 shows the absorption coefficient of the plate. In the linear case, the analytical model correctly predicts the resonance frequency, height and width of the absorption peak. The nonlinear behaviour is also correctly observed, with a slight underestimation of peak values and a no-shift in frequency for higher SPL levels, as expected.

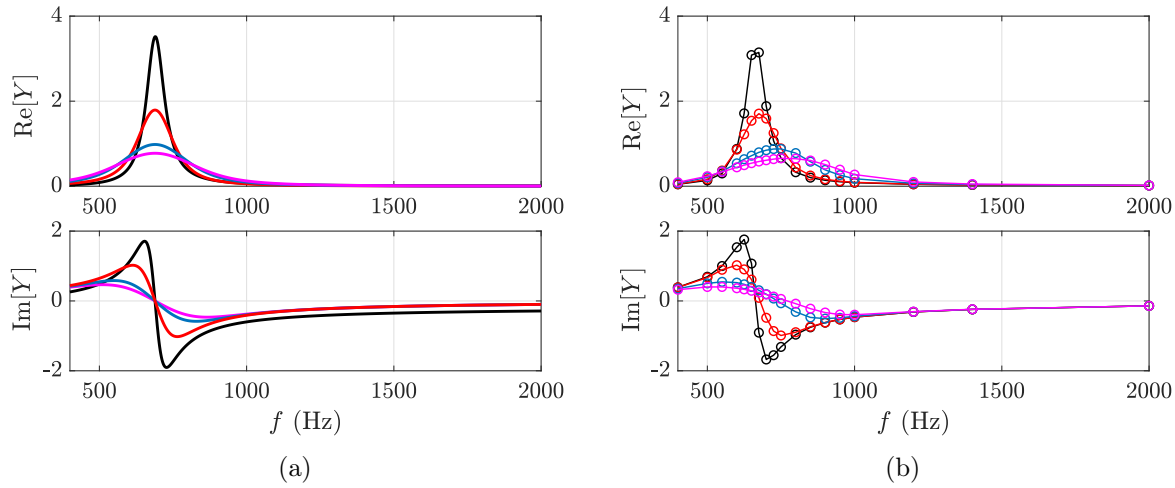

Figure 5.13: Admittance behaviour at different SPL in (a) analytical and (b) Experimental case: —85 dB, —112 dB, —125.3 dB and —130 dB

In Figure 5.13, the behaviour of the admittance is considered. Again, a correct prediction is noted for the linear case and also for the nonlinear case, with a slight underestimation of the resonance frequency in the analytical model.

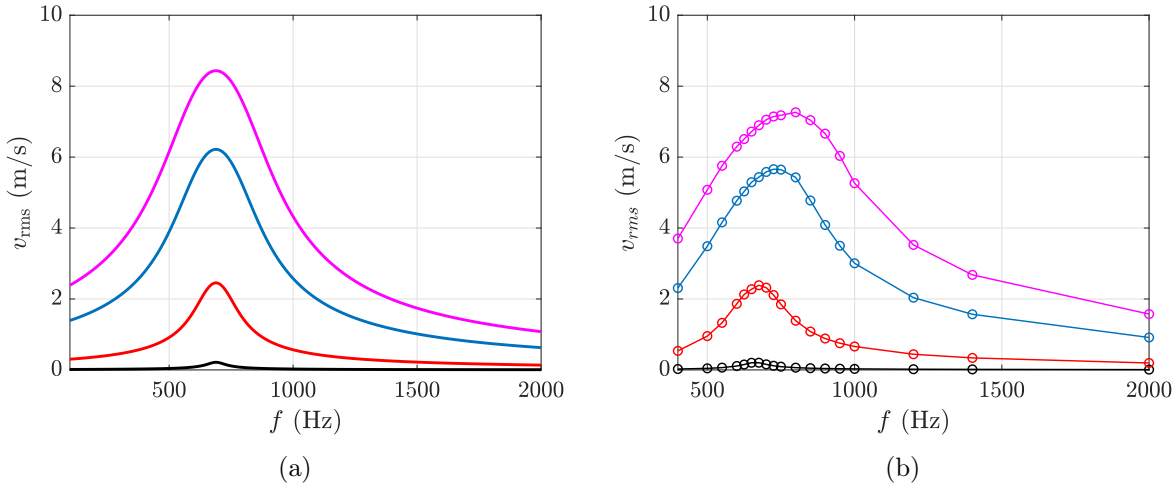

Figure 5.14: Perforation velocity at different SPL in (a) analytical and (b) Experimental case: —85 dB, —112 dB, —125.3 dB and —130 dB

As shown in Figure 5.14, the general evolution of the perforation velocity is correctly predicted, with a slight overestimation in nonlinear regimes, consistent with what has also been observed in the case of a single perforation.

The extension of the nonlinear dynamics approach to a multiperforated plate appears to be effective and to respect the values obtained experimentally.

5.3.2.1 Comparison between approaches

The comparison between the analytical approach, the experimental data, the semi-analytical approach (Guess's surface impedance model) and the numerical Rice-Cummings approach reveals varying degrees

of agreement.

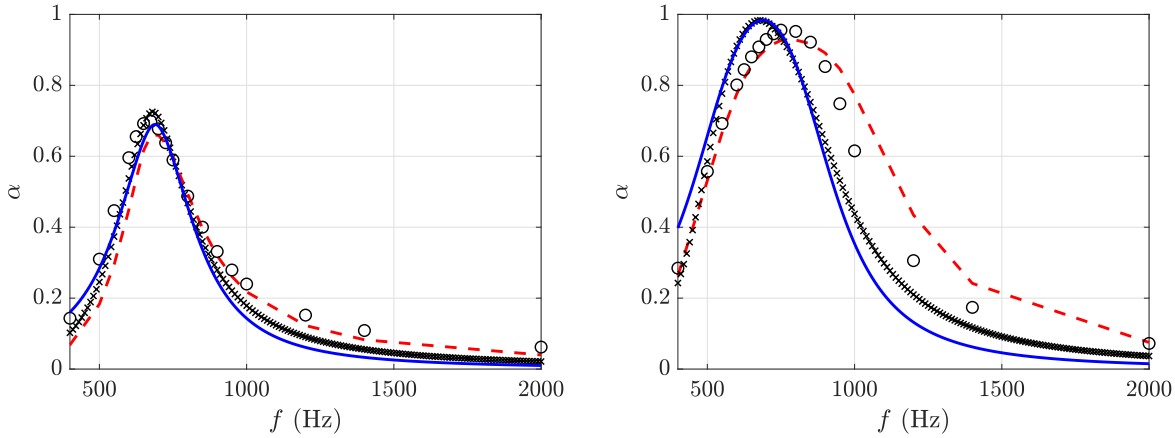

Figure 5.15: Comparison of the absorption coefficient in analytical MSM (—), experimental (○), numerical Cummings (X), and semi-analytical Guess (- - -) at (a) 85 dB (b) 130 dB

Considering the absorption coefficient (Figure 5.15), in the linear case (85 dB), the three methods show consistency in terms of resonance frequency, peak width, and absorption rate. In the nonlinear case (130 dB), Guess's model aligns more closely with the resonance peak compared to the experimental data and the plate's absorption values. However, even in this case, the experimental results fall in an intermediate position between the analytical and semi-analytical approaches. Greater consistency is observed among experimental and analytical at frequencies below resonance, whereas at higher frequencies, the semi-analytical approach aligns better with the experimental values, and the semi-analytical model exhibits curve flattening. The Rice-Cummings model predicts an evolution close to the MSM, as observed for the previous plate. An exact correspondence between the two approaches is observed at resonance.

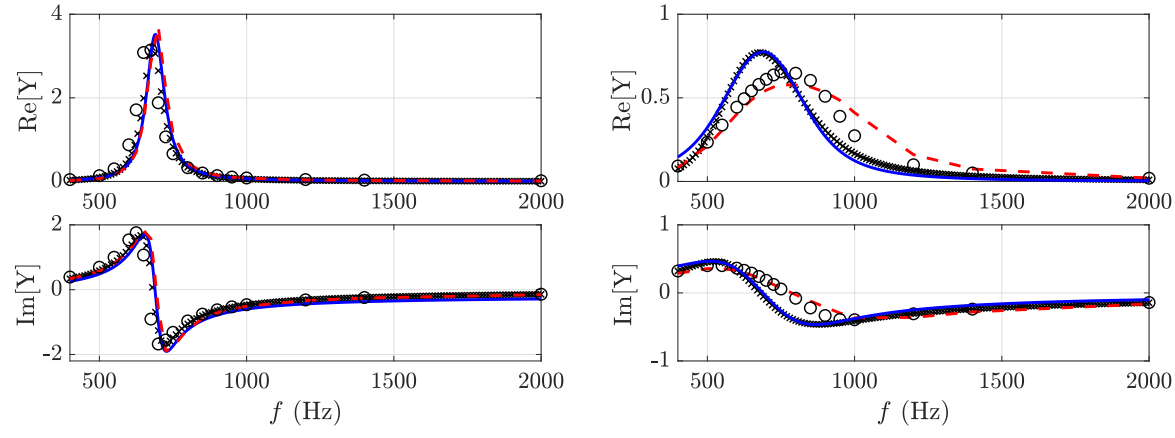

Figure 5.16: Comparison of the admittance in analytical MSM (—), experimental (○), numerical Cummings (X), and semi-analytical Guess (- - -) at (a) 85 dB (b) 130 dB

As shown in Figure 5.16, an analysis of admittance reinforces the previous observations. In the linear case, both models slightly overestimate the peak frequency of the real part of admittance. In the nonlinear case, the analytical model underestimates the imaginary part over the resonance frequency, while the semi-

analytical model shows good agreement with the experimental data. For the real part, the peak value is more consistent between the experimental and semi-analytical results, but the analytical model better reflects the peak's width. Once again, the experimental data occupy an intermediate position between the analytical and semi-analytical models. The Rice-Cummings approach reveals to correctly predict the behaviour of the impedance, with exact correspondence to the MSM at resonance.

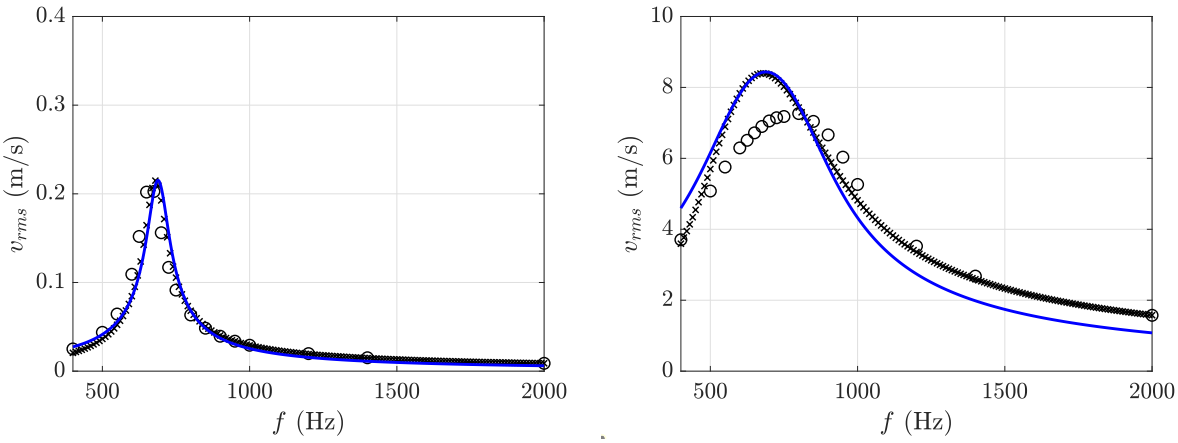

Figure 5.17: Comparison of the rms acoustic velocity in analytical MSM (—), experimental (○), numerical Cummings (X), and semi-analytical Guess (- - -) at (a) 85 dB (b) 130 dB

Finally, Figure 5.17 illustrates the comparison of the rms acoustic velocity. At linear regime, the three approaches are coincident. The Rice-Cummings method aligns with the MSM in the linear case and matches exactly at resonance in the nonlinear case. While the overall trend is maintained, this approach tends to over predict the velocity evolution compared to experimental data. Additionally, no frequency shift is observed when nonlinearities are introduced.

5.4 Conclusion

This chapter focused on the nonlinear dynamics of perforated plates. By employing the multiple scales method (MSM), a robust analytical approach was developed to systematically account for nonlinear damping effects such as jet formation, vortex shedding, and viscous losses. These effects, which become dominant at higher sound pressure levels, significantly alter the acoustic behaviour of perforated plates, necessitating extensions to classical models.

The nonlinear dynamics approach derived in this study offered valuable insights into the interaction between linear and nonlinear mechanisms, especially near resonance. The governing equations captured key phenomena such as peak broadening and the influence of damping on acoustic indicators like absorption performance. When applied to single and multi-perforated plate configurations, the model demonstrated its versatility and applicability across varying porosity and acoustic regimes.

In the linear regime (85 dB), the analytical predictions closely matched experimental results, accurately describing resonance frequency, peak width, and absorption coefficients. This agreement validates the assumptions and mathematical formulation underlying the proposed model. In the nonlinear regime (up to 130 dB), where complex phenomena dominate, the analytical model revealed good predictions even presenting some limitations, notably a slightly underestimation of nonlinear damping effects. These discrepancies highlight the inherent challenges of analytically modeling nonlinear behaviour while maintaining computational simplicity. The fact of not considering the corrected length ℓ and the parameter R

as dependant on acoustic velocity v implied a no-shift in resonance frequency in nonlinear regime, which is a limitation of the actual model. Gourdon, Vargas et al. [4] also introduce a quadratic and cubic terms for higher level of excitation to take into account the frequency shift, consideration that can be added in the present study. According to Cummings [44], the equivalent length can also be time-dependent, bringing to a more complex and accurate prediction. This definition, with the implementation of an SPL-dependent corrected length and R, can represent an ulterior starting point for an improvement of the actual model.

The extension of the nonlinear dynamics approach to multi-perforated plates further demonstrated its robustness. By treating the perforations as independent resonators and incorporating the perforation ratio, the model successfully describes the acoustic behaviour of multi-perforated plates in both linear and nonlinear regimes. Despite minor deviations in high-intensity cases, the predictions remain consistent with experimental trends, demonstrating the potential of the approach for applications involving complex geometries. The present analytical approximation is much quicker to calculate for real-time simulations than numerical simulations.

A comparison with the semi-analytical Guess impedance model provided additional validation and context. While the Guess model aligned more closely with experimental data for certain resonance peaks, particularly in the nonlinear regime, the analytical approach offered a deeper understanding of the underlying physical processes. The ability to dissect and quantify linear and nonlinear contributions, while extending the method to multi-perforated systems, marks a significant advancement in the modeling of nonlinear dynamics applied to perforated plates.

In conclusion, this study presents a comprehensive and versatile analytical approach for understanding and modeling the nonlinear dynamics of perforated plates. By systematically incorporating nonlinear effects and validating the model against experimental data, this research bridges the gap between theoretical precision and practical applicability. In the present model, we only derive the first order y_0. The analytical approximation could be anyway improved by considering higher orders of ε scale (on terms $y_1, y_2, y_3 .... \varepsilon^2, \varepsilon^3$) and by considering more terms in the Fourier developments in the dissertation. The comparative analysis with established methods, such as the Guess impedance model, underscores the versatility and innovation of the proposed approach. These findings lay a solid foundation for optimising the design of perforated plates and liners, particularly for applications requiring enhanced performance under high acoustic level conditions.

6 Study of the acoustic behaviours of an improved perforated plate liner

Contents

Abstract

This chapter focuses on the development of an acoustic liner by refining its impedance properties to improve sound attenuation under flow and nonlinear regimes. While traditional models like the Cremer-Tester approach offer a theoretical basis for impedance calculations, they often assume ideal conditions that fail to reflect real-world complexities, especially in ducts under flow and nonlinear behaviours. To overcome these challenges, this study introduces an improved impedance conception method using a multimodal approach. By systematically examining resistance and reactance variations, it develops an accurate impedance map for better noise reduction. The chapter combines experimental observations with numerical simulations to improve impedance characterisation. A redesigned liner is introduced to assess the impact of material properties, perforation rate, and structural configuration on acoustic absorption. The study also emphasizes assembly techniques to reduce leakage and maintain consistent performance. Furthermore, it seeks to clarify the distinct effects of acoustic nonlinearities and of the flow, which were not always visible for the reference liner studied in Chapter 4.

6.1 Improved plate development

This section presents the optimisation process for the design and development of a new efficient liner in the nonlinear acoustic regime and in the presence of flow. Beginning with the presentation of an optimal impedance for an infinite and a finite duct, we proceed with the explanation of the realisation process of such a liner, to subsequently study its acoustic behaviour and validate the optimisation process.

6.1.1 The Cremer-Tester optimal impedance

One of the most established approaches to identify an optimal liner impedance is the one proposed by Cremer [41], who introduces an impedance expression for an infinite rectangular duct without flow based on its geometric characteristics and excitation frequency. The calculation is based on the idea that there is a mode that attenuates less than the others. In doing so, the amplitudes of the other modes become insignificant at a given distance from the acoustic source, leaving only the considered mode present in the vein. At this point, the treatment related to the less-damped mode is the only one that induces sound reduction. This assumption holds true in the low-frequency region, where the higher modes become insignificant and just a few modes propagate in the vein. The optimal Cremer impedance is calculated from the frequency f, the duct height L_y and the sound speed c_0 as:

$$Z_C = (0.91 - 0.76\mathrm{j})\frac{2L_y f}{c_0} \tag{6.1}$$

Cremer's formulation is later generalised by Tester [147], adding the presence of a mean uniform flow in the treated duct:

$$Z_T = \frac{1}{(1+M)^2}(0.929 - 0.747\mathrm{j})\frac{2L_y f}{c_0} \tag{6.2}$$

Abom [3] revisited the impedance taking into account the applicable boundary conditions within the low-frequency limit, showing the margin for improvement and accuracy that can be applied to the model. However, given the validity and simplicity of the conditions, the Cremer-Tester theory can be applied to predict an optimal characterisation of sound reduction in a duct.

6.1.2 Multimodal impedance calculation

In this section, the procedure for obtaining an improved impedance in the case of a finite length liner with and without flow is presented, employing the multi-modal approach presented in Section 3.1.

Firstly, we define the geometrical characteristics of the ideal duct recalling those of the Caiman bench, where L_x=0.07 m and L_y=0.11 m and the length of the treated region is L_z=0.3 m (see Figure 3.1). For the multi-mode study, l=15 and m=15 are considered. A cartography is then produced of TL as a function of the resistance and reactance of the treated section, varying the resistance values in the range $[-2; 2]$ and the reactance the range $[-3; 3]$ for each frequency considered. For each value pair, a TL value is obtained, following the procedure of Sellen [131].

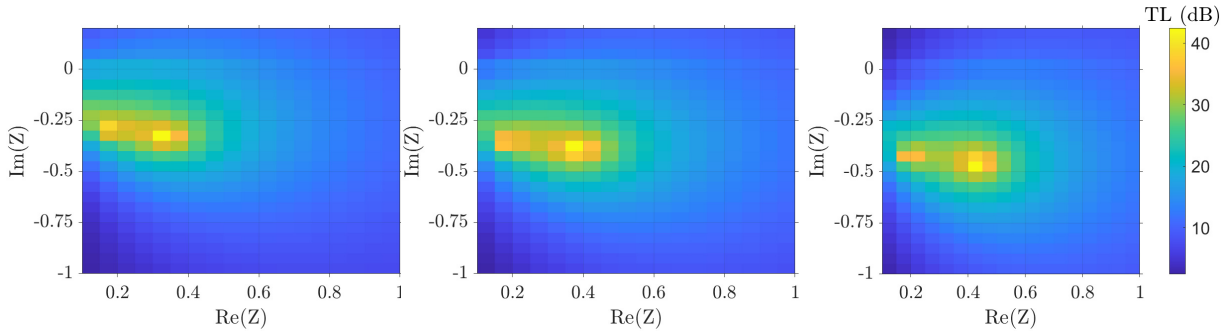

(a) $f = 700$ Hz (b) $f = 800$ Hz (c) $f = 900$ Hz

Figure 6.1: Cartography of TL as a function of the resistance and reactance at a different frequencies from multi-modal approach

Examples of such a mapping are presented in Figure 6.1. Three frequencies close to resonance are presented, showing how for each case the TL maximum is concentrated at a specific value and gradually decreases as we move away from these values. It can be seen how the peak tends to increase in resistance and decrease in reactance as the frequency considered increases. Once the calculation has been performed for the entire frequency spectrum considered, two impedance curves are obtained at M=0 and M=0.1 for the maximum of TL at each frequency.

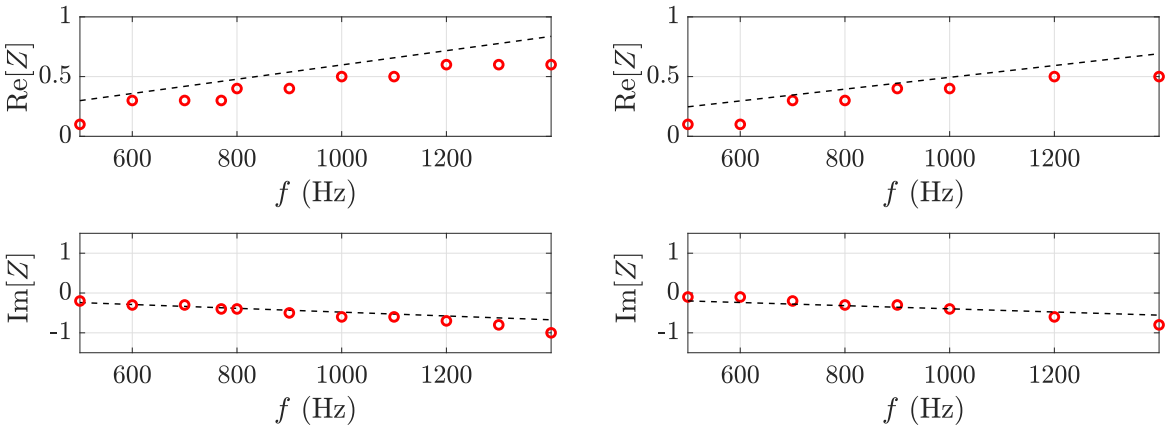

(a) (b)

Figure 6.2: Comparison between the multimodal approach impedance (○) and the Cremer-Tester optimal impedance (- - -) at (a) M = 0 and (b) M = 0.1

Figure 6.2 shows the evolution of the multi-modal impedance compared to the case of optimal impedance in an infinite long liner. It is noted how the two approaches show a substantial coincidence in reactance and how the resistance in the finite case is slightly lower than in the infinite case, showing an ideal treatment behaviour at a weaker resistance. It is also evident that for the case at M = 0.1 the resistance values are slightly lower than for the case without flow, indicating the influence of flow on the optimal performance of the liner. These values are taken as a target for the study of a new liner with high absorption performance under flow and nonlinear regime. The impedance imposed on the wall is assumed to be uniform. There is no change along the liner, which is not true in the cases observed from numerical simulation.

6.1.3 Comparison between multimodal and reference liner impedances

Before proceeding to the design of a new liner, a comparison is made of the optimum Tester impedance with the one calculated for the liner described in Chapter 4. For this liner, the maximum TL value was found for the linear, no-flow case at 92 dB. The nonlinear acoustic effect was found to be a lowering of the TL peak and a shift towards higher frequencies, as shown in the 130 dB case. The effect of flow was found to be predominant over the nonlinear effect in all cases, where the TL curve was significantly flattened compared to the case without flow.

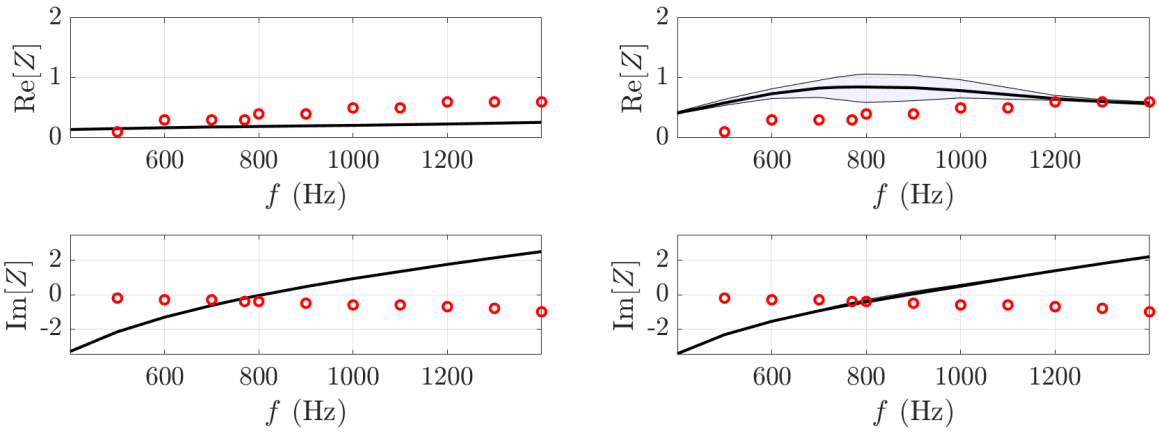

(a) 92dB

(b) 130dB

Figure 6.3: Comparison between the multimodal optimal impedance (○) and the numerical impedance (—) as a function of the frequency with relative error at M = 0 at (a) 92 dB and (b) 130 dB for the liner presented in Chapter 4

A comparison of the impedance in the linear and nonlinear regime without flow is presented in Figure 6.3. It can be seen that at resonance values, approximately 790 Hz, the resistance of the liner in the linear case is close to the optimum resistance. As far as the nonlinear regime is concerned, a broader peak at the resonance value of 820 Hz can be seen. This is higher slightly more detached in comparison to the optimal impedance. As far as the reactance is concerned, it can be seen that the intercept of the two curves is at the TL peak, i.e. at the liner resonance. In the nonlinear case, it can be seen that this is shifted towards the other frequencies. These two facts have a direct influence on the behaviour of TL: the value of the resistance close to the optimum one suggests an increase in the liner's efficiency in terms of TL. The intercept between the two reactance curves shows us the frequency value at the peak of TL.

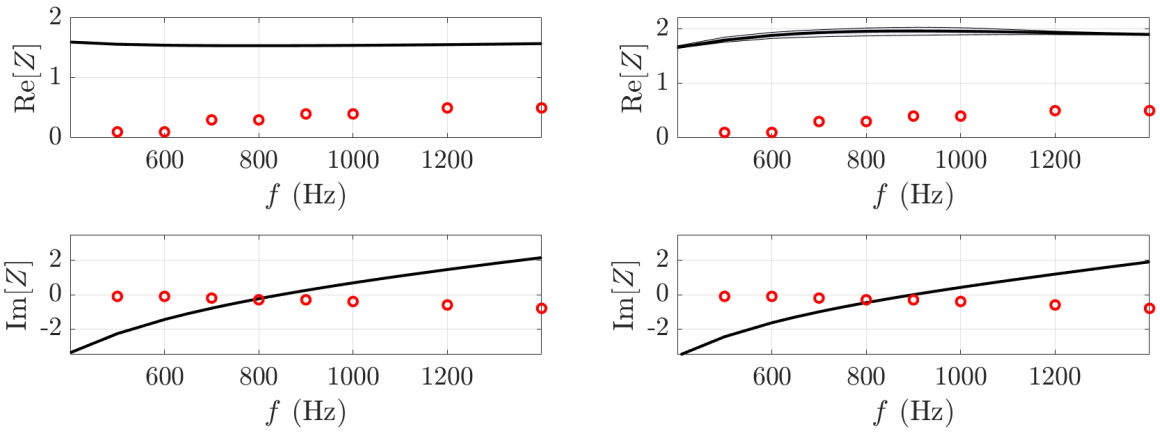

(a) 92dB (b) 130dB

Figure 6.4: Comparison between the multimodal optimal impedance (○) and the numerical impedance (—) as a function of the frequency with relative error at M = 0.1 at (a) 92 dB and (b) 130 dB for the liner presented in Chapter 4

When considering the case with flow at M = 0.1, as shown in Figure 6.4, it can be seen how the resistance values for both regimes deviate considerably from that of the optimum resistance. As far as the reactance is concerned, similar considerations can be made to those for the case without flow. For the resistance, it can be seen how an increasingly higher discrepancy from the optimum values results in an increasingly lower TL. The behaviour of the reference liner and, in particular, the poor performance with flow can be explained by the distance induced from the optimum values of resistance and reactance.

In light of these behaviours, we now concentrate on the study of a new liner with a resistance in the mainly nonlinear cases without flow and also with flow as close as possible to the optimum Tester's values, that should allow to observe improved performances with flow and nonlinearities.

6.1.4 Improved plate design and implementation

The aim of the following section is to design and then produce a liner with impedances close to the multimodal optimum found previously. In order to ensure consistency with previous studies and enable a direct comparison with the liner analyzed in Chapter 4, the perforated plate dimension and honeycomb structure are maintained unchanged. The perforation diameter remains constant to preserve the propagation within the liner and sustain the previously observed jet phenomena. Even the thickness of the perforation and of the cavity is kept the same in order to have the same phenomena. The only parameter left to change is the POA. Increasing the perforation rate reduces the spacing between perforations, potentially amplifying interaction effects among them. Additionally, the honeycomb structure is kept unchanged for practical considerations, as an increased perforation rate implies a greater number of perforations per cell. Above the geometrical properties of the plate, another aspect subject to improvement is the liner assembly. In the previous chapter, discrepancies in TL values, particularly in the absence of flow, were attributed to potential efficiency losses in the experimental setup. These losses are hypothesized to result from an imperfect liner seal and leakage at both transverse sections and duct walls.

The objective of the new liner design is to achieve high performance under nonlinear conditions, particularly in the presence of flow, to maximize TL. This should enable a clearer distinction between acoustic nonlinearities and flow effect. Based on optimal multimodal impedance values for a Caiman-sized duct with and without flow, a parametric study was conducted by first varying the POA of the perforated plate under normal incidence. Using this parameter in the Guess model allowed for an initial assessment,

comparing the impedance results from numerical simulations with the optimal multimodal impedance. Chapter 4 indicated that the resistance and reactance of the round perforated plate closely matched those computed for the liner perforated plate.

For what concern the effects of the POA on the behaviour of the plate, increasing the POA makes the resistance to decrease and the plate reactance to increase, shifting the resonance towards higher frequencies. From the comparisons between the reference plate impedance and the multimodal one, in order to get an impedance closer to the optimal, the resistance have to decrease. To achieve so, we are operating a gradual increase of POA, concentrating on the case with flow and in nonlinear regime. The limitation stands in the limit reachable in the reactance values, since the correspondence between the plate impedance and the optimal one cannot pass the duct cutoff frequency of 1550 Hz, which is utterly inferior with flow. The best compromise between a decrease of resistance and a reactance inferior to the cutoff frequency has been found for a POA = 5.5%.

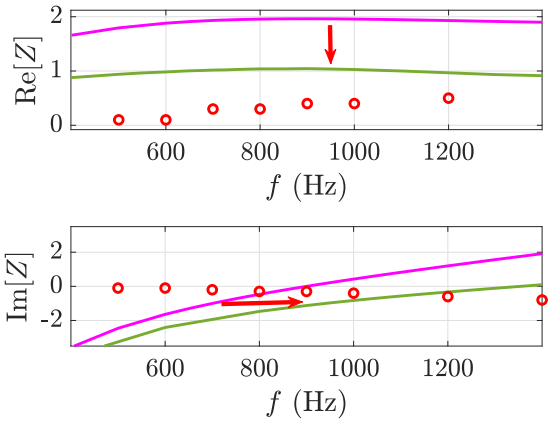

Figure 6.5: Comparison of impedance of plates with — POA = 1.99% (reference liner) and — POA = 5.5% with ○ multimodal impedance at 130 dB, M = 0.1 downstream case

Figure 6.5 presents the comparison between the reference impedance, for a a POA = 1.99%, the impedance found for a plate with POA = 5.5% and the multimodal. The comparison is made at 130 dB, at M = 0.1 in downstream case. As expected, the resistance decrease to values closer to the optimal ones, and the reactance increase, maintaining the intersection with the optimal reactance considerably below the cutoff frequency of the duct. In particular, near resonance, both resistance and reactance are closer to the optimal multimodal values. This suggest that the impedance improvement procedure might be promising, leading to a POA that is a compromise for an improved behaviour maintaining feasible values.

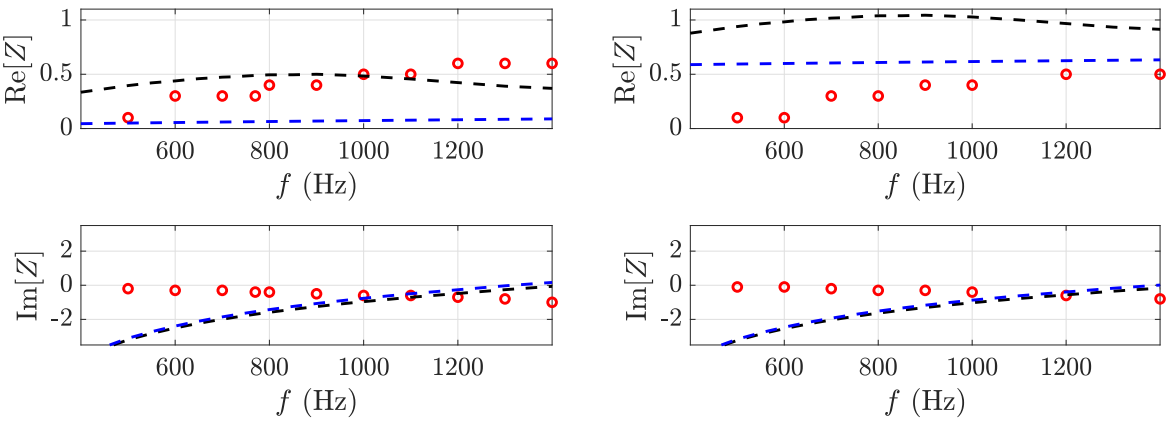

(a) M = 0 (b) M = 0.1

Figure 6.6: Preliminary comparison between the multimodal impedance (○) and the Guess analytical impedance at (- - -) 92 dB and (- - -) 130 dB at (a) M = 0 and (b) M = 0.1 downstream case for a POA = 5.5%

The global results of the comparison of the Guess analytical impedance for a plate with POA = 5.5% at M = 0 and M = 0.1 with the multimodal values are presented in Figure 6.6. This evaluation considered cases at 92 dB and 130 dB. The results show that resistance align most closely with optimal values in the M = 0 case at 130 dB, and that cases with flow also approach optimal conditions in both linear and nonlinear regimes. A liner with a POA of 5.5% is then selected for the study in grazing incidence. The selected POA value was implemented in a FDTD numerical simulation of the liner, analyzing TL for M = 0 and M = 0.1 at 92 dB and 130 dB.

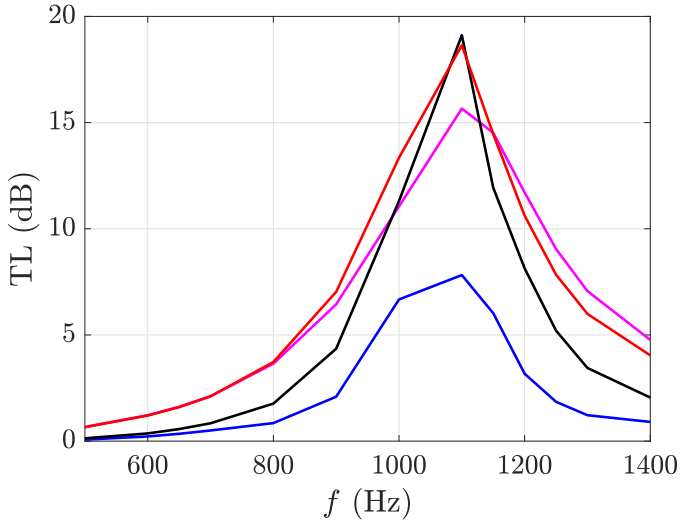

Figure 6.7: Preliminary numerical TL for M = 0 at — 92 dB, — 130 dB and for M = 0.1 downstream at — 92 dB, — 130 dB for a POA = 5.5%

The preliminary results of TL presented in Figure 6.7 indicated a general increase in TL values in nonlinear regime and in presence of flow. Notably, the cases at M = 0 and 130 dB, as well as those at M = 0.1, exhibit TL levels considerably superior to the linear case without flow. Only few frequencies are considered for this preliminary study. A refinement of frequencies around the resonance peak will lead to a better study of the TL. The main conclusion is that a liner presenting such POA results promising for

an improved efficacy in nonlinear regime and under flow.

Once validated the POA, the focus shifts to the production of the liner, both improving the Caiman assembly and making plates that comply with the POA determined earlier. The objective is to select a POA value as close as possible to the target value of 5.5% while ensuring feasibility in manufacturing. Concerning the round plate intended for the impedance tube, the closest achievable configuration presents a POA of 5.7%, slightly higher to the target value. This plate features twelve symmetrically arranged perforations, as illustrated in Figure 6.8.

Figure 6.8: Front view of the optimised circular plate

With regard to the liner, the POA closest to 5.5 % was found for the plate presented in Figure 6.9, presenting two-hundred-and-fifteen perforations for an overall POA of 5.13 %, slightly lower than the target. With reference to the sectional dissertation for the interior of the cells (Paragraph 2.2.2, Figure 2.11, three perforations are found in 66 % of the cells, presenting a POA of 5.55 %, and two perforations in 34 % of the cells, with a POA varying from 4.2 % to 5 %.

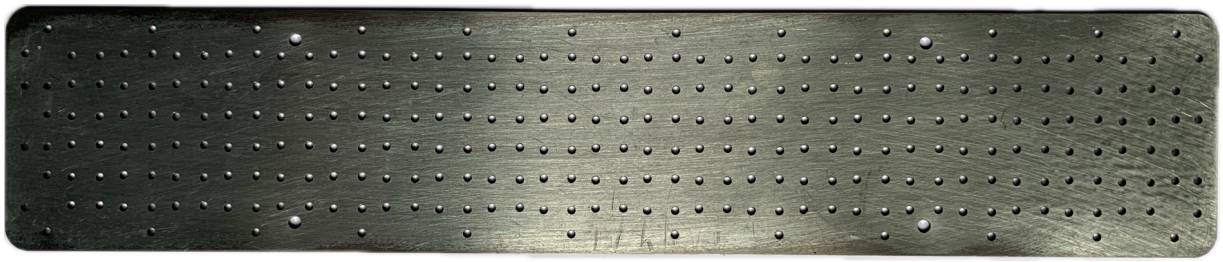

Figure 6.9: Front view of the optimised liner metallic perforated plate

For the assembly of the liner, the clearance with the support walls was decreased by 5 micrometres perimeter, further decreasing the space between the two, and a more rigid material was used for the HC structure. In addition, for this liner, the allocations of the supports were foreseen a priori directly within the plate, without having to resort to mechanical drilling to obtain them a posteriori. Once the different components were manufactured, they were tested experimentally, following the same protocol presented for the results in Chapter 4, and compared with the results by numerical approach.

6.1.5 Validation of the improved liner perforated plate impedance

In order to validate the improvement procedure, the numerical impedance evolution of the improved liner of Figure 6.9 is compared to the multi modal impedance.

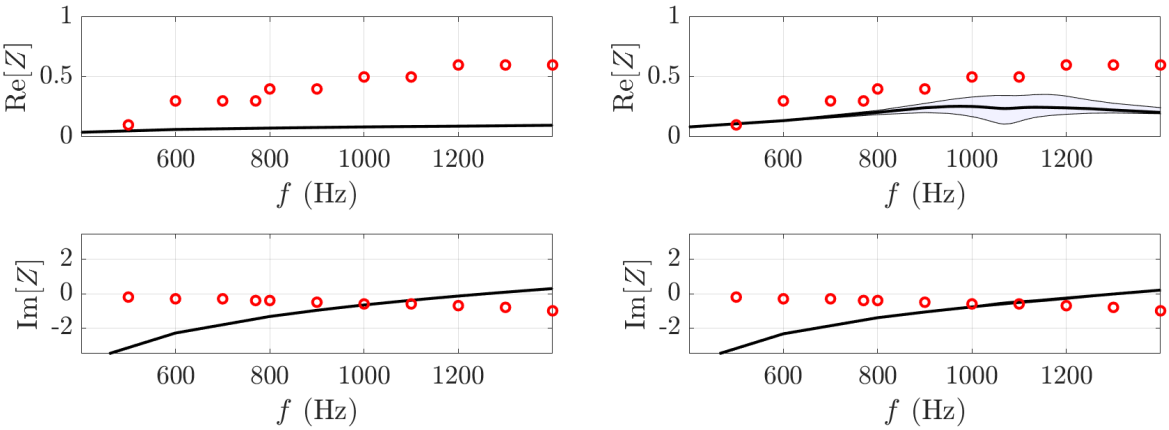

(a) 92 dB (b) 130 dB

Figure 6.10: Comparison between the multimodal impedance (○) and the numerical impedance (—) as a function of the frequency at M = 0 at (a) 92 dB and (c) 130 dB

Figure 6.10 presents the case without flow. It can be observed that, in this case, the nonlinear level exhibits resistance values closer to the optimal ones compared to the linear case, in contrast to what was observed for the previous liner. In the linear case, resistance remains nearly constant for the considered frequencies, whereas in the nonlinear case, a peak appears at the resonance frequency. Additionally, the intersection with the optimal reactance occurs near the liner's resonance frequency, which corresponds to the maximum peak of transmission loss.

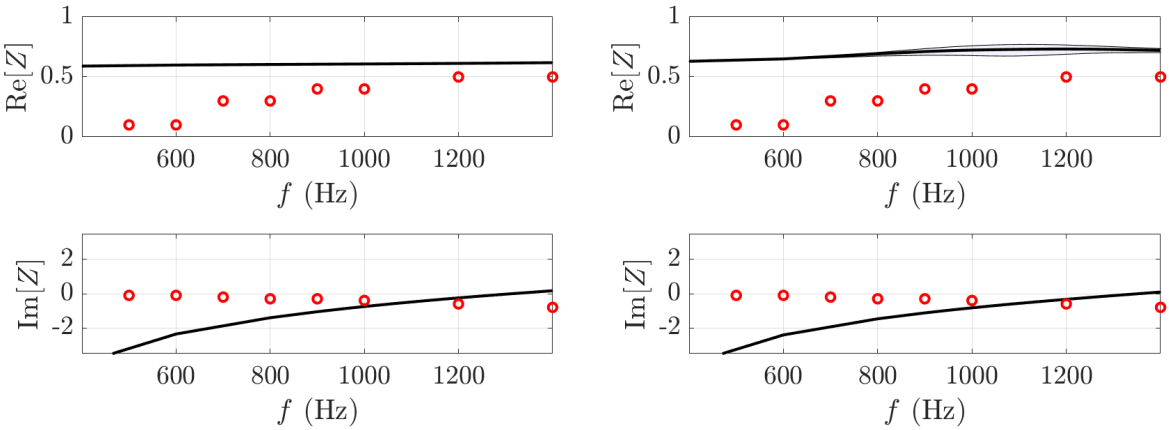

(a) 92dB (b) 130dB

Figure 6.11: Comparison between the multimodal optimal impedance (○) and the numerical impedance (—) as a function of the frequency at M = 0 at (a) 92 dB and (b) 130 dB

Figure 6.11 presents the results for the case with M = 0.1. It is evident that, in both the linear and nonlinear cases, resistance is superior but remains close to the multi modal values. This difference from the reference liner suggests the possibility of achieving efficient absorption performance even in the

presence of flow. Once validated the impedance, we can proceed to the discussion of the results of the new improved plates, first in normal incidence and then in the Caiman flow duct. Experimental findings will be compared to numerical and analytical simulations.

6.2 Acoustic behaviours of the improved perforated plate in normal incidence

In this section the acoustic behaviour of the round plate depicted in Figure 6.8 in impedance tube is investigated. As in the previous study, a comparison is considered between the experimental case and an theoretical concerning the semi-empirical Guess analytical impedance model and the numerical one with the FDTD method of Section 3.2. First of all, it is remarked how increasing the POA of the plate shift towards higher values the frequency of the resonance, assessing for this configuration around 1350 Hz.

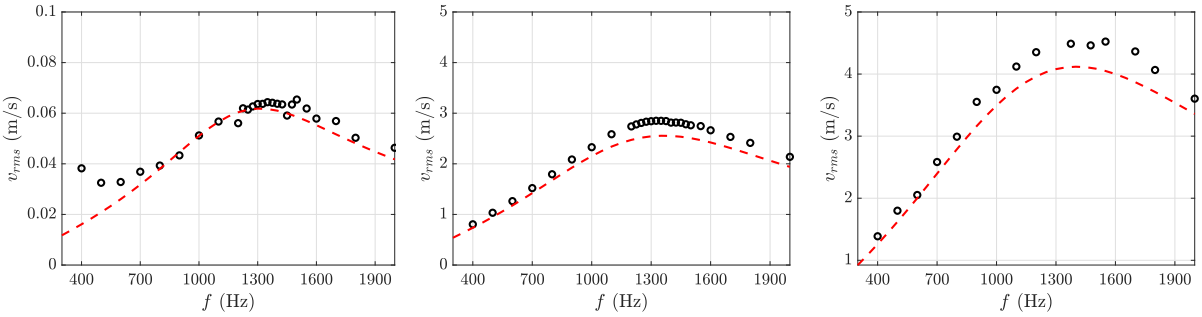

(a) 92 dB (b) 125.3 dB (c) 130 dB

Figure 6.12: Perforation acoustic velocity comparison between experimental (○) and numerical (- - -) approaches at (a) 92 dB (b) 125.3 dB (c) 130 dB

In Figure 6.12, the evolution of the velocity in the perforations in the linear and nonlinear case is represented. The more the acoustic level is increased, the more the velocity has the tendency to increase and widen its peak, always remaining at the resonance peak frequency of about 1300 Hz. It can be seen that the more the level is increased, the more there is a gap between the experimentally measured velocities and the numerically calculated one. In particular, an underestimation of the velocity can be observed in the more nonlinear case. This fact may be related to a greater resistance developed inside the perforations.

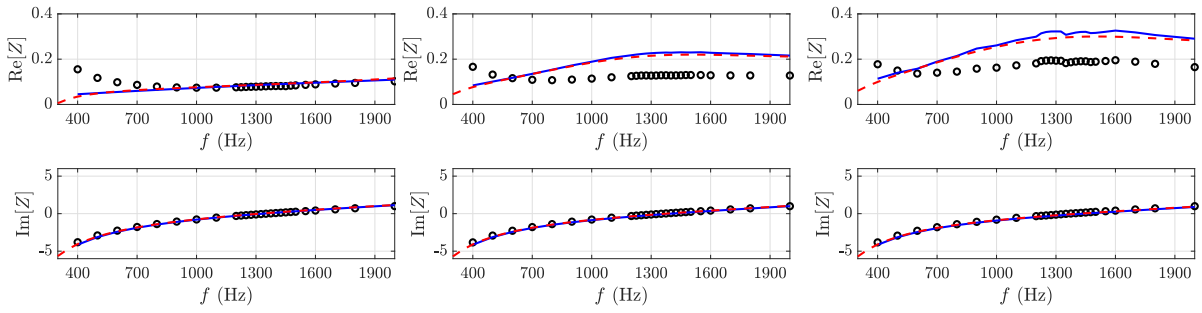

(a) 92 dB (b) 125.3 dB (c) 130 dB

Figure 6.13: Impedance comparison between experimental (○), analytic (—) and numerical (- - -) approaches at (a) 92 dB (b) 125.3 dB (c) 130 dB

In this regard, the impedance behaviour at the three levels considered in Figure 6.13 is observed. It can be noted that for the nonlinear cases, the resistance is overestimated in the analytical and numerical cases. This means that the plate is in fact less resistant and therefore consistently presents a higher perforation velocity value. It can be observed that for all cases considered the peak frequency is actually respected in linear and nonlinear in both the numerical and theoretical cases. This value corresponds to the zero transition of the reactance.

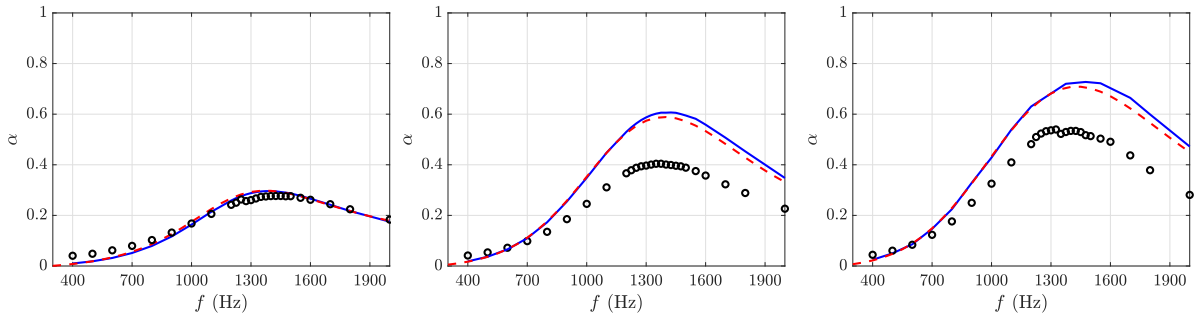

(a) 92 dB (b) 125.3 dB (c) 130 dB

Figure 6.14: Absorption coefficient comparison between experimental (○), analytical (—) and numerical (- - -) approaches at (a) 92 dB (b) 125.3 dB (c) 130 dB

In the absorption coefficient curves in Figure 6.14, consistent with what has been observed for the reference liner, a plate with a higher resistance exhibits stronger absorption. Particularly noticeable is how, consistent with velocity, the absorption peak tends to increase with sound level and how the theoretical models overestimate absorption compared to the experimental case.

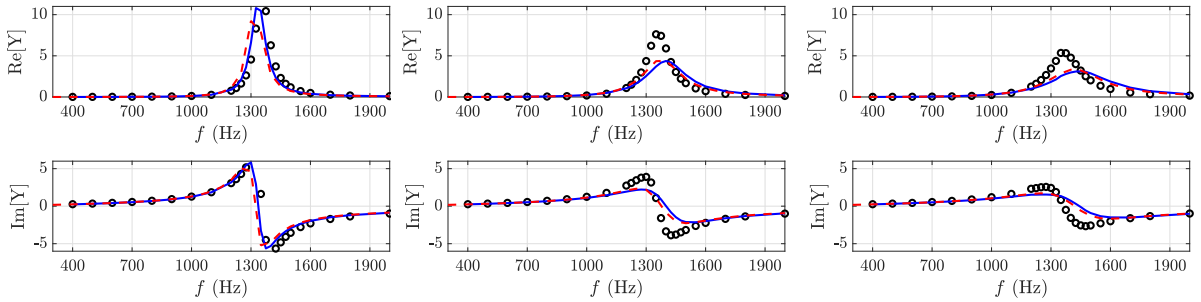

(a) 92 dB (b) 125.3 dB (c) 130 dB

Figure 6.15: Admittance comparison between experimental (○), analytical (—) and numerical (- - -) approaches at (a) 92 dB (b) 125.3 dB (c) 130 dB

Finally, for completeness we present in Figure 6.15 the trends of admittance, for which inverse behaviour is observed. In fact, it is noticeable that at 130 dB the experimental values correspond to those observed at 125.3 dB in the numerical and analytical studies.

Once these properties have been analysed,in the next section we are concentrating on the acoustic behaviour of the liner under grazing incidence with flow.

6.3 Acoustic behaviours of the improved perforated liner in Caiman wind tunnel

The behaviour of the liner transmission loss in cases with and without flow is now analyzed. Finally, the numerical prediction of the evolution of velocity and impedance along the liner and in the frequency range will also be presented.

6.3.1 Transmission loss

To begin the dissertation, a general overview of the experimental TL evolution at different cases is presented, with particular attention to the general trends and behaviour. Focus will then be made on the refinements of each case, comparing with numerical simulations. For all the cases, it is presented just a linear case at 92 dB and a nonlinear case at 130 dB.

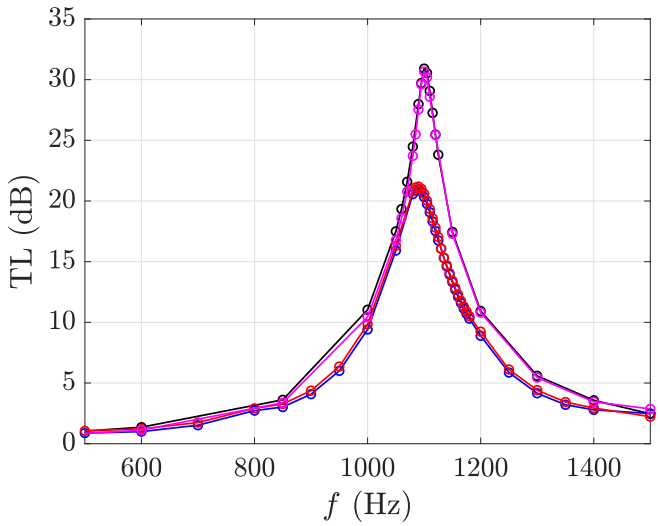

Figure 6.16: General TL comparison at M = 0 between the configuration downstream at ○ — 92 dB, —○— 130 dB and upstream at —○— 92 dB, —○— 130 dB by experimental approach

Figure 6.16 provides a general overview of the transmission loss in the case without flow. First, it is noted that the resonance frequency of the liner is shifted towards higher values, at approximately 1100 Hz. As observed in the reference liner, without a flow there is no consistent difference between the downstream and the upstream configuration, as expected, in both linear and nonlinear regimes. In this liner, the highest TL is successfully obtained in nonlinear regime, positively accomplishing the objective of the improvement process. Similar to the reference liner, a shift towards higher frequencies is observed when moving to nonlinear regime. Higher values of reached TL are observed compared to the reference liner, achieving 32 dB. We are now introducing a mean flow.

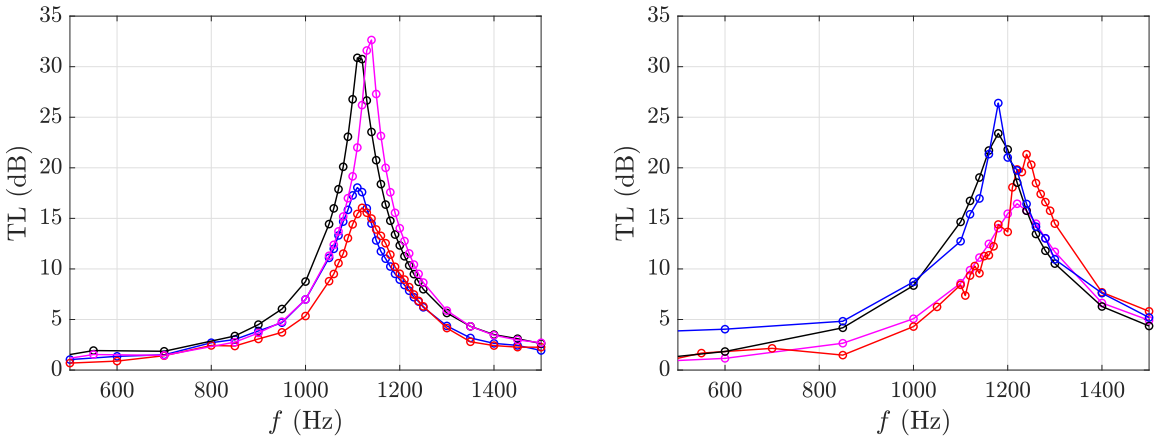

(a) M = 0.05 (b) M = 0.1

Figure 6.17: General TL comparison at (a) M = 0.05 and (b) M = 0.1 between the configuration downstream at 92 dB, 130 dB and upstream at 92 dB, 130 dB by experimental approach

Figure 6.17 presents the cases at M = 0.05 and M = 0.1, both downstream and upstream. In presence of a weak flow, at M = 0.05, the higher TL values are obtained for the nonlinear case. The values reached slightly outcomes the case without flow, reaching 34 dB in downstream configuration. For this case, a shift between downstream and upstream is observed, being the downstream cases at higher frequencies range, consistent to the reference liner. In contrast to what observed in the reference liner, the maximum TL is observed for the nonlinear case in downstream configuration.

When increasing the flow at M = 0.1, the tendencies align with the reference liner, presenting a higher TL in linear regime, for decreasing in nonlinear regime. First, it is observed with success a reaching of values close to 25 dB even for this case, having considerably augmented the performance compared to the reference liner. The difference between linear and nonlinear, in both downstream and upstream, remain relatively small. The downstream case presents lower values of TL, shifted at higher frequencies. For both cases, the TL peaks begin to widen and to enlarge. At a first observation, it seems that at M = 0.1 the flow effect overtakes the acoustic nonlinearity effect, both in terms of peak values and in terms of distance between the linear and the nonlinear case.

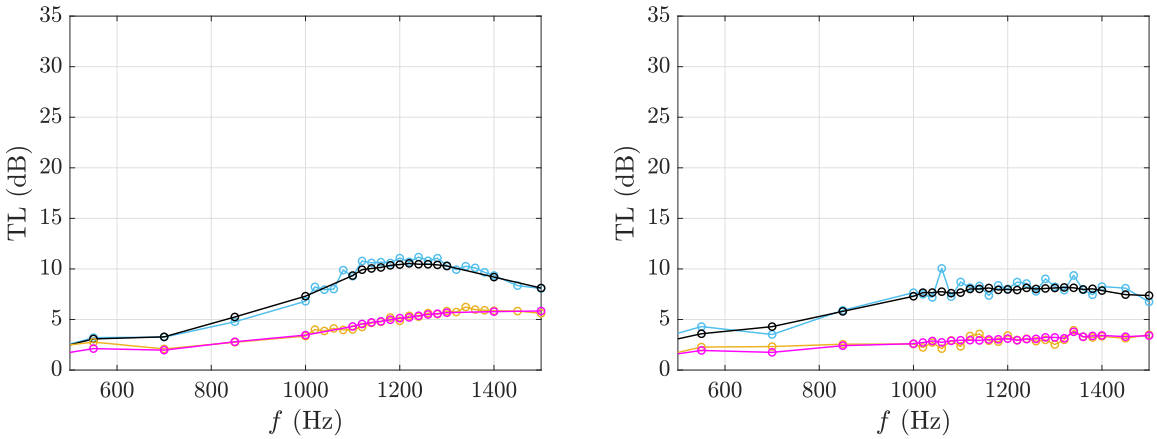

(a) M = 0.2 (b) M = 0.3

Figure 6.18: General TL comparison at (a) M = 0.2 and (b) M = 0.3 between the configuration downstream at 112 dB, 130 dB and upstream at 112 dB, 130 dB by experimental approach

For stronger flows, Figure 6.18 presents the cases at M = 0.2 and M = 0.3, both downstream and upstream. In these cases, the liner regime is obtained at 112 dB. The measures at 92 dB revealed complicated to perform and quite unstable. It is noted that in these cases, the upstream cases presents higher values than the downstream cases, shifted toward lower frequencies. In general, higher values of TL are reached, arriving at 11 dB at M 0 = 0.2 and 9 dB at M = 0.3. The TL peaks are very large and flattened, with a maximum peak in the downstream cases that exceed the cutoff frequency of the duct. No consistent difference is remarked between the liner and the nonlinear case. The acoustic effect is more and more attenuated but still maintains higher TL levels than the reference liner.

Due to the sharp TL peak, a more detailed analysis is now presented by comparing different cases, focusing on a TL peak enlargement to gain deeper insight into the behaviour at each level. Direct comparisons are made with numerical simulations implementing the Guess impedance model in the bi-dimensional FDTD simulation. Results are presented separately as a matter of clearness and comprehensibility, due to the sharp nature of the peaks.

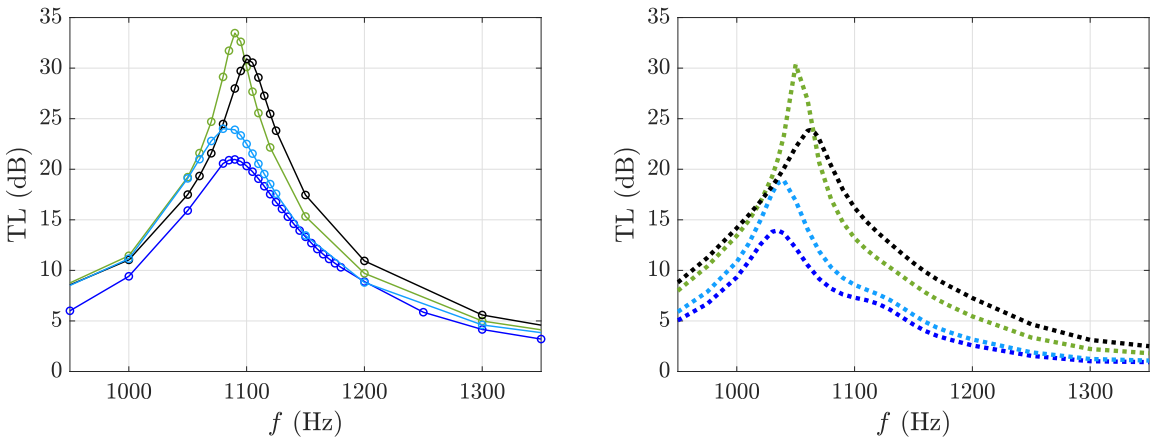

(a) Experimental (b) Numerical

Figure 6.19: TL at M = 0 at (—) 92 dB, (—) 112 dB, (—) 125.3 dB, (—) 130 dB in experimental (a) experimental [—] and (b) numerical [- - -] approaches

Figure 6.19 presents the results for the no-flow case, just in the downstream configuration. When comparing experimental (A) and numerical (B) data, an almost perfect match is observed between the extreme upstream and downstream cases, so only the experimental case is shown. The nonlinear level at 92 dB exhibits a lower transmission loss, around 20 dB, with a peak at approximately 1090 Hz, consistent with design predictions. An impedance closer to the optimal value results in a higher TL, reaching about 30 dB (an increase of 10 dB compared to the linear case). For intermediate configurations, TL progressively increases, peaking at 125.3 dB before slightly decreasing at 130 dB. This behaviour is attributed to the fact that at this peak frequency level, the liner's resistance is even closer to the optimal value. At 130 dB, a slight peak shift toward higher frequencies is observed, around 1100 Hz. For lower levels, TL remains constant at the same frequency until reaching a maximum, then decreases and shifts toward higher frequencies.

From a numerical perspective, the same trend observed experimentally is confirmed, although the Transmission Loss value is slightly lower than the experimental data. The peak frequency is also lower than in the experimental results, likely due to variations in the liner's perforation rate compared to initial assumptions. In fact, the POA of the individual cell is higher than the global POA, causing an increase in the resonance frequency. The behaviour observed at 125 dB, followed by a decrease at 130 dB and a shift toward higher frequencies, is also confirmed in numerical simulations, ruling out measurement anomalies. Additionally, the level difference in the two approaches is smaller than that observed in the reference liner. This suggests that the tighter assembly of the new liner has reduced leakage-related errors, while still producing values slightly lower than the experimental data.

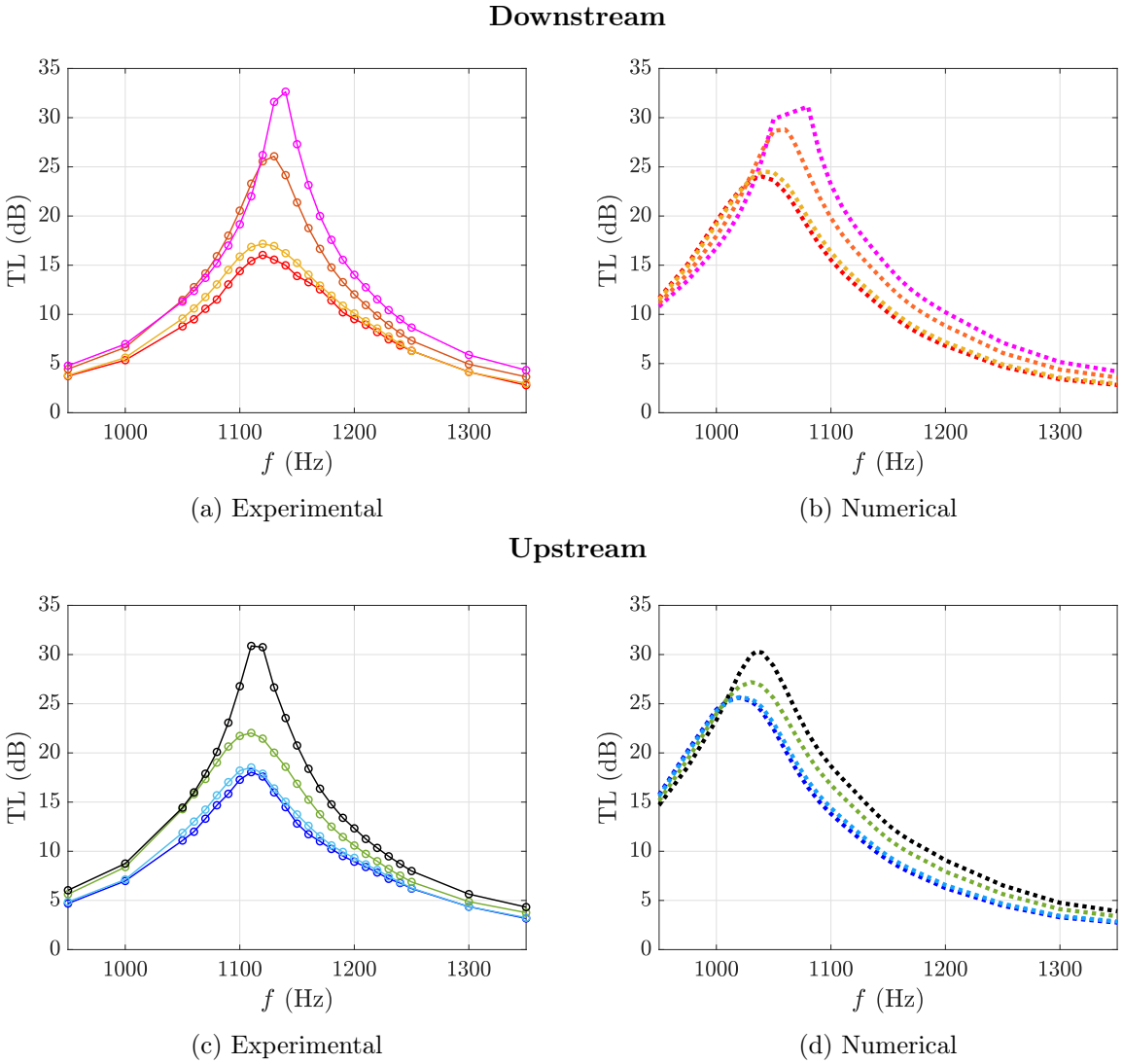

(a) Experimental (b) Numerical

(c) Experimental (d) Numerical

Figure 6.20: TL at M = 0.05 in downstream configuration at (—) 92 dB, (—) 112 dB, (—) 125.3 dB, (—) 130 dB and upstream configuration at (—) 92 dB, (—) 112 dB, (—) 125.3 dB, (—) 130 dB in (a),(c) experimental [—o—] and (b),(d) numerical [- - -] approaches

Next, the case of M = 0.05 is considered in Figure 6.20. It is observed that the upstream case exhibits transmission loss values at higher frequencies compared to the upstream case, as previously noted for the reference liner. The downstream peak value is slightly higher than in the upstream case, in contrast with previous observations in reference liner. As in the no-flow case, TL increases from the linear to the nonlinear case; however, in this case, the maximum occurs at 130 dB without a subsequent TL reduction. A slight frequency shift is observed, though it is less pronounced than in the previous liner. From a numerical perspective, the overall behaviour of the liner is consistent across all acoustic levels and both upstream and downstream configurations, correctly reproducing the increasing order of transmission loss. The numerical model overestimates the experimental value starting from the linear case, with a difference of approximately 5 dB between the two extreme cases.

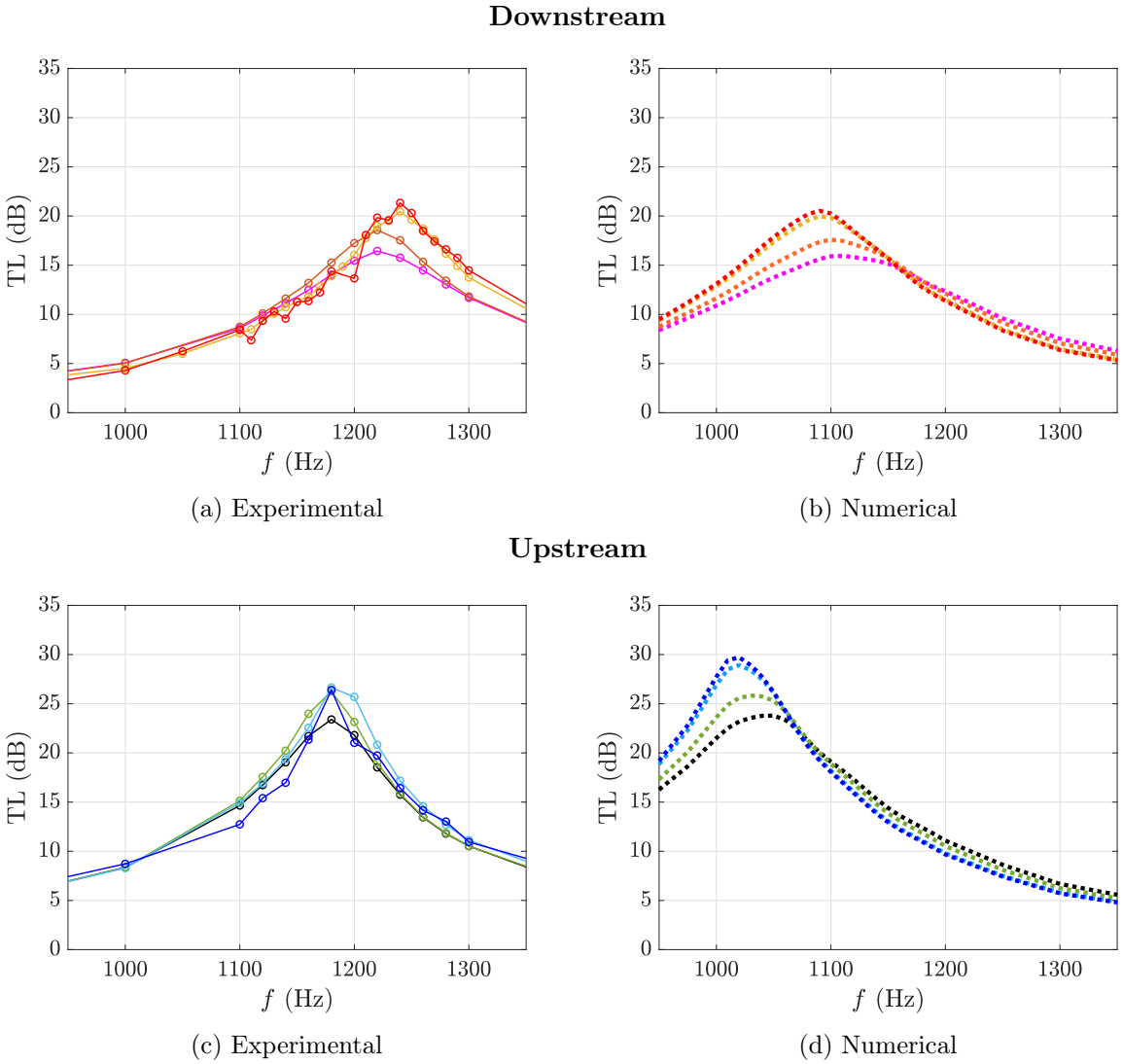

(a) Experimental (b) Numerical

(c) Experimental (d) Numerical

Figure 6.21: TL at M = 0.1 in downstream configuration at (—) 92 dB, (—) 112 dB, (—) 125.3 dB, (—) 130 dB and upstream configuration at (—) 92 dB, (—) 112 dB, (—) 125.3 dB, (—) 130 dB in (a),(c) experimental [—o—] and (b),(d) numerical [- - -] approaches

Figure 6.21 considers the case at M = 0.1. One of the key observations is that the numerical model accurately predicts the trends observed experimentally. In particular, it provides a good estimation of both the TL values in all analyzed cases and the peak width. The model also correctly predicts the shift between downstream and upstream cases, displaying downstream peak values at higher frequencies. Furthermore, the upstream case exhibits higher peak values compared to the downstream case. Once again, a pronounced difference is observed between the peak frequencies obtained experimentally and those predicted numerically, with a discrepancy of approximately 150 Hz. This difference tends to increase with higher flow regimes.

Regarding the acoustic behaviour, the highest value is recorded in the linear acoustic case, then gradually decreases by about 5 dB in each configuration until reaching the nonlinear case at 130 dB. Additionally, a slight frequency shift is noted between the linear and nonlinear cases. Compared to the previous liner configuration, estimating a resistance closer to the optimal value has resulted in significantly higher TL values. This has also allowed for a clearer distinction between acoustic and flow effects. However, the flow effect remains dominant over the acoustic effect, confirming the findings from Chapter 4. The observation of higher levels and more pronounced differences between cases serves as strong

evidence supporting this explanation.

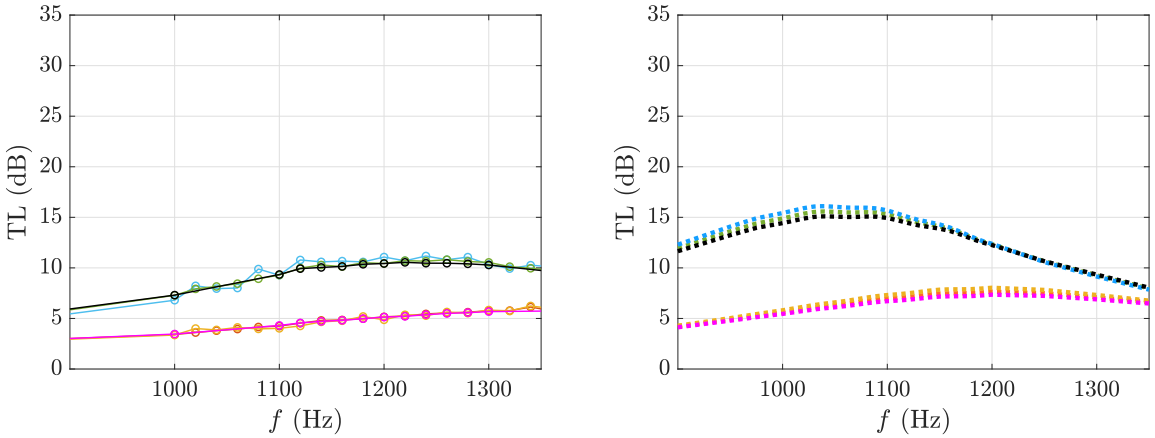

(a) Experimental (b) Numerical

Figure 6.22: TL at M = 0.2 in downstream configuration at (—) 112 dB, (—) 125.3 dB, (—) 130 dB and in upstream configuration at (—) 112 dB, (—) 125.3 dB, (—) 130 dB in (a) experimental [o] and (b) numerical [- - -] approaches

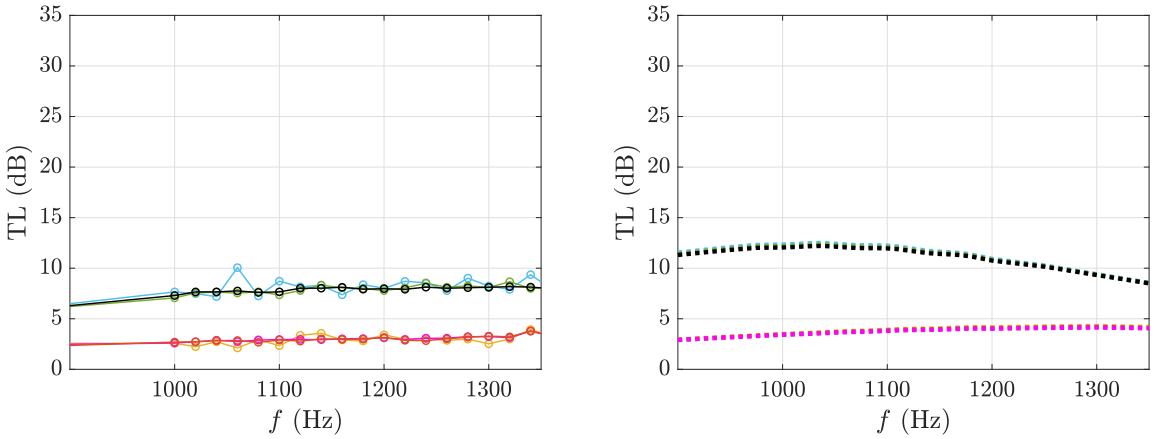

(a) Experimental (b) Numerical

Figure 6.23: TL at M = 0.3 in downstream configuration at (—) 112 dB, (—) 125.3 dB, (—) 130 dB and in upstream configuration at (—) 112 dB, (—) 125.3 dB, (—) 130 dB in (a) experimental [o] and (b) numerical [- - -] approaches

Finally, Figure 6.22 depicts the observed behaviours for M = 0.2 and Figure for the 6.23 M = 0.3 case. For the numerical analysis in the configuration at M = 0.3, the cavity propagation method of Section 3.2.3.2 was adopted, as the reference method of Section 3.2.3.1 introduced real poles. In both configurations, the numerical simulation effectively reproduces the experimentally observed trends, albeit with a slight overestimation of transmission loss. In both cases, the configuration exhibits a transmission loss approximately 10 dB higher than the downstream case. Specifically, in the downstream case, a peak flattening is observed, extending over a broader frequency range and exceeding the duct's cut-off frequency. In these cases, the acoustic effect is entirely canceled out by the flow effect, yet it maintains a more stable trend, particularly in the experimental case, compared to what was observed in the previous liner configuration.

In conclusion, the liner designed with impedance closer to the optimal value has yielded higher transmission losses in all cases, particularly in the presence of flow and nonlinear acoustic conditions. The numerical simulation correctly reproduces the experimental behaviours, with some differences that can be attributed to model assumptions and measurement uncertainties. The process of improvement have been successful, having higher performances in both nonlinear regime and in presence of flow than the reference liner, allowing to a more precise analysis of the two effects.

6.3.1.1 Numerical evolution of the improved liner acoustic properties

After having analysed the evolution of the impedance at the beginning of the section, we are now presenting the other acoustic properties.

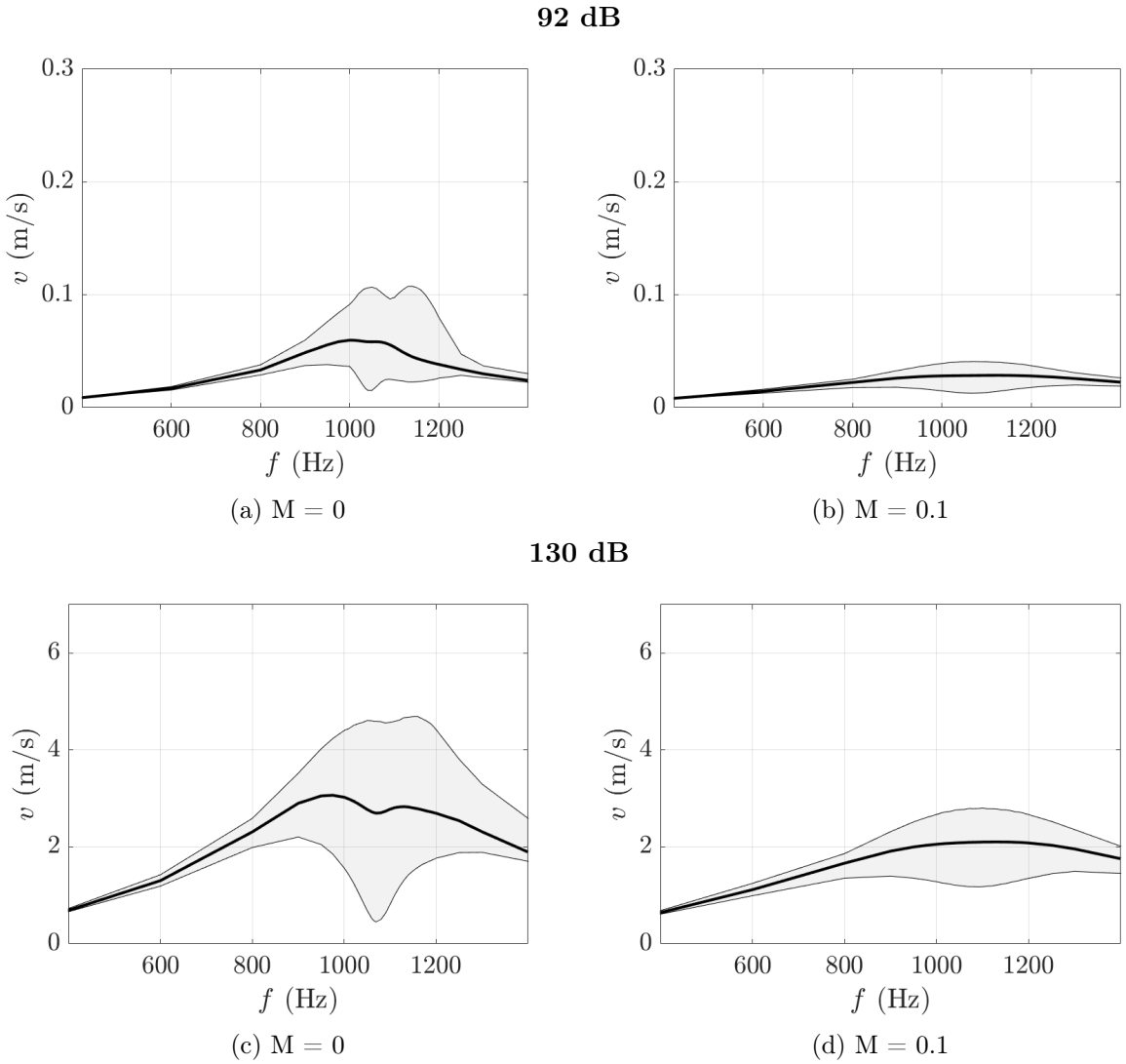

(a) M = 0 (b) M = 0.1

(c) M = 0 (d) M = 0.1

Figure 6.24: Numerical evolution of the rms acoustic velocity as a function of the frequencies considered for different sound level and Mach number configurations

For completeness, Figure 6.24 presents the rms velocity profiles at the perforation within the liner. For the considered acoustic configurations, it is observed that in linear cases, at 92 dB, the acoustic velocity is nearly zero. In nonlinear case, at 130 dB, it progressively increases. In particular, without flow, the velocity is higher than in the flow case, where the error is also more significant, especially at resonance

frequencies. Focus is now made on the spatial evolution of the properties along the liner surface, with particular influence of nonlinearities and of flow.

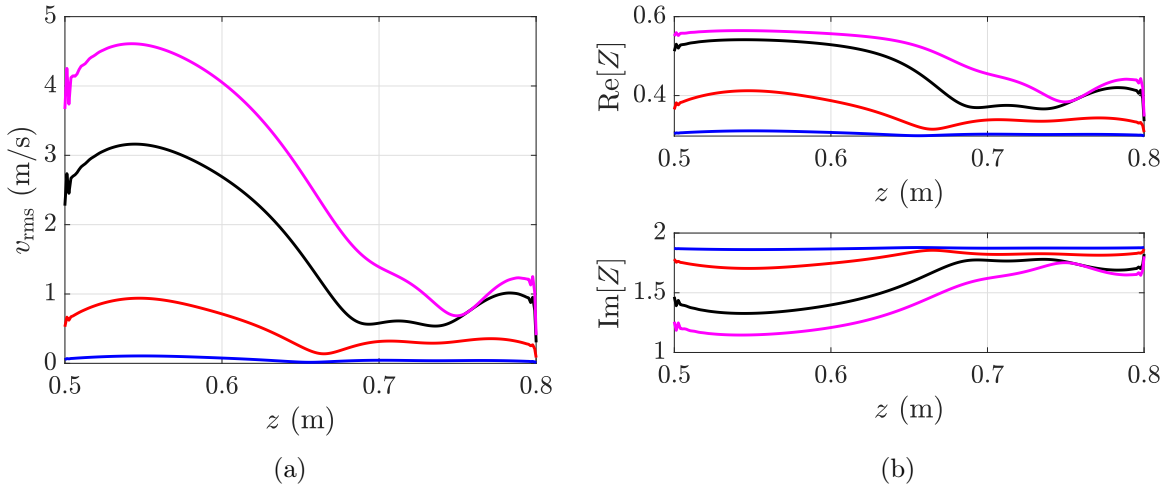

Figure 6.25: Numerical predictions of (a) acoustic velocity and (b) impedance along the liner surface at — 92 dB, — 112 dB, — 125.3 dB, — 130 dB at 1050 Hz and M = 0

Figure 6.25 shows the evolution of the rms velocity in the perforations and of the impedance along the liner surface at 1050 Hz (close to the resonance frequency) and without flow, for different incident SPL. The acoustic velocity increases gradually along the liner as the SPL increases. In linear regime, the velocity remains uniform along the liner. Higher values are observed at 130 dB compared to the reference liner. The trend of the evolution recalls the reference liner, having a strong decrease of the velocity along the liner. A sudden rebounding at the liner extremity is observed when considering nonlinear regime.

The impedance behaviour finds analogy with the velocity. Starting at a linear regime with both resistance and reactance that maintain uniform along the liner. In nonlinear regime, the resistance increase with the acoustic level, having an evolution along the liner similar to the one of the velocity. The reactance decreases in analogue way, having always positive values in contrast to the negative values observed in the reference liner.

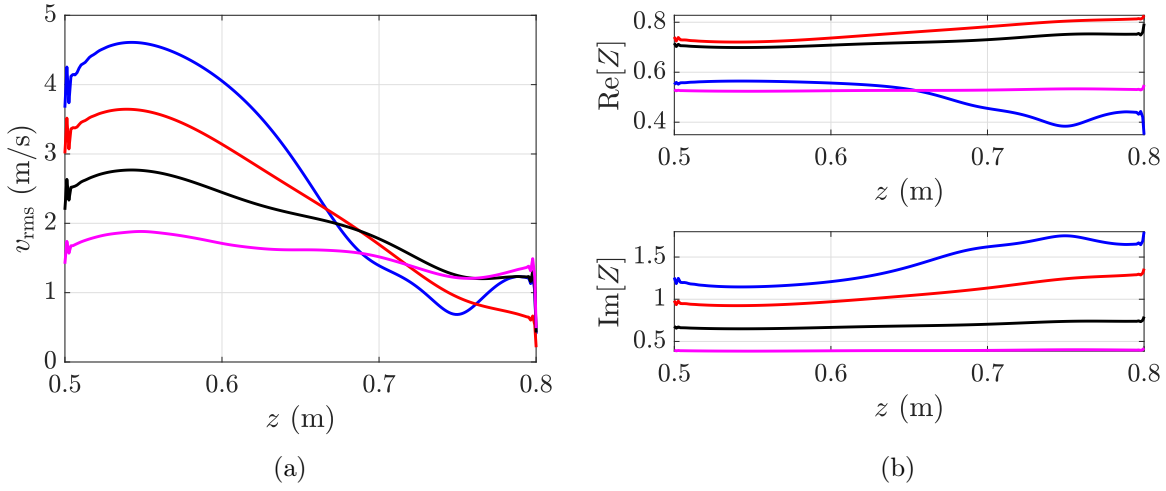

Figure 6.26: Numerical predictions of (a) acoustic velocity and (b) impedance along the liner surface in downstream configuration at — M = 0, — M = 0.05, — M = 0.1, — M = 0.2 at 1050 Hz and SPL = 130 dB

In conclusion, Figure 6.26 shows the evolution of the rms velocity in the perforations and of the impedance along the liner surface around the resonance, at 1050 Hz at 130 dB, for different Mach numbers, in order to study the influence of the flow in nonlinear regime. For what concern the velocity, an increasing flow translates in a decrease of the velocity. The higher the flow, the more uniform is the velocity on the liner surface, with a more monotone behaviour, without rebounding at the end of the liner.

For the impedance, the tendency is to flatten both resistance and reactance with a higher flow. At M = 0.2, resistance values are near the values without flow. In fact, the presence of a flow notably increases the resistance (with a double at the end of the liner), for gradually flattening and decreasing in values the stronger the flow becomes. In contrary, the reactance tends to diminish in a monotonic way till the flattening to M = 0.2 to values close to zero.

6.4 Conclusions

This chapter introduced the improvement process for a new acoustic liner, emphasizing the improvement of impedance properties for increasing sound attenuation. The main aspect of the chapter is the conception and implementation of the methodology used, which allows the a priori design of a perforated plate liner from classical multimodal models and impedance varying with flow and nonlinear regime. The measurements confirm the validity of the method. The study employed both theoretical and experimental approaches, incorporating the Cremer-Tester model and a multimodal optimisation method. The aim was to develop a liner with impedance characteristics close to the optimal values, ensuring improved acoustic absorption in both linear and nonlinear regimes, with and without flow. The improvement methodology is based on a simple parametric increasing of the liner POA in order to achieve an impedance close to the multimodal target. By systematically varying resistance and reactance, a precise impedance map was obtained, allowing the identification of optimal values. This methodology provided a more accurate representation of realistic conditions compared to classical infinite-length liners.

Experimental validation confirmed the effectiveness of the improved liner. The numerical and experimental results are concordant and not always consistent with the results obtained previously with the reference liner. This largely depends on the plate parameters. Compared to previous designs, the new liner exhibited higher transmission loss values, particularly in nonlinear acoustic regimes and under flow conditions. The resistance values of the liner were consistently closer to optimal, leading to better performance in noise attenuation. Moreover, the peak of TL was more concentrated around specific frequencies. The study also highlighted the role of liner assembly and perforation parameters in optimising performance. Adjustments of liner sealing significantly minimized leakage effects, contributing to more reliable experimental results. The comparison between numerical and experimental data demonstrated that the optimised liner maintained high TL levels across various acoustic pressures and flow regimes. Another core aspect was the ability to distinguish more clearly between acoustic nonlinearities and aerodynamic effects. While previous design struggled to isolate these effects at high Mach regimes, the improved liner provides a better-defined response, helping to separate the impact of flow from acoustic interactions. This distinction is crucial for future designs, as it allows for more targeted optimisations in specific operating conditions.

To summarize, in this chapter we started from a classic multimodal methodology to define a duct target impedance and we than proceeded to implement a real improved liner, dealing optimal impedance values with feasibility and limitations of the real duct. We concentrated on changing just the POA in order to get to the target values, guaranteeing a simple and agile approach to liner modelling. Experimental and numerical results confirmed the effectiveness of this methodology, and allowed us to better define the acoustic and flow effects on the perforations. Moreover, experimental data collected in this study presents a solid and important database for future studies.

General conclusion

General synthesis of the thesis

This thesis investigates the nonlinear acoustic behaviour of perforated plates under grazing flow. The study combines experimental, numerical, and analytical approaches to improve the understanding and prediction of acoustic impedance in such configurations. The primary objective was to analyze the effects of high sound pressure levels and flow conditions on the impedance characteristics of perforated structures, with applications in noise control technologies, particularly in aeronautics. A comprehensive methodology was developed in Chapter 1 to address these challenges, by comparing existing well-established impedance models in the nonlinear case and with flow.

Experimental investigations were conducted using an impedance tube and a wind tunnel to measure the acoustic response of perforated plates under controlled conditions. These measurements provided detailed insights into the variations in impedance under different excitation levels and flow regimes, as presented in Chapters 4 and 6. The development of a novel experimental procedure allowed precise control of incident pressure levels, ensuring reliable data acquisition, as detailed in Chapter 2. The experimental results revealed significant dependencies of impedance and acoustic indicators like absorption coefficient and transmission loss on both sound amplitude and grazing flow, confirming the necessity of incorporating nonlinear and flow effects into predictive models. Moreover, the experimental results presented in this study represent a solid and accurate database for further studies, both experimental and numerical.

On the numerical front, finite-difference time-domain (FDTD) simulations were employed to model the acoustic propagation in ducts. A key advancement was the implementation of a time-domain admittance boundary condition (TDABC), presented in Chapter 3, which allowed for more accurate simulation of perforated plate impedance as a function of frequency and perforation acoustic velocity. These numerical models were validated against experimental data, demonstrating their capability to capture the complex interactions between sound waves, perforations, and flow. The strong agreement between numerical and experimental results reinforced the effectiveness of the developed approach in predicting impedance variations in practical scenarios, as presented in Chapters 4 and 6.

Analytical modeling played a crucial role in this study, providing fundamental insights into the governing physical mechanisms. Classical impedance models, such as the Guess model and the equivalent fluid approach, were analyzed and extended to account for nonlinearities and flow effects. The Rice-Cummings formulation, originally developed for Helmholtz resonators, was adapted to perforated plates by means of a Multiple Scale Approach, leading to a refined impedance expression for the dynamic transient analysis of nonlinear resonators. The modifications introduced in this thesis provide a more comprehensive understanding of the factors influencing acoustic resistance and reactance in perforated structures, with particular applications to perforates plates, as presented in Chapter 5. These improvements enable easier predictions of impedance behaviour at high sound pressure levels and in the presence of grazing flow, addressing a key challenge in the field.

The main effects observed considering a nonlinear regime are the shift of the resonance frequency towards higher values and a broadening of the evolution of the acoustic indicator. This fact has been

observed for absorption coefficient and impedance in normal incidence and for TL in grazing incidence. When introducing a grazing flow, the effects are similar, with an utter shift of frequency and broadening of the peak, leading to more and more weak performances of the liner. It has been noticed that after a certain regime, the flow effects become preponderant on the nonlinear effects, with consequences on a weaker performance and an homogenisation of impedance and velocity along the liner. For regimes without flow and for weak flows, the impedance and the acoustic velocity resulted to be not uniform along the liner. From here the necessity of considering the acoustic velocity along the liner surface, leading to an impedance boundary condition not uniform at the interface with the duct.

Beyond the theoretical and numerical predictions, this thesis contributes to practical applications in improving noise control liners. The improved understanding of perforated plate behaviour enabled the design of more effective acoustic liner in nonlinear regime and under flow, as presented in Chapter 6, with better performances both in nonlinear regime and with flow.

The main findings of this research highlight the critical role of nonlinear effects in perforated plates. The introduction of grazing flow further modifies the impedance response and transmission loss and altering sound propagation behaviour. These findings emphasize the limitations of purely linear models and the necessity of incorporating nonlinear and flow-dependent corrections for accurate impedance predictions.

Perspectives for future research

The methods presented in this study have several limitations. Acoustic propagation has been considered exclusively in the linear regime. However, to better replicate conditions relevant to aeronautical applications, it would be highly beneficial to extend the analysis to the nonlinear domain.

Time domain approaches are well adapted for considering nonlinear propagation. This is interesting if both employing an impedance boundary condition, as for the Guess and EFM approaches, and a differential equation boundary condition, as for the Rice-Cummings approach. The basis given in this thesis represents a solid and wide potential for developing future investigations.

While the numerical results successfully predict the overall behaviour of the liners, certain discrepancies have emerged, particularly regarding the resonance frequency under grazing incidence and the transmission loss in the absence of flow. Further investigation into the causes of these inconsistencies is recommended for future research, focusing both on improving numerical and analytical modeling and on developing alternative liner configurations to validate the method.

From an experimental perspective, conducting measurements at higher acoustic levels and increased flow velocities would be valuable, aiming to recreate increasingly realistic scenarios for noise reduction in aeronautical applications. In terms of liner technology, several approaches remain unexplored and could be refined, particularly by employing more advanced 3D printing techniques than those used in this study. Additionally, while the current mounting setup for the liner on the CAIMAN test bench has proven to be efficient and robust, further refinements could help minimize potential leaks and imperfections. Regarding the acoustic signal used, employing a sweep signal would be particularly interesting for studying the influence of the sound source on the liner's behaviour. Another interesting aspect to investigate would be a vibrational study on the plate, by means of a numerical simulation or using a commercial tool. A further study considering microperforated plates would be interesting, and the comparison between macro and micro perforations would give an utter insight in the different behaviours of the two configurations applied to liners.

In this study, impedance under grazing incidence and flow conditions has been investigated solely through numerical analysis. The validity of these results has been inferred based on the strong agreement between experimental measurements and numerical simulations of transmission loss. Given recent advancements in experimental impedance measurement techniques, particularly the impedance eduction method [15, 28, 29, 65, 91], it would be beneficial to implement the necessary setup on the CAIMAN test bench to conduct such measurements and validate numerical findings. Considering the versatility of the CAIMAN facility, which features a liner holder with transparent walls, and following recent studies by Leon and Piot [96] and Alomar and Auregan [9], it would be advisable to perform optical velocity and impedance measurements within the duct. This would provide deeper insights into real viscous and

nonlinear effects near the perforations, further enhancing the understanding of liner behaviour.

Appendix

A Details on the methods for the determination of transmission loss

In this Appendix we are detailing the mathematical procedures for the determination of transmission loss introduced in Chapter 2. In Appendix A.1 the one source method proposed by Bolton for a symmetric duct with flow and an anechoic termination is detailed, both for downstream and upstream case. In Appendix A.2 the matrix calculation for the two-source method will be detailed.

A.1 One source method for a symmetric duct with flow and an anechoic termination

In this section, the one source method proposed by Bolton for a symmetric duct with flow and an anechoic termination is detailed for the determination of the reflection and transmission coefficients, first in downstream and then in upstream configurations.

A.1.1 Downstream case

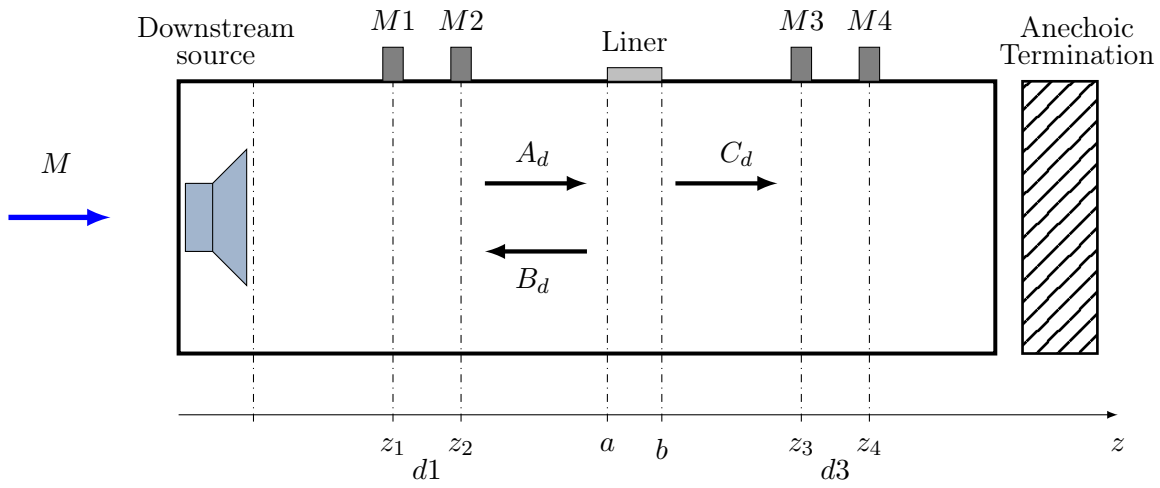

Figure 27: Schematic of one source method: downstream case

First, let us consider the downstream configuration, sketched in Fig. 27. The acoustic propagation direction is the same as the flow (downstream). We note A_d the incident wave amplitude, B_d the reflected wave amplitude before the liner, C_d the transmitted wave after the liner. The acoustic pressure field at the microphones can be decomposed as follow:

$$\begin{cases} p_{1,d} = A_d e^{-ik^+ z_1} + B_d e^{ik^- z_1} \\ p_{2,d} = A_d e^{-ik^+ z_2} + B_d e^{ik^- z_2} \\ p_{3,d} = C_d e^{-ik^+ z_3} \\ p_{4,d} = C_d e^{-ik^+ z_4} \end{cases} \tag{3}$$

We can derive the wave amplitudes as follows:

$$\begin{aligned} A_d &= \frac{p_{2,d} - p_{1,d} e^{ik^-(x_2 - x_1)}}{e^{-ik^+(x_2 - x_1)} - e^{ik^-(x_2 - x_1)}} \\ B_d &= \frac{p_{1,d} e^{ik^+(x_2 - x_1)} - p_{2,d}}{e^{-ik^+(x_2 - x_1)} - e^{ik^-(x_2 - x_1)}} \\ C_d &= \frac{p_{4,d} - p_{3,d} e^{ik^-(x_4 - x_3)}}{e^{-ik^+(x_4 - x_3)} - e^{ik^-(x_4 - x_3)}} \end{aligned} \tag{4}$$

The transmission loss , one source downstream can be expressed as:

$$\mathrm{TL} = 20 \log_{10} \left| \frac{C_d}{A_d} \right| \tag{5}$$

Eluding from the hypothesis of the formulation, if considering a quasi-anechoic termination we could define a reflection coefficient as:

$$r = \left| \frac{D_d}{C_d} \right| \tag{6}$$

with D_d the reflected wave after the liner.

A.1.2 Upstream case

In this section the Bolton one source method in perfectly anechoic termination and symmetric duct will be detailed for the determination of the reflection and transmission coefficients in upstream case. In Figure 28 a schematic of an excitation in a upstream case is considered. For calculation simplicity, we consider a relative coordinate systems z' which follows the direction of the acoustic excitation (z'=-z).

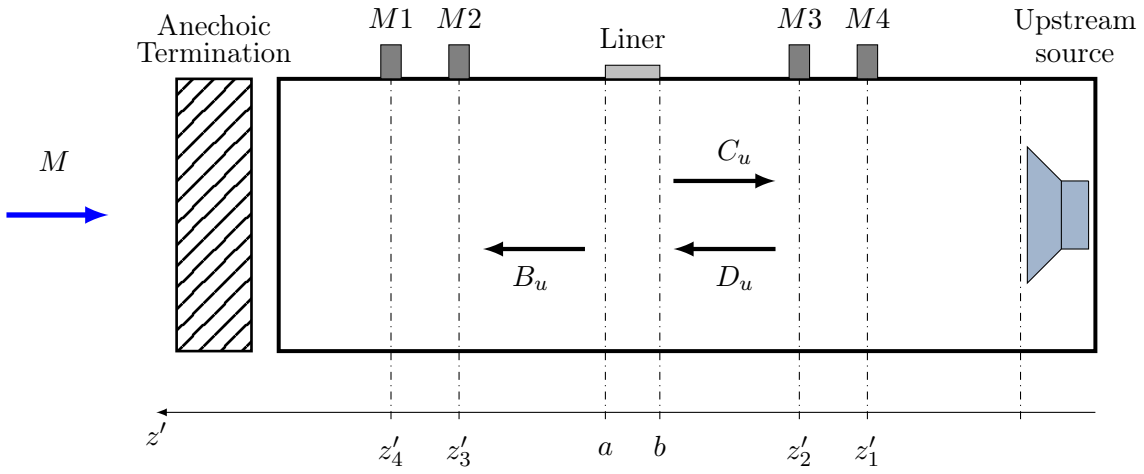

Figure 28: Schematic of one source method: upstream case

Considering the acoustic excitation direction, which is opposite to the flow (upstream) D_u is the incident wave amplitude, C_u the reflected wave amplitude before the liner, B_u the transmitted wave after the liner. The acoustic pressure field inside the duct can be decomposed as follow:

$$\begin{cases} p_{4,u} = D_u e^{-ik^- z'_4} + C_u e^{ik^+ z'_4} \\ p_{3,u} = D_u e^{-ik^- z'_3} + C_u e^{ik^+ z'_3} \\ p_{2,u} = B_u e^{-ik^- z'_2} \\ p_{1,u} = B_u e^{-ik^- z'_1} \end{cases} \tag{7}$$

We can derive the wave amplitudes as follows:

$$\begin{aligned} D_u &= \frac{p_{3,u} - p_{4,u} e^{ik_0^+ (z'_4 - z'_3)}}{e^{-ik^- (z'_3 - z'_4)} - e^{ik_0^+ (z'_4 - z'_3)}} \\ C_u &= \frac{p_{4,u} e^{ik_0^- (z'_4 - z'_3)} - p_{3,u}}{e^{-ik^- (z'_3 - z'_4)} - e^{ik_0^+ (z'_4 - z'_3)}} \\ B_u &= \frac{p_{1,u} - p_{2,u} e^{ik_0^+ (z'_2 - z'_1)}}{e^{-ik^- (z'_2 - z'_1)} - e^{ik_0^+ (z'_2 - z'_4)}} \end{aligned} \tag{8}$$

The transmission loss can be expressed as:

$$TL = 20 \log_{10} \left| \frac{D_u}{B_u} \right| \tag{9}$$

Eluding from the hypothesis of the formulation, if considering a quasi-anechoic termination we could define a reflection coefficient as:

$$r = \left| \frac{A_u}{B_u} \right| \tag{10}$$

with A_u the reflected wave after the liner.

A.2 Determination of transmission loss by two-source method: detailed procedure

The two-source method is widely used for characterizing acoustic liner [2, 23, 60, 66, 89, 94, 95]. We detail this method in this paragraph (see Fig. 29).

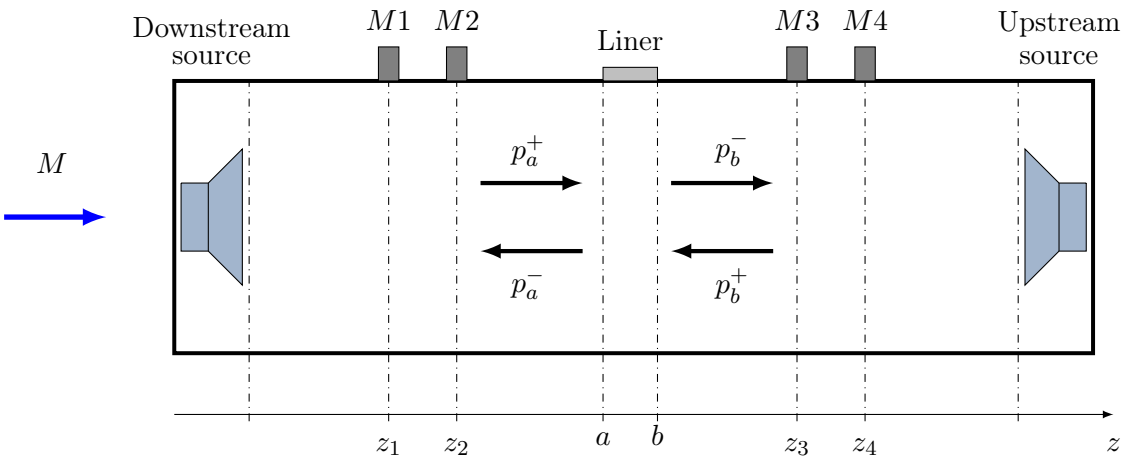

Figure 29: Schematic of two-source method

The condition $d1, d3 < 2c_0/(5f_{max})$ is respected (0.0354 m and 0.0345 m are smaller than 0.085m) [114]. $\boldsymbol{D}$ is the scattering matrix defined as:

$$\begin{pmatrix} p_a^- \\ p_b^- \end{pmatrix} = \boldsymbol{D} \begin{pmatrix} p_a^+ \\ p_b^+ \end{pmatrix} \tag{11}$$

Exciting before the downstream source and then the upstream source, we can apply the matrix for the two cases described in the previous section, with the index d for the downstream configuration and the index u for the upstream configuration:

$$\begin{pmatrix} p_{a,d}^- \\ p_{b,d}^+ \end{pmatrix} = \boldsymbol{D} \begin{pmatrix} p_{a,d}^+ \\ p_{b,d}^- \end{pmatrix} \qquad \begin{pmatrix} p_{a,u}^- \\ p_{b,u}^+ \end{pmatrix} = \boldsymbol{D} \begin{pmatrix} p_{a,u}^+ \\ p_{b,u}^- \end{pmatrix} \tag{12}$$

which can be transmitted into the form of a matrix as

$$\begin{pmatrix} p_{a,d}^{-} & p_{a,u}^{-} \\ p_{b,d}^{+} & p_{b,u}^{+} \end{pmatrix} = \boldsymbol{D} \begin{pmatrix} p_{a,d}^{+} & p_{a,u}^{+} \\ p_{b,d}^{-} & p_{b,u}^{-} \end{pmatrix} \tag{13}$$

From which it is possible to derive the definition of the scattering matrix $\boldsymbol{D}$ as:

$$\boldsymbol{D} = \frac{\begin{pmatrix} p_{a,d}^{-} & p_{a,u}^{-} \\ p_{b,d}^{+} & p_{b,u}^{+} \end{pmatrix}}{\begin{pmatrix} p_{a,d}^{+} & p_{a,u}^{+} \\ p_{b,d}^{-} & p_{b,u}^{-} \end{pmatrix}} = \begin{pmatrix} D_{11} & D_{12} \\ D_{21} & D_{22} \end{pmatrix} \tag{14}$$

D_{11} is the reflection coefficient in the downstream case, D_{22} the reflection coefficient in the upstream case, D_{12} the transmission coefficient in the downstream case, and D_{21} the transmission coefficient in the upstream case.

The transmission loss in the downstream direction is defined as:

$$\mathrm{TL}^{+} = 10 \log_{10} \left(\frac{1}{|D_{21}|^2} \right) \tag{15}$$

and the transmission loss in the upstream direction is defined as:

$$\mathrm{TL}^{-} = 10 \log_{10} \left(\frac{1}{|D_{12}|^2} \right) \tag{16}$$

B Modified equivalent fluid model for macroperforated plates

The equivalent fluid model presented in Section 1.4 is based on the impedance model firstly proposed by Atalla [13] in a linear regime for a micro perforated plate. Laly et al. [93] then extended the model to a nonlinear acoustic regime, finding good agreements with experimental. This model was used by Diab et al. [51] for both micro and macro perforations. Results presented better agreement with experiments using microperforations rather than macroperforations. The objective of this section are twofold. First, it aimed at modifying the EFM in order to fit the experimental results for the macroperforated plate in Sec. 4.1. Second, it aimed at comparing the results obtained with this modified approach at normal incidence and grazing incidence with flow with those obtained with the Guess model and the reference EFM.

B.0.1 Formulation in nonlinear regime with flow

In this paragraph, we present the modified parameters of the EFM (see Sec. 1.4 for details). We recall the general form of the impedance as:

$$Z = \frac{\mathrm{j}\omega h}{c_0\phi}\alpha_{\infty\mathrm{NL}}\left(1+\frac{\sigma_{\mathrm{NL}}\phi}{\mathrm{j}\omega\varrho_0\alpha_{\infty\mathrm{NL}}}\sqrt{1+\frac{4\mathrm{j}\omega\varrho_0\eta\alpha_{\infty\mathrm{NL}}^2}{\phi^2\sigma_{\mathrm{NL}}^2\Lambda^2}}\right)-\coth(\mathrm{j}kH) \tag{17}$$

The nonlinear resistivity in presence of flow is:

$$\sigma_{\mathrm{NL}} = \sigma + \frac{\beta\sqrt{2}\varrho_0 c_0}{\pi h C_D^2}\frac{(1-\phi^2)}{\phi}\left(\frac{|v_{\mathrm{rms}}|}{c_0}+k_G M\right) \tag{18}$$

with the modified parameters $\beta = 0.56$ and $C_D = 0.6$ based on experimental values. The linear flow resistivity is also modified to:

$$\sigma = \frac{56\eta}{\phi r_p^2} \tag{19}$$

considering a higher value than for the microperforated case.

The nonlinear tortuosity α_{NL} is modified as:

$$\alpha_{\infty\mathrm{NL}} = 0.85 + \frac{1.7\epsilon_{\mathrm{NL}}}{h} \tag{20}$$

For the end correction ϵ_{NL}, the nonlinear form is modified as:

$$\epsilon_{\mathrm{NL}} = \epsilon\left(1+\frac{0.07\sqrt{2}v_{\mathrm{rms}}}{\phi c_0}\right)^{-1}\left(\frac{1}{1+305M^3}\right) \tag{21}$$

with the effect of v_{rms} slightly reduced. Finally, we modify in the linear end correction ϵ:

$$\epsilon = \Psi 0.48\sqrt{\pi}r_p\left[\sum_{n=0}^{8}a_n(\sqrt{\phi})^n\right] \tag{22}$$

the coefficient Ψ with a value set to Ψ=3.2.

B.1 Comparison between impedance models in normal incidence

The first validation of the modified EFM is implemented in normal incidence, recalling the results presented in Chapter 4.

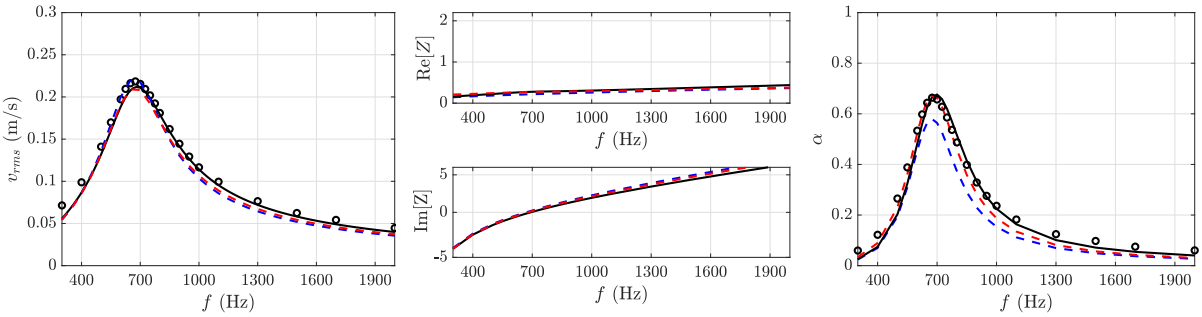

(a) (b) (c)

Figure 30: Comparison between base EFM, modified EFM and Guess model at 92 dB for (a) rms velocity, (b) impedance and (c) absorption coefficient

Figure 30 compares the properties in the linear regime. It is noted that the modified model manages to successfully predict the behaviour of the absorption coefficient, both in value and in peak, compared to the baseline model. Good agreements are found both with experimental and with Guess model. This fact can be due to a higher predicted resistance of the plate compared to the baseline model, in particular at resonance, while the reactance seems to be almost unchanged. Even for what concern the rms velocity, the predictions are satisfactory.

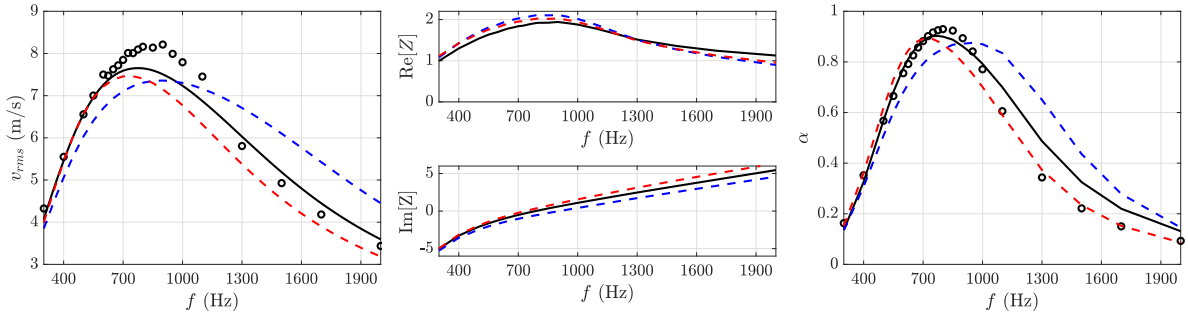

(a) (b) (c)

Figure 31: Comparison between base EFM, modified EFM and Guess model at 130 dB for (a) rms velocity, (b) impedance and (c) absorption coefficient

The nonlinear regime at 130 dB is analysed in Figure 31. The plate resistance results to be inferior to the baseline EFM and closer to the Guess model predictions, while the reactance is slightly overestimated, resulting in a zero value at lower frequencies. This affects the absorption coefficient by managing to predict an exact response at low frequency, but a lower peak at a smaller frequency compared to the experimental. At frequencies superior to 1100 Hz, the agreement returns good compared to experimental. The smaller peak at resonance ca be due to the prediction of the rms velocity, which underestimate the nonlinear effect compared to experiments, following closely the Guess model.

In general, it can be concluded that the modified EFM succeeds in better predict the plate behaviour at normal incidence, both in linear and in nonlinear regime, rather than the baseline EFM. This is partially due to the fact that the model parameters are fitted to the experimental results. A further validation is

performed in grazing incidence with an extended perforated plate.

B.2 Comparison of TL between models in grazing incidence

In this section we are comparing TL predictions for the three approaches. Particular focus will be made on the difference in nonlinear regime and in presence of flow. As explained in Chapter 4, the three impedance models represent the base for a TDABC implemented in a FDTD simulation of the Caiman duct and the macroperforated liner described in Section 2.8.

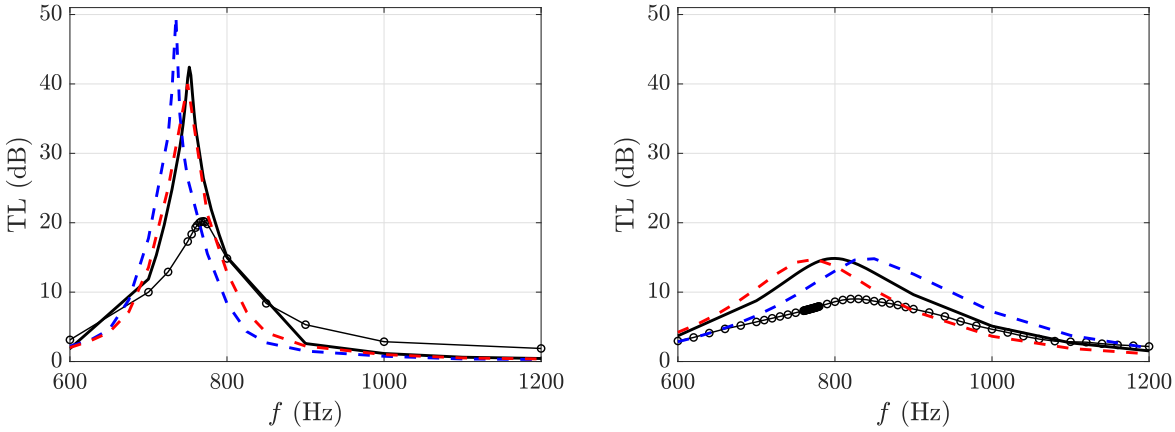

(a) 92 dB (b) 130 dB

Figure 32: TL obtained at $M = 0$ from Experimental, base EFM, modified EFM and Guess model at 130 dB

Figure 32 presents the TL comparison at $M = 0$ in linear and nonlinear case. At 92 dB, the modified EFM presents excellent agreement with the Guess model, both in peak frequency and width and in TL values. The difference between micro and macro perforations is consistent, in particular in this case in linear regime and without flow. At 130 dB, the modified EFM confirms the TL values of the predictions of the Guess model and the base EFM, correctly considering the nonlinear effect. Even in this approach, a distance with the experimental values is observed. For what concern the peak shift, the modified EFM stands at lower frequencies, slightly underestimating the shift observed experimentally.

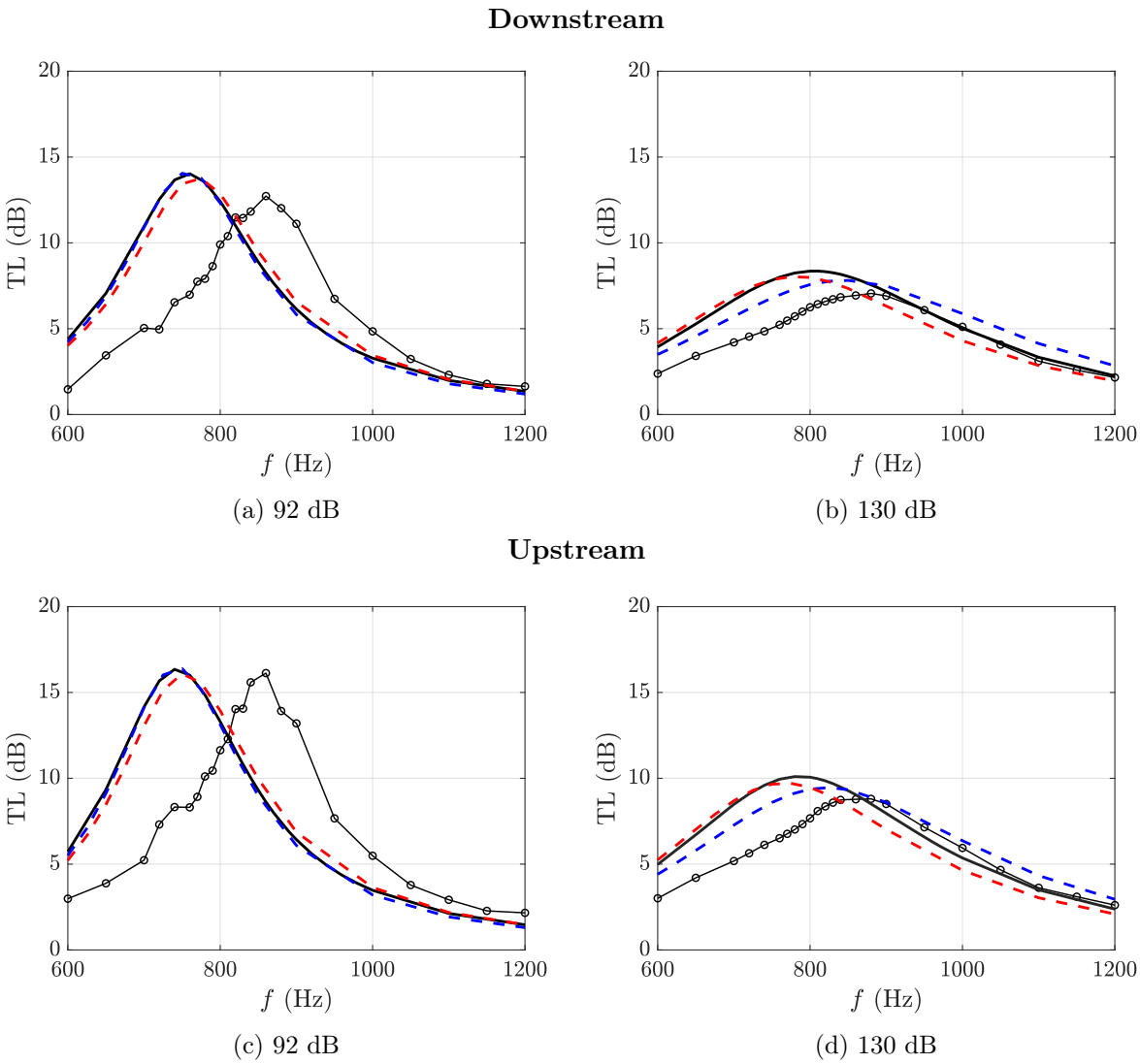

(a) 92 dB (b) 130 dB

(c) 92 dB (d) 130 dB

Figure 33: TL comparison obtained by downstream and upstream approaches at M = 0.05 from in Experimental —o—, - - - base EFM, - - - modified EFM and —— Guess model

The presence of a flow, both downstream and upstream, is considered in Figure 36. The observation for the two cases are similar, with the relative differences already observed in Chapter 4 and successfully reproduced by the modified EFM. At 92 dB, the three approaches are in good agreement, with a slight increase in the frequency range for the modified EFM. In the nonlinear case, consistent to the case without flow, the modified EFM stand at comparable values and with of TL than the other two models, with a slight shift to lower frequencies.

Numerical predictions of acoustic properties of the liner

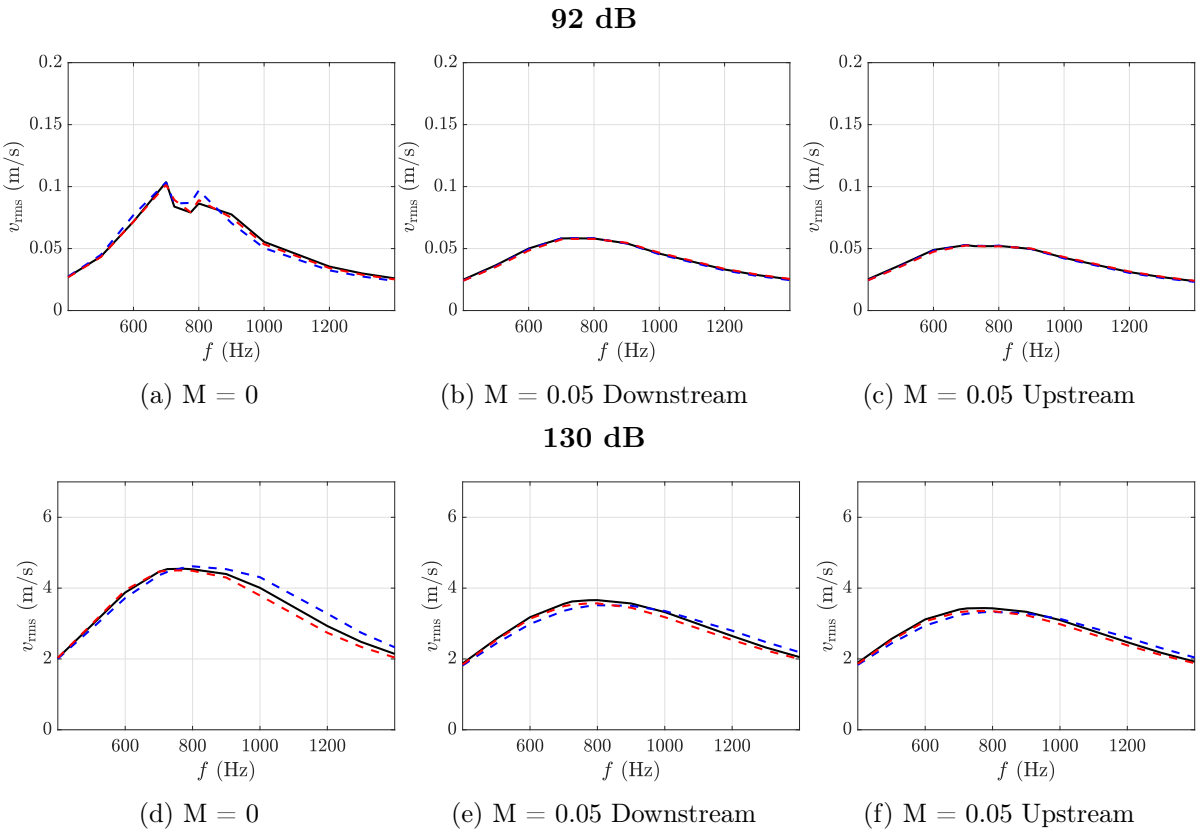

(a) M = 0 (b) M = 0.05 Downstream (c) M = 0.05 Upstream

(d) M = 0 (e) M = 0.05 Downstream (f) M = 0.05 Upstream

Figure 34: Numerical evolution of the mean rms acoustic velocity as a function of the frequencies considered for different sound levels and Mach numbers for - - - base EFM, - - - modified EFM and — Guess model at 130 dB

The mean perforation rms velocity evolution in the frequency range is presented in Figure 34. It can be noted that the modified EFM is in good agreement with the Guess model, both in linear and nonlinear, and with and without flow.

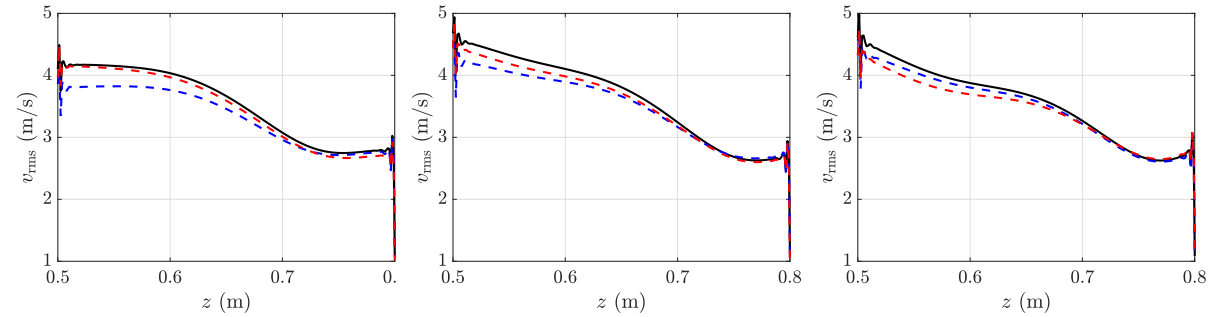

(a) (b) (c)

Figure 35: Numerical predictions of rms acoustic velocity along the liner surface for M = 0.05 downstream at (a) 700 Hz, (b) 800 Hz and (c) 900 Hz for - - - base EFM, - - - modified EFM and — Guess model at 130 dB

Figure 35 presents a more detailed comparison, focusing on the evolution of velocity along the liner for

three frequencies near resonance in nonlinear regime at M = 0.05. For all frequencies, the spatial velocity evolution in the EFM is underestimated compared to the Guess model. Anyway, the trend is absolutely similar and the values are in the range of the ones observed both for Guess and for the base EFM.

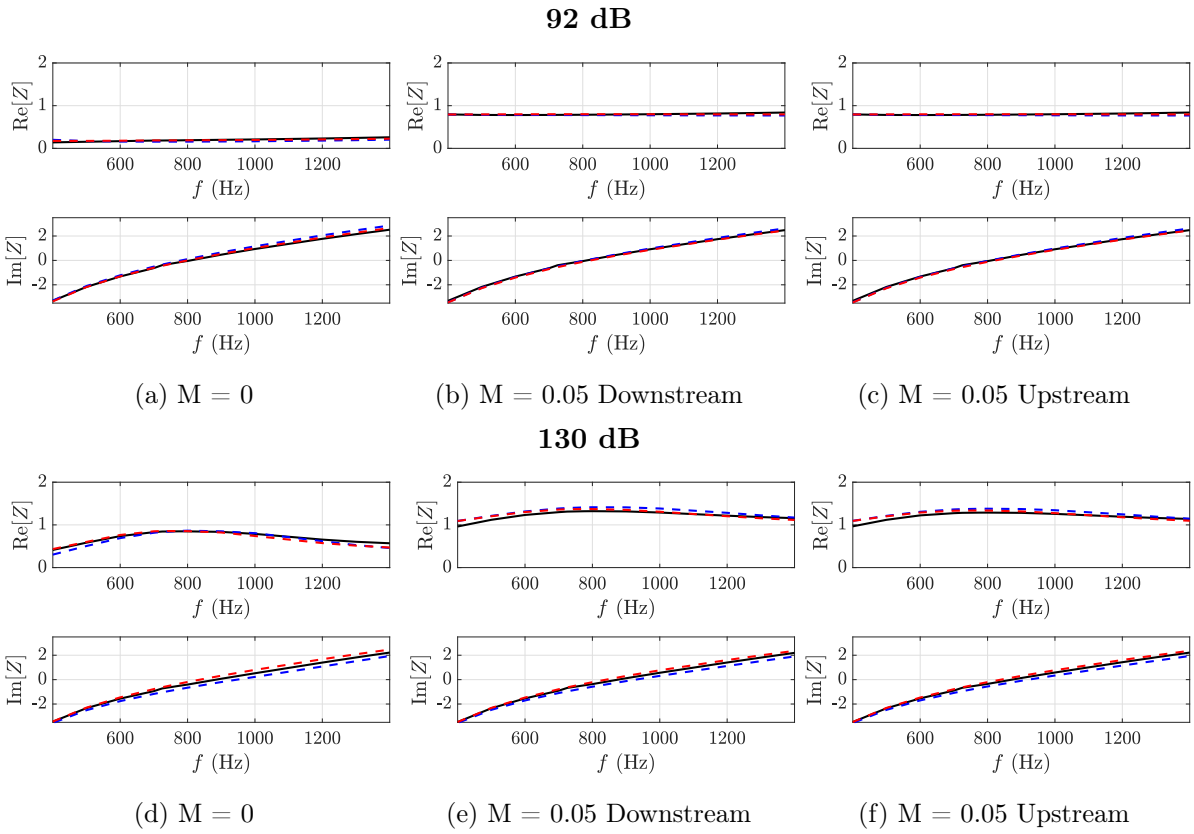

(a) M = 0 (b) M = 0.05 Downstream (c) M = 0.05 Upstream

(d) M = 0 (e) M = 0.05 Downstream (f) M = 0.05 Upstream

Figure 36: Numerical evolution of the mean impedance as a function of the frequencies considered for different sound levels and Mach numbers for - - - base EFM, - - - modified EFM and — Guess model at 130 dB

In Figure 36 we depict the evolution of the mean impedance with the frequency in all the cases considered. Globally, the values of the resistance are always in good agreement with the other two models, predicting similarly the effect of flow and of nonlinearities, especially around resonance. For the reactance, the modified EFM presents a weak increase of the values, justifying the lower peak frequency of the TL observed previously.

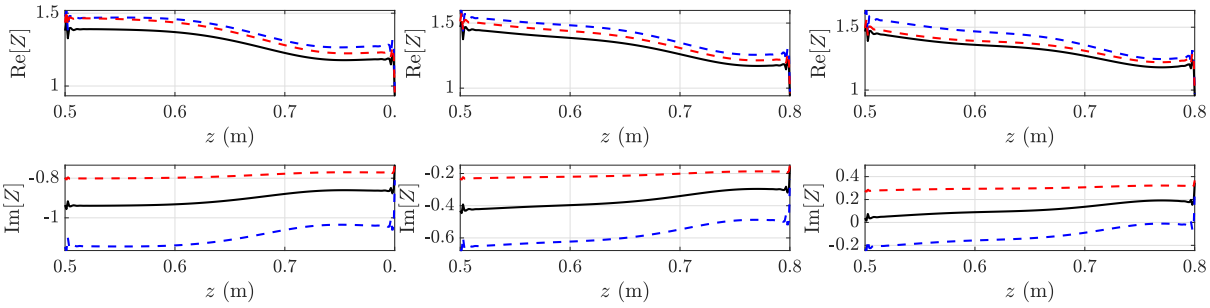

Figure 37: Numerical predictions of impedance along the liner surface for M = 0.05 downstream at (a) 700 Hz, (b) 800 Hz and (c) 900 Hz for - - - base EFM, - - - modified EFM and — Guess model at 130 dB

When considering the spatial evolution of the impedance, as in Figure 37, the general observation is that in presence of flow, nonlinear regime and around resonance, the modified EFM always overestimate both resistance and reactance compared to the other models.

Conclusion

In conclusion, the modification to the EFM to better fit the macroperforated case has proven successful, both in normal and in grazing acoustic incidence. Partially due to the values fitted on the experimental results, the acoustic properties of the plates resulted better modeled than in the baseline EFM. Nevertheless, in order to enlarge the validation of the model, it is aimed to use apply the modified EFM to other plates, with different POA and even diameters.

C Determination of I and R

In this appendix we will show the derivation of the incident and reflection amplitudes I and R and of the global pressure at the plate p_g without flow.

Recalling Figure 2.15, we have the pressure at the microphones expressed as:

$$\begin{cases} p_1 = I\mathrm{e}^{-\mathrm{j}kz_1} + R\mathrm{e}^{\mathrm{j}kz_1} \\ p_2 = I\mathrm{e}^{-\mathrm{j}kz_2} + R\mathrm{e}^{\mathrm{j}kz_2} \\ p_g = p(z=0) = I + R \end{cases} \tag{23}$$

We can define:

$$R = \frac{p_1 - I\mathrm{e}^{-\mathrm{j}kz_1}}{\mathrm{e}^{-\mathrm{j}kz_1}} = p_1\mathrm{e}^{-\mathrm{j}kz_1 - I\mathrm{e}^{-2\mathrm{j}kz_1}} (24)$$

$$R = \frac{p_1 - I\mathrm{e}^{-\mathrm{j}kz_1}}{\mathrm{e}^{-\mathrm{j}kz_1}} = p_1\mathrm{e}^{-\mathrm{j}kz_1} - I\mathrm{e}^{-2\mathrm{j}kz_1} \tag{25}$$

We have:

$$p_2 = I(\mathrm{e}^{-\mathrm{j}kz_2} - \mathrm{e}^{\mathrm{j}k(z_2-2z_1)}) + p_1\mathrm{e}^{\mathrm{j}k(z_2-z_1)} \tag{26}$$

So we can write I and R as:

$$I = \frac{p_2 - p_1\mathrm{e}^{\mathrm{j}k(z_2-z_1)}}{\mathrm{e}^{-\mathrm{j}kz_2} - \mathrm{e}^{\mathrm{j}}} \tag{27}$$

From which we can have R and p_g.

Bibliography

[1] Åbom, M. Measurement of the scattering-matrix of acoustical two-ports. *Mechanical systems and signal processing 5*, 2 (1991), 89–104.

[2] Åbom, M. A note on the experimental determination of acoustical two-port matrices. *Journal of sound and vibration 155*, 1 (1992), 185–188.

[3] Abom, M., and Sack, S. Revisiting the Cremer Impedance. *Forum Acusticum, Dec 2020, Lyon, France* (2020), 4 pages. Artwork Size: 4 pages Publisher: e-Forum Acusticum 2020.

[4] Alamo Vargas, V.and Gourdon, E., and Ture Savadkoohi, A. *Nonlinear softening and hardening behavior in Helmholtz resonators for nonlinear regimes.* Nonlinear Dyn 91, 217–231, 2018.

[5] Alamo Vargas, V. *Transfert energetique irreversible grace a un resonateur acoustique a comportement non-lineaire.* Theses, Universite de Lyon, Sept. 2018.

[6] Allam, S., and Abom, M. A New Type of Muffler Based on Microperforated Tubes. *Journal of vibration and acoustics 133* (Mar. 2011).

[7] Allard, J. F. Propagation of sound in porous media: Modelling sound absorbing materials.

[8] Allard, J.-F., and Champoux, Y. New empirical equations for sound propagation in rigid frame fibrous materials. *The Journal of the Acoustical Society of America 91*, 6 (1992), 3346–3353.

[9] Alomar, A., and Aurégan, Y. Particle image velocimetry measurement of an instability wave over a porous wall in a duct with flow. *Journal of Sound and Vibration 386* (2017), 208–224.

[10] Alomar, A., Dragna, D., and Galland, M.-A. Time-domain simulations of sound propagation in a flow duct with extended-reacting liners. *Journal of Sound and Vibration 507* (2021), 116137.

[11] Alomar, A. I., Dragna, D., and Galland, M.-A. Extended-reacting liners in time-domain simulations for broadband attenuation with flow. *The Journal of the Acoustical Society of America 146*, 4_Supplement (2019), 2786–2786.

[12] Astley, R., Cummings, A., and Sormaz, N. A finite element scheme for acoustic propagation in flexible-walled ducts with bulk-reacting liners, and comparison with experiment. *Journal of Sound and Vibration 150*, 1 (1991), 119–138.

[13] Atalla, N., and Sgard, F. Modeling of perforated plates and screens using rigid frame porous models. *Journal of Sound and Vibration 303*, 1 (2007), 195–208.

[14] Auregan, Y., and Pachebat, M. Measurement of the nonlinear behavior of acoustical rigid porous materials. *Physics of fluids 11*, 6 (1999), 1342–1345.

[15] Avallone, F., Paduano, A., Pereira, L. M., Bonomo, L. A., Cordioli, J. A., Casalino, D., and Cerizza, D. On the comparison of different methods for impedance eduction applied to a numerical database. In *30th AIAA/CEAS Aeroacoustics Conference (2024)* (2024), p. 3294.

[16] Bellet, R., Cochelin, B., Herzog, P., and Mattei, P.-O. Experimental study of targeted energy transfer from an acoustic system to a nonlinear membrane absorber. *Journal of Sound and Vibration 329*, 14 (2010), 2768–2791.

[17] Berland, J., Bogey, C., and Bailly, C. Low-dissipation and low-dispersion fourth-order runge–kutta algorithm. *Computers and Fluids 35*, 10 (2006), 1459–1463.

[18] Berland, J., Bogey, C., Marsden, O., and Bailly, C. High-order, low dispersive and low dissipative explicit schemes for multiple-scale and boundary problems. *Journal of Computational Physics 224*, 2 (2007), 637–662.

[19] Betgen, B. *Comportement d'un absorbant actif en écoulement : étude théorique et expérimentale*. PhD thesis, 2010. Thèse de doctorat dirigée par Galland, Marie-Annick et Simon, Frank Acoustique Ecully, Ecole centrale de Lyon 2010.

[20] Bi, W., Pagneux, V., Lafarge, D., and Aurégan, Y. Sound propagation in non-uniform lined duct by the multimodal method. In *Proceedings of 10th International Conference on Sound and Vibration* (2003), pp. 3229–3236.

[21] Billard, R. *Study of perforated liners for aeronautics*. Phd thesis, Le Mans, Apr. 2021.

[22] Billard, R., Tissot, G., Gabard, G., and Versaevel, M. Numerical simulations of perforated plate liners: Analysis of the visco-thermal dissipation mechanisms. *The Journal of the Acoustical Society of America 149*, 1 (2021), 16–27.

[23] Bodén, H., and Du, L. The effect of changes in downstream acoustic termination on the nonlinear acoustic properties of perforates. Cited by: 1.

[24] Bogey, C., and Bailly, C. A family of low dispersive and low dissipative explicit schemes for flow and noise computations. *Journal of Computational physics 194*, 1 (2004), 194–214.

[25] Bogey, C., De Cacqueray, N., and Bailly, C. A shock-capturing methodology based on adaptative spatial filtering for high-order non-linear computations. *Journal of Computational Physics 228*, 5 (2009), 1447–1465.

[26] Bolton, J. S., Yoo, T., and Olivieri, O. Measurement of normal incidence transmission loss and other acoustical properties of materials placed in a standing wave tube. *Brüel & Kjær Technical Review 1* (2007), 1–44.

[27] Bonomo, L., Avallone, F., Pereira, L., Quintino, N., da Silva, A., Cordioli, J., and Casalino, D. Extracting the acoustic-induced velocity within the orifice of a conventional acoustic liner: Post-processing methods.

[28] Bonomo, L. A., Quintino, N. T., Cordioli, J. A., Avallone, F., Jones, M. G., Howerton, B. M., and Nark, D. M. A comparison of impedance eduction test rigs with different flow profiles. In *AIAA AVIATION 2023 Forum* (2023), p. 3346.

[29] Bonomo, L. A., Quintino, N. T., Spillere, A., Cordioli, J. A., and Murray, P. B. A comparison of in-situ and impedance eduction experimental techniques for acoustic liners with grazing flow and high spl. In *28th AIAA/CEAS Aeroacoustics 2022 Conference* (2022), p. 2998.

[30] Borelli, D., and Schenone, C. A finite element model to predict sound attenuation in lined and parallel-baffle rectangular ducts. *HVAC&R Research 18*, 3 (2012), 390–405.

[31] Borelli, D., and Schenone, C. On the acoustic transparency of perforated metal plates facing a porous fibrous material. *Noise Mapping 8*, 1 (2021), 185–203.

[32] Canuto, C., Tabacco, A., Canuto, C., and Tabacco, A. Serie di fourier. *Analisi Matematica II* (2014), 81–116.

[33] Carcione, J. M., Kosloff, D., and Kosloff, R. Viscoacoustic wave propagation simulation in the earth. *Geophysics 53*, 6 (1988), 769–777.

[34] Cardano, G., and Witmer, T. R. Ars magna, or, the rules of algebra. *(No Title)* (1993).

[35] Chu, W. Extension of the two-microphone transfer function method for impedance tube measurements. *The Journal of the Acoustical Society of America 80*, 1 (1986), 347–348.

[36] Chung, J., and Blaser, D. Transfer function method of measuring in-duct acoustic properties. i. theory. *The Journal of the Acoustical Society of America 68*, 3 (1980), 907–913.

[37] Chung, J., and Blaser, D. Transfer function method of measuring in-duct acoustic properties. ii. experiment. *The Journal of the Acoustical Society of America 68*, 3 (1980), 914–921.

[38] Cochelin, B., Herzog, P., and Mattei, P.-O. Experimental evidence of energy pumping in acoustics. *Comptes Rendus Mecanique 334*, 11 (2006), 639–644.

[39] Cockburn, B. Numerical resolution of maxwell's equations in polarisable media at radio and lower frequencies. *SIAM journal on scientific and statistical computing 6*, 4 (1985), 843–852.

[40] Crandall, I. B. *Theory of vibrating systems and sound*. D. Van Nostrand Company, 1926.

[41] Cremer, L. Theory regarding the attenuation of sound transmitted by air in a rectangular duct with an absorbing wall, and the maximum attenuation constant produced during this process. *Acustica 3, 249-263* (1953), 249–263.

[42] Crouse, B., Senthooran, S., Freed, D., Balasubramanian, G., Gleason, M., Puskarz, M., Lew, P.-T., and Mongeau, L. Experimental and numerical investigation of a flow-induced cavity resonance with application to automobile buffeting. In *12th AIAA/CEAS Aeroacoustics Conference (27th AIAA Aeroacoustics Conference)* (2006), p. 2494.

[43] Cummings, A. Acoustic nonlinearities and power losses at orifices. *AIAA journal 22*, 6 (1984), 786–792.

[44] Cummings, A. Transient and multiple frequency sound transmission through perforated plates at high amplitude. *The Journal of the Acoustical Society of America 79*, 4 (1986), 942–951.

[45] Dai, X., and Aurégan, Y. Acoustic of a perforated liner with grazing flow: Floquet-Bloch periodical approach versus impedance continuous approach. *The Journal of the Acoustical Society of America 140* (Sept. 2016), 2047–2055.

[46] De Bono, E., Collet, M., Ouisse, M., Lissek, H., Volery, M., Billon, K., Sergeev, S., and Mardjono, J. Electroacoustic liner for tonal and broadband noise attenuation of turbofans. In *INTER-NOISE and NOISE-CON Congress and Conference Proceedings* (2024), vol. 270, Institute of Noise Control Engineering, pp. 4853–4858.

[47] Dean, L., and Feder, E. Analytical and experimental studies for predicting noise attenuation in acoustically treated ducts for turbofan engines. Tech. rep., NASA, 1969.

[48] Dean, P. An in situ method of wall acoustic impedance measurement in flow ducts. *Journal of Sound and Vibration 34*, 1 (1974), 97–IN6.

[49] Deng, Y. *Time-domain simulation of sound propagation in a lined flow duct : characterization and suppression of hydrodynamic instabilities*. PhD thesis, 2020.

[50] Deng, Y., Alomar, A., Dragna, D., and Galland, M.-A. Characterization and suppression of the hydrodynamic instability in the time domain for acoustic propagation in a lined flow duct. *Journal of Sound and Vibration 500* (2021), 115999.

[51] Diab, D., Dragna, D., Salze, E., and Galland, M.-A. Nonlinear broadband time-domain admittance boundary condition for duct acoustics. application to perforated plate liners. *Journal of Sound and Vibration 528* (2022), 116892.

[52] Dragna, D., Pineau, P., and Blanc-Benon, P. A generalized recursive convolution method for time-domain propagation in porous media. *The Journal of the Acoustical Society of America 138*, 2 (2015), 1030–1042.

[53] Fahy, F. *Sound intensity*. CRC Press, 2017.

[54] Fok, V. Theoretical study of the conductivity of a circular hole in a septum placed across the tube. In *Dokladi Akademii nauk SSSR 31* (1941).

[55] Forner, K., Temiz, M. A., Polifke, W., Arteaga, I. L., and Hirschberg, A. On the non-linear influence of the edge geometry on vortex shedding in helmholtz resonators. In *Proceedings of the 22nd International Conference on Sound and Vibration* (2015), pp. 2015–1341.

[56] Gabard, G. A comparison of impedance boundary conditions for flow acoustics. *Journal of Sound and Vibration 332*, 4 (2013), 714–724.

[57] Gallerand, L., Legrand, M., Dupont, T., and Leclaire, P. Vibration and damping analysis of a thin finite-size microperforated plate. *Journal of Sound and Vibration 541* (2022), 117295.

[58] Gallerand, L., Legrand, M., Panneton, R., Leclaire, P., and Dupont, T. Added non-linear damping of homogenized fluid-saturated microperforated plates in forchheimer flow regime. *Journal of Sound and Vibration 606* (2025), 119018.

[59] Gavin, H. P. The levenberg-marquardt algorithm for nonlinear least squares curve-fitting problems. *Department of Civil and Environmental Engineering Duke University August 3* (2019).

[60] Glav, R., and Åbom, M. A general formalism for analyzing acoustic 2-port networks, 1997.

[61] Groeneweg, J. F. Current understanding of helmholtz resonator arrays as duct boundary conditions. In *Basic Aerodynamic Noise Research: A Conference Held at NASA Headquarters, Washington, DC, July 14-15, 1969* (1969), vol. 207, Scientific and Technical Information Division, National Aeronautics and ..., p. 357.

[62] Guess, A. Calculation of perforated plate liner parameters from specified acoustic resistance and reactance. *Journal of Sound and Vibration 40*, 1 (1975), 119–137.

[63] Hersh, A. S., and Walker, B. Acoustic behavior of helmholtz resonators: part ii: Effects of grazing flow. *CEAS/AIAA 95-079 595-604* (1995).

[64] Hesthaven, J. S., and Warburton, T. *Nodal discontinuous Galerkin methods: algorithms, analysis, and applications*. Springer Science & Business Media, 2007.

[65] Howerton, B. M., Vold, H., and Jones, M. G. Application of swept sine excitation for acoustic impedance eduction. In *25th AIAA/CEAS Aeroacoustics Conference* (2019), p. 2487.

[66] Hu, Y. *Développement de panneaux hybrides passifs/actifs pour l'acoustique*. PhD thesis, 2010. Thèse de doctorat dirigée par Galland, Marie-Annick et Chen, Kean Acoustique Ecully, Ecole centrale de Lyon 2010.

[67] Ih, J.-G. On the inertial end correction of resonators. *Acta Acustica united with Acustica 78*, 1 (1993), 1–15.

[68] Inagaki, M., Murata, O., Kondoh, T., and Abe, K.-i. Numerical prediction of fluid-resonant oscillation at low mach number. *AIAA journal 40*, 9 (2002), 1823–1829.

[69] Ingard, U. On the theory and design of acoustic resonators. *Journal of the Acoustical Society of America 25* (1953), 1037–1061.

[70] Ingard, U., and Ising, H. Acoustic Nonlinearity of an Orifice. *The Journal of the Acoustical Society of America 42*, 1 (July 1967), 6–17.

[71] Jamois, A. *Modélisation et réalisation d'absorbants acoustiques par impression 3D : étude en incidence normale et application au traitement d'un conduit*. 2024. Thèse de doctorat dirigée par Galland, Marie-Annick Acoustique Ecully, Ecole centrale de Lyon 2024.

[72] Jamois, A., Dragna, D., and Galland, M.-A. Impact of manufacturing uncertainties on the acoustic properties of 3d printed materials. In *29th International Congress on Sound and Vibration, ICSV 2023* (2023).

[73] Jaouen, L., and Chevillotte, F. Length correction of 2d discontinuities or perforations at large wavelengths and for linear acoustics. *arXiv preprint arXiv:1804.09391* (2018).

[74] Johnson, D. L., Koplik, J., and Dashen, R. Theory of dynamic permeability and tortuosity in fluid saturated porous media. *Journal of Fluid Mechanics 176* (1987), 379 – 402. Cited by: 2060.

[75] Joly, N. Finite element modeling of thermoviscous acoustics on adapted anisotropic meshes: Implementation of the particle velocity and temperature variation formulation. *Acta acustica united with acustica 96*, 1 (2010), 102–114.

[76] Joly, N., Bruneau, M., and Bossart, R. Coupled equations for particle velocity and temperature variation as the fundamental formulation of linear acoustics in thermo-viscous fluids at rest. *Acta Acustica united with Acustica 92*, 2 (2006), 202–209.

[77] Jones, M., Tracy, M., Watson, W., and Parrott, T. Effects of liner geometry on acoustic impedance.

[78] Jones, M., Watson, W., and Parrott, T. Benchmark data for evaluation of aeroacoustic propagation codes with grazing flow. In *11th AIAA/CEAS Aeroacoustics Conference* (2005), p. 2853.

[79] Jones, M. G., Simon, F., and Roncen, R. Broadband and low-frequency acoustic liner investigations at nasa and onera. *AIAA Journal 60*, 4 (2022), 2481–2500.

[80] Jones, M. G., Watson, W., Howerton, B., and Busse-Gerstengarbe, S. Effects of mean flow assumption and harmonic distortion on impedance eduction methods. *AIAA Journal 53*, 6 (2015), 1503–1514.

[81] Jones, M. G., Watson, W. R., Nark, D. M., Howerton, B. M., and Brown, M. C. A review of acoustic liner experimental characterization at nasa langley.

[82] Jones, M. G., Watson, W. R., Nark, D. M., and Schiller, N. H. Evaluation of spanwise variable impedance liners with three-dimensional aeroacoustics propagation codes. In *23rd AIAA/CEAS Aeroacoustics Conference* (2017), p. 3021.

[83] Kaczynski, J., Ranacher, C., and Fleury, C. Computationally efficient model for viscous damping in perforated mems structures. *Sensors and Actuators A: Physical 314* (2020), 112201.

[84] Kampinga, W., Wijnant, Y. H., and de Boer, A. Performance of several viscothermal acoustic finite elements. *Acta acustica united with Acustica 96*, 1 (2010), 115–124.

[85] Kampinga, W., Wijnant, Y. H., and de Boer, A. An efficient finite element model for viscothermal acoustics. *Acta Acustica united with Acustica 97*, 4 (2011), 618–631.

[86] Kinsler, L., Frey, A., and Coppens, A. Fundamentals of acoustics. vol. 4th ed. New York: John Wiley and Sons, Inc„ 4th ed. New York: John Wiley and Sons, Inc.

[87] Kirby, R. Simplified techniques for predicting the transmission loss of a circular dissipative silencer. *Journal of Sound and Vibration 243*, 3 (2001), 403–426.

[88] Kooi, J., and Sarin, S. An experimental study of the acoustic impedance of Helmholtz resonator arrays under a turbulent boundary layer. In *7th Aeroacoustics Conference*, Aeroacoustics Conferences. American Institute of Aeronautics and Astronautics, Oct. 1981.

[89] Lacombe, R., Föller, S., Jasor, G., Polifke, W., Auregan, Y., and Moussou, P. Identification of aero-acoustic scattering matrices from large eddy simulation: Application to whistling orifices in duct. *Journal of Sound and Vibration 332*, 20 (2013), 5059–5067.

[90] Lafarge, D., Lemarinier, P., Allard, J. F., and Tarnow, V. Dynamic compressibility of air in porous structures at audible frequencies. *The Journal of the Acoustical Society of America 102*, 4 (1997), 1995–2006.

[91] Lafont, V., Mery, F., Roncen, R., Simon, F., and Piot, E. Liner impedance eduction under shear grazing flow at a high sound pressure level. *AIAA Journal 58*, 3 (2020), 1107–1117.

[92] Laly, Z., Atalla, N., and Meslioui, S.-A. Acoustical modeling of micro-perforated panel at high sound pressure levels using equivalent fluid approach. *Journal of Sound and Vibration 427* (2018), 134–158.

[93] Laly, Z., Atalla, N., Meslioui, S.-A., and Khalid, e. b. Modeling of acoustic lined duct with and without grazing air flow by an analytical method. *Noise Control Engineering Journal 66* (July 2018), 340–352.

[94] Laly, Z., Feng, X., and Atalla, N. An experimental transfer matrix method to characterize acoustic materials at high sound pressure levels in airflow environment. *Applied Acoustics 206* (2023), 109311.

[95] Lavrentjev, J., Åbom, M., and Boden, H. A measurement method for determining the source data of acoustic two-port sources. *Journal of sound and vibration 183*, 3 (1995), 517–531.

[96] Leon, O., Piot, E., Sebbane, D., and Simon, F. Measurement of acoustic velocity components in a turbulent flow using ldv and high-repetition rate piv. *Experiments in fluids 58* (2017), 1–19.

[97] Ma, R., Slaboch, P. E., and Morris, S. C. Fluid mechanics of the flow-excited Helmholtz resonator. *Journal of Fluid Mechanics 623* (Mar. 2009), 1–26.

[98] Maa, D.-Y. Microperforated panel at high sound intensity. In *INTER-NOISE and NOISE-CON Congress and Conference* (1994), pp. 1511–1514.

[99] Mallick, S., Shock, R., and Yakhot, V. Numerical simulation of the excitation of a helmholtz resonator by a grazing flow. *The Journal of the Acoustical Society of America 114*, 4 (2003), 1833–1840.

[100] Malmary, C., Carbonne, S., Auregan, Y., and Pagneux, V. Acoustic impedance measurement with grazing flow. In *7th AIAA/CEAS Aeroacoustics Conference and Exhibit* (2001), p. 2193.

[101] Mangin, B., Daroukh, M., and Gabard, G. An application of the multiple-scales theory to acoustic double transition in ducts with flow. *Journal of Sound and Vibration 539* (2022), 117252.

[102] Mangin, B., Gabard, G., and Daroukh, M. In-duct flow computation and acoustic propagation using the admittance multimodal formulation. *The Journal of the Acoustical Society of America 155*, 5 (2024), 3461–3474.

[103] Martin, L., Bogey, C., Clair, V., and Gabard, G. Computational study on sound scattering by jet shear layers. In *30th AIAA/CEAS Aeroacoustics Conference (2024)* (2024), p. 3183.

[104] Martin-Martin, L., Clair, V., Bogey, C., and Gabard, G. Numerical study of the scattering of acoustic waves by an elliptic vortex. *The Journal of the Acoustical Society of America 155*, 3 (2024), 1707–1718.

[105] Meissner, M. The influence of acoustic nonlinearity on absorption properties of helmholtz resonators. part ii. experiment. *Archives of Acoustics 25*, 2 (2000).

[106] Meissner, M. The response of a helmholtz resonator to external excitation. part ii: Flow-induced resonance. *Archives of Acoustics 30*, 1 (2005).

[107] Melling, T. The acoustic impendance of perforates at medium and high sound pressure levels. *Journal of Sound and Vibration 29*, 1 (1973), 1–65.

[108] Meng, Y., Xin, B., Jing, X., Sun, X., Boden, H., and Åbom, M. Semi-empirical impedance model of perforated plate under grazing flow. In *25th AIAA/CEAS Aeroacoustics Conference* (Delft, The Netherlands, May 2019), American Institute of Aeronautics and Astronautics.

[109] Monteghetti, F., Matignon, D., and Piot, E. Energy analysis and discretization of nonlinear impedance boundary conditions for the time-domain linearized euler equations. *Journal of Computational Physics 375* (2018), 393–426.

[110] Motsinger, R., and Kraft, R. 14 design and performance of duct acoustic treatment. *Aeroacoustics of flight vehicles: theory and practice 1* (1991), 165.

[111] Moufid, I. *Étude théorique et modélisation numérique du comportement acoustique des milieux poreux rigides en régime temporel*. PhD thesis, Institut Supérieur de l'Aéronautique et de l'Espace (ISAE), 2022.

[112] Moufid, I., Matignon, D., Roncen, R., and Piot, E. Energy analysis and discretization of the time-domain equivalent fluid model for wave propagation in rigid porous media. *Journal of Computational Physics 451* (2022), 110888.

[113] Moufid, I., Roncen, R., Matignon, D., and Piot, E. Time-domain simulation of the acoustic nonlinear response of acoustic liners at high sound pressure level. *Nonlinear Dynamics 112*, 5 (2024), 3133–3162.

[114] Munjal, M. L., and Doige, A. G. Theory of a two source-location method for direct experimental evaluation of the four-pole parameters of an aeroacoustic element. *Journal of Sound and Vibration 141*, 2 (1990), 323–333.

[115] NAYFEH, A. H., and MOOK, D. T. Nonlinear oscillation. *Wiley and Sons, New York* (1979).

[116] Özyörük, Y., Long, L. N., and Jones, M. G. Time-domain numerical simulation of a flow-impedance tube. *Journal of Computational Physics 146*, 1 (1998), 29–57.

[117] Pavan, G., and Singh, S. A coplanar metamaterial with variable channels for ventilated noise control. *Applied Acoustics 234* (2025), 110638.

[118] Piot, E., Primus, J., and Simon, F. Liner impedance eduction technique based on velocity fields. In *18th AIAA/CEAS Aeroacoustics Conference (33rd AIAA Aeroacoustics Conference)* (2012), p. 2198.

[119] Rice, E. J. A model for the acoustic impedance of a perforated plate liner with multiple frequency excitation. Tech. rep., 1971.

[120] Rienstra, S. W. A classification of duct modes based on surface waves. *Wave motion 37*, 2 (2003), 119–135.

[121] Roche, J.-M. *Simulation numerique de l'absorption acoustique de materiaux resonants en presence d'ecoulement/ Theses. fr*. PhD thesis, Le Mans, 2011.

[122] Roncen, R. Acoustic nonlinearity of a perforated plate backed by a porous material.

[123] Roncen, R., Mery, F., Piot, E., and Klotz, P. Spatially-varying impedance model for locally reacting acoustic liners at a high sound intensity. *Journal of Sound and Vibration 524* (2022), 116741.

[124] Ronneberger, D. The acoustical impedance of holes in the wall of flow ducts. *Journal of Sound and Vibration 24*, 1 (1972), 133–150.

[125] Ronneberger, D. The acoustical impedance of holes in the wall of flow ducts. *Journal of Sound and Vibration 24*, 1 (1972), 133–150.

[126] Rossing, T. *Springer Handbook of Acoustics*. Springer Science & Business Media, June 2007. Google-Books-ID: 4ktVwGe_dSMC.

[127] Rzhevkin, S. N. Resonance sound absorber with yielding wall. Tech. rep., 1951.

[128] Rzhevkin, S. N., Blunn, O., and Doak, P. E. A course of lectures on the theory of sound. *(No Title)* (1963).

[129] Sarpero, E., Gourdon, E., and Borelli, D. Experimental characterisation and optimisation of 3D printed stacks for thermoacoustic refrigeration. In *29th International Congress on Sound and Vibration* (Prague (CZ), July 2023).

[130] Sarpero, E., Gourdon, E., and Borelli, D. Experimental development and optimization of a standing wave thermoacoustic refrigerator using additive manufactured stacks. *International Journal of Refrigeration 146* (2023), 63–73.

[131] Sellen, N. *Modification de l'impédance de surface d'un matériau par contrôle actif : Application à la caractérisation et à l'optimisation d'un absorbant acoustique*. PhD thesis, 2003. Thèse de doctorat dirigée par Galland, Marie-Annick Sciences. Acoustique Ecully, Ecole centrale de Lyon 2003.

[132] Sergeev, S., Lissek, H., Howling, A., Furno, I., Plyushchev, G., and Leyland, P. Development of a plasma electroacoustic actuator for active noise control applications. *Journal of Physics D: Applied Physics 53*, 49 (2020), 495202.

[133] Shah, S. A., Bodén, H., and Boij, S. An experimental study on three-port measurements for acoustic characterisation of the perforate resistance. *Journal of Sound and Vibration 556* (2023), 117686.

[134] Shur, M., Strelets, M., Travin, A., Suzuki, T., and Spalart, P. Unsteady simulations of sound propagation in turbulent flow inside a lined duct. *AIAA Journal 59*, 8 (2021), 3054–3070.

[135] Singh, D., and Rienstra, S. Nonlinear asymptotic impedance model for a helmholtz resonator liner. *Journal of Sound and Vibration 333*, 15 (2014), 3536–3549.

[136] Sivian, L. J. Acoustic Impedance of Small Orifices. *The Journal of the Acoustical Society of America 7*, 2 (Oct. 1935), 94–101.

[137] Soon-Hong, P. A design method of micro-perforated panel absorber at high sound pressure environment in launcher fairings. *Journal of Sound and Vibration 332*, 3 (2013), 521–535.

[138] Spillere, A. M., Braga, D. S., Seki, L. A., Bonomo, L. A., Cordioli, J. A., Rocamora Jr, B. M., Greco Jr, P. C., dos Reis, D. C., and Coelho, E. L. Design of a single degree of freedom acoustic liner for a fan noise test rig. *International Journal of Aeroacoustics 20*, 5-7 (2021), 708–736.

[139] Spillere, A. M. N., Bonomo, L. A., Cordioli, J. A., and Brambley, E. J. Experimentally testing impedance boundary conditions for acoustic liners with flow: Beyond upstream and downstream. *Journal of Sound and Vibration 489* (2020), 115676.

[140] Stewart, I. *Galois theory*. Chapman and Hall/CRC, 2022.

[141] Tam, C. K., Kurbatskii, K. A., Ahuja, K., and Gaeta Jr, R. A numerical and experimental investigation of the dissipation mechanisms of resonant acoustic liners. *Journal of Sound and Vibration 245*, 3 (2001), 545–557.

[142] Tao, Z., and Seybert, A. A review of current techniques for measuring muffler transmission loss. *SAE transactions* (2003), 2096–2100.

[143] Tayong, R., Dupont, T., and Leclaire, P. On the variations of acoustic absorption peak with particle velocity in micro-perforated panels at high level of excitation. *The Journal of the Acoustical Society of America 127*, 5 (2010), 2875–2882.

[144] Tayong, R., Dupont, T., and Leclaire, P. Experimental investigation of holes interaction effect on the sound absorption coefficient of micro-perforated panels under high and medium sound levels. *Applied Acoustics 72*, 10 (2011), 777–784.

[145] Temiz, M., Lopez Arteaga, I., and Hirschberg, A. Sound absorption measurements for micro-perforated plates : the effect of edge profile. In *Euronoise 2015, the 10th European Congress and Exposition on Noise Control Engineering, May 31 - June 3, 2015, Maastricht, The Netherlands* (May 2015), European Acoustics Association, pp. 1–5.

[146] Temiz, M. A., Lopez Arteaga, I., Efraimsson, G., Åbom, M., and Hirschberg, A. The influence of edge geometry on end-correction coefficients in micro perforated plates. *The Journal of the Acoustical Society of America 138*, 6 (Dec. 2015), 3668–3677.

[147] Tester, B. J. The optimization of modal sound attenuation in ducts, in the absence of mean flow. *Journal of Sound and Vibration 27*, 4 (1973), 477–513.

[148] Tissot, G., Billard, R., and Gabard, G. Optimal cavity shape design for acoustic liners using helmholtz equation with visco-thermal losses. *Journal of Computational Physics 402* (2020), 109048.

[149] Toulorge, T., and Desmet, W. Optimal runge–kutta schemes for discontinuous galerkin space discretizations applied to wave propagation problems. *Journal of Computational Physics 231*, 4 (2012), 2067–2091.

[150] Troian, R., Dragna, D., Bailly, C., and Galland, M.-A. Broadband liner impedance eduction for multimodal acoustic propagation in the presence of a mean flow. *Journal of Sound and Vibration 392* (2017), 200–216.

[151] van Schaik, W., Grooten, M., Wernaart, T., and van der Geld, C. High accuracy acoustic relative humidity measurement in duct flow with air. *Sensors (Basel, Switzerland) 10* (08 2010), 7421–33.

[152] Wen, H., Wu, C., Wu, T., and Guo, J. Acoustic impedance extraction method and acoustic characteristics analysis of perforated plates under grazing flow. *Journal of Low Frequency Noise, Vibration and Active Control 43* (Mar. 2024), 289–304.

[153] White, F. M., and Majdalani, J. *Viscous fluid flow*, vol. 3. McGraw-Hill New York, 2006.

[154] Williamschen, M., Gabard, G., and Bériot, H. Performance of the dgm for the linearized euler equations with non-uniform mean-flow. In *21st AIAA/CEAS Aeroacoustics Conference* (2015), p. 3277.

[155] Yu, G., Zhang, Y., and Shen, Y. Nonlinear amplitude-frequency response of a helmholtz resonator.

[156] Zhang, X., and Cheng, L. Acoustic impedance of micro-perforated panels in a grazing flow. *The Journal of the Acoustical Society of America 145*, 4 (Apr. 2019), 2461–2469.

Emanuele SARPERO

CENTRALE LYON

AUTORISATION DE SOUTENANCE DE THÈSE

Numéro NNT : 2025ECDL0017
Doctorant : Emanuele SARPERO
École Doctorale : MEGA
Date de soutenance prévue : 18 juin 2025
Lieu de soutenance : 36, avenue Guy de Collongue, bâtiment W1, 69130 Écully

Vu l'avis des rapporteurs :

- Madame Estelle PIOT, Directrice de recherche
- Monsieur Gwénaël GABARD, Professeur des universités

Proposition de la Direction de thèse :	**Avis de la Direction de l'École Doctorale :**
Favorable Date : 3 juin 2025 Marie-annick GALLAND	Favorable Date : 3 juin 2025 Etienne PARIZET

Décision du Chef d'Établissement :

La soutenance est **autorisée**

Date : 3 juin 2025